Free-breathing cardiac diffusion imaging

Kevin Moulin

To cite this version:

Kevin Moulin. Free-breathing cardiac diffusion imaging. Cardiology and cardiovascular system. Université de Lyon, 2016. English. <NNT : 2016LYSE1007>. <tel-01359576>

HAL Id: tel-01359576
https://tel.archives-ouvertes.fr/tel-01359576

Submitted on 2 Sep 2016

N°d'ordre NNT : **07 - 2016**

THESE de DOCTORAT DE L'UNIVERSITE DE LYON
opérée au sein de
l'Université Claude Bernard Lyon 1

Ecole Doctorale N° accréditation
L'Ecole Doctorale Interdisciplinaire Sciences Santé (EDISS)

Spécialité de doctorat :
Discipline : (Eventuellement)

Soutenue publiquement le 20/01/2016, par :
Kévin Moulin

Imagerie de diffusion cardiaque en respiration libre

Devant le jury composé de :

Dacher, Jean-Nicolas Professeur des Universités, Praticien Hospitalier, Université de Rouen	Président
Felblinger, Jacques Professeur des Universités, Université de Nancy	Rapporteur
Saint-Jalmes, Hervé Professeur des Universités, Université de Rennes	Rapporteur
Le Bihan, Denis Directeur de recherche, Institut d'Imagerie Biomédicale du CEA, Gif-sur-Yvette	Examinateur
Beuf, Olivier Directeur de recherche, CREATIS CNRS UMR 5220, Université de Lyon	Examinateur
Viallon, Magalie Ingénieure de recherche HDR, CREATIS CNRS UMR 5220, Université de Lyon, Université de Saint-Etienne	Directrice de thèse
Croisille Pierre Professeur des Universités, Praticien Hospitalier, CREATIS CNRS UMR 5220, Université de Lyon, Université de Saint-Etienne	Co-directeur de thèse

UNIVERSITE CLAUDE BERNARD - LYON 1

Président de l'Université	**M. François-Noël GILLY**
Vice-président du Conseil d'Administration	M. le Professeur Hamda BEN HADID
Vice-président du Conseil des Etudes et de la Vie Universitaire	M. le Professeur Philippe LALLE
Vice-président du Conseil Scientifique	M. le Professeur Germain GILLET
Directeur Général des Services	M. Alain HELLEU

COMPOSANTES SANTE

Faculté de Médecine Lyon Est – Claude Bernard	Directeur : M. le Professeur J. ETIENNE
Faculté de Médecine et de Maïeutique Lyon Sud – Charles Mérieux	Directeur : Mme la Professeure C. BURILLON
Faculté d'Odontologie	Directeur : M. le Professeur D. BOURGEOIS
Institut des Sciences Pharmaceutiques et Biologiques	Directeur : Mme la Professeure C. VINCIGUERRA
Institut des Sciences et Techniques de la Réadaptation	Directeur : M. le Professeur Y. MATILLON
Département de formation et Centre de Recherche en Biologie Humaine	Directeur : Mme. la Professeure A-M. SCHOTT

COMPOSANTES ET DEPARTEMENTS DE SCIENCES ET TECHNOLOGIE

Faculté des Sciences et Technologies	Directeur : M. F. DE MARCHI
Département Biologie	Directeur : M. le Professeur F. FLEURY
Département Chimie Biochimie	Directeur : Mme Caroline FELIX
Département GEP	Directeur : M. Hassan HAMMOURI
Département Informatique	Directeur : M. le Professeur S. AKKOUCHE
Département Mathématiques	Directeur : M. le Professeur Georges TOMANOV
Département Mécanique	Directeur : M. le Professeur H. BEN HADID
Département Physique	Directeur : M. Jean-Claude PLENET
UFR Sciences et Techniques des Activités Physiques et Sportives	Directeur : M. Y.VANPOULLE
Observatoire des Sciences de l'Univers de Lyon	Directeur : M. B. GUIDERDONI
Polytech Lyon	Directeur : M. P. FOURNIER
Ecole Supérieure de Chimie Physique Electronique	Directeur : M. G. PIGNAULT
Institut Universitaire de Technologie de Lyon 1	Directeur : M. le Professeur C. VITON
Ecole Supérieure du Professorat et de l'Education	Directeur : M. le Professeur A. MOUGNIOTTE
Institut de Science Financière et d'Assurances	Directeur : M. N. LEBOISNE

Abstract

Diffusion magnetic resonance imaging is a technic allowing a sensitization of the magnetic resonance signal to Brownian motion of water molecules. This method was used to probe structural information of tissue in neuroimaging and became a tool of paramount importance in the management of patient with acute cerebral vascular accident for the detection of ischemic cerebral zone. The motivation is high to develop diffusion magnetic resonance imaging in cardiology which could complete actual cardiac MR method for the diagnostic of acute infarct or myocarditis. However this technique is very sensitive to motion and face in cardiology to breathing and cardiac motion. Until now, the methods proposed to take care of these motions increased considerably the scan time and are not compatible with clinical constraints.

The aim of this thesis is to develop cardiac diffusion magnetic resonance imaging compatible with such constraints which could be used for clinical applications. We proposed a new approach of free-breathing technique allowing scanning during all the respiratory cycle. This new diffusion sequence is based on echo navigator, a 1D image given prospectively and in real time the lung/liver interface. The information given by the navigator is used to adapt the slice position according to breathing phase in real time. This method called “slice-following” correct the head foot displacement of the heart induced by the breathing and was validated on a reproducibility study on 10 volunteers.

Retrospective correction techniques were also proposed to handle cardiac motion signal loss and residual in-plane displacement not corrected by slice following. New registrations steps, were developed and evaluated through proposed methodology and quantification.

Finally, recently published motion compensation gradient waveforms for diffusion encoding were quantitatively compared in free-breathing conditions. A theoretical study was conducted in collaboration with the Camille Jourdan mathematical institute to simulate the impact of cardiac motion on these schemes. The effect of breathing motion was evaluated through an ex-vivo study using the mobile phantom of Centre d’Imagerie Biomédical (CIBM) of Lausanne. In-vivo study was proposed on 7 volunteers to compare result of previous studies on real conditions. For each patient, cardiac contraction curve (strain) and respiratory phase were also recorded and compared to the presence of artefact. This methodology was used to

compare fairly the diffusion encoding scheme and correlations were found between cardiac strain and artefact for non-motion compensated diffusion preparation.

Taking into account the methodological achievements of this thesis, first clinical results were obtained on 40 patients presenting various pathologies using a 5 short axis slices, 2-min protocol. A longitudinal research study on ultra-trailer was also conducted on 50 subjects enrolled from the “Tor des géants” (Vallée d’Aoste, Italie, 330km, +24000m climb).

Résumé

L'imagerie par résonance magnétique (IRM) de diffusion est une technique permettant de sensibiliser un signal de résonance magnétique au mouvement brownien des molécules d'eau. Cette méthode a été utilisée pour accéder à l'information structurelle des tissus en neurologie et est devenu un outil crucial de prise en charge des patients à la phase aigüe de l'accident vasculaire cérébral pour la détection de la zone d'ischémie cérébrale. Il est pressenti que de disposer de ce type d'imagerie en cardiologie pourrit compléter avantageusement les outils d'IRM cardiaque pour le diagnostic de pathologie cardiovasculaire courantes, à la phase aigüe ou chronique de l'infarctus du myocarde mais aussi pour le suivi de toutes cardiomyopathies. Cependant cette technique, sensible au mouvement des molécules d'eau, est confrontée en cardiologie aux mouvements cardiaques et respiratoires. Les méthodes présentées actuellement dans la littérature pour faire face à ces mouvements nécessitent des temps d'acquisition considérables et donc incompatible avec une application clinique de l'IRM de diffusion en cardiologie.

L'objectif de la thèse est de développer l'IRM de diffusion cardiaque compatible avec les contraintes clinique pour en permettre le transfert vers une application en routine clinique. Notre travail s'est tout d'abord concentré sur le développement d'une technique séquence et d'une stratégie d'acquisition en respiration libre permettant une acquisition continue pendant toute la totalité du cycle respiratoire. Cette séquence de diffusion, utilise l'écho navigateur, image 1D fournissant prospectivement l'information de position de l'interface foie/poumon en temps réel, pour adapter en temps réel la position de coupe en fonction de la phase respiratoire, permettant ainsi de compenser le déplacement tête-pied du cœur induit par la respiration. Cette méthode appelé « slice-following » a été validée pour l'imagerie de diffusion cardiaque dans une étude de reproductibilité conduite sur 10 volontaires.

Parallèlement une suite algorithmique de méthodes rétrospectives de correction de mouvement cardiaque (recalage, débruitage, PCATMIP etc..) a été mise en place, afin de corriger le mouvement résiduel induit par la méthode de suivi de coupe. Les nouvelles méthodes de recalage ont été adaptées et cette suite de pré et de post-traitements a été évaluée en proposant une méthodologie d'évaluation capable de rendre compte quantitative des améliorations en introduisant notamment un critère de recalage, et un taux de corruption des images pondérées en diffusion par le mouvement cardiaque.

Enfin plusieurs schémas d'encodage de la diffusion présentant divers niveaux de compensation de mouvement (1er ordre, 2nd ordre) ont été comparés quantitativement dans le contexte de notre technique en respiration libre. Une étude de l'impact du mouvement cardiaque sur chacun des schémas de diffusion a par ailleurs été conduite sur le plan théorique et au travers de simulations, en collaboration avec l'institut mathématique Camille Jourdan. L'impact de la respiration à quand a lui été évaluée de façon découplée, sur le fantôme mobile du Centre d'Imagerie Biomédicale (CIBM) de Lausanne. Une étude de reproductibilité in-vivo sur sept volontaires a été réalisée afin de comparer dans des conditions réelles ces schémas de sensibilisation à la diffusion. Pour chaque volontaire, des courbes de contraction cardiaque (Strain) ont été calculées et les phases respiratoire correspondant aux acquisitions en diffusion ont été enregistrées afin d'étudier les relations entre le taux d'artefacts dans les images et l'amplitude du mouvement régional du myocarde, et objectiver d'éventuelles corrélations. Ces données ont permis d'établir une corrélation direct entre contraction cardiaque et présence d'artefact et la méthodologie proposée pour la quantification d'artefact a permis de comparer équitablement les méthodes entre elles, et permettra dans le futur de démontrer la valeurs ajoutée de toutes innovations prétendant améliorer soit la chaine de traitement ou soit les méthodes d'acquisition.

Les développements présentés ici ont permis d'établir un protocole d'acquisition de 5min pour 5 coupes petit-axe. Des premiers résultats cliniques ont été obtenus sur 40 patients présentant des pathologies différentes, et sur 50 sujets d'une étude longitudinale visant a étudié l'impact d'un effort intense et de très longue durée sur le myocarde (Etude MUST qui s'est déroulée sur le marathon de Montagne du Tor des Géants (Vallée d'Aoste, Italie, 330km, +24000m de dénivelé positif).

Remerciement

En premier lieu, je tiens à remercier ma famille et ma compagne, qui m'ont soutenu et ce malgré les absences et les distances que m'imposé ce travail.

Pendant ces trois ans au laboratoire CREATIS, j'ai eu la chance de rencontré des personnes aussi passionné que moi par la recherche. Je remercie l'équipe 5 et l'équipe 1 pour leurs accueils chaleureux ainsi que tous les membres du laboratoire qui m'ont aidé pendant cette thèse. Olivier, Hélène, Patrick pour leurs gentillesses et leurs patiences à mon égard.

J'aimerai également remercié les équipes des services de radiologies des hôpitaux Est de Lyon et des hôpitaux Nord de Saint-Etienne pour m'avoir accueilli et permis de réaliser des manips.

Je tiens à remercier les rapporteurs Jacques Felblinger et Hervé Saint-Jalmes de m'avoir faire part de leurs remarques constructives et de l'intérêt qu'ils ont porté à mon travail. Je remercie également les autres membres du jury, Jean-Nicolas Dacher et Denis Le Bihan pour la discussion passionnante que nous avons eu pendant la soutenance.

Ce travail n'aurai pas eu de sens sans le soutient que j'ai reçu de la part de Siemens, notamment de Agnès Malgouyres et Christian Bert qui m'ont véritablement aidé à évolué au sein de Siemens France. Je n'oublie pas également les conseils techniques inestimables que j'ai reçus de la part de Thomas Troalen, Benjamin Robert et Thorsten Feiweier.

Pour finir j'aimerai remercier mes encadrants de thèse, Magalie Viallon et Pierre Croisille, pour m'avoir formé et accompagné pendant ces 3 ans mais également pour toutes les expériences partagées, l'Italie, la Suisse, les manips, les congrès, les formations et encore beaucoup trop d'autres choses.

«Tout le monde est un génie. Mais si vous jugez un poisson sur ses capacités à grimper à un arbre, il passera sa vie à croire qu’il est stupide.»

Contents

Abbreviations

ADC: Apparent Diffusion Coefficient

AHA: American Heart Association

AMC: Acceleration Motion Compensation

AS: Ascendant

bSSFP: balanced Steady State Free Precession

CAIPI: blipped controlled aliasing

CDWI: cardiac Diffusion Weighted Imaging

CMRI: cardiac Magnetic Resonance Imaging.

CVD: Cardiovascular Disease

DALY: Disability Adjusted Life Year

DCM: Dilated Cardiomyopathy

DOT: Diffusion Orientation Transformation.

DPI: Diffusion Propagator Imaging.

DS: Descendant:

DTI: Diffusion Tensor Imaging

DWI: Diffusion-Weighted Imaging

ECG: Electrocardiogram

ED: End Diastole

EPI: Echo Planar Imaging

FA: Fraction of Anisotropy.

HARDI: High Angular Resolution Diffusion Imaging

HCM: Hypertrophic Cardiomyopathy

HVMB: Helical Ventricular Myocardial Band

IVIM: Intra-Voxel Incoherent Motion

IVPCM: Intra-Voxel Partially Coherent Motion

LGE: Late Gadolinium Enhancement

LS: Left Segment

LV: Left Ventricular

LVEF: Left Ventricular Ejection Fraction

MBH: Multi Breath-Hold

MD: Mean Diffusivity

MEG: Motion Encoding Gradient

MRI: Magnetic Resonance Imaging

NMR: Nuclear Magnetic Resonance

ODF: Orientation Distribution Functions

PCA: Principal Component Analysis

PDF: Probability Density Function

PLI: Polarized Light Imaging

QBI: Q-ball Imaging.

RD: Right Segment

ROI: Region Of Interest

RV: Right Ventricle

RVEF: Right Ventricular Ejection Fraction

SA: Short Axis.

SE: Spin Echo

SMS: Simultaneous Multi-Slice

SNR: Signal Noise Rate

STEAM: Stimulated Echo Acquisition Mode

TD: Trigger Delay.

TMIP: Temporal Maximum Intensity Projection

TR: Repetition Time.

TRSE: Twice Refocus Spin Echo

US: Ultrasound.

WHO: World Health Organization

PART
I

Introduction and background

1. Introduction

According to the World Health Organization (WHO), cardiovascular disease (CVD) represented 39% of all-cause death in the world in 2011 (Mendis *et al.*, 2015). Population growth and improved longevity are leading to increased proportion of elderly people, with population ageing emerging as a significant trend in many parts of the world. With populations aging, annual death cause by CVDs are projected to rise substantially from 17.5 million to 24.5 million in the next 20 years. These diseases regroup a large panel of pathologies like coronary heart disease, vascular disease (stroke), raised blood pressure (hypertension), peripheral artery disease, congenital heart disease and heart failure. Causes leading to disorders in the heart are linked to the lifestyle and principally include tobacco, alcohol and obesity. Treatments are various but all depend on the capacity to provide early detection.

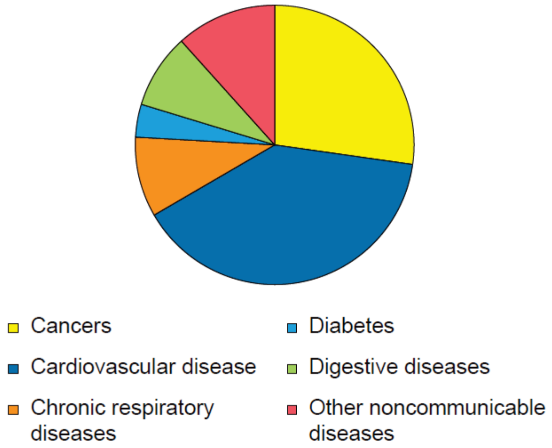

Figure 1.1 : Repartition of no communicable death in the world. © World Health Organization report 2015

In this context is it crucial to improve clinical diagnostic so as it could give a better understanding of the body’s tissue aggressions by providing early and the clear signature of disorders all along the evolution of these chronic diseases. As a non-invasive and non-ionizing technique Magnetic Resonance Imaging (MRI) would stand as a reference modality in cardiovascular imaging, penalized only by the low availability and some contra-indications. Cardiac Magnetic Resonance is the reference method for quantifying global left-ventricular (LV) function (ejection fraction), mass, infarction size and location by late Gadolinium enhancement (LGE). The quantification of central process like inflammatory (edema) or infiltration (fibrosis) has also motivated recent developments of quantitative MRI methods such as T1 mapping (Messroghli *et al.*, 2004) and T2 mapping (Giri *et al.*, 2009).

Diffusion-Weighted Imaging (DWI) in the brain has been gaining a growing importance and belongs in any protocol aiming the characterization of neurological pathologies. The motivation is high to develop method allowing exploration of the potential of DWI-related biomarkers for cardiac disease investigations. Combined to mathematical models diffusion imaging has also the unique ability to provide non-invasive structural information of tissue with for example the Diffusion Tensor Imaging (DTI) model but information on tissue compartments(perfusion fraction, extracellular and/or intracellular diffusion) using multiple b-values model such as Intra Voxel Incoherent Motion (IVIM) or QBall imaging.

Like in other striated muscles, the cardiac muscle contraction is fundamentally linked to the organization of cardiac cells in laminar sheets, leading to the so-called "fiber" architecture. The analysis of the structure of myocardial fibers in-vivo could be a way to understand the alteration of this architecture by cardiomyopathies or arrhythmias. This was the original objective of histological techniques but which are limited to small part of the heart. A 3D approach proposed by Jouk (Jouk *et al.*, 2007) using Polarized Light Imaging (PLI) has provided the orientation of myocardial fibers of ex vivo fetal heart with a resolution of 0.1 x 0.1 x0.5 mm^3. Ex vivo cardiac DTI on fiber atlas study has also been reported by Lombaert (Lombaert *et al.*, 2012) with a resolution of 2 x 2 x 2 mm^3.

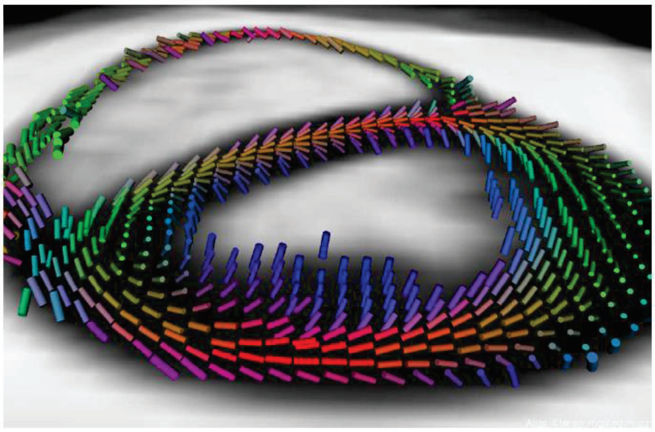

Figure 1.2 : Heart architecture obtained by diffusion tensor imaging, Orientation of cylinder represents the first eigenvector ot tensor system. The Color indicates local orientation of the "fiber". © ADDIN EN.CITE (

Despite more than 20 years of research already in the field of cardiac Diffusion Weighted Imaging (cDWI), in-vivo diffusion measurements in an organ that is affected by breathing and cardiac motion remains very challenging. First cardiac cDWI in-vivo human acquisition was achieved using a stimulated echo acquisition mode (STEAM) sequence (Edelman *et al.*, 1994). STEAM preparation presents the advantage of having much shorter effective sequence time but need two consecutives cardiac beat to encode and decode the diffusion which imposes long scan time. Spin Echo (SE) sequence is an alternative approach that can be applied within a single heartbeat (Gamper *et al.*, 2007) but that is more sensitive to cardiac motion. In parallel specific reconstruction algorithm to handle cardiac motion based on principal component analysis (PCA) and temporal maximum intensity projection (TMIP) have been proposed (Pai *et al.*, 2011) (Rapacchi *et al.*, 2011) (Delattre *et al.*, 2012). To avoid multiple breath holding and improve patient compliance, free-breathing acquisition was also proposed using navigator-driven acquisition scheme but with a considerable increase of the total acquisition time (Nielles-Vallespin *et al.*, 2013) that makes cDWI inapplicable to clinical constraints.

The current and most efficient management of cardiac and respiratory motions for cDWI in the literature prevent so far its use in clinical conditions that in turn is a major limitation if the CMR community wants to explore the potential unique information that could be brought by cDWI. The aim of this work was therefore to to make applicable cDWI to clinical conditions, imposing a drastic constrain in acquisition time.

In the first part of this thesis a short review of heart anatomy is given, Nuclear Magnetic Resonance (NMR) and Diffusion basis are described in chapter 3 and 4. A novel method based on navigator for free-breathing acquisition with maximal scanning efficiency (100% duty respiratory cycle) is introduced in chapter 5. This technique, called slice-following, enables continuous real-time slice tracking and slice real-time repositioning to compensate movement induces by the heart. This method was evaluated through a reproducibility study and was used for a longitudinal study aiming the effects of prolonged intense exercise on the myocardium, the MUST study realized on ultra-trail marathon of “Tor des géants” (330km +24000 meters of positive elevation). Chapter 6 explained our pre and post-processing pipeline but also an estimator for motion corruption of cDWI data. In the chapter 7, we proposed the implementation and the evaluation of recently published motion compensated gradient waveforms, as new options for free-breathing cDWI sequence. Comparison of all diffusion encoding schemes in free-breathing conditions was performed under simulation, ex-vivo and in-vivo measurement in volunteers. Finally general conclusion and perspective are given in chapter 8.

2. Human cardiac structure and function

2.1.Human heart anatomy

Location: The heart is localized inside the chest - delimited on its back by the spine and anteriorly by chest wall (the sternum and the ribs). Its long axis of the has a double-obliquity orientation and is rotated to the left (~45°) and to the bottom (~45°).

Global structure: The heart have left and right portions or cavities, also called left and right heart, separated by a muscular wall: the septum. Each of them contains two chambers. Upper and posterior chambers are called left and right atrium whiles the lower and more anterior ones, the left and right ventricles. The right heart is filled by unsaturated or de-oxygenated blood coming from the venous return. The right heart ejects it into the lungs and the pulmonary circulation, whereas the left heart is filled by newly oxygenated blood from the lungs, which is then ejected in the arterial circulation and the main vessels.

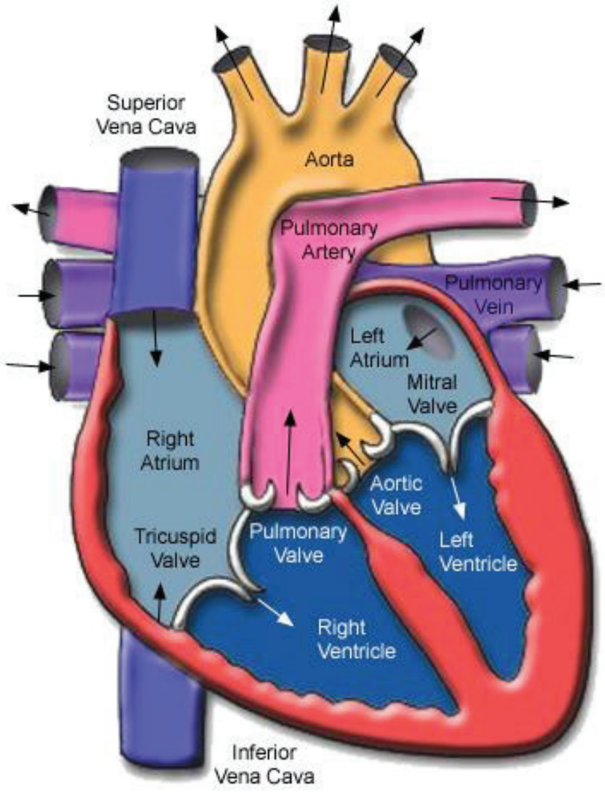

Figure 2.1 : Heart anatomical structure at macroscopic scale.

©*http://healthinformation1.4arabs.com/heart/2.html*

The pericardium: Both cardiac cavities and the origin are located in a containing envelope : the pericardium. The pericardium is made of two layers: an outer fibrous and parietal layer (the fibrous pericardium), and an inner visceral layer (visceral pericardium). They create an inner cavity, the pericardial cavity. The inner surface is lined by mesothelial cells producing a serous fluid. In normal and physiologic conditions, the amount of serous fluid approximate 25ml, but that may vary among individuals. The pericardial fluid helps in optimizing mechanical function of the heart within the wall, reducing friction of the contracting myocardium within the non-moving structures.

Cardiac chambers: As shown in Figure 2.1, the left atrium (LA) and right atrium (RA) plays the role of admission chambers while the left ventricle (LV) and right ventricle (RV) are ejection chambers. The large venous vessels that fill the right heart collect deoxygenated blood coming from the upper half and the lower half of the body through respectively the superior vena cava (SVC) and the inferior vena cava (IVC). The RA collects blood and fills RV through the tricuspid valve. RV ejects blood to the pulmonary artery through the pulmonary valve. The pulmonary circulation will achieve re-oxygenation of the blood coming from the right heart. Once re-oxygenated, blood is then collected by the pulmonary veins (upper and inferior right, upper and inferior left) to the LA. The admitted blood is pumped to the LV. The two left cavities are separated by the mitral valve. Finally blood is ejected to the aorta and the arterial circulation after crossing the aortic valve. Note that the coronary arteries that supply oxygen and substrates to the myocardium itself are located immediately at the root of the aorta after the aortic valve.

Both atria are thin-walled cavities. The two ventricles have thick walls adapted to the pressure of the pulmonary circulation (low pressure / RV), and the arterial or systemic circulation (high pressure / LV). Right ventricle wall thickness is 3-5mm, while LV wall thickness is ~10mm. While the RV has a global shape of triangle, LV has a shape of an ellipse.

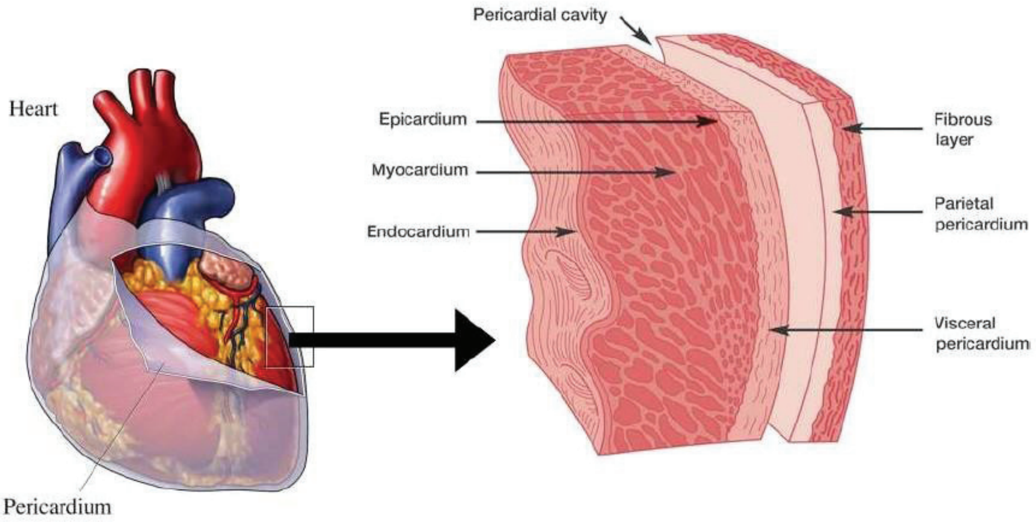

Figure 2.2: Myocardium wall.

©*http://www.beltina.org/health-dictionary/pericardium-function-definition.html*

The myocardium wall: Cardiac wall is anatomically divided in 2 parts: - an outer part or epicardium, and an inner part or endocardium (Figure 2.2).

The epicardium is directly related to pericardium itself and where lays the macro-vasculature (coronary arteries and veins). Vascularization within the wall will be performed by perforating division branches and capillary network. The endocardium is closely related to the blood cavity with an endothelial layer.

2.2.Cardiac function

Because cardiac contraction is a periodic motion, it is common to describe the events that describe cardiac function in a single cardiac cycle.

Cardiac cycle: The cardiac cycle contains two successive phase: the ejection phase or systole and the filling phase or diastole. For a normal heart rate of 60 beats per min (bpm), systole last for approximately 1/3 or ~300ms and diastole ~700ms..

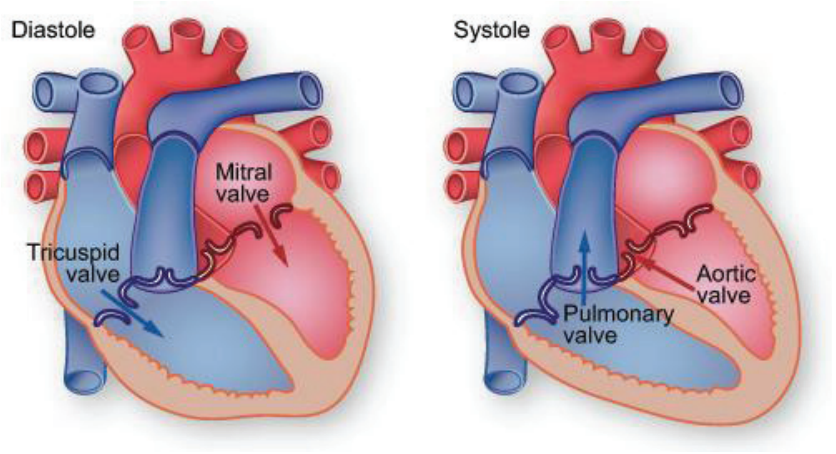

Figure 2.3: Heart diastole and systole.

©*http://www.texasheartinstitute.org/HIC/anatomy/systole.cfm*

The cardiac cycle typically starts at the end of diastole (ED) of the previous cycle and ends at the end of diastole of the current cycle. It is commonly described for the left heart that represents 2/3 of cardiac mass, and the right heart follows the same phases. More precisely, the cardiac cycle is divided into seven particular phases. The first 2 phases are part of systole, the 3 others part of diastole.

- *isovolumetric* contraction: This phase corresponds to the contraction of the ventricles while all valves closed, with a subsequent increase of intra-ventricular pressure. This phase is contemporary to the ascending R wave of the ECG.

- *ejection phase*: When intraventricular pressure becomes higher than aortic pressure , the aortic valve opens and blood is ejected out of the LV. The atrio-ventricular valve, the mitral valve, remains closed. Ejection phase ends when aortic pressure equals intraventricular pressure.

Diastole has 2 distinct periods: an active relaxation period (isovolumetric relaxation phase and rapid filling phase), an active relaxation phase. It lasts for only 30% of diastole duration, but is leading to 70% of LV volume filling. Then follows a slow filling period where pressure/volume relationship will be driven by the compliance of the container: the ventricle. Last, the LA contraction will fill the remaining of the end-diastolic volume.

- *isovolumetric relaxation phase*: This phase is characterized by a rapid drop of the LV pressure while aortic valve and mitral valve are closed. This phase is also particular by the elastic recoil of the LV that will lead to a succion effect to the next phase.

- *rapid filling phase*: When intraventricular pressure becomes lower than atrial one, the atrio-ventricular valve opens to fill the ventricle. The ventricles continue to relax and intraventricular pressure continues to decrease.

- *diastasis*: Once ventricular and atrial pressures equals, an reduced filling phase is observed while changes in volume are mainly due to pulmonary veins inflow that contributes to 5% of the LV filling.

- *active atrial contraction*: This phase corresponds to the contraction of the atrium itself, and this phase contributes to 20-30% of the total LV filling.

These phases can be explored using various physiologic parameters, such as, the ECG, heartbeat sounds, volume curves, and pressure curves. Figure 2.4 gives an overview the temporal changes of these parameters during cardiac cycle. Cardiac function can be assessed by global parameters assessing changes in volumes between diastole and systole. One can calculated an ejection fraction for both LV (LVEF) and RV (RVEF), that summarize the fraction of ventricular blood ejected every heartbeat.

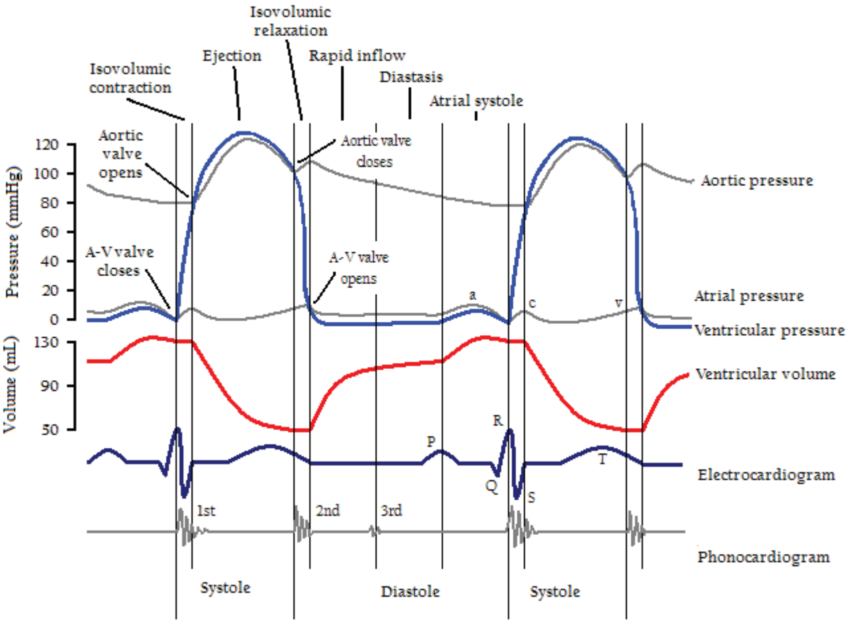

Figure 2.4: Pressure and volume chronogram during the cardiac cycle.

©*http://en.wikipedia.org/wiki/Cardiac_cycle*

2.3.Cardiac fiber architecture

Myocardium mainly consists of muscular fibers that are organized as a syncytial network interleaved with an extracellular fibrous matrix. At a microscopic scale, this network is organized at a mesoscale in laminar sheets (D. D. Streeter, Jr. *et al.*, 1969; LeGrice *et al.*, 1995). Sheet orientation varies continuously across myocardial wall from the sub-endocardium to the sub-epicardium. Fiber architecture has been considered to condition cardiac mechanical function (Costa *et al.*, 2001) and cardiac electrophysiology patterns (Hooks *et al.*, 2002) . For instance, the torsion of the LV has been shown as directly related to the orientation of cardiac fibers (Russel *et al.*, 2009) while electrical conductivity is greater along fiber direction (Hooks *et al.*, 2007). Fiber architecture complexity is not fully described in humans and has been extrapolated from experimental studies performed in other species based on sparse and complex histopathological analyses. Various models have been proposed and recently reviewed (Buckberg *et al.*, 2008).

At a macroscopic scale, one of the earliest hypothesis was that cardiac muscle may consist of 4 myocardial bundles (Mall, 1911), with subsequent hypotheses of a spiral muscle sandwiched onto itself (Rushmer *et al.*, 1953), or toroïdal surfaces with doughnuts-like structure (D. D. Streeter, Jr. *et al.*, 1969) (Torrent-Guasp *et al.*, 2005), or finally of a unique band folded around itself.

Among the numerous models describing the structure of myocardium, we present some of the most representative ones.

2.3.1. Myocardial band model

The helical ventricular myocardial band (HVMB) model was proposed by F.Torrent-Guasp (Torrent Guasp, 1972a) (Torrent Guasp, 1972b). It is based on the helical rope principle, that was a totally new concept to approach myocardial anatomy and structure, providing a breakthrough proposal to relates macroscopic architecture of the heart based on dissections studies. By making the hypothesis of a single band filling the gap between anatomy and function, Torrent-Guasp brought an innovative concept to improve our understanding of the global, 3D, functional architecture of the ventricular myocardium.

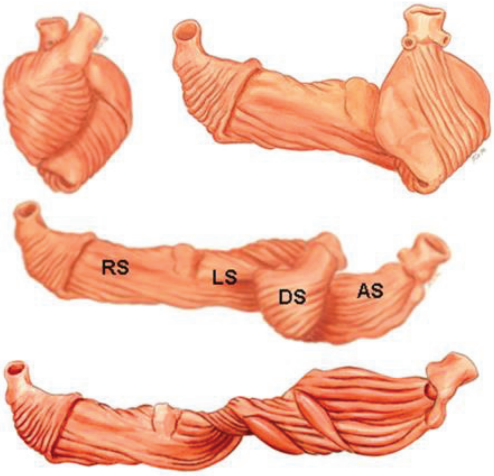

Figure 2.5: Torrent-Guasp's myocardial band model

©*http://jtcs.ctsnetjournals.org/cgi/figsearch?fulltext=torrent&resourcetype=3*

Figure 2.5 illustrates the successive steps of a dissection specifically applied to unravel the ventricular tissue into the HVMB. The HVMB model is considered as divided in two loops, each resulting of two segments. The central 180° fold of the HVMB defines the 2 two loops: the basal loop (from the root of the pulmonary artery to the beginning of the central fold; and an apical loop (from the beginning of the central fold to the root of the aorta).

As explained in (Torrent Guasp, 1972b): "*The posterior interventricular sulcus, which coincides topographically with the posterior linear border of the right ventricular cavity, divides the basal loop into two segments: the right segment (RS), coinciding with the RV free wall; and the left segment (LS), coinciding with the LV. It is interesting to note here that the right and the left segments of the basal loop define the outer (non-septal) border of the tricuspid and the mitral orifices, respectfully. The apical loop can be also divided into two segments. After the 180° twist (at the central fold of the HVMB), the descendant (DS) fibers of the apical loop, make a 90° turn around the apex becoming the ascendant (AS) fibers. The posterior papillary muscle (belonging to the descendant segment) demarcates the border between the descendent and the ascendant segments of the HVMB apical loop*".

Despite having been only built from macroscopic observations, the HVMB model merges the knowledge of the myocardial muscular trajectories obtained from dissection techniques and gives reasonable explanations about the linking between mechanical properties and cardiac function that remain a landmark in the understanding of the cardiac structure.

2.3.2. Geodesic model

The geodesic model was first proposed by Streeter (D Streeter, 1979), making the hypothesis that myocardial fibers can be modeled as running like geodesics on a nested set of toroidal bodies of revolution. Few decades later, Jouk (Jouk *et al.*, 2007) refined it, with a clear explanation about this model using the Figure 2.6.

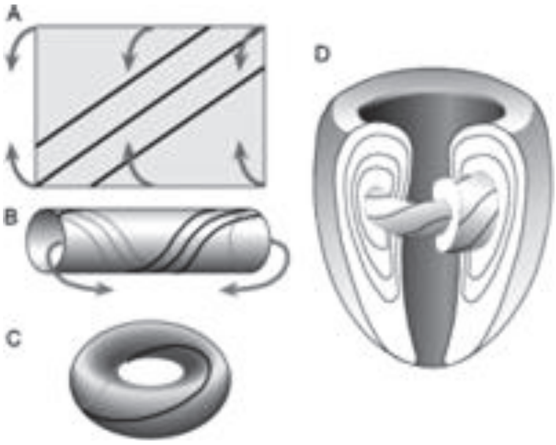

Figure 2.6: Geodesic model

"*Firstly, take a piece of paper and draw three parallel lines, these lines could be considered as the geodesics of the plane surface. Secondly, roll the paper making the superior border against the inferior border and forms a cylinder, the drawn lines in the first step becomes the geodesics of the cylinder. Thirdly, bend the cylinder until the left reaches the right, a torus will be generated and the lines are still geodesics. Finally, Streeter's conjecture supposed that from inner to outer the myocardial muscle nested by the elongated tori like Russian dolls*", as shown in Figure 2.7.

While Streeter's model gives only the cardiac fiber map of LV, and as an extension of Streeter's conjecture, Jouk refined it with the pretzel model (Jouk *et al.*, 2007) with the main advantage to integrate the whole ventricular mass fiber architecture as illustrated in Figure 2.7.

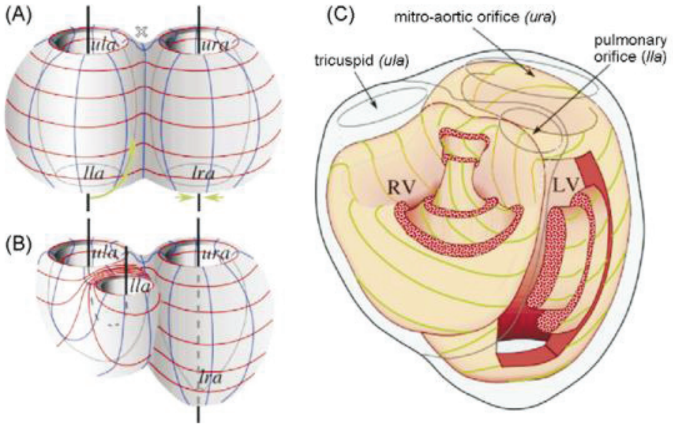

Figure 2.7: An extension of geodesic model: the pretzel model. Like the pretzel cookies, two joined torus form a pretzel in this model. (A). Four special positions are defined: lower left aperture (lla), lower right aperture (lra), upper left aperture (ula) and upper right aperture (ura). For mimicking the right ventricle structure, the torus on the left was bent in such a way that the lower aperture comes up to the upper aperture. However, for the left ventricle, it is mimicked by shrinking the lower right aperture into a point, as shown in subfigure (B). In subfigure (C), it explains how LV and RV could nest together and form a pretzel model, where the green lines represent the geodesic on the nested pretzels (Jouk et al., 2007)

In addition, this model also provides a new recognition about the fiber arrangement of the RV. The upper left aperture would correspond to the tricuspid annulus and the pulmonary annulus. These regions are separated by the supraventricular crest. This hypothetical model still requires further mathematical and experimental validations.

2.3.3. Laminar structure model

All models cited in the previous section assumes that myocardial material properties are transversely isotropic according to the myofiber axis, and making the assumption that interconnected myocytes are uniformly coupled within myocardial syncytial network. LeGrice and coworkers (Legrice *et al.*, 1997) demonstrated however that ventricular myocardium is structurally orthotropic, with myocytes arranged in layers that are considered having four cells thick, as shown in Figure 2.8. These layers are separated from adjacent ones by so-called cleavage planes .

Cardiac microstructure is therefore considered with 3 axes of symmetry: the first one, the fiber axis is aligned with myocyte fiber orientation; the second one, the sheet axis, is defined as orthogonal to the fiber axis, lying in the myocardial sheet plane; last, the sheet-normal direction which isorthogonal to the two previous ones.

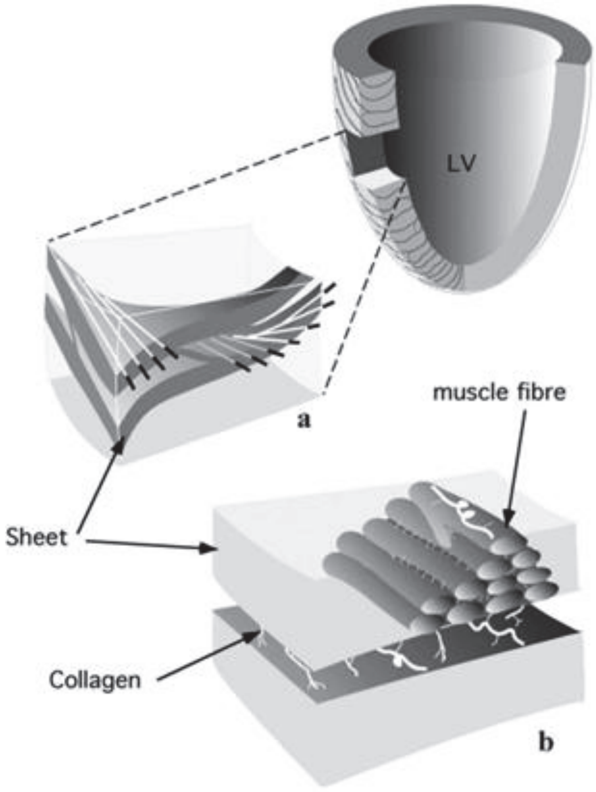

Figure 2.8: Organization of cardiac fibers as laminar sheets © (Jouk *et al.*, 2007)

2.3.4. Relation between fiber structure and heart function

Understanding of myocardial function and regional myocardial mechanics, including systolic thickening with reorientation of myofiber structure has made progresses by linking global and regional macroscopic changes with new understanding of the micro and mesostructure of the myocardium. Recent results obtained by Nielles and co-workers illustrated bellow have demonstrated in-vivo that the assumed reorganization of cardiac fibers i.e. variation in orientation of the diffusion tensor over the cardiac cycle can be sampled using DTI (Figure 2.9). It is expected that the growing capability to describe myocardial fiber structure and its dynamic changes through cardiac cycle, especially when combined with myocardial strain imaging approaches, could provide novel insights into the structure-function relation in the heart and their abnormalities in normal and various pathologies that induce changes of myocardial wall with infiltrative processes or focal lesions such as necrosis and fibrosis.

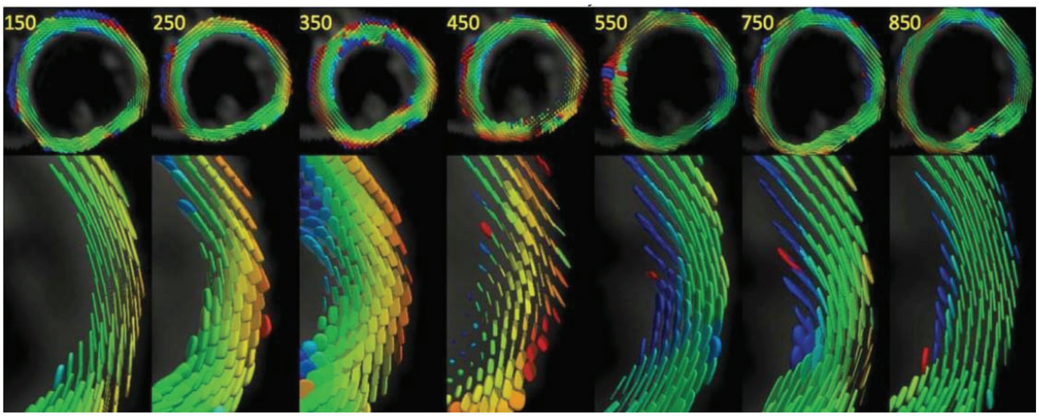

Figure 2.9: Cardiac DTI(diffusion tensor imaging) at various time-points of the cardiac cycle. (Nielles-Vallespin et al., 2013)

3. Magnetic Resonance Imaging principles

Since its discovery by Isaac Rabi in begin of the 20th, the concept of Nuclear Magnetic Resonance (NMR), property of certain atomic nuclei, has considerably evolved to become an entire new field of physics. Through the work of Felix Bloch and Edward Purcell in 1950, the principle of NMR has been used to study the chemical properties of materials. Twenty years after, the principles of Magnetic Resonance Imaging (MRI) was state by Paul Lauterbur and Perter Mansfield. Their work was follow by huge efforts of research and development which built the actual MRI, a unique non-invasive medical diagnostic tool.

Due to the preponderance of hydrogen in all of the human body, proton MRI sequences are used in all of organ today with a growing importance. In this context, Cardiac Magnetic Resonance Imaging (CMRI) stands one of the top techniques to provide accurate pathology detection and help to treatment choice. However imaging a complex and moving organ like the heart required specific methods which developed a real field of research in MRI.

We proposed in this chapter to make a short review of MRI physics, starting to the NMR signal until the image formation with modern techniques. Common cardiac and respiratory synchronization technique involved in CMRI was also presented. This chapter was based on three references books: “Magnetic Resonance Imaging – physical principles and sequence design” by Mark Haacke, Robert Brown, Michael Thompson and Ramesh Venkatesan for the MRI physic basis, “Handbook of MRI pulse sequences.” by Matt Bernstein, Kevin King and Xiaohong Joe Zhou for the sequence principles, but also “Imagerie de résonance magnétique – bases physiques et methodes” by Michel Decorps which was an undeniable help all along of this thesis for the quality of explanations and it pedagogic approach of MRI physics.

3.1.Nuclear magnetization

The origin of the NMR phenomena comes from the magnetic properties of some nuclei. A nucleus characterized by non-null angular moment *S,* own a magnetic moment μ depending of its gyromagnetic ratio γ:

$$\vec{\mu} = \gamma \vec{S} \qquad 3.1$$

This angular moment is linked to the spin kinetic moment *I* through the Plank constant $\hbar$:

$$\vec{S} = \hbar \vec{I} \qquad 3.2$$

The gyromagnetic ratio, the spin kinetic moment and its algebraic value are intrinsic properties of nucleus dependent of its proton and neutron composition, commonly the spin feature is represented by a vector. For a nucleus composed of *A* nucleon and *Z* protons, if *A* and *Z* are pair *I*=0; if *A* is pair and *Z* impair *I* is entire; if *A* are impair I is a half entire.

At a macroscopic view on a homogenous population of a given nucleus and in absence of external field, the sum of all individual magnetic momentum leads to a resulting macroscopic magnetization M almost null:

$$\vec{M} = \sum \vec{\mu} \simeq 0 \qquad 3.3$$

Nucleus	Spin	γ x 10^-7 (rad/T.s)	Natural abundance (%)
^{1}H	1/2	26.752	99.985
^{3}He	1/2	-20.379	0.00014
^{13}C	1/2	6.728	1.11
^{14}N	1	1.934	99.63
^{15}N	1/2	-2.712	0.37
^{17}O	5/2	-3.628	0.037
^{19}F	1/2	25.162	100
^{23}NA	3/2	7.080	100
^{31}P	1/2	10.814	100
^{39}K	3/2	1.250	93.1
^{129}Xe	1/2	-7.441	26.44
^{131}Xe	3/2	2.206	21.18

Table 3-1: Characteristics of the most common used nuclei in NMR.

This means that the distributions of the magnetic moment are random and point in all directions. But in the presence of an external magnetic field B_0, for example following the Z axis, all the individual magnetic momentums will start to precess around the Z axis.

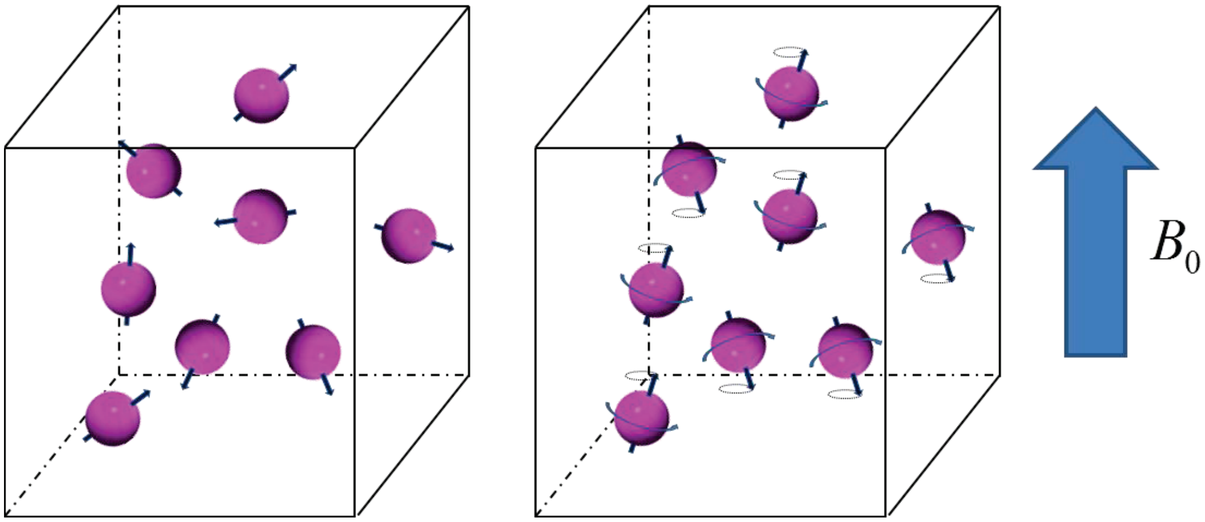

Figure 3.1: Distribution of magnetic moment without and with external magnetic field.

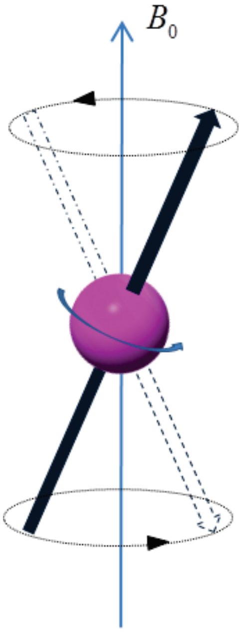

The potential energy of such system is given by:

$$E = -\vec{\mu}\vec{B_0} = -\mu_z B_0 = -|\gamma| S_z B_0 = -|\gamma| \hbar I_z B_0 \qquad 3.4$$

For a given nucleus I=1/2, the magnetic momentum will be distributed according two configurations: parallel and anti-parallel to B_0, corresponding to two energies levels:

High energy state: $$E- = \frac{-\gamma\hbar}{2} B_0 \qquad 3.5$$

Low energy state: $$E+ = \frac{\gamma\hbar}{2} B_0 \qquad 3.6$$

Figure 3.2 : Representation of the two states of a magnetic moment for a nucleus I=1/2 under an external magnetic field B_0.

The difference of energy between these two states is given by:

$$\Delta E = |\gamma| \hbar B_0 \qquad 3.7$$

Posing the product of the strength of the magnetic field by the gyromagnetic ratio, we obtain the Larmor equation, given the pulsation of transition ω_0 (rad/s) also written $f_0 = \omega_0/2\pi$ and called Larmor frequency.

$$|\omega_0| = |\gamma| B_0 \qquad 3.8$$

At a thermal equilibrium state the difference of population between the nuclei at the high energy state and nuclei at low energy state is given by the Boltzmann statistic:

$$\frac{n_\downarrow}{n_\uparrow} = \exp(-\frac{\Delta E}{k_B T}) \qquad 3.9$$

Where K_b is the Boltzmann constant and T the temperature in Kelvin. The number of nuclei at low energy state $n_\uparrow$ is always superior to those at high energy $n_\downarrow$ but the difference is tie, explaining why the NMR is a low sensitive spectroscopic technique as shown in Table 3-2

Magnetic field B0	Ratio $\frac{n_\downarrow}{n_\uparrow}$	Parts per million (ppm)
0	1	0
1.5	0,99999008	9,91948758
3	0,99998016	19,8388768
7	0,99995371	46,2901002
11	0,99992726	72,740624

Table 3-2: Example of proton population ratio at 36°C (309.15° K) given for various scanner magnetic fields B_0.

The excess population in the low energy state leads to a non-null magnetic moment *M* aligned with B_0 and expressed by the difference of population between nuclei at low and high energy states:

$$\vec{M} = \sum \vec{\mu} \simeq |\gamma| \hbar \frac{n_{\uparrow} - n_{\downarrow}}{2} \qquad 3.10$$

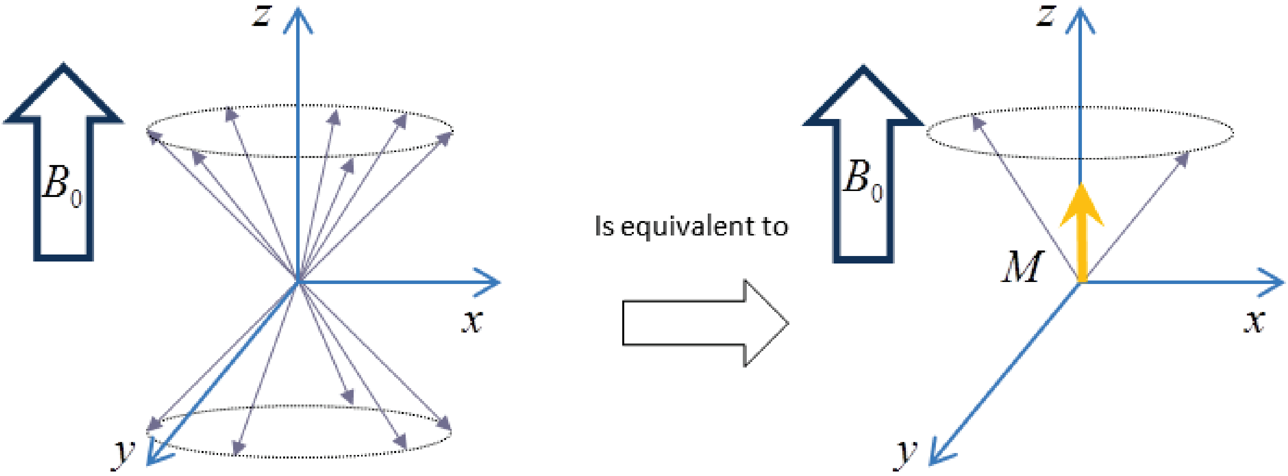

Figure 3.3: The excess of population in low energy state is vectorially equivalent to a system with macroscopic magnetic moment aligned on B_0*.*

3.2. Precession, resonance, and relaxation

3.2.1. Precession process of macroscopic magnetization

As we have seen in the previous paragraph, a population of nuclei under an external magnetic field has a resulting non-null magnetic moment aligned on B_0. But if this resulting magnetization M is shifted from its initial position, it undergoes the restoring torque:

$$\Gamma = M \times B_0 \qquad 3.11$$

Like we have posed M the macroscopic magnetic moment, we pose J the macroscopic angular moment according to:

$$M = \gamma J \qquad 3.12$$

The previous torque affects this angular moment:

$$\frac{\partial J}{\partial t} = M \times B_0 \qquad 3.13$$

And consequently the magnetization:

$$\frac{\partial M}{\partial t} = \gamma M \times B_0 \qquad 3.14$$

This can be rewrite as a differential system:

$$\frac{\partial M_x}{\partial t} = \gamma M_y \times B_0 \qquad 3.15$$

$$\frac{\partial M_y}{\partial t} = \gamma M_x \times B_0 \qquad 3.16$$

$$\frac{\partial M_z}{\partial t} = 0 \qquad 3.17$$

The NMR literature prefers used the complex notation for the transverse magnetization:

$$M_\perp = M_x + iM_y \qquad 3.18$$

With this notation, the solution of the previous system becomes:

$$M_{\perp}(t) = M_{\perp}(0)\exp(i\omega_0 t) \qquad 3.19$$

$$M_z(t) = M_z(0) \qquad 3.20$$

These equations describe a transverse magnetization performing a precession around the Z axis at the Larmor frequency. Due to this phenomenon, a coil placed along the transverse plane created a current proportional to the transverse magnetization and thus record the NMR signal.

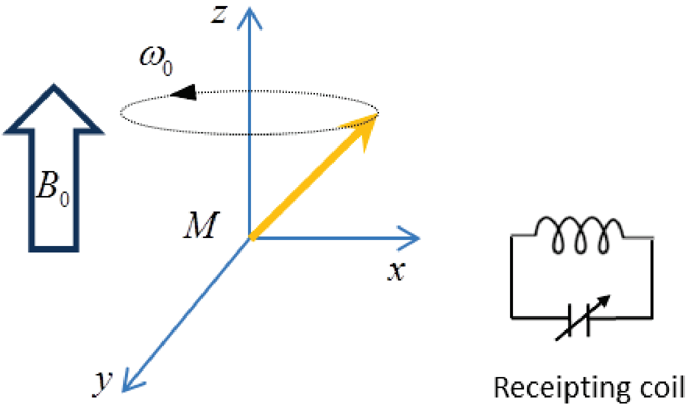

Figure 3.4: Principle of reception of NMR signals using a coil.

3.2.2. Resonance

The principle of the NMR can be summarized in moving the magnetic moment from its initial position into a magnetization not aligned on B_0, which creates a current in the receiving coil. The "resonance" phenomenon of the nuclei is used to displace this macroscopic magnetic moment M. As we seen in equation 3.4, under an external magnetic field the individual moment magnetization of nuclei I=1/2 follow two configurations corresponding to two energy levels. An electromagnetic wave with a frequency corresponding to ΔE will be able to stimulate exchange between these two levels affecting the macroscopic magnetization.

According to the Planck equation:

$$E = h\nu \qquad 3.21$$

Where E is the energy and v the frequency (Hz) of the electromagnetic wave. Introducing the equation 3.21 into 3.7, the frequency of the RF pulse can be expressed as:

$$\Delta E = h\nu_0 \qquad 3.22$$

$$h\nu_0 = |\gamma|\hbar B_0 \qquad 3.23$$

$$\nu_0 = \frac{|\gamma| B_0}{2\pi} \qquad 3.24$$

$$\nu_0 = \frac{\omega_0}{2\pi} \qquad 3.25$$

To switch magnetization from low energy state to high energy state, the electromagnetic wave should oscillate at the Larmor frequency, "on resonance" with the nuclei. For a majority of nuclei and for usual magnetic fields, this frequency has a wavelength in the domain of radio wave consequently this impulsion is often called radiofrequency (RF) wave or pulse. The effect of the RF pulse on the macroscopic magnetization M can be view as a virtual external magnetic field B_1 oscillating at the Larmor frequency parallel to xy plane. This magnetic field will toggle the magnetization on the transverse plane, forming an angle with the Z axis. These pulses are generated using the coil described upper which can worked as emission.

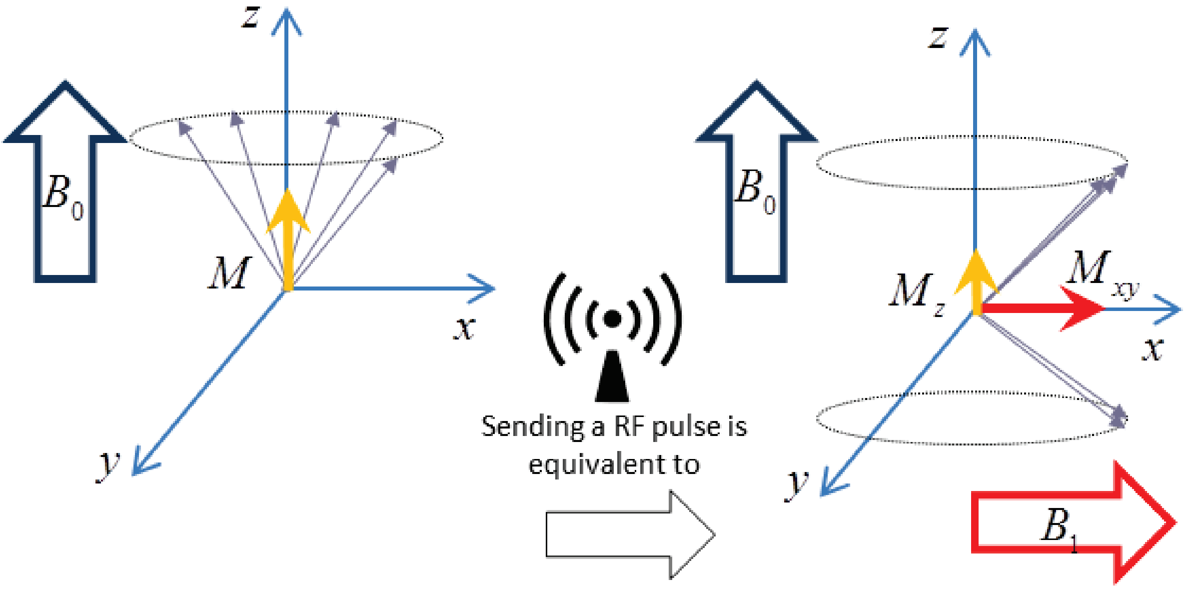

Figure 3.5:RF pulse switch microscopic magnetic moments from low energy state to high energy state. During all the duration of it application, RF pulse act like an external magnetic field B_1 introducing a phase coherence of all individual magnetic moments.

3.2.3. Relaxations

After the application of the RF pulse, the individual magnetic moment and thus the macroscopic magnetic moment slowly tend to regain its original precession state following two characteristics times: *T1* and *T2*.

3.2.4. Spin-lattice relaxation: *T1*

The longitudinal relaxation or spin-lattice relaxation results from energies exchange with the environment of particles. The T1 value describes the time needed by the system to regain its initial position, introducing this value in the equation 3.17 we obtain the differential equation:

$$\frac{\partial M_z}{\partial t} = -\frac{(M_z - M_0)}{T_1} \qquad 3.26$$

This has for solution, displayed in Figure 3.6:

$$M_z(t) = M_0 - (M_0 - M_z(0))\exp(-\frac{t}{T_1}) \qquad 3.27$$

3.2.5.

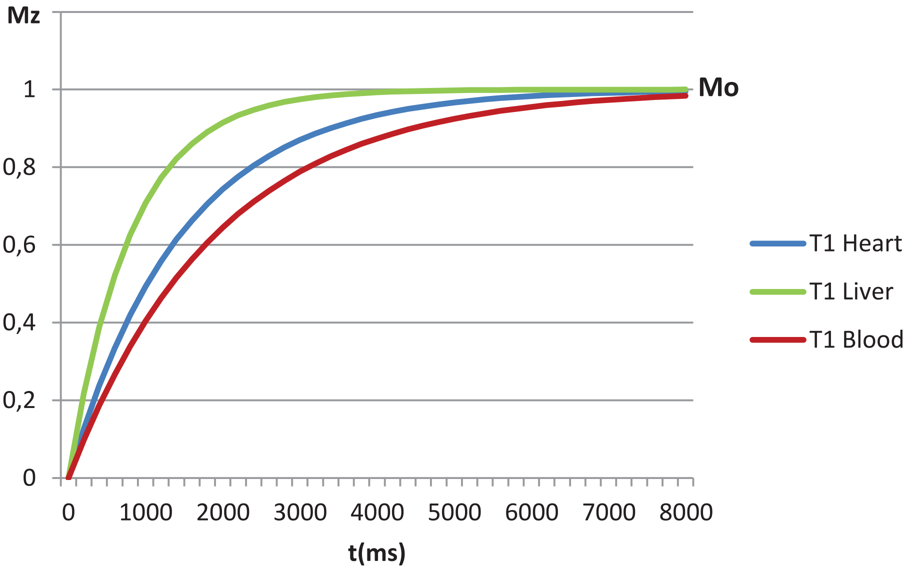

Figure 3.6 : Longitudinal relaxation time curves obtained at 1.5T using T1 values measured at 37°C by Stanisz (Stanisz et al., 2005).

3.2.6. Spin-spin relaxation: *T2*

The transverse relaxation or spin-spin relaxation is a phenomenon due to energies exchanged between nuclei. These interactions quickly lead to a loss of phase coherence between microscopic magnetization moments. Introducing an additional attenuation depending of time on the transverse magnetization, the equation 3.15 and 3.16 become:

$$\frac{\partial M_x}{\partial t} = \gamma M_y \times B_0 - \frac{M_x}{T_2} \qquad 3.28$$

$$\frac{\partial M_y}{\partial t} = \gamma M_x \times B_0 - \frac{M_y}{T_2} \qquad 3.29$$

And thus the solution for the transverse magnetization becomes:

$$M_\perp(t) = M_\perp(0)\exp(i\omega_0 t)\exp(-\frac{t}{T_2}) \qquad 3.30$$

To simplify the notation and the representation, these equations are often rewrite in a rotating frame oscillating at the Larmor frequency has shown in Figure 3.7.

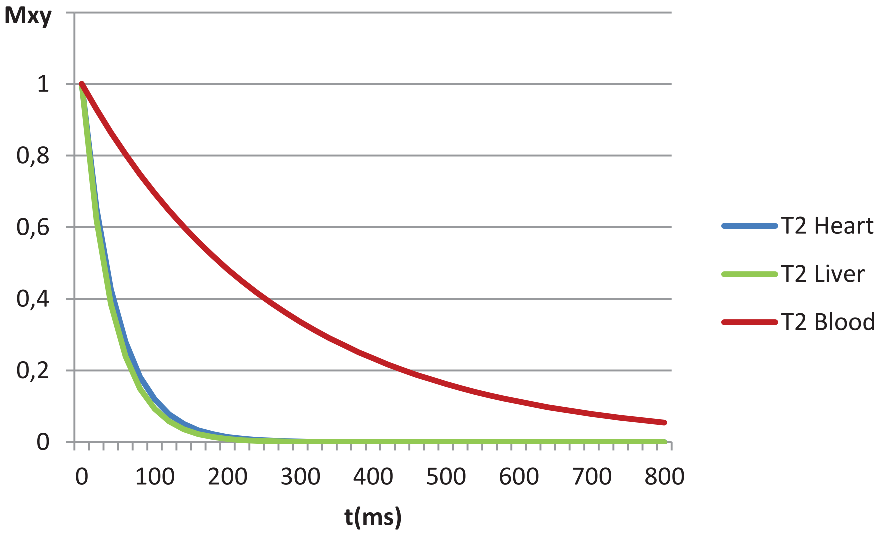

Figure 3.7: Transversal relaxation time curves in a rotating oscillating at the Larmor frequency obtained for 1.5T using T2 values measured at 37°C by Stanisz (Stanisz et al., 2005).

3.2.7. Bloch equations

Combining the two previous solutions and rewriting the global differential system, we obtain the famous Bloch equations introduced by Felix Bloch in 1946:

$$\frac{\partial M_x(t)}{\partial t} = \gamma (M(t) \times B(t))_x - \frac{M_x(t)}{T_2} \tag{3.31}$$

$$\frac{\partial M_y(t)}{\partial t} = \gamma (M(t) \times B(t))_y - \frac{M_y(t)}{T_2} \tag{3.32}$$

$$\frac{\partial M_z(t)}{\partial t} = \gamma (M(t) \times B(t))_z - \frac{M_z(t) - M_0}{T_1} \tag{3.33}$$

Or in reduce form:

$$\frac{\partial M}{\partial t} = \gamma M \times B - \frac{M_x \vec{i} + M_y \vec{j}}{T_2} - \frac{(M_z - M_0)\vec{k}}{T_1} \tag{3.34}$$

An example of the relaxation decay curve, also called free induced decay (FID), are given in Figure 3.8 after a RF pulse of 90°:

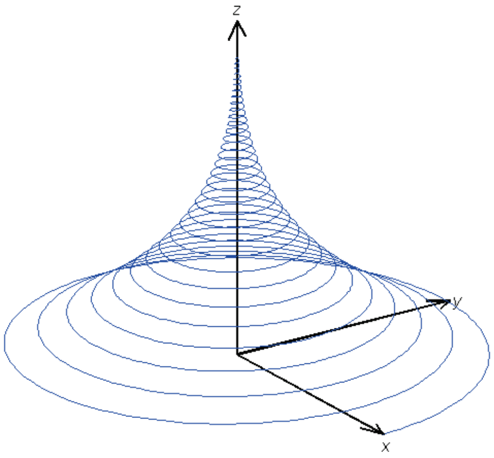

Figure 3.8: Global path of relaxation for the magnetic moment M after a RF pulse of 90°.

3.2.8. Repetition time and Steady State

If the repetition time (TR,time between two RF pulses) is shorter than T1, M_z will not regain its initial maximum value M_0. In this situation a new steady-state longitudinal magnetization M_{ss} will be established, where $M_{ss} < M_0$. This phenomenon reduces the signal available for imaging and thus lead to a smaller signal –noise rate (SNR).

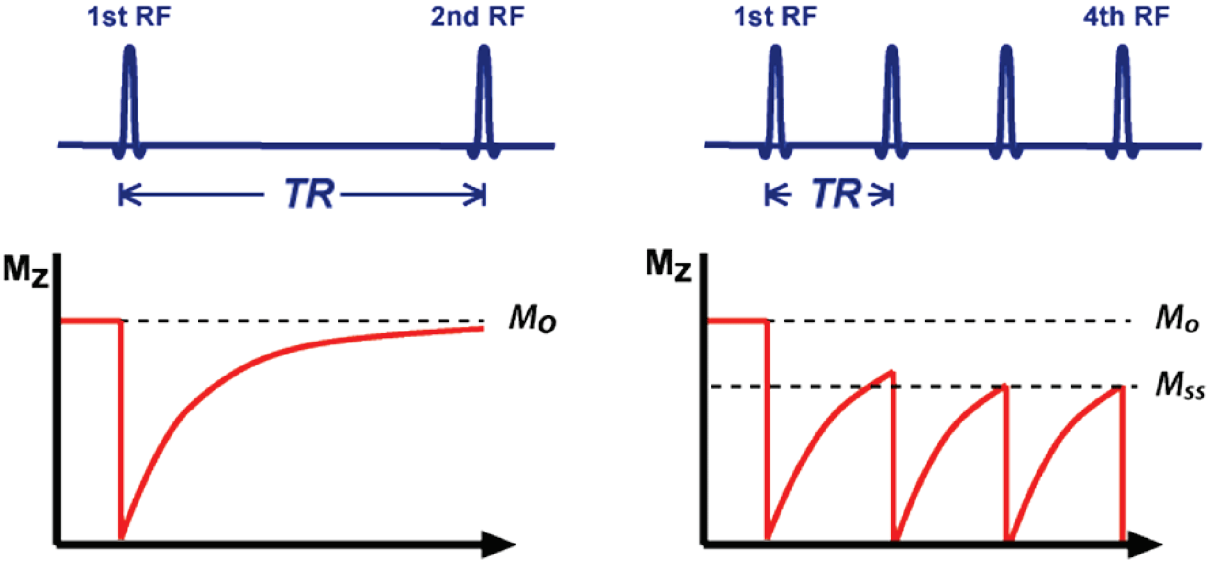

Figure 3.9: Reduction of TR and introduction of partial saturation through development of steady-state magnetization (M_{ss}) © http://mri-q.com/how-is-signal-higher.html

3.3. Spatial Encoding of the magnetization

3.3.1. 1D encoding using gradient magnetic field

Until this point, the previously described NMR experiment simply consisted in introducing a sample in a magnetic field B_0, send an RF pulse for a short moment and catch a current which signal intensity relates to the available magnetization and follow relaxation rules established above. But we are not able to differentiate two samples at two different locations; the resulting signal will be the sum of signals of these two samples. To accomplish that, we need a method to spatially differentiate the objects. Given the direct relation of magnetization M and B_0 this can be achieved by modifying locally the magnetic field. Indeed a gradient coils can linearly modify the magnetic field across the imaging volume, for example along the Z-axis as shown on

.

Figure 3.10: Representation of gradient varying magnetic field along Z-axis.

The magnetic field seen by the samples will thus vary according of their Z-positions:

$$B(\vec{r}) = G(t).r_z + B_0 \qquad 3.35$$

The Larmor frequency of each sample became Z-dependent:

$$\omega_0(\vec{r}) = \gamma B(\vec{r}) = \gamma(G(t).r_z + B_0) \qquad 3.36$$

Neglecting the relaxations effects and in a simple expression, the signal *S(t)* obtained by a coil on a volume of spin *p(r)dr* can be expressed as:

$$\partial S(t) = \rho(\vec{r})\exp(i\omega_0(\vec{r})t)\partial r \qquad 3.37$$

Introducing 3.35 into 3.37:

$$\partial S(t) = \rho(\vec{r})\exp(i\gamma(G(t).r_z + B_0)t)\partial r \qquad 3.38$$

$$S(t) = \int_{sample} \rho(\vec{r})\exp(i\gamma(\int_0^t (G(t).r_z + B_0)\partial t))\partial r \qquad 3.39$$

We obtain a signal depending of time and positions.

3.3.2. Reciprocal lattice: K-space

Create an image from the previous equation corresponds to express the spin density *p(r)* at any position in function of the signal received by the coil. In this way, using this signal received by the coil we will be able to know the density of spin at each position. Taking back the equation 3.37 in general form in the rotating frame ω_0:

$$S(t) = \int_{sample} \rho(\vec{r})\exp(i\gamma\int_0^t G(t).\vec{r}\partial t)\partial r \qquad 3.40$$

Posing:

$$\vec{k} = \gamma\int_0^t G(t)\partial t \qquad 3.41$$

We obtain:

$$S(\vec{k}) = \int_{sample} \rho(\vec{r})\exp(i\vec{k}.\vec{r})\partial r \qquad 3.42$$

Under this form we can extract the spin density *p(r)dr* as the Fourier transform of the signal *S(k)*:

$$\rho(\vec{r}) = \int_{sample} S(\vec{k})\exp(i\vec{k}.\vec{r})\partial k \qquad 3.43$$

This equation establishes a virtual space also called Reciprocal space or k-space which can be explored to describe *p(r)*. In practice discrete Fourier transform is used to recreate the image, leading to all limitations behind discrete signal sampling (Nyquist criterion, aliasing …). The two samples can now be differentiated along the z direction but the spatial differences in Magnetization along the x and y axes are still unknown using a unique magnetic field gradient aligned with B_0.

3.3.3. 2D Encoding and k-space readout

To browse a k-space in 2D dimensions, 2 encoding steps are mandatory: the phase encoding and the frequency encoding. Phase encoding consists in applying a phase variations according spin positions on the y-axis and similarly a frequency variation according the x-position for the frequency encoding. We have seen above that frequency variation according a direction can simply be obtained by playing a gradient of magnetic field in this specific direction. As shown in Figure 3.11, this frequency can be used to differentiate spin on the x-axis.

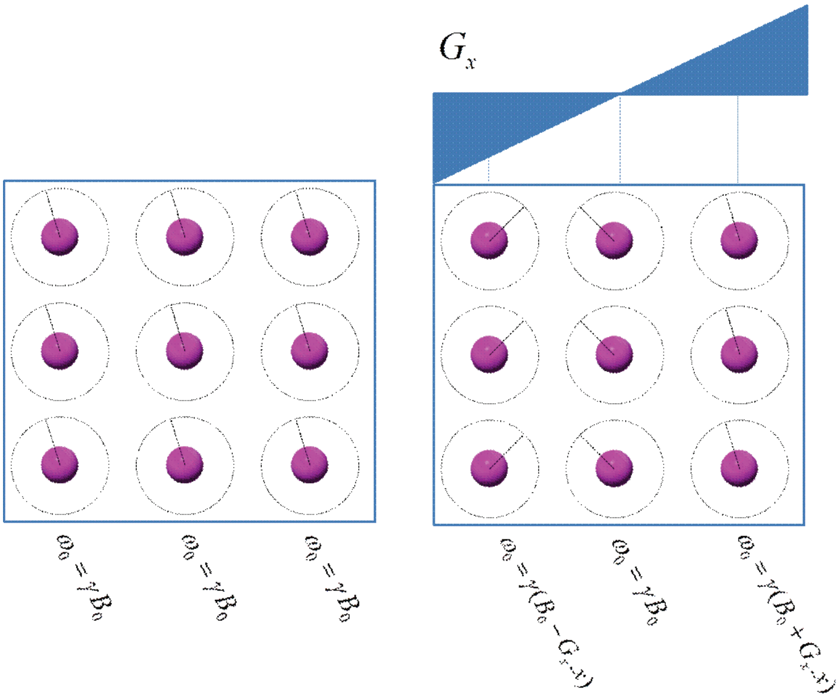

Figure 3.11: Diagram of frequency encoding, before and during application of a gradient of magnetic field.

At the end of application of this gradient, the spins will undergo at the Larmor frequency, but diphase from each other's. The accumulated phase will be position dependent and given as:

$$\phi = \gamma \int_0^t G(t)\partial t \qquad 3.44$$

As shown in Figure 3.12, this accumulated phase can be used to differentiate spins on the y-axis.

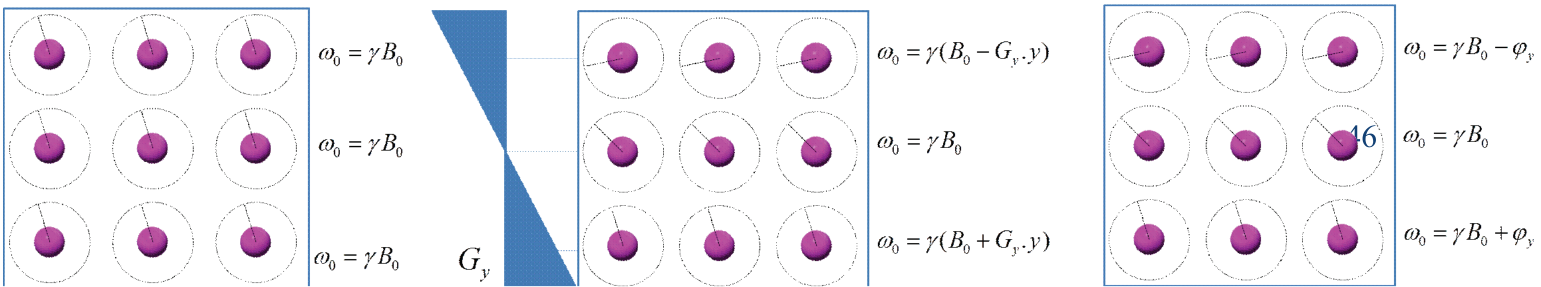

Figure 3.12: Diagram of phase encoding, before, during and after the application of a gradient of magnetic field.

Making the parallel between equations 3.40 and 3.44, the accumulated phase corresponds to a displacement on the k-space according the direction of application of the gradient. The sampling of a line of k-space can be realized be sequentially performing the phase encoding and the frequency encoding as shown in Figure 3.13. The signal is catch by the coil during the step of frequency encoding also called readout.

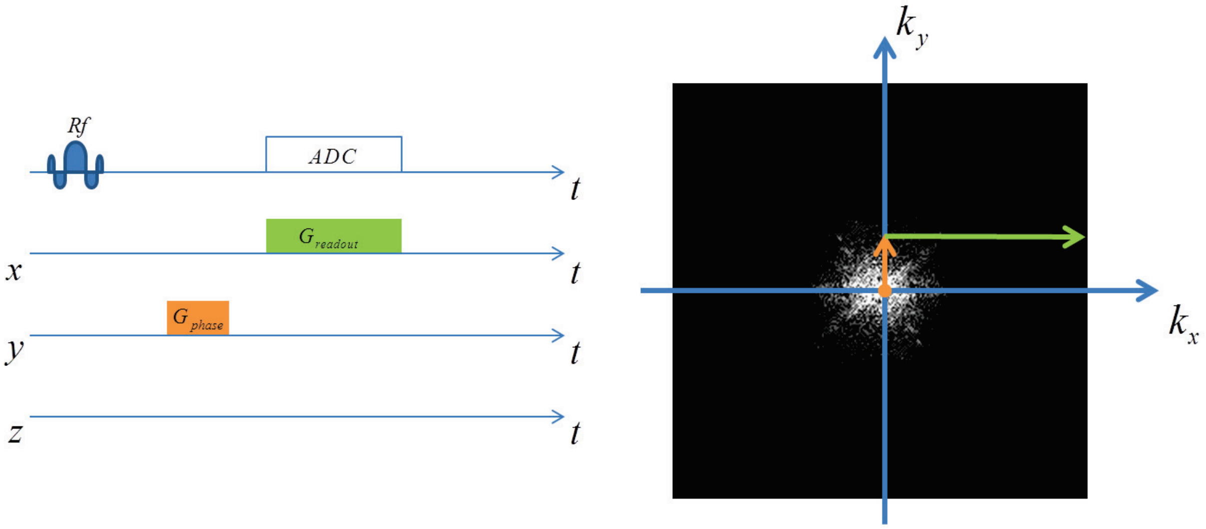

Figure 3.13: Chronogram of phase and frequency encoding. Analogic-to-digital converter (ADC) is executed in the same time of the frequency encoding to catch the NMR signal.

These operations correspond to the acquisition of a simple half line of the reciprocal space and need to be repeated to fill the entire k-space. They can be extended in 1, 2 or 3D with in accordance 1 2 or 3 encoding steps.

3.3.4. Slice selection

A slice selection can be performed by adding a linear gradient to the static field B_0 along a desired direction while applying simultaneously a RF pulse. Because the Larmor frequency is position dependent when a gradient of magnetic field is applied, playing a RF pulse with an adjusted frequency and bandwidth will lead to excite a corresponding slice with a specific thickness.

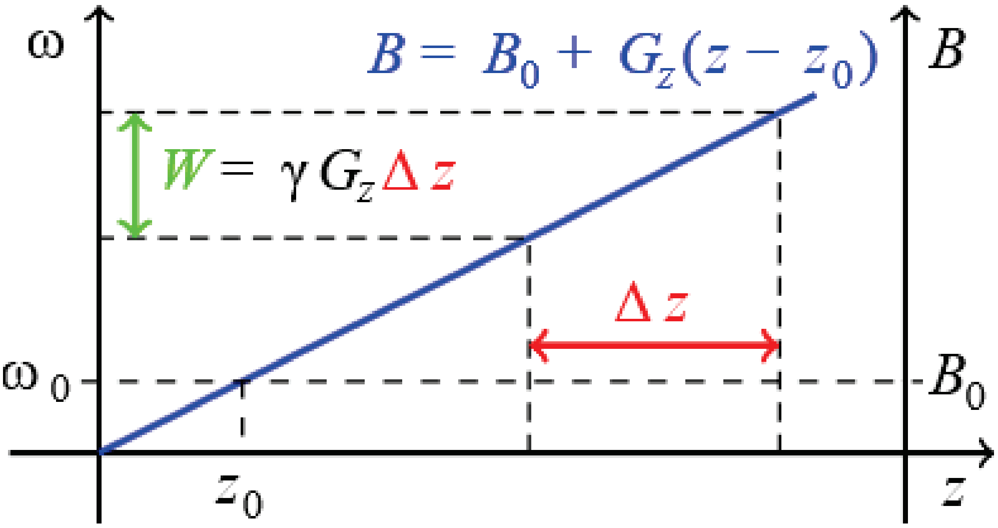

Figure 3.14: MRI slice selection principle. A magnetic gradient G creates a linear relationship between the magnetic field B and the spins location along the axis z. Thus spins resonance frequency depends on z according to the Larmor equation. Finally only the spins whose frequency is within range of excitation pulse frequency are excited: only a slice along axis z is excited.

3.4. Basic sequences

3.4.1. Spin Echo

In real experiment, transverse magnetization decay is always faster than describes by spin-spin interaction mechanism. This value noted T2* is always inferior to the original T2 and come in majority to magnetic field inhomogeneity. A technique invented by Erwin Han in 1953, called Han echo or spin Echo, is based on the application of another RF pulse to null the dephasing impact of homogeneities. The idea is to use a 180° refocusing pulse to reverse the magnetization on the transverse plan, in this way the dephasing introduced between the initial pulse and the refocusing pulse will be null at twice this time. An echo will rise at this moment with an amplitude corresponding to the initial T2 curve. The echo time TE can be adjusted by varying the time between the initial pulse and the refocusing pulse as shown in Figure 3.15.

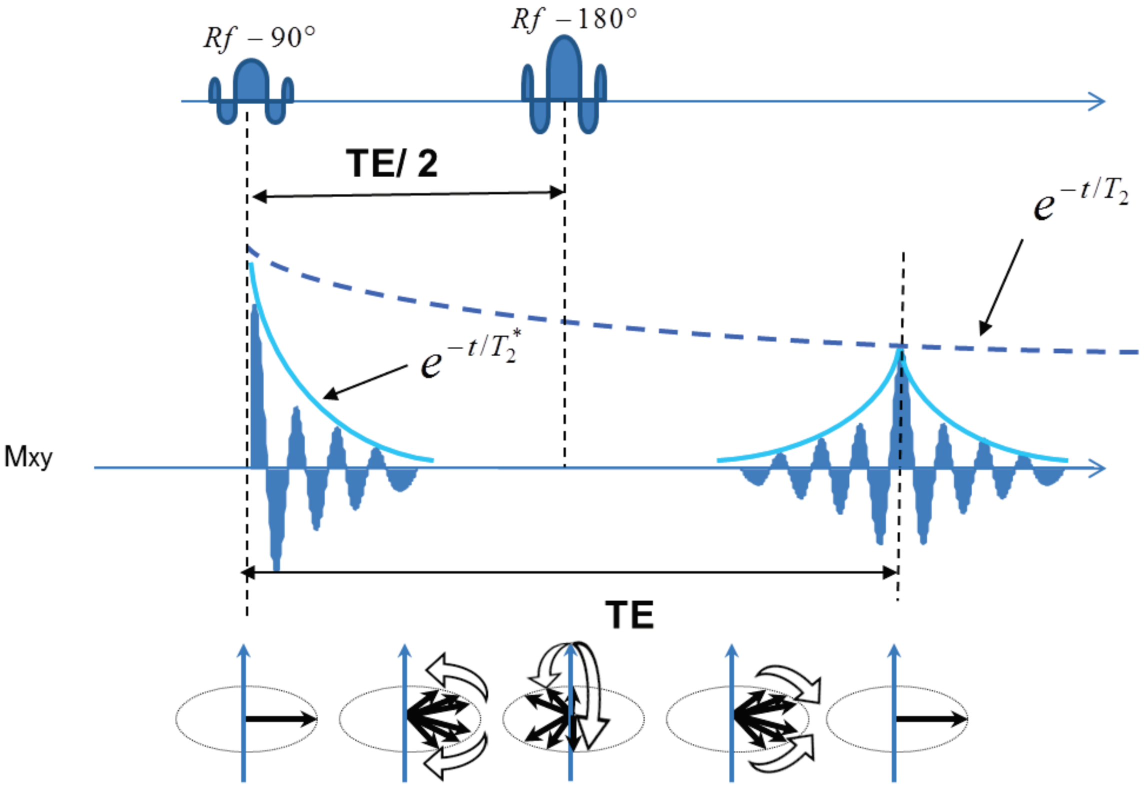

Figure 3.15: Spin echo principle. At time TE/2 a pulse of inversion reverse the accumulated phase due to inhomogeneity which conduct to a null phase a time TE.

3.4.2. Gradient Echo

A gradient echo can be produced by dephasing the spins using a gradient and then re-phasing theses spins with a gradient with opposite amplitude as shown on Figure 3.16. In the frequency direction, gradient echo correspond to the readout of an entire line of k-space.

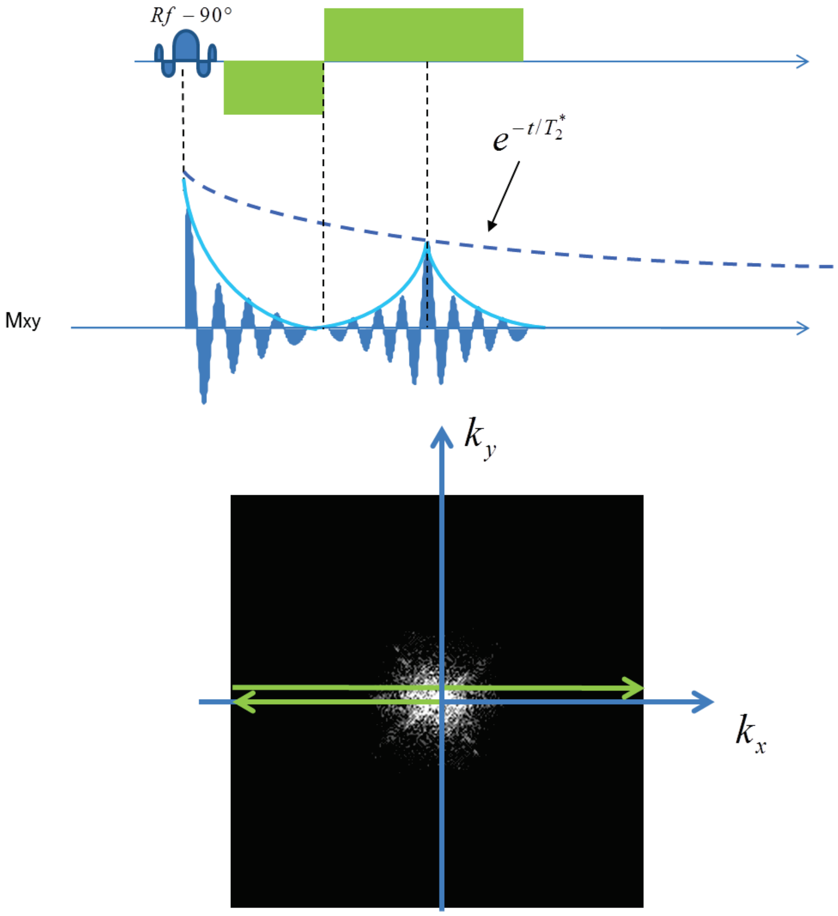

Figure 3.16: Gradient echo principle and corresponding path into the k-space.

3.4.3. Echo planar Imaging

Techniques to read the K-space in one time exist, these sequence are called single shot in opposite to the previous called multi-shot. The most popular of them is the Echo planar Imaging (EPI), it consist in a repetition of gradient echo interleaf of ultra-short phase encoding gradient called “blips”. This technique is very fast, the readout duration for the whole k-space is about less than 20ms in this work, but the alternation of positive and negative readout gradients create “Foucault currents”\“Eddy Currents” in the gradient coil. In short, the eddy currents generate magnetic fields that vectorially combine with the other gradient pulses. In the case of EPI, this error in the local gradients will shift the echo position and lead to ghost in the final image. Some corrections have been proposed over the year, but this remain the main limitation of the EPI technique, nevertheless is it the most used readout scheme nowadays in diffusion on any organ.

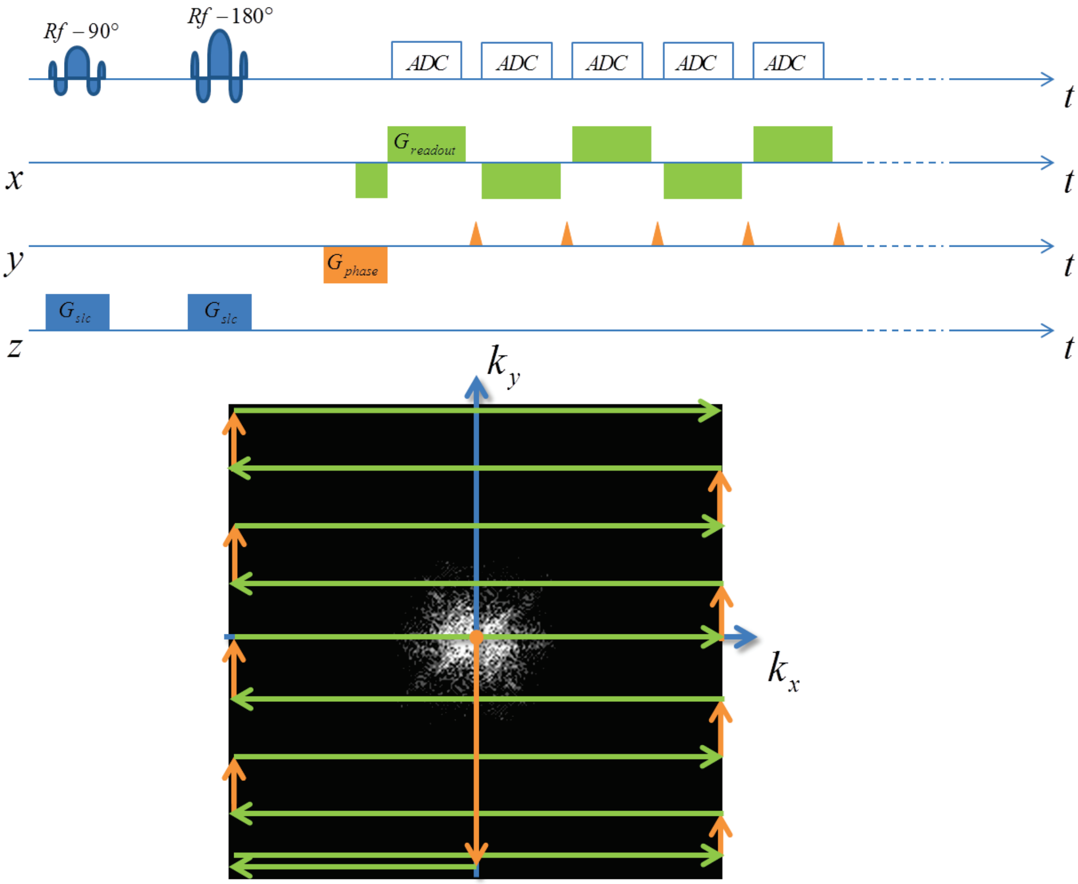

Figure 3.17: Echo Planar Imaging (EPI) is based on the repetition of gradient echo interleaved by short gradient in the phase encoding direction. The k-space is sample in a single time.

3.5.Cardiac Imaging

3.5.1. Cardiac synchronization and acquisition strategies

As seen above, signal acquisition performed line-by-line, takes a certain time to sample the entire k-space. The acquisition duration is often not compatible with requirements of imaging on moving objects, since motion will prevent sampling of a coherent k-space. Indeed, in the previous formalism, it is mandatory that object position remain unchanged during all the encoding process. In cardiac imaging, one solution is to synchronize the sampling of a maximum number of k-space line with a motionless period of the organ of interest, generally identified using physiological information like the R-wave of the electro-cardiogram (ECG). A 20ms single-shot EPI readout can easily be achieved in a unique cardiaque cycle without suffering from motion, and a subsequent slice can thus be acquired at the next RR interval in a very efficient way. The acquisition could also be positionned at any time-window within the cardiac cycle, like for example in systole to investigate the wall-thickening, or repeated through out the cardiac cycle to illustrate the organ motion. For higher resolution or specific acquisitionthe k-space sampling can thus be divided in short readout segments and distributed over several cardiac cycles using a multi shot sequence. A solution to explore different time points is to divide the cardiac cycle in multiple phases, and organise an appropriate sampling of a reduced number of k-space lines for each phase-interval. The acquisition of such images serie, will also need to be distributed over several cardiac cycles as shown in Figure 3.18.

For the myocardium, the longest motionless interval is the end-diastole corresponding to full loading of the heart with freshly oxygenated blood and caracterized by a near constant maximal volume of blood in the cavity.

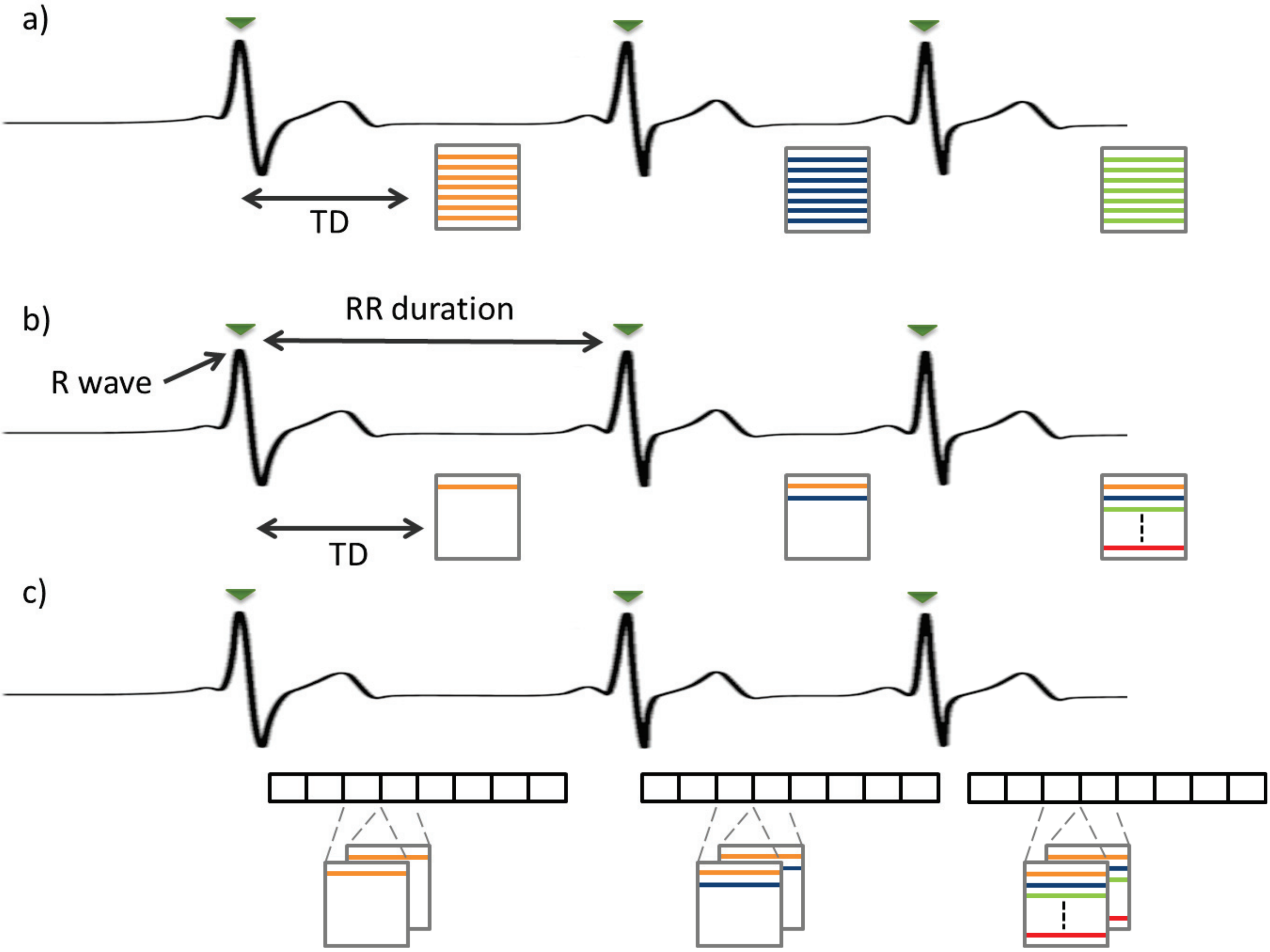

Figure 3.18 : Acquisition is synchronized with the R-wave of the ECG. The time between the R wave and the start of the measurement is called Trigger Delay (TDs). a) For single shot sequence like EPI, the k-space is fill in a single heartbeat b) For multi-shot sequence, read of k-space can be distributed over many heart beat c) Cardiac cycle can be divided in multiple phase to explore different time points.

3.5.2. Breathing management : prospective approach

To acquire images uncorrupted by respiratory motion artifacts, cardiac imaging is often performed on patient holding the breath. However, many patients are not able to hold the respiration for more typical 15-20 sec breath-hold duration or measurements may be continuous or prolonged (for example to explore the distribution of a contrast agent injection during several minutes). In these cases, alternative techniques need to be developed, and one is using so-called navigators (Firmin and Keegan, 2001). Navigators are additional RF-pulses describing a spatially localized cylinder combined with fast readout providing a 1D image generally acquired prior the sequence acquisition. . This prospective method is used to dynamically track anatomic motion and provide the position of the organ during the respiratory cycle. Such 1D navigator cannot be used to track the respiratory motion directly on the heart since it induces signal saturation in the tissue where it has been placed. For breathing synchronization in cMRI, navigators usually explore the head-foot motion of the liver and are placed on the dome of the liver (Figure 3.19). More sophisticated method exists such as 2D or 3D navigators (Butts *et al.*, 1996) (Atkinson *et al.*, 2006) (Porter and Heidemann, 2009) or strategies based on external sensor like Ultra-Sound system (Feinberg *et al.*, 2010) or external sensor (Ooi *et al.*, 2009).

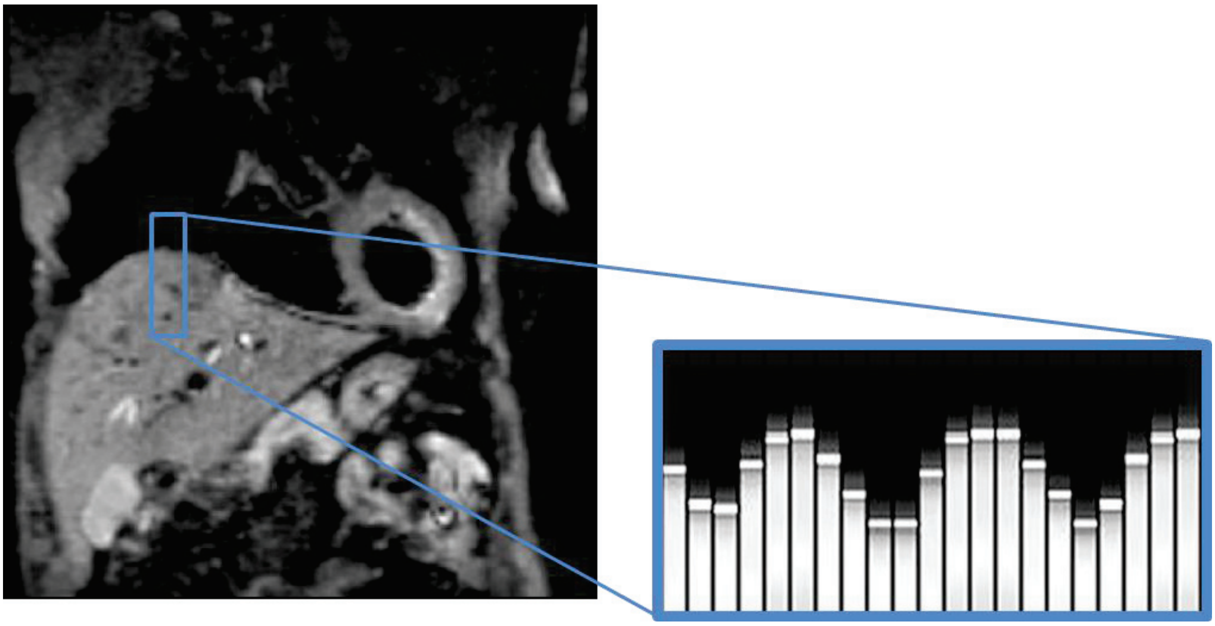

Figure 3.19: Navigator is place on the dome of the liver to derive the interface lung/liver.

We further details here only the two 1D navigator used in this work but which are also used and widespread for abdominal application in the MRI literature (van Heeswijk *et al.*, 2012).

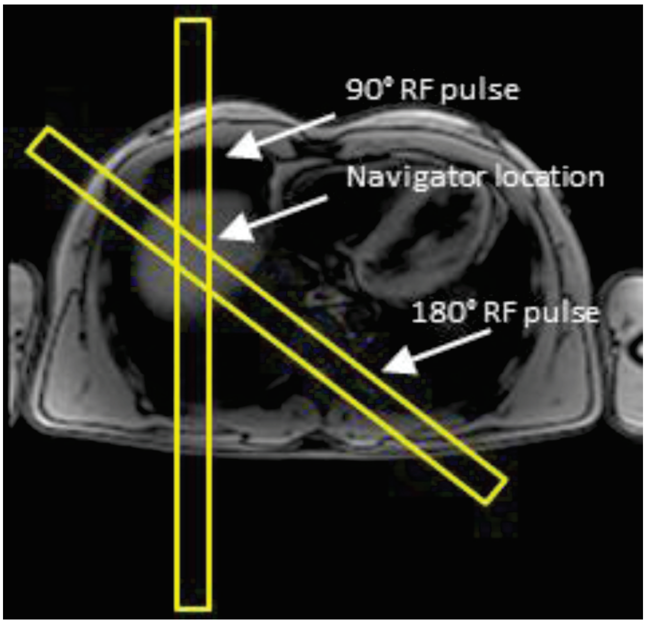

Cross pair navigator consist in a spin-echo approach where the 90° RF excitation and 180° RF refocusing pulses are obliquely aligned. A spin echo will rise in the overlapping area describing a tube. Fast one line readout is then applied to catch this signal.

Figure 3.20: Cross-pair navigator is composed of 2 RF pulse cross to produce an echo in the overlapping area.

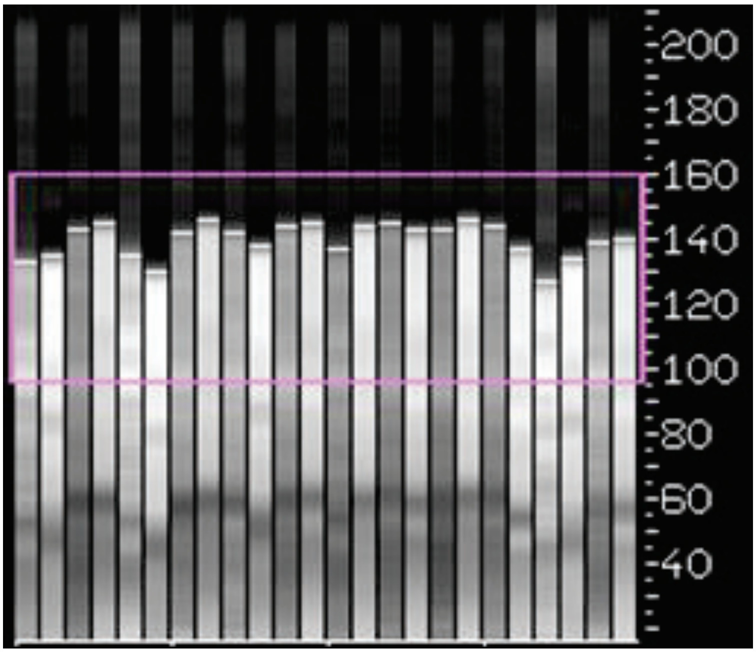

The 1D image reconstructed is analyzed by a Siemens in-line automatic segmentation algorithm which extracts the Liver/Lung interface. The relative simplest implementation and robustness of this navigator has motivated its spreading.

Figure 3.21: Each column is a cross-pair 1D image, the white part is the Liver and the black part the Lung. The horizontal white bar is determined by the in-line algorithm, the purple scare is the gate defined by the user.

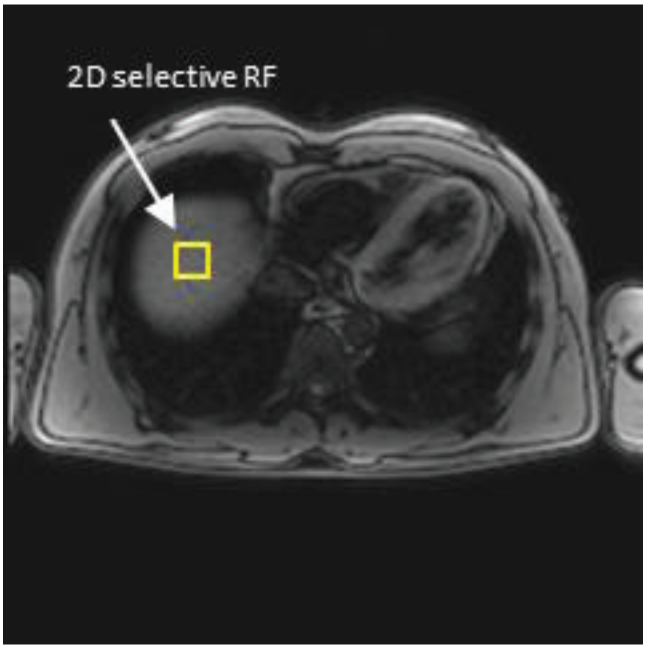

Pencil beam navigator is based on the zonal selective RF pulse. The reciprocal emission space is sample with a blipped planar path resulting in exciting only a small cylinder. The corresponding flip angle is about 30° and fast gradient echo readout is then applied to catch this signal.

Figure 3.22: Pencil beam navigator is composed of a 2D RF selective associate with a short readout.

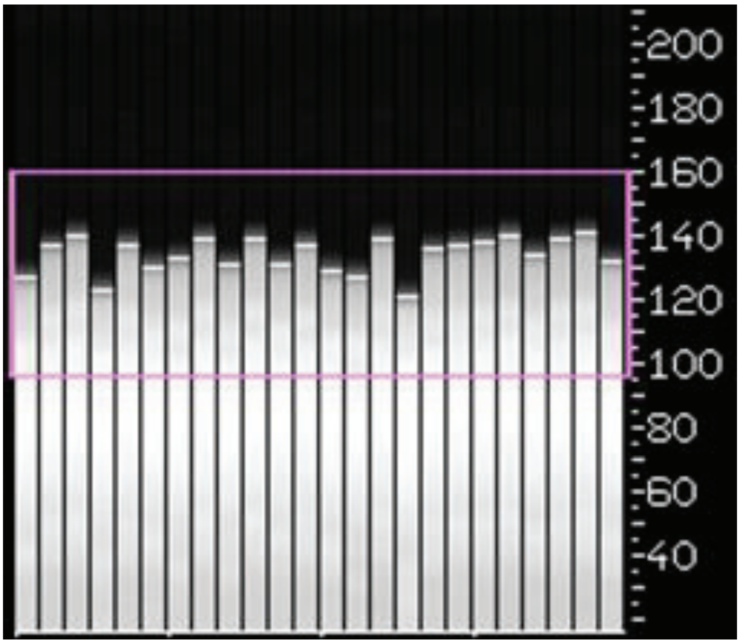

Signal and thus contrasts are stronger with the pencil beam navigator. However in the current implementation the rotation of the 2D-RF pulse is not well managed. Consequently the pencil beam approach was considered as limited in comparison to the cross pair navigator and was abandoned on the recent Siemens software version.

Figure 3.23: Similarly to Figure 3.21, each column is a pencil beam 1D image representing the Liver/Lung interface.

In this work, pencil beam navigator was used during validations realized on Avanto system (Chapter 5). Cross-pair navigator was used on the most recent system like Aera/Prisma system with equivalent result (Chapter 7).

The physiological information derived from navigators can be used with two different acquisition strategies in Siemens system. The first one is the so-called "gating" approach, which consist in keeping images acquired only at expiratory breathing phase, a well know reproducible phase were the movement due to the respiration is minimum. Immediately prior the sequence, the 1D navigator image is acquired and compared to an interval of value defined by the user (the "gate" as shown in Figure 3.24). If the information is inside this window the image is kept over wise it is reject and the acquisition is repeated. It is important to note that even if the navigator information is outside the gate, the sequence is played, which maintains the TR equal to one RR and thus the steady-state. This strategy is well design only for non-selective pulse acquisitions like single slice or 3D acquisitions. Indeed due to the displacement of the heart due to respiratory, at a none-expiratory phase, selective RF pulses will be played at a bad anatomic location which will break the steady state.

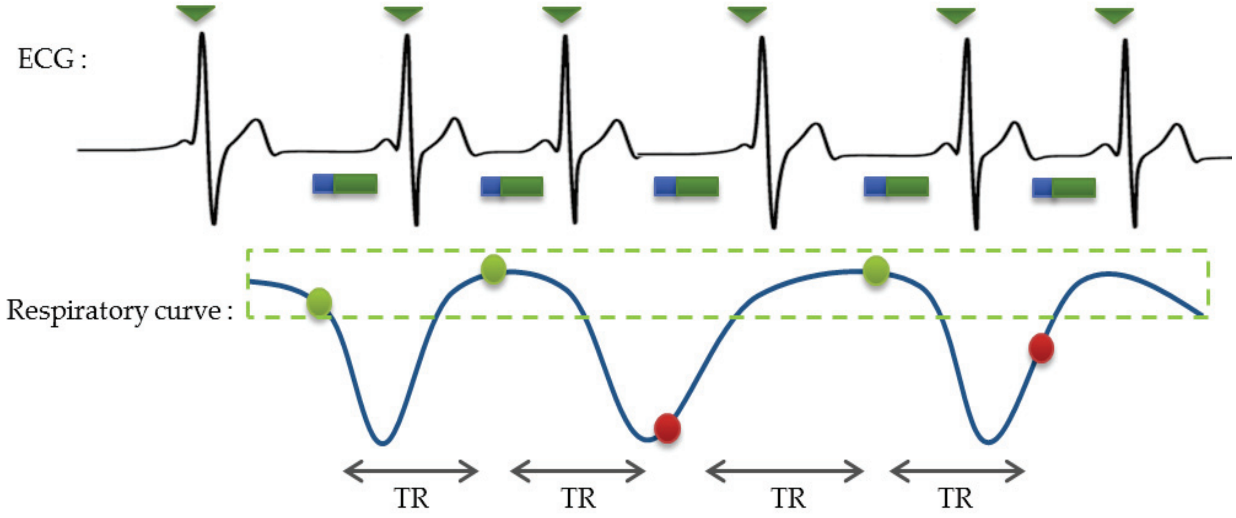

Figure 3.24: The navigator (blue) is played before the sequence (green), if the information obtained with the navigator is outside the windows the sequence is played but the image is not kept and need to be re-acquired.

The second one is the “triggering” approach with the sequence not played continuously like previously. Similarly to gating approach, the 1D navigator information is compared with the window condition imposed by the user. This time, if this information is outside this window, the acquisition is just simply not launch. In this condition TR is strongly dependent of breathing cycle but multiple slice protocols or selective pulse acquisitions can be organized in a way to provide the optimal steady state.

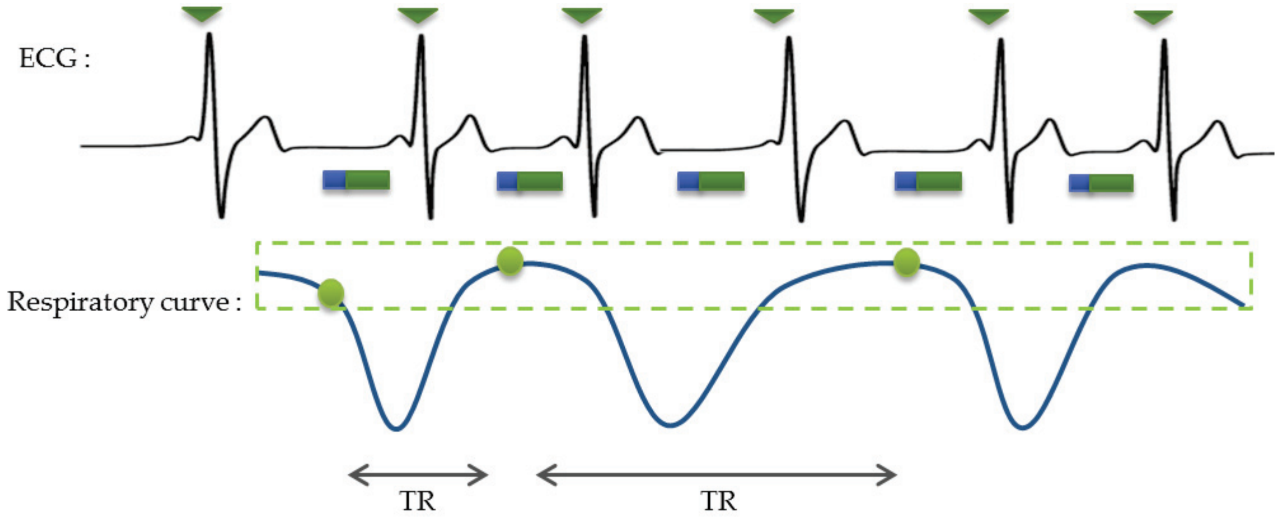

Figure 3.25: The navigator (blue) is played before the sequence (green), is the information obtained with the navigator is outside the windows the sequence is not played.

3.5.3. Breathing management: Retrospective approach

In case of multi-shot sequences, breathing motion induces an inconsistency of k-space sampling and hence creates ghost in the image. Retrospective motion correction methods proposed by {Atkinson, 1999 #1543} are based on the application of transformation matrix on the corrupt k-space according a known motion. Theses method limited to simple translation/rotation has been extended by {Batchelor, 2005 #1542} to non-rigid motion using inverse problem. Main limitation behind these works is the characterization of motion which imposes external sensor to measure the breathing cycle during the acquisition Recently {Odille, 2008 #1540} have completed these techniques by introducing a model to predict cardiac and respiratory motions during the experiment based on prior knowledge provided by external sensor. As presented above navigators could be an alternative to measure this physiological motion during the acquisition for direct correction or to fill up a motion model.

For single shot acquisitions which are generally shorter, breathing motion does not impact the k-space sampling but induces displacement in the finale image depending of the respiration phase. If this displacement occurs in the acquired image (i.e. for 2D images in x and y directions) it is possible to extract a displacement filed from a reference and then apply a correction which is the general idea behind registration algorithm. Motion occurring though the image (i.e. for 2D images in Z direction) cannot be corrected retrospectively. Registration algorithm and general reconstruction used in this work were detail in chapter 6.

4. Diffusion concept

In biology, molecular diffusion, usually called diffusion, is one the main form of transport and exchange of material between compartments like cells, capillary, extra-cellular space... Water molecules in tissue are mainly affected by self-diffusion induced by thermal energy within surround architecture and other molecules. In a macroscopic view, diffusion is the result of all random microscopic interactions but the global displacement of all these molecules is measurable and well described by statistical law.

In pathology affecting tissues, changes of compartments like cells can affect the intra-cellular and extra-cellular volume and in turn affect the diffusion of water molecules. Diffusion-base measurement is a promising bio-maker to explore quantitatively pathologic processes. Also measuring the anisotropy of diffusion is an indirect way to explore tissue architecture.

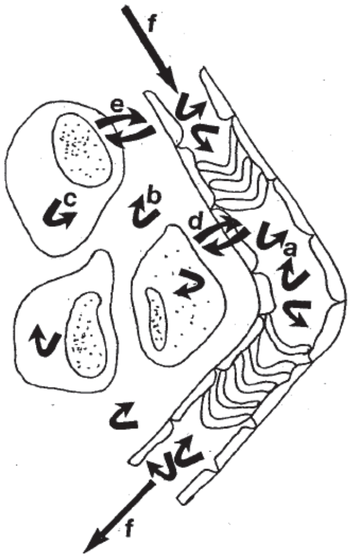

Figure 4.1: All potential sources of incoherent motion in tissue © (Le Bihan et al., 1988)

We proposed in this chapter to explain physical concept behind free, surround and restricted diffusion. Diffusion acquisition and diffusion encoding scheme were also discussed. Gaussian diffusion model and effect of motion on diffusion measurement were then briefly described. Finally we proposed a short overview of principal Cardiac Diffusion Weighted Imaging (CDWI) studies.

4.1. Diffusion physics

4.1.1. Free diffusion

Making a parallel with the thermal diffusivity, Adolf Fick introduced in 1855 his well-known laws governing the transport of mass through diffusive means. These equations describe the flux of material due to the difference of concentration through the molecular displacement also called diffusivity or coefficient of diffusion.

$$J = -D\,\mathbf{grad}\,\phi \qquad 4.1$$

Where D is the coefficient of diffusion (m^2/s), $J(r,t)$ the material flux and $\phi(r,t)$ the molecular concentration. Introducing the mass conservation law:

$$\frac{\partial \phi}{\partial t} = -\,\mathbf{div}\,J \qquad 4.2$$

He obtained the diffusion equation also knonw as the second Fick's law:

$$\frac{\partial \phi}{\partial t} = D\frac{\partial^2 \phi}{\partial x^2} \qquad 4.3$$

In 1905, Albert Einstein has demonstrated that this macroscopic coefficient of diffusion is related to microscopic Brownian motion of molecules described 80 years earlier by Robert Brown. Posing boundaries on the second Fick's law, he obtained the probability density function (PDF) which describes the probability of a molecule located at position r_0 to move to the position r_Δ after the time interval Δ. Posing $r = r_\Delta - r_0$:

$$P(r,\Delta) = \frac{1}{\sqrt{4\pi D\Delta}}\exp^{-\frac{r^2}{4D\Delta}} \qquad 4.4$$

In a pure free media the PDF function is a Gaussian which means that for group of molecules the diffusion is isotropic and the sum of all displacements is null as shown in Figure 4.2. In these conditions the mean quadratic distance occurred by molecules in a time Δ in 3D media is given by:

$$< r^2 >= 6D\Delta \qquad 4.5$$

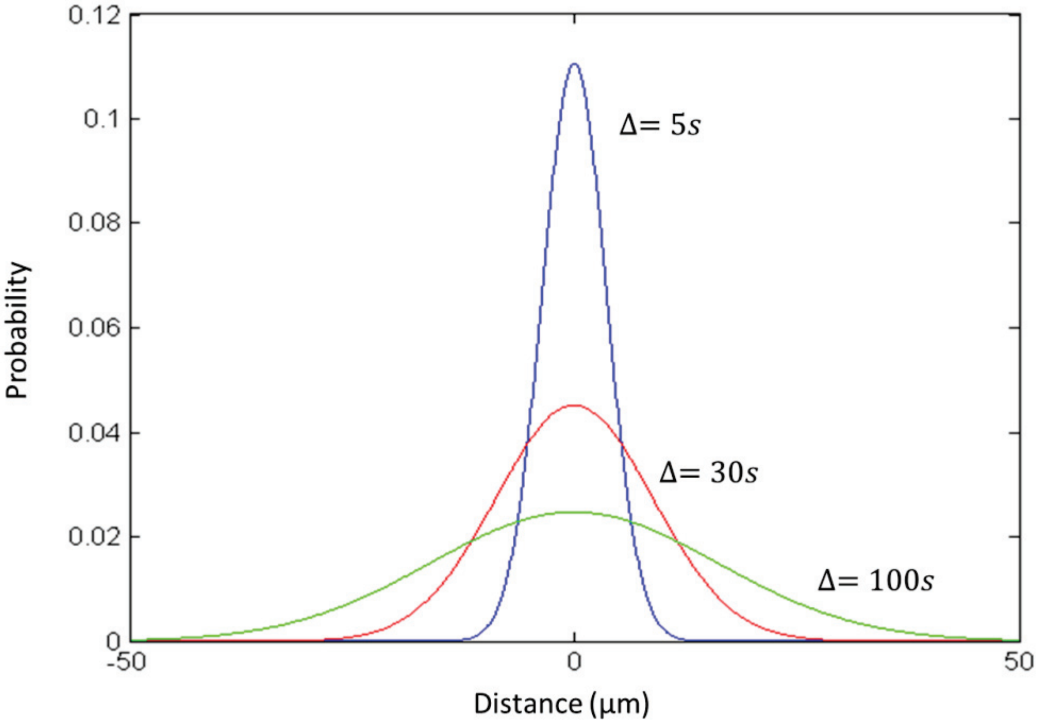

Figure 4.2: Probability Density Function (PDF) at three different Δ with a coefficient of diffusion of $1.5x10^{-3}$ *mm²/s.*

The effect of diffusion on the NMR signal was described by Carr Purcell in 1954 (Carr and Purcell, 1954) and added in the Bloch equation by Torrey in 1956 (Torrey, 1956), in now called Bloch-Torrey equation:

$$\frac{\partial M}{\partial t} = \gamma M \times B - \frac{M_x \vec{i} + M_y \vec{j}}{T_2} - \frac{(M_z - M_0)\vec{k}}{T_1} + \nabla . D \Delta M \qquad 4.6$$

4.1.2. Hindered diffusion, extracellular water

Hindered diffusion usually happens in inhomogeneous environment when water molecule has to skirt around larger obstructing object like molecules cells, cytoplasm, proteins… Distribution of these obstacles in the tissue is generally arranged according an architecture, like in muscle. Diffusivity can thus be reduced in specific directions leading to anisotropy of the coefficient of diffusion.

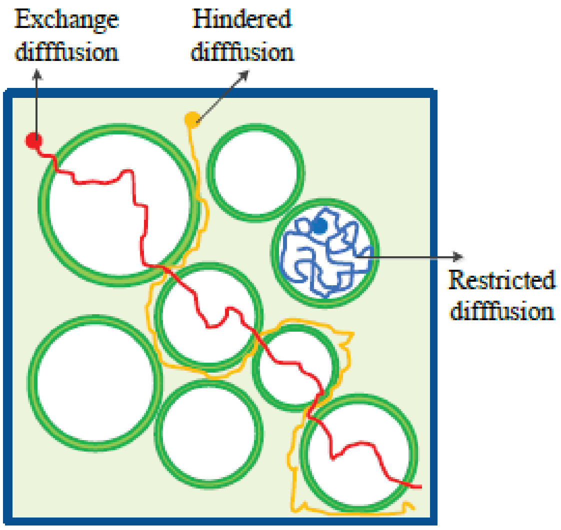

Figure 4.3: Hindered diffusion and others regime of diffusion © Wang thesis 2013

4.1.3. Restricted diffusion, intracellular water

Restricted diffusion appears when water molecules are confined into a small space like intra-cellular volume. In this case, diffusivity of these molecules is very limited and influenced by the size of the cellule. According to the work of Price (Price, 1997) (Price, 1998), if we consider a reflecting sphere of radius R with a molecules of coefficient of diffusion D evolving during a time Δ, we can define the dimensionless variable:

$$\xi = D\Delta / R^2 \qquad 4.7$$

This time scale can help to define the measure of restricted diffusion as shown in Figure 4.4.

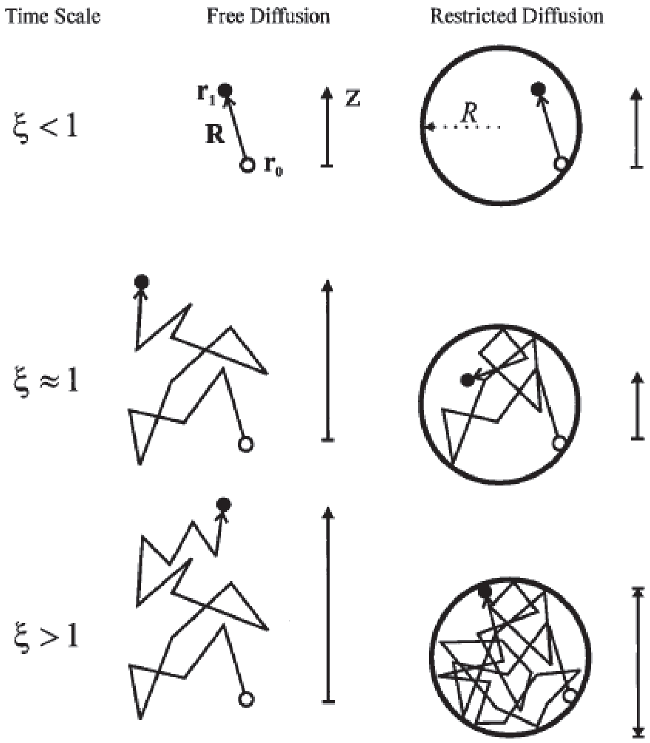

Figure 4.4 : Comparison of free diffusion and restricted diffusion in function of time scale © (Price, 1997).

4.2. Diffusion acquisition techniques

4.2.1. Principles

The first MRI sequence dedicated to diffusion measurement was developed by Stejskal and Tanner in 1965 (Stejskal and Tanner, 1965). This sequence is based on a SE sequence, one symmetric pair of diffusion-weighted gradients is added to either side of the refocusing 180º RF pulse in each encoding directions (slice selection, phase and frequency encoding), illustrated in Figure 4.6.

Assuming a very short gradient of amplitude *G* and duration δ after the initial excitation, the transverse magnetization of a particle at position r_0 accumulates a phase according to equation 3.44:

$$\phi_{x0} = \gamma G \delta r_0 \qquad 4.8$$

After a time $\Delta(\Delta >> \delta)$, if a gradient with amplitude $-G$ is played (or with amplitude *G* but after a refocusing pulse), the phase accumulated is proportional to the distance $r = r_1 - r_0$ traveled by the particle:

$$\phi_{r1-r0} = \gamma G \delta (r_1 - r_0) \qquad 4.9$$

From this equation three cases can be described for a group of particles as shown in Figure 4.5:

A) Static molecules ($r_1=r_0$), the phase accumulated is null.
B) Moving molecules ($r_1\sim=r_0$) with coherent motion like flow, the phase is proportional to the displacement occurred during the time Δ, the macroscopic magnetization is diphase accordingly.
C) Moving molecules ($r_1\sim=r_0$) with incoherent motion like self-diffusion, the phase distribution corresponds to the PDF function detailed in chapter 4.1. The microscopic magnetizations of all molecules are diphase between them; the macroscopic magnetization is still in phase but attenuated like in the T2 process.

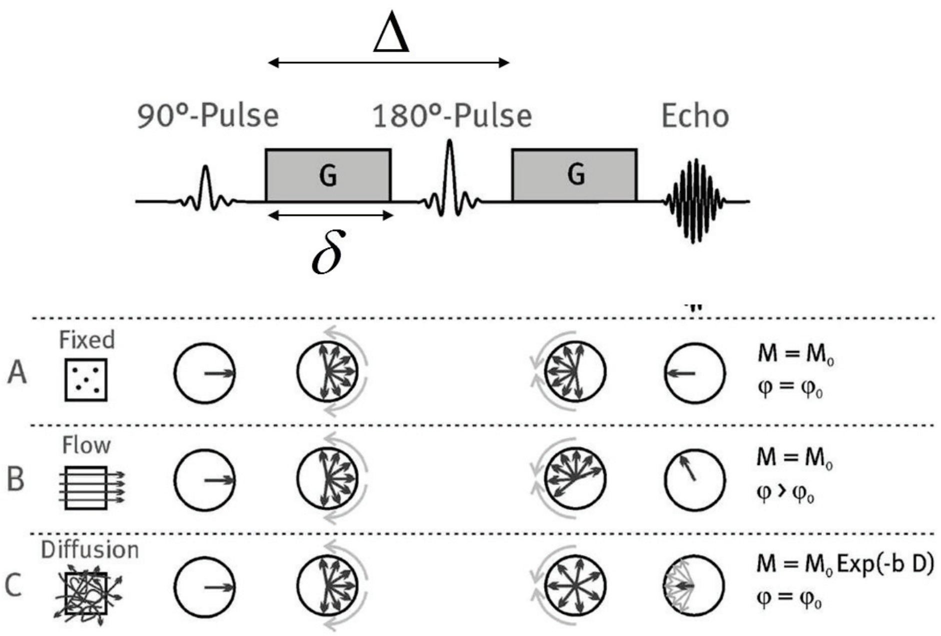

Figure 4.5: Stejkal-tanner diffusion encoding scheme and it influence on NMR signal for A) fixed molecules, B) flowing molecules and C) diffusive molecules. © (Froeling et al., 2014)

The third case is of course the case of interest here but the second one shows that diffusion measurement is also sensitive to bulk motion. Transverse magnetization is given as function of PDF as follow:

	$M_{xy} \propto M_0 . \int_{-\infty}^{+\infty} P(r,\Delta)\exp^{-i\gamma G\delta r}\partial r$	4.10

Where P(r,Δ) is the probability of water molecules located at position r_0 to move to position r_1 after the time interval Δ. The probability distribution can be obtained using the Fourier transform of the measured ratio M_{xy}/M_0 as a function of the diffusion encoding waveform G(t). Making parallel with equation 3.43 describing the reciprocal encoding k-space, a reciprocal diffusion q-space can be introduced in the same way (Stejskal and Tanner, 1965; P. Callaghan *et al.*, 1988; Wedeen *et al.*, 2005) (Cory and Garroway, 1990) (P. T. Callaghan *et al.*, 1999).

	$P(r,\Delta) = \int_{q-space} E(q,\Delta)\exp^{-iq.r}\partial^3 q = F^{-1}(E(q,\Delta))$	4.11

Where P(r,Δ) is PDF equal to the inverse 3D Fourier transform F^{-1} of the diffusion signal *E*, *r* the average diffusion displacement and *q* the moving vector in the q-space described as:

$$\vec{q} = \gamma \int_0^t \vec{G}(t)\partial t \qquad 4.12$$

But for a simple case of an isotropic coefficient of diffusion *D,* the diffusion attenuation of signal can be simply given as a particular solution of Bloch Torrey equation as function of gradient parameter:

$$A_{diff} = \exp^{-b.D} \qquad 4.13$$

Where *b*, so called *b-value,* is related to the gradient duration and time between gradients as:

$$b = \gamma^2 \int_0^{TE} (\int_0^t \vec{G}(t')\partial t')\partial t \qquad 4.14$$

For the Stejkal-Tanner case: $$b = \gamma^2 G^2 \delta^2 (\Delta - \frac{\delta}{3}) \qquad 4.15$$

Finally signal intensity in DWI is affected by all kind of incoherent motions, as soon as the distribution of these motions have a null area like it's the case for Gaussian PDF. Non null distribution impact also the signal but as a phase shift like for flow.

4.3.Diffusion models

Various models have been proposed to analyze diffusion signal from cDWI acquisitions. The simplest model is the Apparent Diffusion Coefficient (ADC) (Moseley *et al.*, 1990) which consists in extracting the diffusion information in a specific direction from two diffusion weighted images. In increasing the number of direction acquired the Diffusion Tensor Imaging (DTI) (Basser *et al.*, 1994; Kingsley, 2006a; Kingsley, 2006b; Kingsley, 2006c) can be used to study the anisotropy of Gaussian diffusion. Another approach consists in extracting the influence of diffusion compartment by applying an important range of b-values which is the general idea behind Intravoxel Incoherent Motion (IVIM) (Le Bihan *et al.*, 1986). High Angular Resolution Diffusion Imaging (HARDI) includes a large number of models which consider diffusion in tissue as non-Gaussian like mixture models (Y. C. Wu and Alexander, 2007), Q-ball Imaging (QBI) (Tuch, 2004), Diffusion Spectrum Imaging (DSI) (Wedeen *et al.*, 2005), Diffusion Orientation Transformation (DOT) (Ozarslan *et al.*, 2006) and Diffusion Propagator Imaging (DPI) (Descoteaux *et al.*, 2009),etc. These models proposed to sample q-space with a high resolution allowing for example the use of Orientation Distribution Functions (ODF) in turn aiming at circumventing the limitation of the tensor model in voxel, showing crossing of the major pathways.

Here we introduce in details the ADC, IVIM and DTI model used in this work.

4.3.1. Apparent Diffusion Coefficient (ADC)

As explained in chapter 4.2, sensitization of diffusion is realized by inducing attenuation on the NMR signal using motion encoding gradient (MEG). However, the diffusion-weighted images obtained are also sensitive to *T1* and *T2* contrast. The *T1* and *T2* relaxation time influence can be removed by acquiring a non-diffusion weighted image S_0 which can be subtracted to the diffusion-weighted image S of known b-value b:

$$S = S_0 \exp^{-b.D} \tag{4.16}$$

$$D = \ln\left(\frac{S}{S_0}\right) \Big/ -b \tag{4.17}$$

D corresponds to the diffusion coefficient in the direction of applied MEG. This simplest model requires at least two acquisitions which is the minimum to be able to extract the diffusion information from the images. But it is possible to extract the coefficient of diffusion D from two diffusion images S_1 and S_2 with two different b-values b_1 and b_2.

$$ADC = \frac{\ln\left(\frac{S_2}{S_1}\right)}{b_2 - b_1} \tag{4.18}$$

Where the diffusion coefficient D is replaced by an Apparent Diffusion Coefficient ADC to indicate that the diffusion measured in imaging is modulated by all sources possible of incoherent motion as shown in Figure 4.1.

4.3.2. Intra-Voxel Incoherent Motion (IVIM)

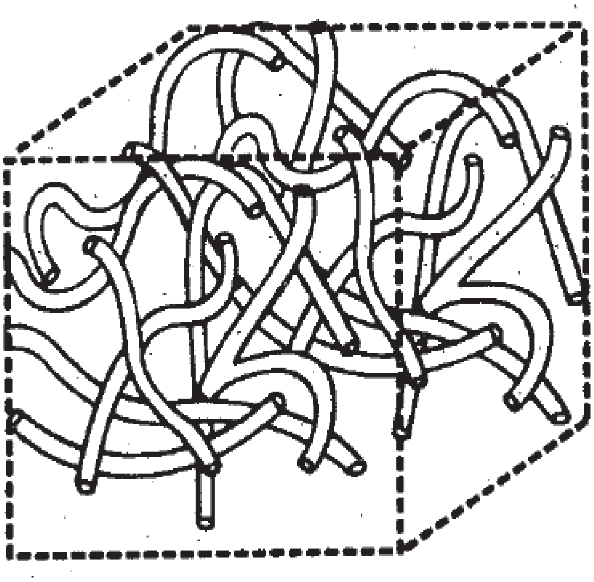

Signal intensity in DWI is affected by the Brownian motion of water molecules present in intra- and extra- cellular but also by all sources of incoherent motion. Pseudo-random distribution of vessels and capillaries within a voxel conduct the blood flow to be view as macroscopic incoherent motion and in turn participating to the diffusion weighting signal intensity. Since speed of blood flow is in a different regimen than self-diffusion, it can be extracted using a multi compartmental model.

Figure 4.6: Pseudo-random distribution of capillary in a voxel © (Le Bihan et al., 1988)

The IVIM model (Le Bihan *et al.*, 1986) aims at the separation of the respective contribution of water molecules diffusion and pseudo diffusion (or perfusion) blood flow in capillaries.

$$S(b) = S_0\left[(1-f)\exp^{-bD} + f\exp^{-b(D+D^*)}\right] \qquad 4.19$$

Where D is the coefficient of diffusion, D^* the coefficient of pseudo diffusion or perfusion, f the fraction of perfusion. This equation describes the signal intensity as a function of the b-value, depending on the D and D^* coefficients and ratio of perfusion/diffusion. For a coefficient of pseudo diffusion higher than diffusion ($D^*>>D$), perfusion affects more the signal at low b-value while diffusion is preponderant at high b-value. A Multi-b-values acquisition, with at least 4 b-values (including b-value=0), and a 4 parameters fit are generally needed to estimate the parameters of interest but several other strategies have also been proposed (Lemke *et al.*, 2010; Delattre *et al.*, 2012) .

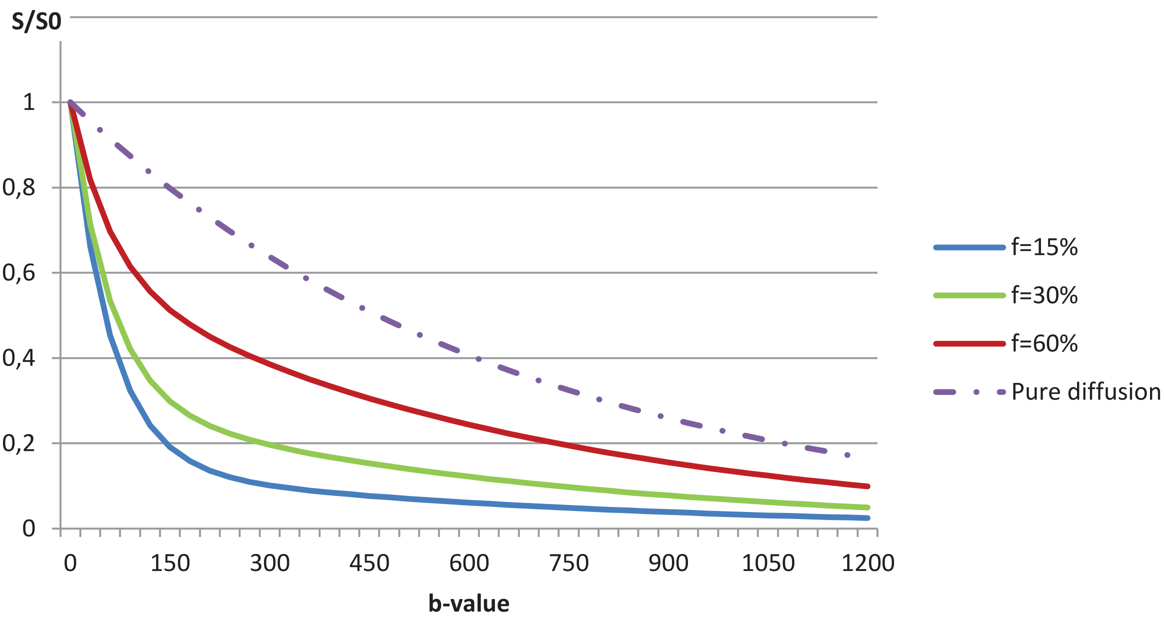

Figure 4.7: Evolution of signal S/S0 as function of b-value for D=0.015 mm²/s, D=0.0015mm²/s for three fraction of perfusion f. Pure diffusion curve was given for D=0.0015mm²/s*

Variant of this model has been proposed by Lemke (Lemke *et al.*, 2010) including the effects of *TR*, *TE* on *T1* and *T2* of blood and cardiac compartment:

$$S(b) = S_0 \frac{(1-f)(1-\exp^{-TR/T_1^{Myo}})\exp^{-TE/T_2^{Myo}} \exp^{-b.D} + f(1-\exp^{-TR/T_1^{Blood}})\exp^{-TE/T_2^{Blood}} \exp^{-b(D+D*)}}{(1-f)(1-\exp^{-TR/T_1^{Myo}})\exp^{-TE/T_2^{Myo}} + f(1-\exp^{-TR/T_1^{Blood}})\exp^{-TE/T_2^{Blood}}} \qquad 4.20$$

It is worth noting that the distribution of micro vessels in the skeletal muscles, the myocardium, the meninges, and the periosteum of tubular bones is anisotropic (Mathieu *et al.*, 1983; Poole and Mathieu-Costello, 1990). As classical diffusion, pseudo-diffusion may have a directional effect depending of the distribution of capillaries. A model termed Intravoxel Partially Coherent Motion (IVPCM) has also been proposed by Karampinos (Karampinos *et al.*, 2010). Such modelling requires a high number of b-values/directions to provide accurate estimate of the capillaries microstructure and anisotropy, consequently this model was not used in this work.

4.3.3. Diffusion Tensor Imaging (DTI)

Diffusion of water molecules in tissue is influenced by surrounding architecture and can be restricted in specific directions leading to anisotropy of the diffusivity. Based on the assumption that diffusion is still Gaussian, DTI is a model which proposes to describe this anisotropy through a tensor (Basser *et al.*, 1994). Introducing an anisotropic diffusion into equation 4, the following solution for the attenuation is obtained:

$$S = S_0 \exp^{-\sum_{i,j} b_{ij} D_{ij}} \qquad 4.21$$

Where b_{ij} is the b-value and D_{ij} the diffusion coefficient in a specific direction ij. If the diffusion is Gaussian it can be described by an ellipsoid through a symmetric tensor of coefficient of diffusion:

$$\bar{D} = \begin{bmatrix} D_{xx} & D_{xy} & D_{xz} \\ D_{yx} & D_{yy} & D_{yz} \\ D_{zx} & D_{zy} & D_{zz} \end{bmatrix} \qquad 4.22$$

Equation 4.21 can be rewritten as:

$$S = S_0 \exp^{-b_{xx}D_{xx} - b_{yy}D_{yy} - b_{zz}D_{zz} - 2b_{xy}D_{xy} - 2b_{xz}D_{xz} - b_{yz}D_{yz}} \qquad 4.23$$

The logarithm of S is given as:

$$\ln(S) = \ln(S_0) - b_{xx}D_{xx} - b_{yy}D_{yy} - b_{zz}D_{zz} - 2b_{xy}D_{xy} - 2b_{xz}D_{xz} - b_{yz}D_{yz} \qquad 4.24$$

This can be rewritten as:

$$\ln(S) = BX \qquad 4.25$$

Where:

$$B = (-b_{xx}, -b_{yy}, -b_{zz}, -2b_{xy}, -2b_{xz}, -b_{yz}, 1) \qquad 4.26$$

$$X = (D_{xx}, D_{yy}, D_{zz}, D_{xy}, D_{xz}, D_{yz}, S_0) \qquad 4.27$$

By projection the tensor can be recovered using the following equation:

$$X = B_i^{-1} \ln(S_i) \qquad 4.28$$

From this equation, the diffusion tensor can directly be retrieved from 6 the diffusion-weighted images acquire at 6 different directions and an image without diffusion ponderation. For a higher number of directions (i>6) there is no true inverse B^{-1}_{i}, so a pseudo inverse matric B^{ψ} must be used instead:

$$B^{\psi} = (B^T B)^{-1} B^T \qquad 4.29$$

Introducing 4.29 into 4.28:

$$X = (B_i^{-1} B_i)^{-1} B_i^T \ln(S_i) \qquad 4.30$$

Once the tensor is calculated various descriptors can be extracted using DTI, but also diffusion tensor can be expressed in a eigen system with eigenvalue (λ_1,λ_2,λ_3) and associate eigenvector (v_1,v_2,v_3).

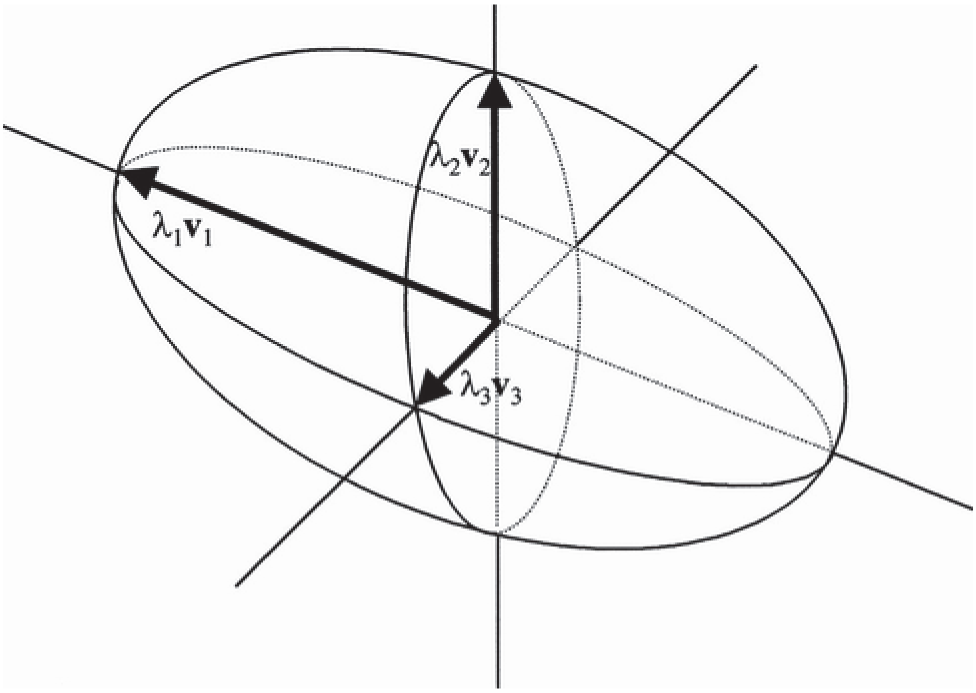

Figure 4.8: Ellipsoidal representation of tensor elements.

The Mean diffusivity (MD) corresponds to the Trace of the diffusion tensor, it represents the mean-squared displacement of the water molecules:

$$MD = (\lambda_1 + \lambda_2 + \lambda_3) / 3 \qquad 4.31$$

The Faction of Anisotropy (FA) represents the spatial heterogeneity of the water molecules displacements that is related to the presence of orientated structures.

$$FA = \sqrt{\frac{3}{2}} \sqrt{\frac{(\lambda_1 - MD)^2 + (\lambda_2 - MD)^2 + (\lambda_3 - MD)^2}{(\lambda_1^2 + \lambda_2^2 + \lambda_3^2)}} \qquad 4.32$$

The main diffusion direction is directly given by the eigenvector with the highest eigenvalue. Usually this direction is used to perform "fiber" tracking and revealed the architecture of tissue.

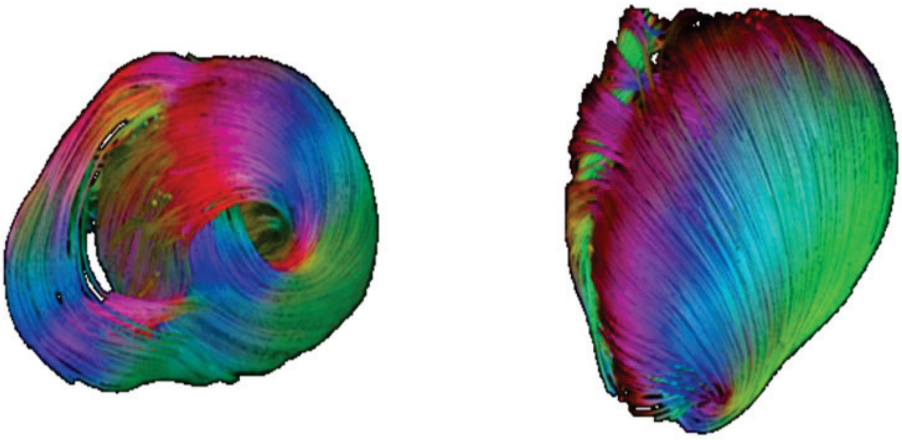

Figure 4.9: Tractography on ex-vivo fetal heart obtained with 192 direction.

4.4. Diffusion encoding schemes

Diffusion encoding scheme are commonly associated to a single shot EPI readout. Various diffusion encoding schemes have been proposed in the literature for CDWI which can be sorted in two categories: the spin echo sequences and the stimulated echo sequences.

A) **Stejkal-Tanner** or **Monopolar** encoding was the first scheme proposed to measure diffusion (Stejskal and Tanner, 1965). It is very sensitive to motion but reach the lower TE for a given b-value.

B) **Bipolar** was first studied for CDWI by Gamper (Gamper *et al.*, 2007), it offers a first order motion compensation (see chapter 7) but has a longer TE than Monopolar scheme for an equivalent b-value.

C) **Twice Refocused Spin Echo** (**TRSE**) was introduced by Reese (Reese *et al.*, 2003) to limit the eddy current formation in case of strong b-value. It is mainly used in neuro-imaging and offers no motion compensation. TE is equivalent to the Bipolar one for a same b-value.

D) **Asymetric Bipolar** was presented by Stoeck (CT Stoeck *et al.*, 2013), the idea behind this scheme is to encode diffusion only on one side of 180° RF pulse while increasing the number of k-space lines read by the EPI readout. This scheme increases the image resolution but double the TE in comparison of the Bipolar scheme.

E) **2nd Order Motion Compensation** or **Acceleration Motion Compensation (AMC)** encoding scheme, are recent development in cardiology (Nakamura *et al.*, 2014; Nguyen *et al.*, 2014; C. T. Stoeck *et al.*, 2015; Welsh *et al.*, 2015). It was designed using gradient moment nulling approach to offer a motion compensation of 2nd order. TE is longer than Bipolar scheme for a given b-value.

F) **Stimulated Echo Acquisition Mode** (**STEAM**) sequence was historically the first encoding scheme proposed for cDWI (Edelman *et al.*, 1994). The principle of this method is to split Monopolar encoding scheme in two parts while locking magnetization in the longitudinal plan, and restoring it through a stimulated echo. In cardiology this sequence is used on two consecutive heart beats which lead to a long mixing time (time between the first and the second part of the sequence). Thus, effective TE needed for a given b-value is extremely low but the resulting signal suffers from a strong T1 decay.

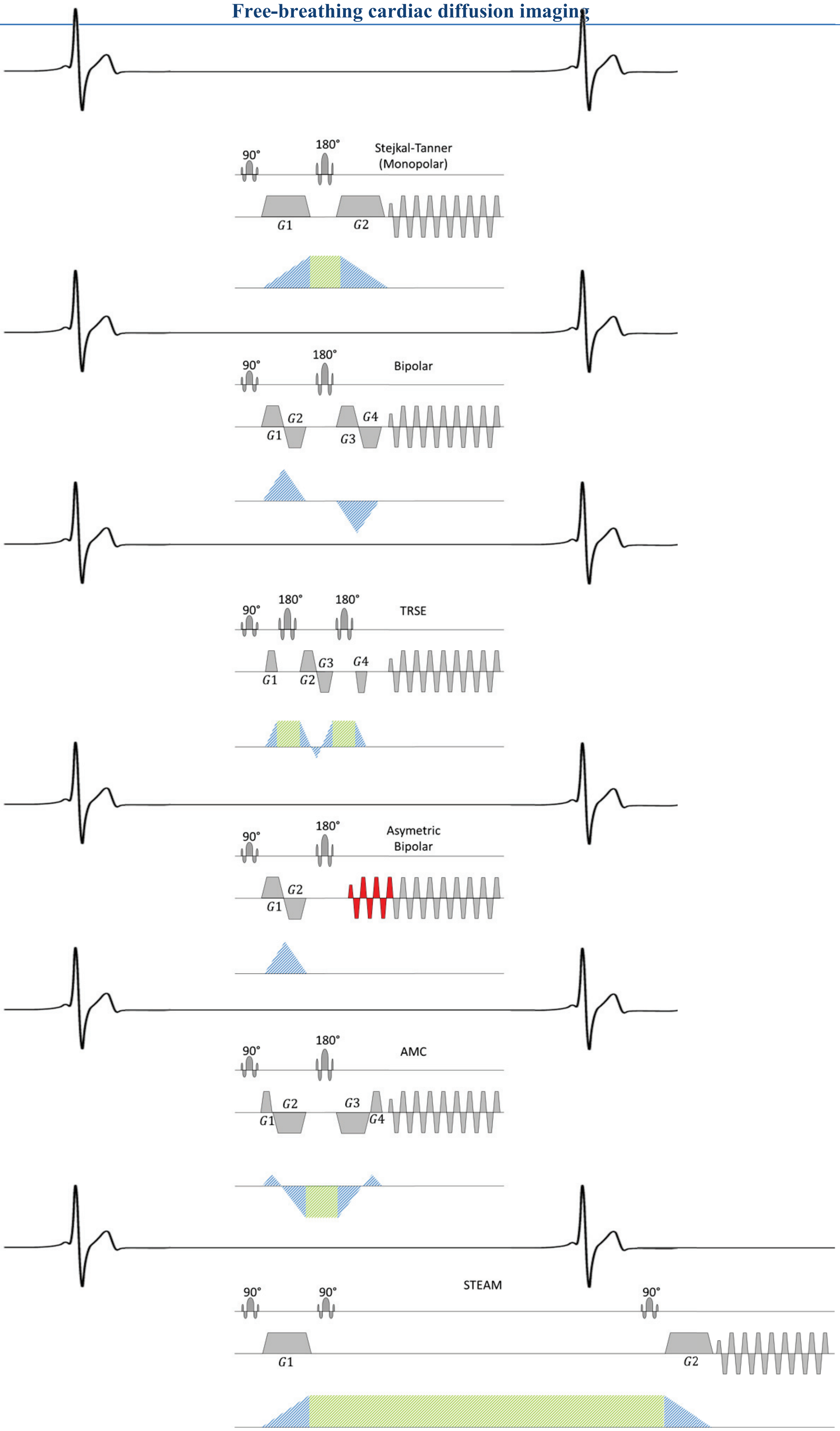

Figure 4.10: Common diffusion encoding schemes proposed in the literature

4.5.Effect of motion on diffusion measurement

The presence of motion during the encoding of diffusion can have a strong impact on the measurement. Indeed coherent intra-scan motion will induce a phase shifting on NMR signal leading to important signal loss or ghosting artefact.

$$\phi_{motion}(\vec{r}(t)) = \gamma \int \vec{G}(t)\vec{r}(t)\partial t \tag{4.33}$$

Even if some studies have proposed numerical simulation, the effect of cardiac motion on the spin echo diffusion measurement is not well known and still investigated. It seems that quick translation/rotation of the heart or bulk motion affects more the SE acquisition (Gamper *et al.*, 2007). For this kind of sequence, two periods of stability, called “sweetest cardiac phase” or “quiescent phase”, correspond to the moment where the heart is the less moving in the cardiac cycle. Due to its short effective duration STEAM sequence it less affected by translational motion but mainly by strain as described in the work of Dou (Dou *et al.*, 2003). Indeed as the heart performs a complete beating cycle during the diffusion encoding, water molecules will moved not only due to diffusion but also due to the heart contraction. This effect leads to two different phases of stability for STEAM sequence, called “sweet spot” where the strain is the less impacting.

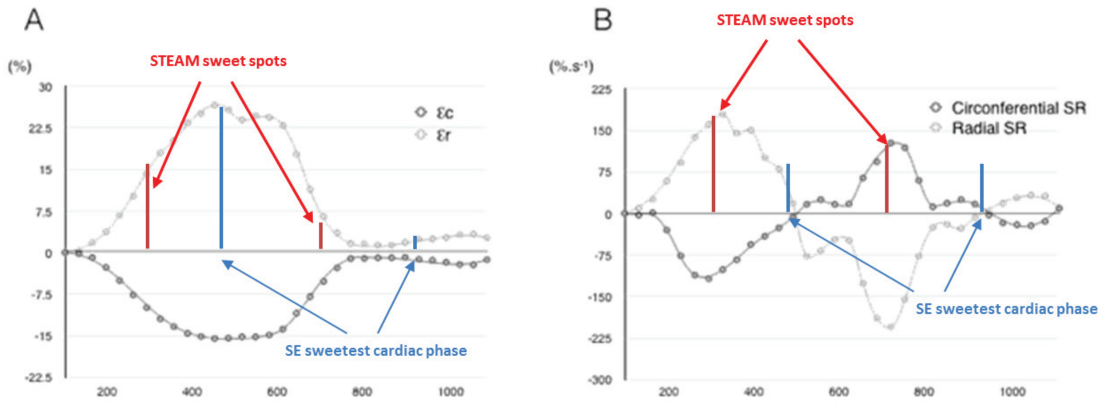

Figure 4.11: Circumferential and radial Strain A) and its derivative the Strain rate B). STEAM sweet spots occur at maximal circumferential strain rate while SE sweetest cardiac phases occur at null strain rate.

The duration of theses phases and motion corruption induced are patient dependent. Consequently a given sequence of given duration (about 80ms to 100ms in this work) can present artefact on a specific patient and not on another one. From user perspective, two ways are possible to reduce the sensibility to cardiac motion:

-Reduce the sequence duration and more specifically the diffusion encoding time

- Use insensitive diffusion encoding scheme.

Considering this, cardiac cycle variability (i.e. reduction of the late diastolic phase) or unpredictable bulk motion can still impact the measurement.

Slow motion like breathing motion does not disrupt directly the measurement but still have a negative impact on the final result. These movements lead to a displacement of the organ of interest and conduct to a miss correspondence of the structure in the different acquisitions which is very problematic for modeling.

4.6.State of the art of CDWI

Most of the publication on CDWI propose STEAM sequence to tackle cardiac motion in-vivo (Edelman *et al.*, 1994; Reese *et al.*, 1995; Tseng *et al.*, 2000; Dou *et al.*, 2003; Tseng *et al.*, 2006; M. T. Wu *et al.*, 2006; M. T. Wu *et al.*, 2009; McGill *et al.*, 2012; Nielles-Vallespin *et al.*, 2013; Ferreira *et al.*, 2014; Scott *et al.*, 2014; Tunnicliffe *et al.*, 2014; McGill *et al.*, 2015). Running over two heart beats and making the assumption that the heart is in the same position at both diffusion-encoding times, this sequence allows a small effective duration without the need of high gradient system. Indeed for a same b-value, the TE reach by a STEAM sequence is considerably lower than a spin echo sequence which reduces the exposition to bulk motion but also distortion due to the EPI readout. However, as the heart performs a whole beating cycle during the diffusion encoding, cardiac strain impacts the diffusivity of water molecules, this effect need to be access using a strain correction method (Dou *et al.*, 2002; C. T. Stoeck *et al.*, 2014). Also, the NMR signal suffers from T1 relaxation during the mixing time which impacts the SNR and constraints the protocols to important number of scan repetition to average the signal. These limitations have for consequences to increase the total scan time and reduce the potential clinical application of this technique.

In spin echo sequences (Gamper *et al.*, 2007; Deux *et al.*, 2011; Rapacchi *et al.*, 2011; Delattre *et al.*, 2012; Wei *et al.*, 2015), the two diffusion gradients being placed at different time points in the heart cycle, cardiac motion can induce important phase shifts and thus “all or none” signal loss (Wedeen *et al.*, 1994). Positioning of theses sequence in the beating cycle is crucial and should be carefully limited to cardiac phases where motion is minimal (Rapacchi *et al.*, 2011). Original work of Gamper (Gamper *et al.*, 2007) was the first one to proposed spin echo acquisition for CDWI and the diffusion encoding scheme used in this study was designed to compensate motion of first order (velocity). Recent study on second order motion compensation (acceleration) have shown promising results in both systole and diastole in the animal model (rat) and human experiments (Nakamura *et al.*, 2014; Nguyen *et al.*, 2014; C. T. Stoeck *et al.*, 2015; Welsh *et al.*, 2015). These sequences shows that it is possible to perform cardiac DWI without the use of the STEAM technique, and therefore to reach a shorter scan time and a higher SNR.

The study of Lau (Lau *et al.*, 2014) has shown the possibility to excite and read three slices at the same time using a simultaneous multi-slice imaging (SMS) and a blipped controlled aliasing readout (CAIPI). These techniques were incorporated in a STEAM sequence and compared to standard STEAM sequence on 10 volunteers with equivalent results. Parallel imaging reduces considerably the scan time but imposes an important gap between the slices excited and prolonged the readout duration.

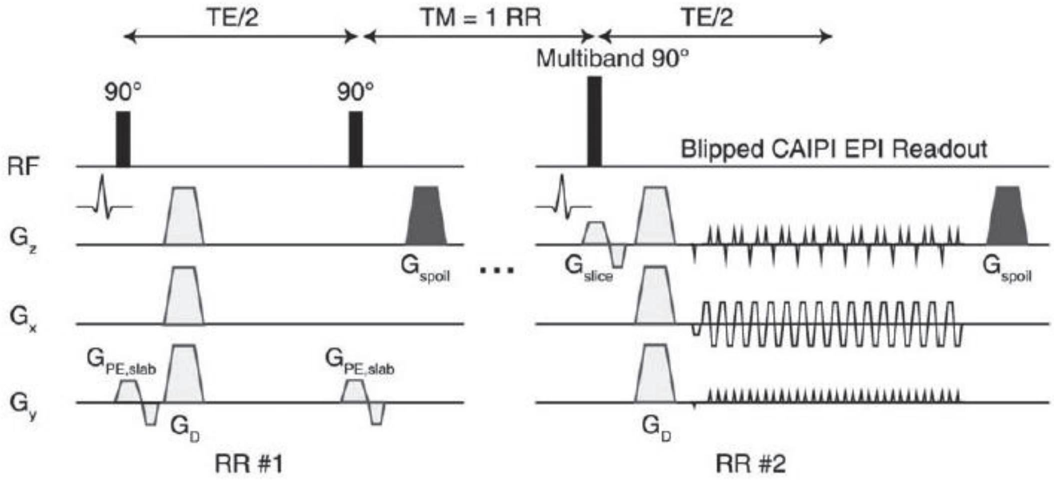

Figure 4.12: SMS excitation coupling to EPI CAIPI readout on Steam sequence. © (Lau et al., 2014)

A sequence based on balanced steady state free precession (bSSFP) with a second order motion compensation was proposed by Nguyen (Nguyen *et al.*, 2014). For a same b-value, diffusion preparation is longer than on the spin echo sequence, leading to an important TE. A multi shot readout is used instead of an EPI so distortions induced in single shot readout are avoided here

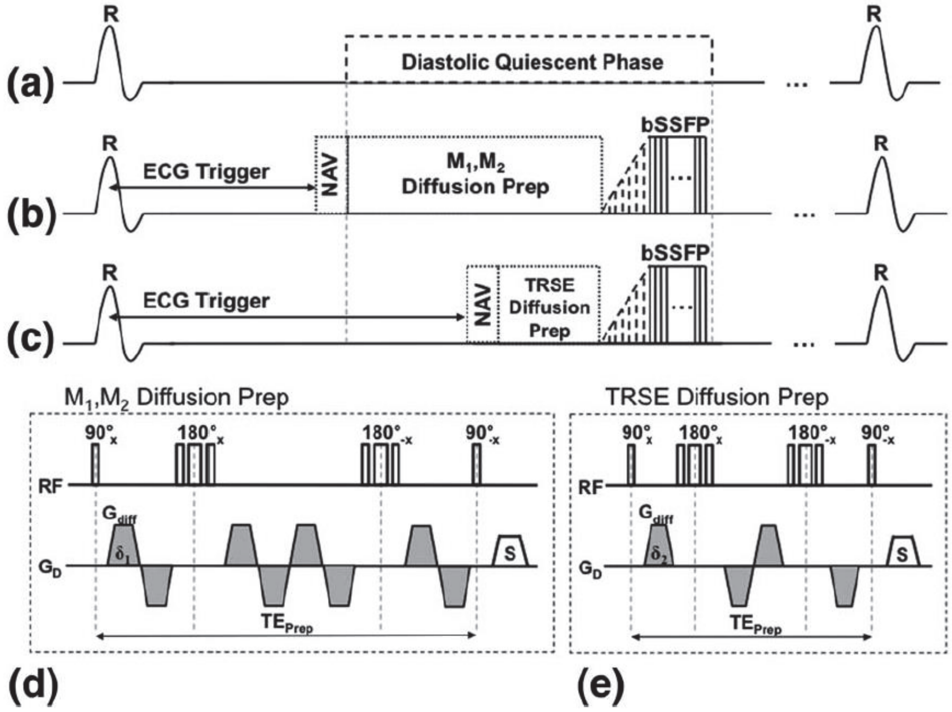

Figure 4.13: Preparation and of 2^{nd} order motion compensated scheme (b-d) and TRSE (c-e) scheme coupling with bSSFP readout. © (Nguyen et al., 2014)

Three type of breathing management has emerged for CDWI: breath-holding, free-breathing and navigator based correction or rejection. Despite of low applicability and patient inconvenience, breath-holding is the most used solution in CDWI but also in cardiology in general. Breath-holding limits corruption by breathing motion during the acquisition, but due to the number of data required for DWI models, breath-hold need to be repeated. To limit the problem of reproducibility when multiple breath-holds are involved, the acquisition protocol is often constrained to one slice per breath-hold, which induces a TR time equivalent to the RR duration (or two RR in the case of STEAM sequence). At 1.5T, T1 value in heart has been report to 800 to 1100ms which is in the range of RR duration (about 1000ms for a heart of 60 bpm) leading to a steady state of the magnetization. To date, CDWI studies using breath hold have not considered the time needed to establish this steady state and the RR variations influencing it. Consequently, during a breath-hold, the first image acquired has not the same T1 ponderation as the last one which can lead to an error after modeling. Moreover the protocols reported in previous DWI studies have important number of repetition to average the signal so it is possible that many breath hold are required for a same slice.

Free breathing acquisitions are based on the assumption that diffusion encoding and EPI readout are rapid enough in comparison to breathing motion. During all the acquisitions the heart moved in both in-plane and through-plane direction due to breathing motion. If the effect of breathing motion appears unseen on the acquisition, a mis-registration exists between all the images acquired. In plane displacement can be handle using registration algorithm but through plane movement cannot be corrected retrospectively. Due to the need for STEAM sequence that the first and second diffusion encoding gradient is at the same position, STEAM sequence can’t be used without handle the breathing.

Emerging navigator techniques have raised the possibility for spin echo sequence and STEAM sequence to be used synchronized with the respiratory. The gating approach has been successfully used on CDWI acquisition with STEAM and spin echo sequence (Nielles-Vallespin *et al.*, 2013; C. T. Stoeck *et al.*, 2014). However the acquisitions were efficient on a small part of the breathing cycle (around 40%) which prolongs the scan time.

A range of values varying between 0.8mm²/s and 1.8mm²/s was reported in the literature for the coefficient of diffusion of a healthy heart. But recent work of von Deuster (von Deuster *et al.*, 2015) shown that STEAM imaging underestimates the measurement (or spin echo overestimate).

Until now CDWI has only been applied in patients with HCM and myocardial infarction. A quantitative study using DTI model with STEAM sequence at high b-value=300s/mm² investigated patients with chronic infarction and reported an increase of MD and a decrease of FA in the infarct zone in comparison to the remote zone (M. T. Wu *et al.*, 2009). Regarding acute infarct, one study mainly reports the added value of CDWI as a dark-blood single-shot sequence, able to identify similar size of the area at risk as T2-STIR sequence (Deux *et al.*, 2011). It has been shown since then that T2 weighted MRI acquired post-acute myocardial reperfusion cannot determinate the area at risk, but only shows the edema extension induced by both injuries: the onset ischemic insult and the reperfusion secondly induced trauma (Viallon *et al.*, 2012). Moreover, CDWI in this study was realized using a TRSE sequence with a low b-value of 50s/mm², and only the T2 weighting semiology was of interest in final.

In HCM patients, two publications using a DTI protocol at b-value=350s/mm² with the STEAM sequence have shown an increase of the anisotropy of the tissue as well as a joint decrease of MD compared to values found in healthy patient acquired with STEAM sequence (McGill *et al.*, 2012; Ferreira *et al.*, 2014).

Until now, the methods proposed to take care of breathing and cardiac motion increased considerably the scan time. A standard protocol of 3 slices, 2 b-values, 6 directions and 8 averages using a STEAM sequence took 24 breath-holds of 18s each (considering a heart rate to 60 beat/min) or 30 min using a gating method. Management of these motions pushes far the potential clinical application of CDWI. Here we propose a new approach which consists in real-time repositioning based on the navigator information. This strategy enables free-breathing acquisition (100% duty respiratory cycle) while correcting the through plane mis-registration due to breathing motion.

*Table 4-1 (bottom): Table summarizing the result of 25 publications of cardiac diffusion imaging on healthy volunteer (Vol) or pathologic case (Infarct or HCM).According to the model used: ADC, DTI or IVIM, values ADC, MD, D, D*or f are reported. (*) Study based on a tensor analysis, parametric maps are not or partially reported. (**)Indices i,r,a indicate infarct, remote and adjacent value respectively.*

Author	Case	Coefficient of diffusion measured (10^{-3}mm²/s)	Sequence	Breathing management	Cardiac phase
(Edelman *et al.*, 1994)	Vol	ADCx=14 ; ADCy=14,8 ; ADCz=17,8	STEAM	Breath-hold	Diastole
(Reese *et al.*, 1995)	Vol	λ1=16 ; λ2=7 ; λ3= 3 ; ADC = 0.87	STEAM	Gating	Diastole
(Tseng *et al.*, 1999)	Vol	~ (*)	STEAM	Breath-hold	Diastole
(Tseng *et al.*, 2000)	Vol	~ (*)	STEAM	Breath-hold	Diastole
(Dou *et al.*, 2002)	Vol	λ1=9 ; λ2=5,8 ; λ3= 3,5 (*); ADC = 0.6	STEAM (Bipolar)	Breath-hold	Diastole
(Dou et *al.*, 2003)	Vol	~ (*)	STEAM	Breath-hold	Diastole
(Tseng *et al.*, 2006)	HCM	~ (*)	STEAM	Breath-hold	Diastole
(M. T. Wu *et al.*, 2006)	Infarct	ADCi=0,824 ; ADCa=0,769 ; ADCr=0,738 (**)	STEAM	Breath-hold	Diastole
(Gamper *et al.*, 2007)	Vol	λ1=1,8 to 2,3 ; λ2=1 to 1,5	Spin echo (Bipolar)	Breath-hold	Diastole
(M. T. Wu *et al.*, 2009)	Infarct	Chronic MDi=0,96 ; MDr=1,4 Recent MDi=0,88 ;MDr=1,12(**)	STEAM	Breath-hold	Diastole
(Deux *et al.*, 2011)Deux	Infarct	~ (*)	Spin echo (TRSE)	Triggering	Diastole
(Rapacchi *et al.*, 2011)	Vol	ADC=7,1	Spin echo (TRSE)	Free-breathing	Diastole
(Delattre *et al.*, 2012)	Vol	D=2,43, D*=76,3, f=15%	Spin echo (TRSE)	Breath-hold	Diastole
(McGill *et al.*, 2012)	HCM	MD=0,75	STEAM	Breath-hold	Systole
(Nielles-Vallespin *et al.*, 2013)	Vol	MD=0,9	STEAM	Gating	Systole
(Ferreira *et al.*, 2014)	HCM	~(*)	STEAM	Breath-hold	Systole
(Nguyen *et al.*, 2014)	Vol	ADC=1,5	SSFP (AMC)	Breath-hold	Diastole
(Scott *et al.*, 2014)	Vol	MD=1,8 to 0,72	STEAM	Breath-hold	Diastole
(C. T. Stoeck *et al.*, 2014)	Vol	MD dias= 0,88 MD syst=1,02	STEAM	Gating	Diastole & Systole
(Tunnicliffe *et al.*, 2014)	Vol	MD dias=1,2 MD syst=1,1	STEAM	Breath-hold	Diastole & Systole
(Lau *et al.*, 2014)	Vol	MD=1,2	STEAM + SMS & CAIPI	Breath-hold	Diastole
(McGill *et al.*, 2015)McGill	Vol	MD=0,87	STEAM	Breath-hold	Diastole
(C. T. Stoeck *et al.*, 2015)	Vol	MD=1,5 (*)	Spin echo (AMC)	Gating	Systole
(Wei *et al.*, 2015)	Vol	MD=0,74	Spin echo (TRSE)	Free-breathing	Diastole
(von Deuster *et al.*, 2015)	Vol	MD spin echo =1.43 MD STEAM = 1.05	STEAM vs Spin echo (AMC)	Breath-hold	Systole

PART
II

Contributions

5. New Slice Following prospective motion correction acquisition

The quantification of inflammatory (edema) or infiltrative (fibrosis) processes is a central interest in cardiology, motivating recent developments of quantitative MRI methods such as T1 mapping (Messroghli *et al.*, 2004) and T2 mapping (Giri *et al.*, 2009). DWI in the brain is a crucial indicator involved in all protocols aiming to the characterization of neurological pathologies, and is a key differentiator for patient management. The motivation is therefore high to explore the potential of DWI-related biomarkers for cardiac disease investigations.

However, all diffusion studies on a moving organ such as the heart are challenging because diffusion measurement is very sensitive to bulk motion, and a specific strategy to manage breathing and cardiac motions becomes mandatory. To date, only a limited number of studies have demonstrated the feasibility of DWI in vivo in the human heart (*Table* 4-1). Proposed techniques to manage the cardiac motion and breathing motion increased considerably the scan time which limit the applicability of cardiac diffusion in clinical side.

In this chapter a new approach which consists in real-time repositioning of slice using navigator was described, and evaluated in a reproducibility study. Furthermore, we provide a list of all developments related to this work.

5.1.Slice following approach

5.1.1. Principle

An hypothesis conmonly admitted is that the use of a single parameter, such as the diaphragm position, is sufficient to fully characterize the respiratory motion of the heart. Indeed Wang et al reported that the displasment of heart during the respiration is dominated by feet-to-head motion that is linearly related to the feet-to-head motion of the diaphragm. A linear link, called tracking factor, was first measured by Wang (Wang *et al.*, 1995) on the right coronary artery root and the left anterior descending coronary artery to 0.57 +- 0.26 and 0.7 +- 0.18. This factor was also measured by Taylor et al. (Taylor *et al.*, 1998) on proximal right coronary artery to 0.49 +/- 0.15, range 0.20-0.70 and on proximal left coronary artery to 0.59 +/- 0.15, range 0.20-0.85. Nehrke et al. (Nehrke *et al.*, 2001) using a multi-navigator technique has shown dynamically the link between the diaphram and the heart during the respiratory (

Figure 5.1), and also reported that a hysteresis phenomenum of the heart motion during the respiratory cycle can exist in certain patient.

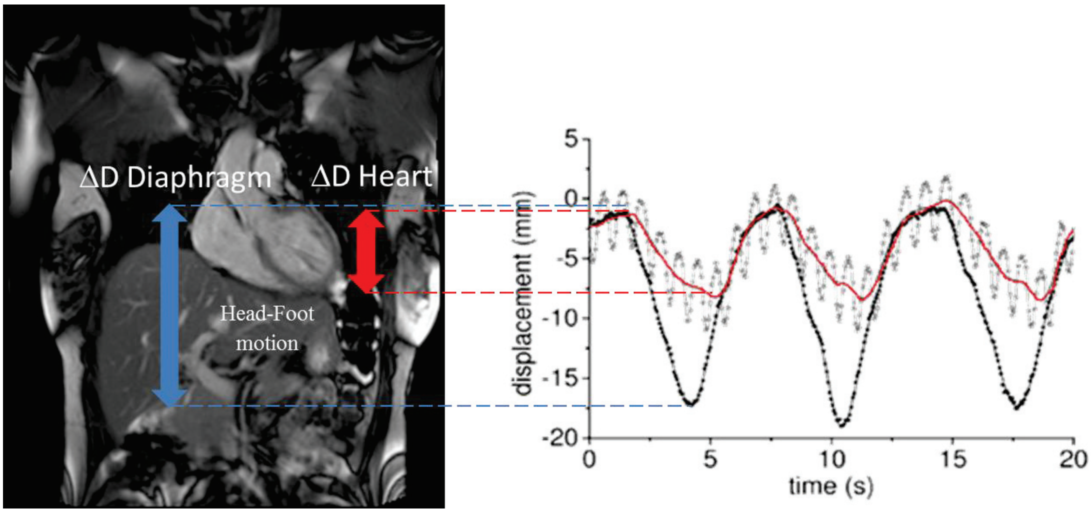

Figure 5.1: Link between cardiac displacement (dashed curve represent the heart beating and the associate full red curve the cardiac motion due to breathing) and diaphragm displacement (black curve). Adapted from © (Nehrke et al., 2001)

During a free breathing acquisition of a short axis slice, the head-foot displacement of the heart leads to an important through-plane displacement as shown on Figure 5.2. Here we propose to correct this head-foot diplacement caused by respiratory motion using the prospective liver position provides by the navigator. Using the tracking factor described above, the position of the heart during the respiratory cycle is deduced from the position of the liver. The proposed method consists in adapting the slice position according to this deduced heart position . This stategy called slice-following or slice-tracking enable free-breathing acquisition and offers optimal breathing motion management and patient compliance with no scan time penalty in comparison of other breathing management methods.

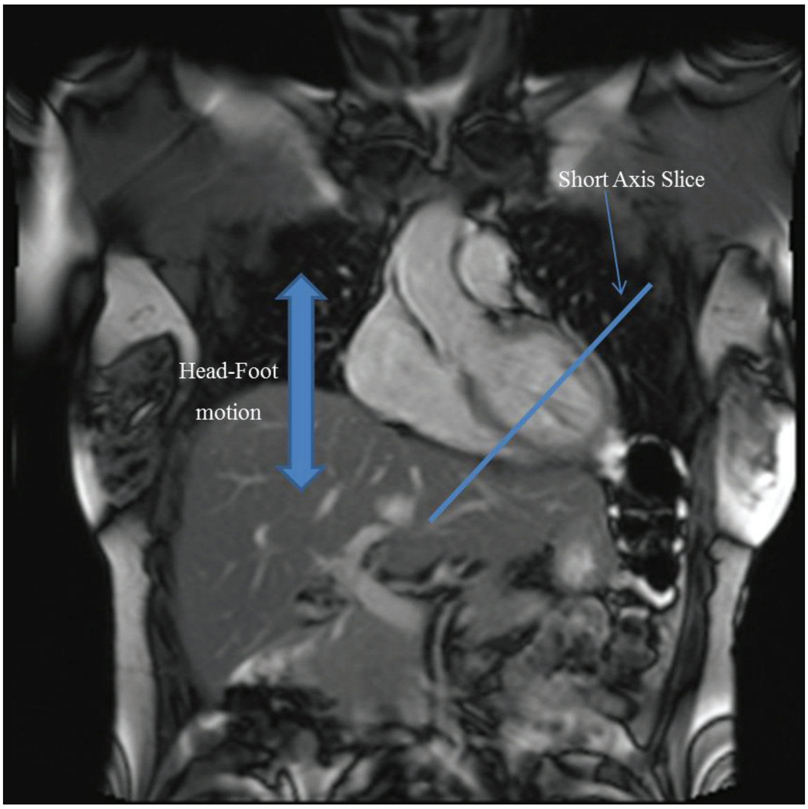

Figure 5.2: Coronal view of chest, the displacement induced by breathing act mainly on the head-foot direction through plane of a short axis slice.

Slice-navigated strategies have been proposed for quantitative and precise temperature monitoring in the liver during HIFU therapy (Ries *et al.*, 2010) but also has shown to considerably improve the diffusion imaging of the liver using an EPI sequence (Ivancevic *et al.*, 2009; Takahara *et al.*, 2010). A derivate technique called self-navigation has been proposed in coronary imaging (Piccini *et al.*, 2012) but is based on radial 3D readout.

5.1.2. Implementation

Slice following approach was developed from the Siemens product diffusion sequence named “EP2D”. A module implementing the navigators and the gating approach was taking back from a cardiovascular sequence and modified to be inserted in the EP2D sequence in place of the previous breathing management method (Trigger). The navigator module includes pencil bean and cross pair navigator, both with duration of 30ms, and can be called before and/or after the sequence independently from diffusion preparation or EPI readout. Sequence duration was increased by 30ms, which in CMR has no impact on the acquisition duration as the sequence is called once by RR.

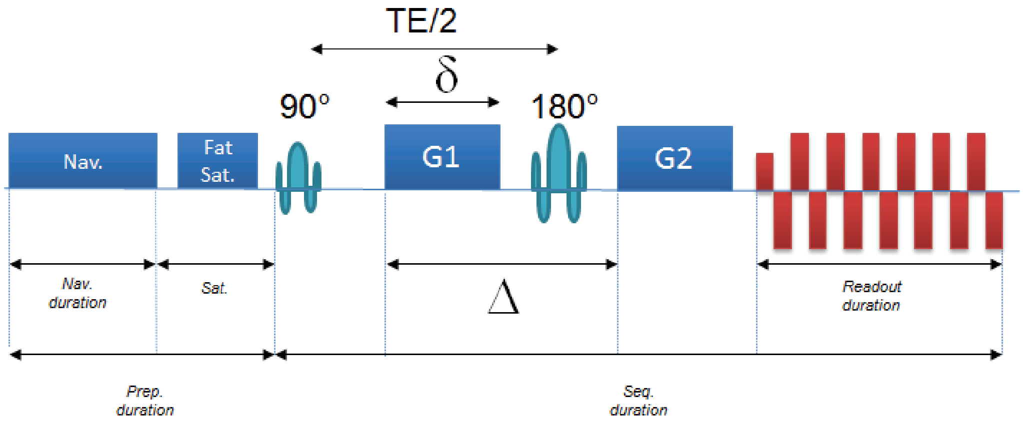

DTI protocol (b-value= 350)	Duration (ms)	% of cardiac cycle(*)	% of breathing cycle(**)
Nav. Duration	30,5	3,05	0,51
Sat.	23	2,3	0,38
TE/2	22,5	2,25	0,38
δ	12,5	1,25	0,21
Δ	20	2	0,33
EPI Duration	17,5	1,75	0,29
Prep. Duration	53,5	5,35	0,89
Seq. Duration	58	5,8	0,97

IVIM protocol (b-value= 400)	Duration (ms)	% of cardiac cycle(*)	% of breathing cycle(**)
Nav. Duration	30,5	3,05	0,51
Sat.	23	2,3	0,38
TE/2	21	2,1	0,35
δ	12	1,2	0,20
Δ	19	1,9	0,32
EPI Duration	17,5	1,75	0,29
Prep. Duration	53,5	5,35	0,89
Seq. Duration	56	5,6	0,93

Figure 5.3: *Global sequence diagram with detailed timing (not to scale). Timings are given for the two protocols proposed in chapter 5.2 in comparison to cardiac cycle and breathing cycle duration. (*) A Cardiac cycle of 1000ms was considered, (**) A Breathing cycle of 6000ms was considered.*

A card named “PACE’ was inserted in the user interface to modify navigator parameters like the “gate” position and size but also the tracking factor as shown on Figure 5.4.

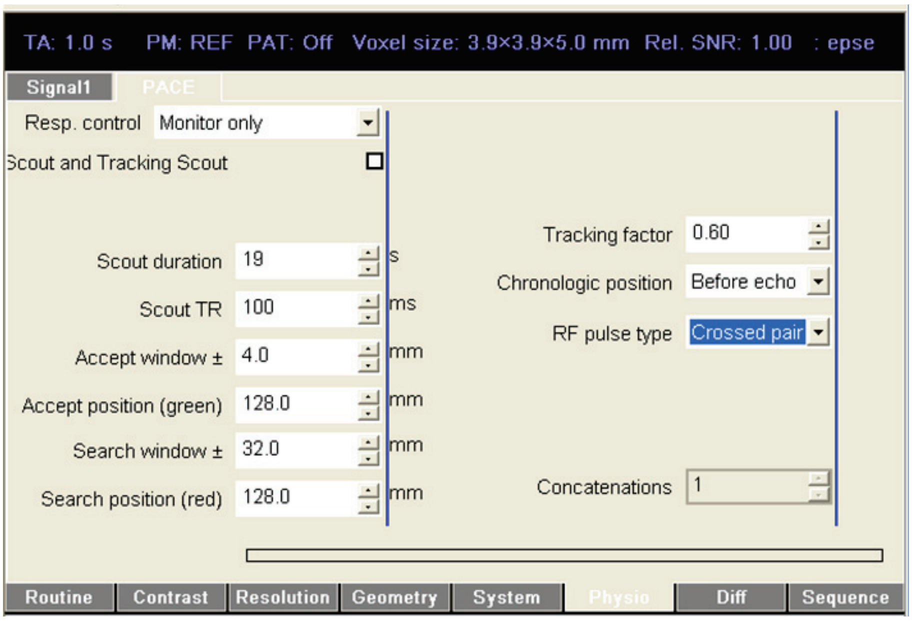
TA: 1.0 s PM: REF PAT: Off Voxel size: 3.9×3.9×5.0 mm Rel. SNR: 1.00 : epse

Resp. control: Monitor only
Scout and Tracking Scout ☐
Scout duration: 19 s
Scout TR: 100 ms
Accept window ±: 4.0 mm
Accept position (green): 128.0 mm
Search window ±: 32.0 mm
Search position (red): 128.0 mm
Tracking factor: 0.60
Chronologic position: Before echo
RF pulse type: Crossed pair
Concatenations: 1

Figure 5.4: Example of User Interface, card “PACE”, including options for managing the navigator parameters.

From the classical Siemens gating approach, all the breathing phases can be kept for measurement by enlarging the gate as shown on Figure 5.5.

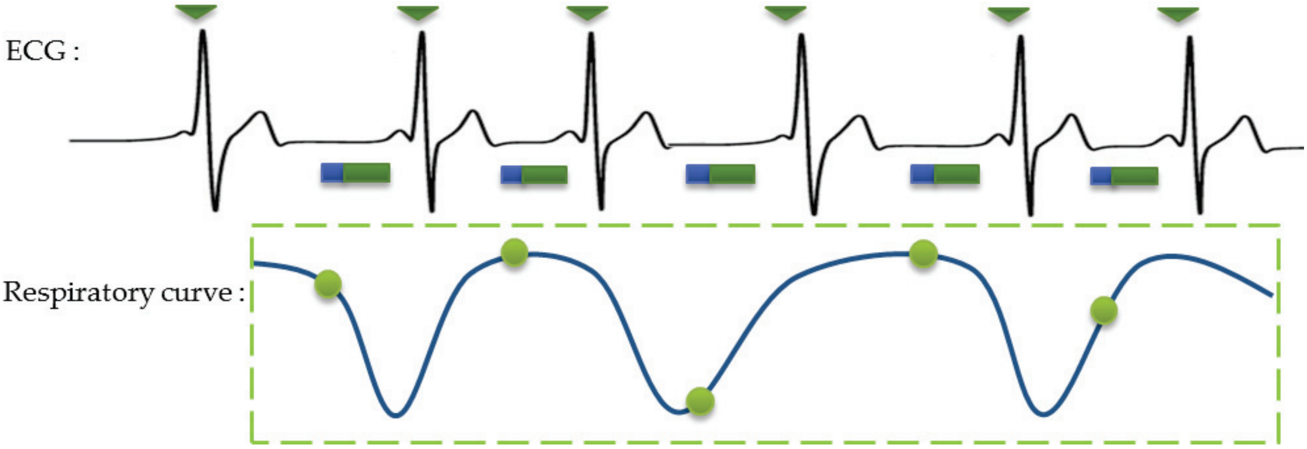

Figure 5.5: The navigator (blue) is played before the sequence (green), the information obtained by the navigator is used to correct the head foot displacement induced by the breathing motion.

The information obtained by the navigator is given in its reference frame in mm. The relative heart displacement from a reference position is calculated using the corresponding displacement of the liver. The reference position of the heart is the slices positions defined by the users on the graphic interface, usually on expiratory scout acquisitions. The corresponding liver position is not known from the system and need to be determined during the acquisition. Here reference liver amplitude is obtained during the dummy scans. Navigator images acquired during the dummy scans are compared and the top amplitude is chosen as reference. This position should correspond to the expiratory phase and thus to the breathing phase where the slices have been placed.

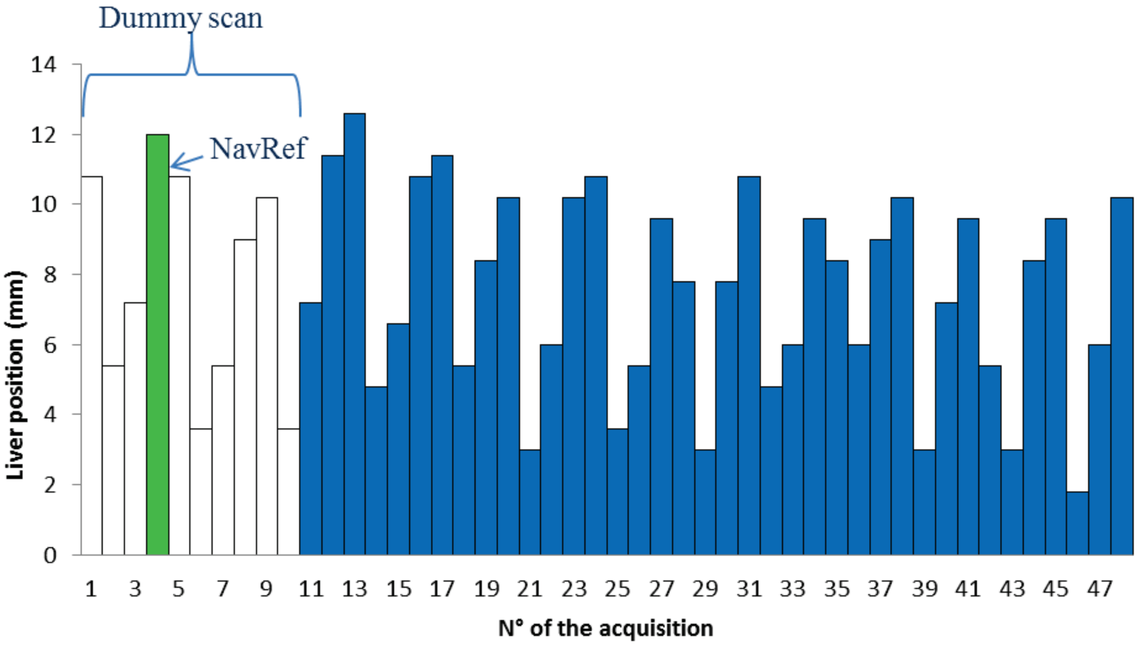

Figure 5.6: The 10 first navigator measurements correspond to the dummy scans used to reach an appropriate steady state. Among them the top position (green) is kept as reference and a correspondence is made with this reference and the slice position defined by the user.

Once the top liver position is defined, at each navigator measurement the correction of the **current** slice position is applied according the following equation:

$$\overrightarrow{\mathrm{SlcPos}} = \overrightarrow{\mathrm{SlcPosRef}} + (\overrightarrow{\mathrm{Nav}} - \overrightarrow{\mathrm{NavRef}}) \text{ x } \mathrm{TF} \qquad 5.1$$

Where *SlcPos* is the new coordinate of the current slice, *SlcPosRef* the coordinate of the current slice (which was defined by the users on the graphic interface), *Nav* the current measure of the navigator, *NavRef* the top position of the liver measured during the dummy scans and *TF* the tracking factor. The new slice position is directly applied on the following sequence by modifying the frequency of the selective RF pulses.

5.1.3. Validation of the prospective breathing motion correction efficiency

Validation of the correction efficiency was evaluated on coronal view images were the head-foot displacement is ideally measurable. Accuracy of the head-foot correction by slice following was evaluated quantitatively by considering the position of the endocardial borders of the LV on a coronal view of the heart acquired with our diffusion sequence at low b-value (b-value=30 s/mm²) on 10 volunteers. The zoomed area of the LV at different breathing phases is displayed in Figure 5.7, and the endocardial border evolution was analyzed for two sequential acquisitions performed with and without navigator correction over 1 min. For the quantitative evaluation, endocardial borders were extracted from a vertical line centered in the LV.

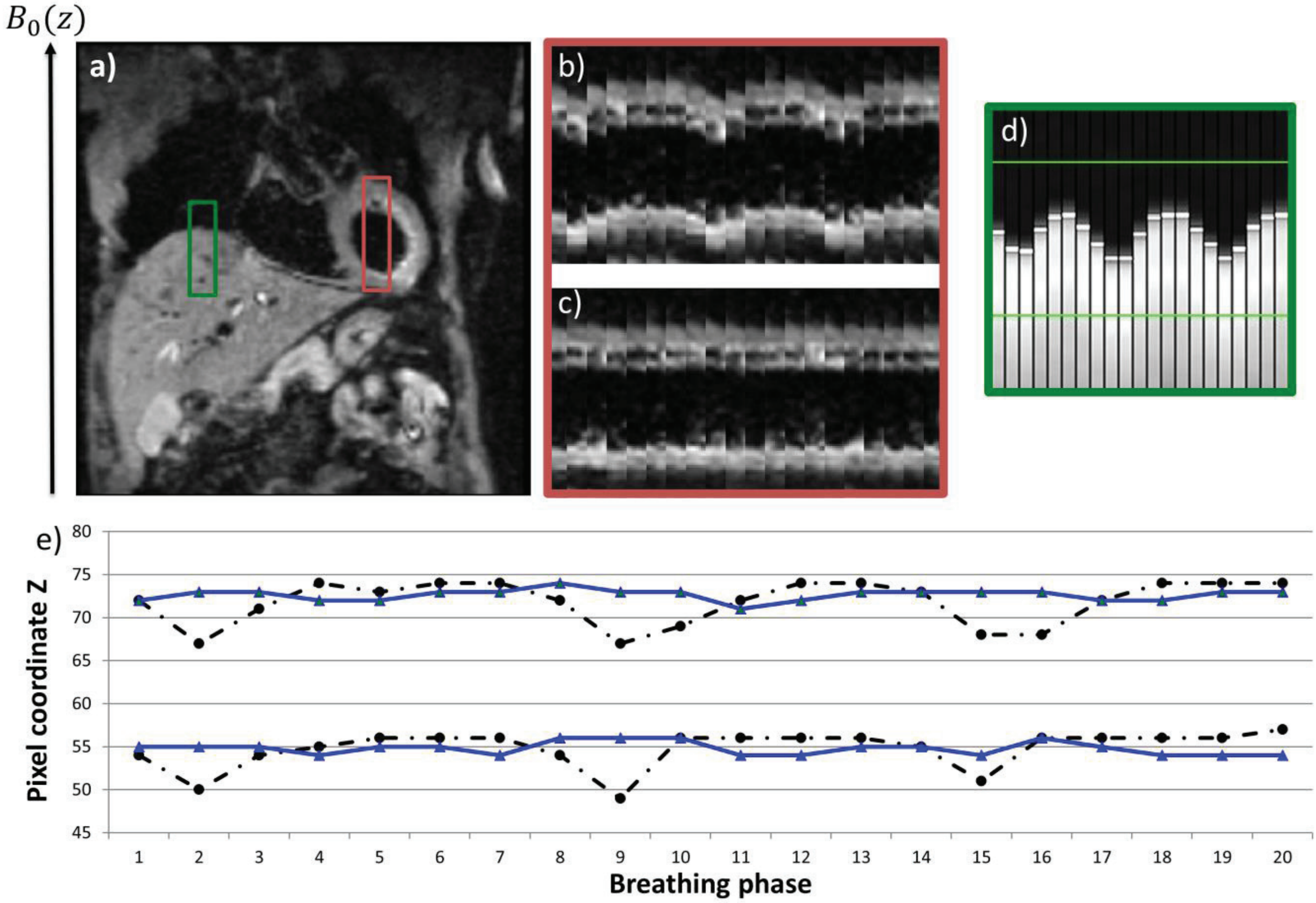

Figure 5.7: Performance of the respiratory head-foot motion correction for SE-EPI diffusion with slice following. a) Coronal images with b-value=30 s/mm² acquired over 1 min. b) and c) Signal intensity evolution in a vertical ROI crossing the left ventricle

along the time axis for a free-breathing coronal acquisition without (b) and with (c) slice following. d) Standard navigator information obtained during the acquisition. e) The bottom graphs display the myocardial edges extracted from a vertical rectangular portion (red rectangular ROI) of the coronal images with (blue curve) and without (black curve) slice following over 3 breathing cycles. The respiratory patterns visible in the non-compensated, non-slice-followed acquisition disappear when activating the slice-following mode.

The residual motion displacement was estimated by subtracting the minimum position to the maximum position measured. Without motion compensation, free-breathing caused a final mean head-foot inter-DW image motion of 10±0.94 mm as measured over 10 healthy subjects, which exceeds the slice thickness commonly used in diffusion (about 5 or 6mm). When using the slice-following strategy, the motion amplitude at the heart level was reduced to 3.375±0.94 mm.

5.1.4. Discussion

The slice following offers the possibility for diffusion imaging to be performed in free-breathing without suffering from prolonged examination time. Through plane motion induced by respiration was considerably reduced and a sufficient positioning of the slices during the whole exam is ensured. Residual in-plane displacement exists but can be handled by specific reconstruction (see chapter 6). Note also that slice following management offers an efficient multiple slices protocol since slices can be acquired sequentially while maximazing the TR between two excitations on the same slice, in turn ensuring an optimal relaxation of the available magnetization and thus of the SNR rate. In this conditions the calculation of TR became:

$$TR = \text{number of slice x RR duration} \qquad 5.2$$

The utilization of multi-slice acquisition offers full T1-relaxation of each slice as soon as the number of slices is greater than 5 (considering a heart rate of 60 bpm, T1 in the heart at 1.5T is about 1000ms). In this situation, the SNR is maximized and the influence of the RR or breathing cycle variability on the relaxation state is considerably reduced. Contrarily, a multi-breath-hold (MBH) acquisition, where each breath-hold corresponds to one slice, is a strategy that inherently imposes a TR of 1RR interval for the Spin-Echo sequence or 2 RR for the stimulated echo sequence. An interleaved order of slice acquisition can also be used to reduce saturation effects due to eventual slice overlapping during slice following.

Because the navigator profile depicts the position of the liver, and not directly the position of the heart, the method has a residual slight sensitivity to individual variation of the tracking factor (a fixed value of 0.6 value was used here), which could affect the tracking accuracy of the myocardium and the diffusion measurement precision. Methods to calculate individual tracking factor (Moghari *et al.*, 2012) are quite long in comparison to the effective gain on the measurement. Tracking factors of 0.6 are commonly spread in literature due to the robustness of this value in the adult (van Heeswijk *et al.*, 2012), even though individual variations have been reported as already discussed in 5.1 .

As a first guess, an apparent limitation of the technique could be the effective delay between the measurement of the liver position by the navigator and the end of the EPI readout. Indeed during this dwell time, the tissue can theoretically continue to move due to respiratory and even cause motion artifacts or phase shifting due to uncorrected motion during the diffusion encoding. Nevertheless for short encoding schemes like Monopolar, the time of exposure to intra-scan motion is very short in comparison of the breathing frequency as shown in . Note that this limitation is also true for any navigator motion-compensated technique or pure free breathing acquisition.

Acquiring images throughout the respiratory cycle could impose small changes in the cardiac geometry due to subtle changes in loading conditions, especially the heart inferior wall. In our specific case, we did not observe significant changes in the geometry, but the question probably needs to be investigated and addressed at higher spatial resolution. As explained in chapter 6, non-rigid registration algorithms could be used to maximize the correspondence between structures even if a small change in the geometry appears e.g. these caused by different breath holds or RR intervals variations.

Finally, the linearity of the breathing might be important. As the navigor describes only the liver position, it cannot differentiate the expiratory phase and inspiratory phase. An assumption is then done that the heart displacement is the same in expiratory and inspiratory. The potential hysteresis effect releaved by Nehkre et al. can also lead to an additionnal miss-registration.

5.2.Reproducibility study

Since direct comparison between breath-hold, gating approach and slice following cannot be conducted with similar steady state level, we propose like others (Nielles-Vallespin *et al.*, 2013) to validate the slice following approach by conducting a reproducibility study. In order to validate the application of Slice following on clinical context we thus proposed a reproducibly study using both IVIM and DTI acquisitions on 10 volunteers.

5.2.1. Materials and Methods

Images were acquired on a clinical MAGNETOM Avanto 1.5T scanner (Siemens Healthcare, Erlangen, Germany) providing a maximum gradient strength 45 mT/m, with a 6-channel body matrix coil and 9 channels from the 24-channel spine coil. Ten healthy volunteers were enrolled in this study, including 7 male and 3 female with a mean age of 32±10 years and a mean heart rate of 56±6 bpm. Each volunteer was scanned twice, with a 1-week delay between measurements for reproducibility assessment of the IVIM and DTI measures. All subjects gave their written informed consent for this institutional board-approved study protocol.

Before the DWI acquisitions, 2- and 4-chamber and short-axis (SA) cine images were obtained for slice planning. T1 and T2 mapping, which was required in the IVIM model, were also obtained in the SA at the mid-ventricle position, using a prototype Modified Look-Locker Inversion recovery (MOLLI) (Messroghli *et al.*, 2004; Kellman and Hansen, 2014) and a prototype T2prep SSFP (Giri *et al.*, 2009) sequence, respectively.

The diffusion-weighted images were acquired using a customized diffusion single-shot EPI sequence with proposed slice following method. Cardiac ECG triggering was implemented with the ability to set a multiple-trigger-delay (TD) loop for sequential sliding of the acquisition window within the RR interval for PCATMIP post-processing as described by Pai and Rapacchi (Pai *et al.*, 2011; Rapacchi *et al.*, 2011)(See chapter 6). In this work, we used an SE-EPI sequence with a monopolar preparation and gradient reversal (Winkler *et al.*, 1988) fat saturation management. Double-oblique short-axis DW images were acquired with a 128 × 80 pixel matrix, rectangular FoV of 350 × 220mm², and parallel imaging (GRAPPA factor 2, 24 external reference lines). Short-axis DW slices (6mm thick) were obtained with an in-plane resolution of 2.7 × 2.7mm² interpolated in-plane to 1.35 x 1.35mm², with a 2442 Hz/pixel bandwidth. No averaging was performed, but multiple TDs shifted every 10 ms were acquired for PCATMIP reconstruction. The pencil beam navigator was placed on the top of the liver, and the tracking factor was fixed to 0.6 (van Heeswijk *et al.*, 2012). Before each acquisition, two complete dummy scans were performed on each slice to reach the magnetization steady state.

DTI acquisition

The DTI acquisitions parameters were as follows: interleaved multi-slice mode with 10 contiguous slices; TE=45ms; TR= number of slices x RR-interval (e.g., 10 s for a heart rate equal to 60 bpm); and 12 diffusion directions with a b-value of 350s/mm² and 10 TDs were acquired. To remove the blood hyper signal on the b-value=0 images, a short gradient was added before and after the 180° pulse, similarly to what has been proposed to crush artifacts from flow and residual magnetization in the brain (Mukherjee *et al.*, 2008). These gradients have an intensity corresponding to a b-value of 5s/mm². For next calculations using the DTI model, the low b-value=5s/mm² acquisitions were considered as b-value=0. The total acquisition time of the DTI protocol was 22 min for a 60 bpm heart rate. From the higher-resolution multi-directional DWI dataset, not only the *FA* and *MD* parameters but also the ratios of the tensor eigenvalues ($\lambda 1/\lambda 2$, $\lambda 2/\lambda 3$) were derived using the conventional DTI model after manual segmentation of the left ventricle.

IVIM acquisition

The IVIM acquisition parameters were as follows: 5 slices with a gap of 100% in the interleaved multi-slice mode; TE=42 ms; TR= number of slices x RR-interval (e.g., 5 s for a heart rate equal to 60 bpm); and 6 diffusion directions with b-values 0, 15, 30, 50, 75, 100, 200, 300, 400 s/mm². Only 5 TDs were acquired, leading to a total acquisition time of 20 min for a 60 bpm heart rate. The following IVIM parameters were calculated pixel-wise, from the multi-b Trace DW images: *D* (true diffusion coefficient), *D** (pseudo diffusion coefficient) and *f* (perfusion fraction) by bi- exponential fitting according to the model of Lemke (Lemke *et al.*, 2010). Using the 6 directions of each b-value, *MD* and *FA* parametric maps were calculated from the DTI model on the IVIM dataset. The mean values by slices are then derived using a manual segmentation of the left ventricular cavity.

In each case, care was also taken to acquire images during the most quiescent cardiac phase in diastole, where the motion is known to be minimal from the cine images. The acquisition window was thus positioned at end diastole, in the iso-volumetric phase that was detected as minimizing motion of the left ventricle on the cine images (Tseng *et al.*, 1999; Rapacchi *et al.*, 2011), and the TD shift was incremented toward early diastole.

Statistics

A linear mixed-effects model was first used to test the significance of the differences across the dependent variables (f, D, D^* and FA, MD for IVIM and DTI model, respectively), with a structure of the covariance matrix for the random effects, taking into account the clustering across volunteers. Since the linear mixed-effects modeling did not demonstrate statistically significant differences for the dependent variables of the IVIM and DTI model across slices in the heart, individual slices were combined for reproducibility analysis.

Inter-measurement reproducibility for f, D, D^*, MD and FA among repeated measures was assessed by the Lin concordance coefficient (Lin CC) (Lin, 2000) and the complementary Bland Altman method (Bland and Altman, 1999). The Lin *CC* contains a measure of the precision (Pearson correlation coefficient), or how far each observation deviates from the best fit line; C_b is a bias correction factor that measures how far the best-fit line deviates from the 45° line through the origin, which is a measure of the accuracy. Agreement between conditions was quantified by Lin's method. The level of agreement was classified as excellent (0.81-1.00), good (0.61-0.80), moderate (0.41-0.60), fair (0.21-0.40), or slight (0.00-0.20). Next, Bland and Altman analysis was applied to further assess the relative contribution of the bias and error for the differences between conditions. The hypothesis of zero/no bias was tested by a paired t-test. Finally, differences in parameters (D, D*, f, MD and FA) changes between measurement sessions were assessed using an ANOVA model with a repeated-measures design and the Box's conservation correction factor. All statistical analyses were performed using Stata 13 (College Station, TX) statistical software. P-values smaller than 0.05 were considered statistically significant.

5.2.2. Results

DTI acquisition

Figure 5.9 shows the DWI directional raw images for b-value=0 and the 12 directions of b-value=350 s/mm² after PCATMIP reconstruction on one volunteer. Mean values on the heart wall for *MD* and *FA* are presented in Figure 5.10 for the repeated acquisitions with a one-week interval. For all ten volunteers, a global mean value of 1.72±0.09 x10^{-3} mm²/s for *MD* and 0.36±0.02 for *FA* was obtained. The $\lambda 1/\lambda 2$ and $\lambda 2/\lambda 3$ Eigenvector ratios were determined to be 1.37±0.08 and 1.48±0.09, respectively. A good reproducibility was found for *MD* (ρ_c=0.835), with high precision (r= 0.93) and accuracy (C_b=0.898), whereas *FA* showed a poorer reproducibility (ρ_c=0.157) that was mostly related to the limited precision (r=0.16) despite an excellent accuracy (C_b=0.983). Repeated measures ANOVA showed no difference between measurements sessions for all DTI (*MD*, *FA*) parameters.

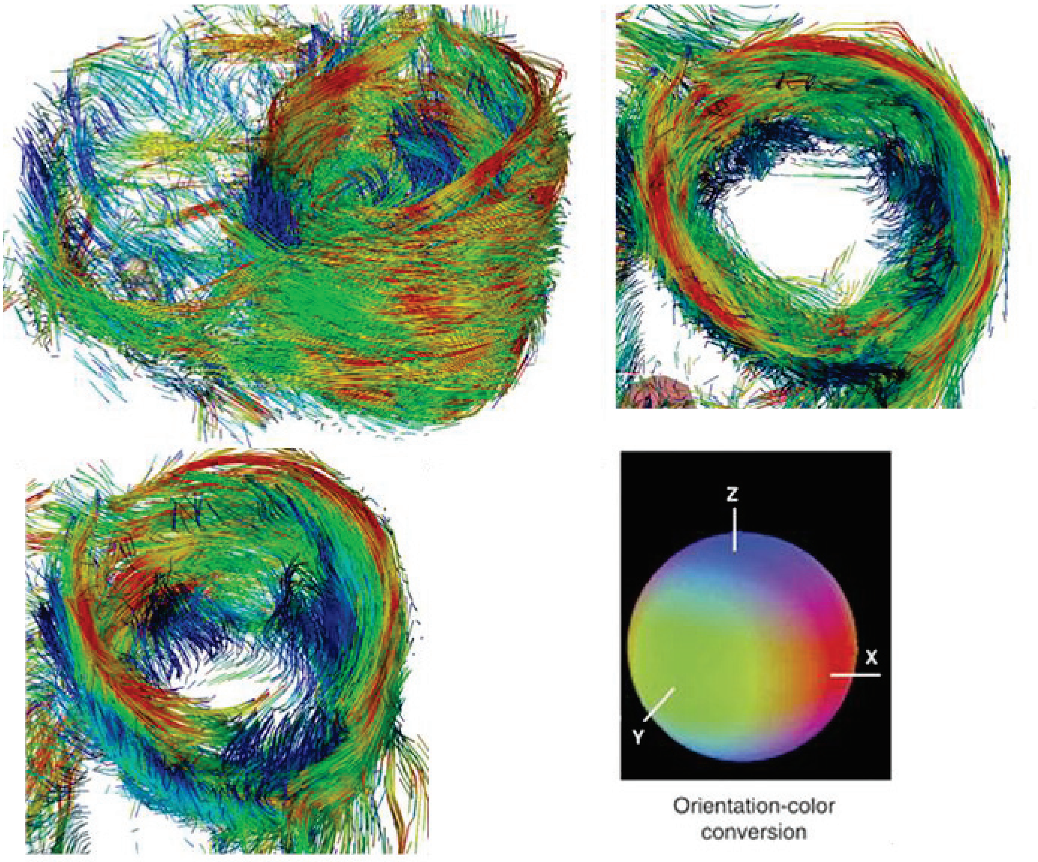

Figure 5.8: Fiber tracking of the DTI protocol, (tractography: 2nd order Runge-Kutta, visualization: own development).

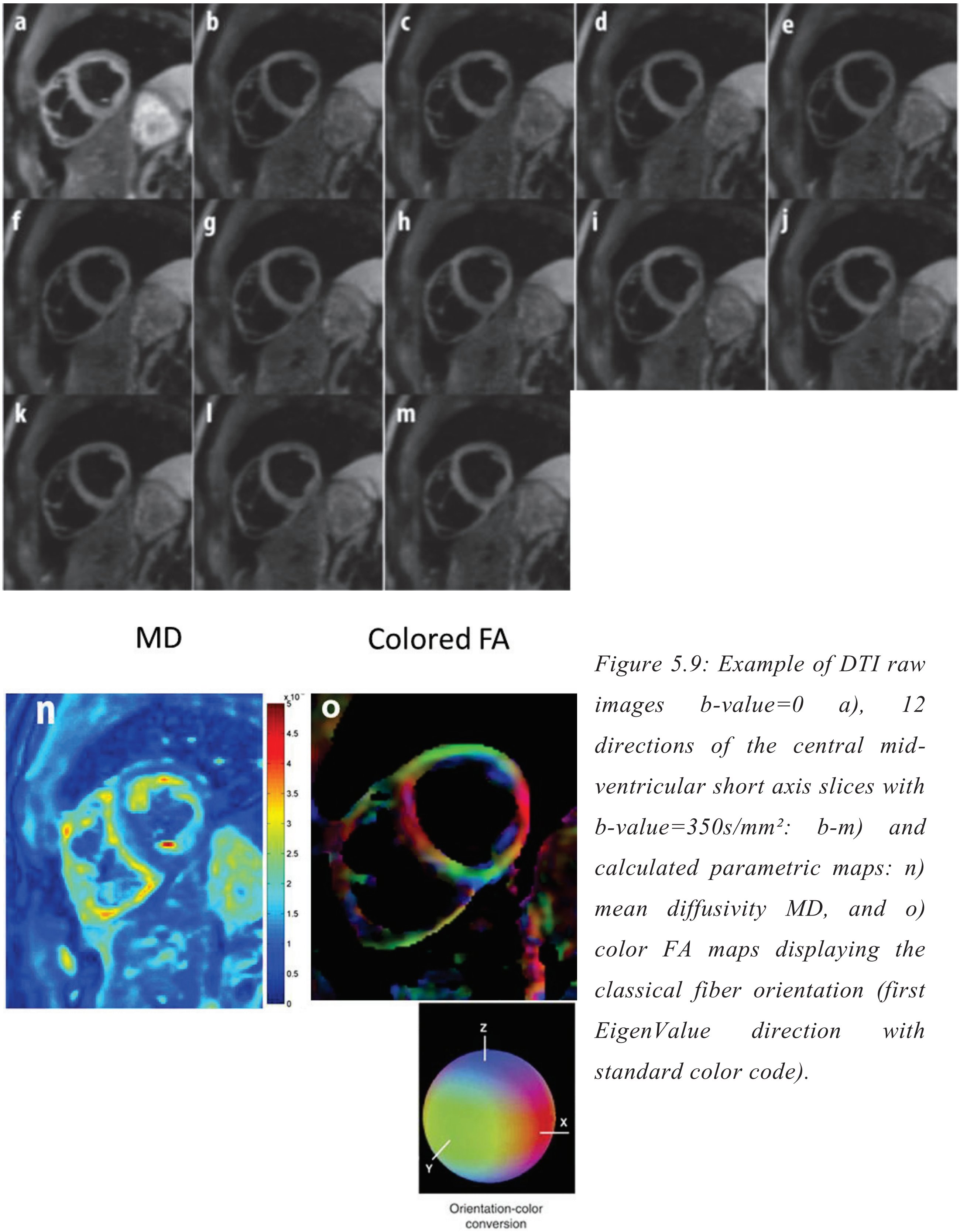

Figure 5.9: Example of DTI raw images b-value=0 a), 12 directions of the central mid-ventricular short axis slices with b-value=350s/mm²: b-m) and calculated parametric maps: n) mean diffusivity MD, and o) color FA maps displaying the classical fiber orientation (first EigenValue direction with standard color code).

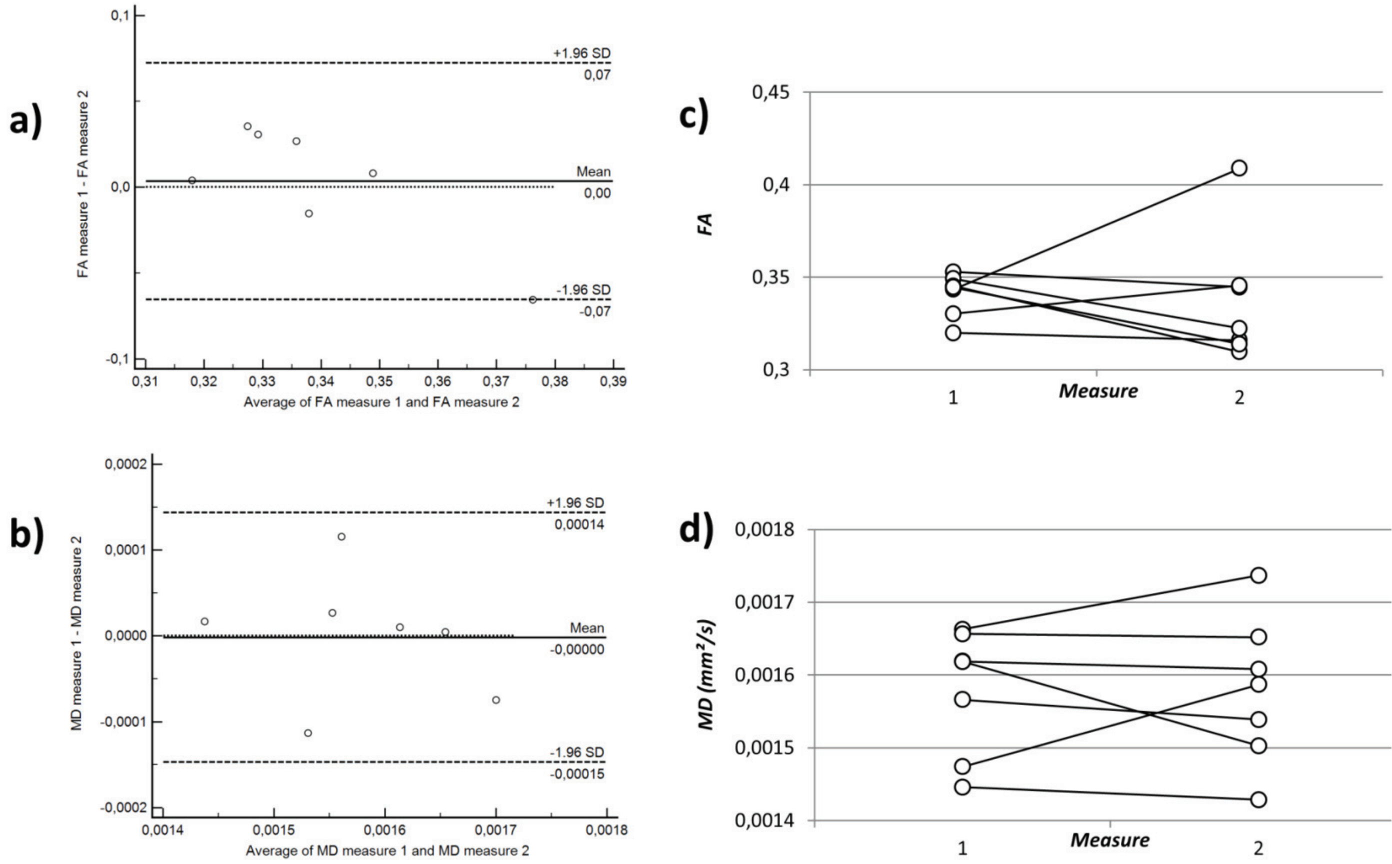

Figure 5.10: Reproducibility of the DTI parameters: Bland-Altman and line plot of the mean measure on the heart wall, demonstrating the interstudy reproducibility for MD (a-c) and FA (b-d). No statistically significant difference was found for FA and MD.

IVIM acquisition

Figure 5.11 presents the DWI Trace data for all b-values after PCATMIP reconstruction in a volunteer. Figure 5.12 shows the mean values on the whole heart for true diffusion D, vascular fraction f and perfusion D^* on the initial and repeated acquisitions. The robustness of the D and f calculation is illustrated by the homogeneity of the corresponding parametric maps. A lower quality of the D^* maps was obtained due to higher expected fit uncertainties of this parameter in the IVIM model. The mean values ±SD for all volunteers are $43.6 \pm 9.2 \times 10^{-3}$ mm²/s for D^*, $1.41 \pm 0.09 \times 10^{-3}$ mm²/s for D and 0.122 ± 0.013 for f. Perfusion fraction f was highly reproducible (ρ_c=0.963), with a high precision (r=0.979) and accuracy (C_b=0.983).A good reproducibility of the diffusion coefficient D (ρ_c=0.762) was found with a good precision (r=0.83) and a high accuracy (C_b=0.918). Pseudo-diffusion coefficient D^* was the less reproducible among the IVIM parameters but remained accurate (ρ_c=0.652, r=0.697 and C_b=0.935). Repeated measures ANOVA showed no difference between measurements sessions for all IVIM (f, D, D*) parameters.

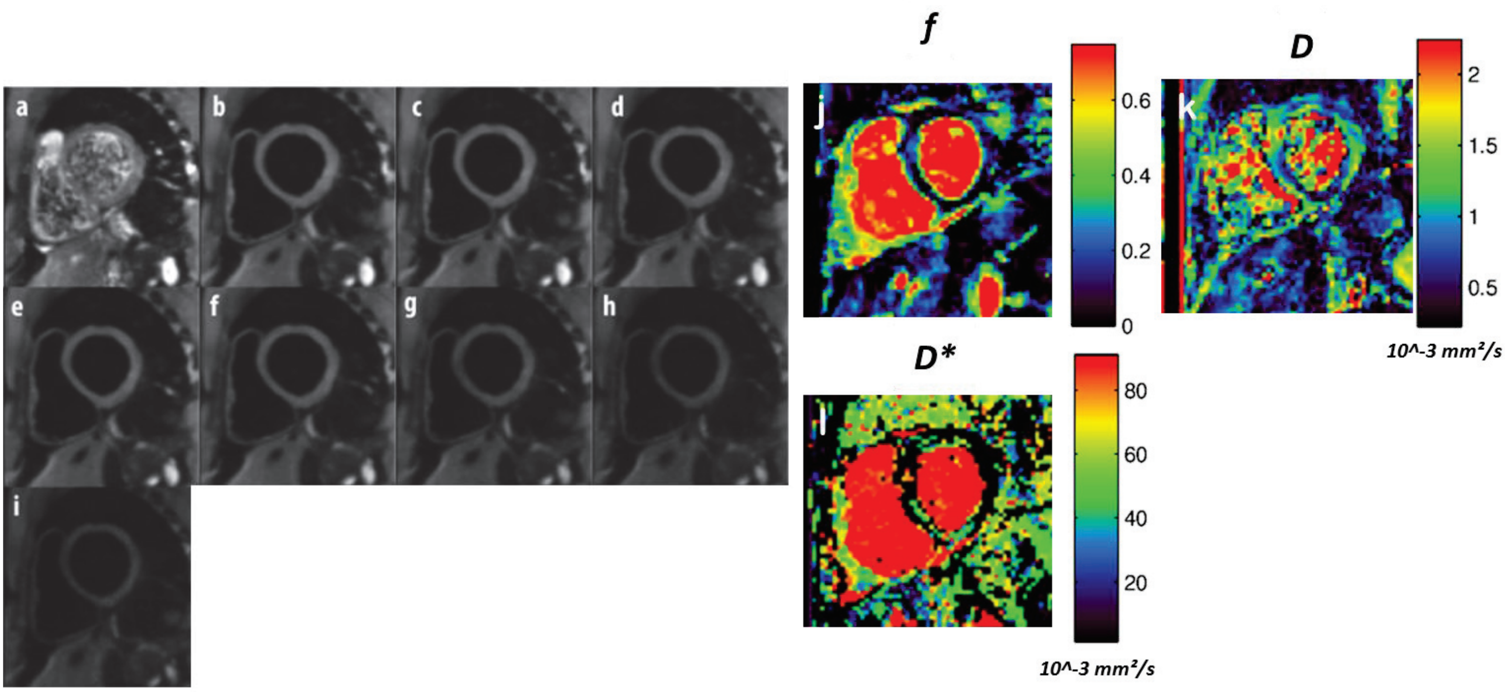

Figure 5.11: Example of IVIM raw images of the central mid-ventricular short axis slices: a) b-value=0 image b-i) b-values=15, 30, 50, 75, 100, 200, 300, 400 s/mm² and calculated parametric maps: j) diffusion D, *k) perfusion fraction* f, *and l)* D* *maps (calculated here from Sphere © Olea medical).*

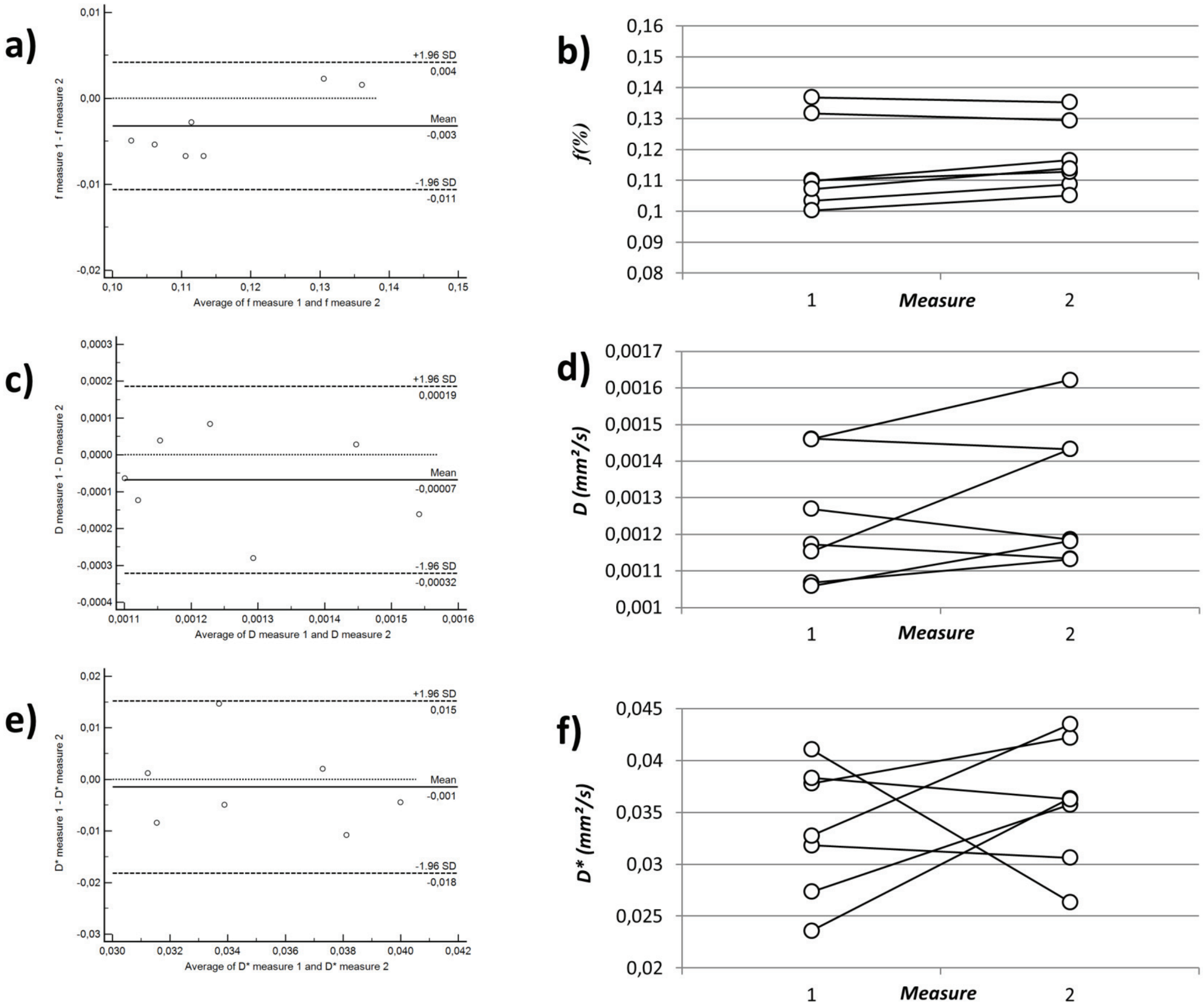

Figure 5.12: Reproducibility of the IVIM parameters: Bland-Altman and line plot of the mean measure on the heart wall, demonstrating the inter-study reproducibility for the f *(a-b),* D *(c-d) and* D* *(e-f) parameters. No statistically significant difference was found for* f,D *and* D*.

Analysis of multi-directional IVIM dataset

Using all 6 directions acquired for the IVIM multi-b multi-direction protocol, *FA* and *MD* were studied using the DTI model for all 10 volunteers. Figure 5.13 represent the calculated *MD* and *FA* parametric maps using sequentially each of the 9 b-values. Further study of FA and *MD* parameters in the whole myocardium as a function of the b-values allows one to generate curves. A decrease of both parameters as a function of the b-value can be observed. *FA* follows a linear decrease while *MD* decreases exponentially and stabilizes after b-value>200s/mm² around a mean diffusivity of 1.7×10^{-3}mm²/s.

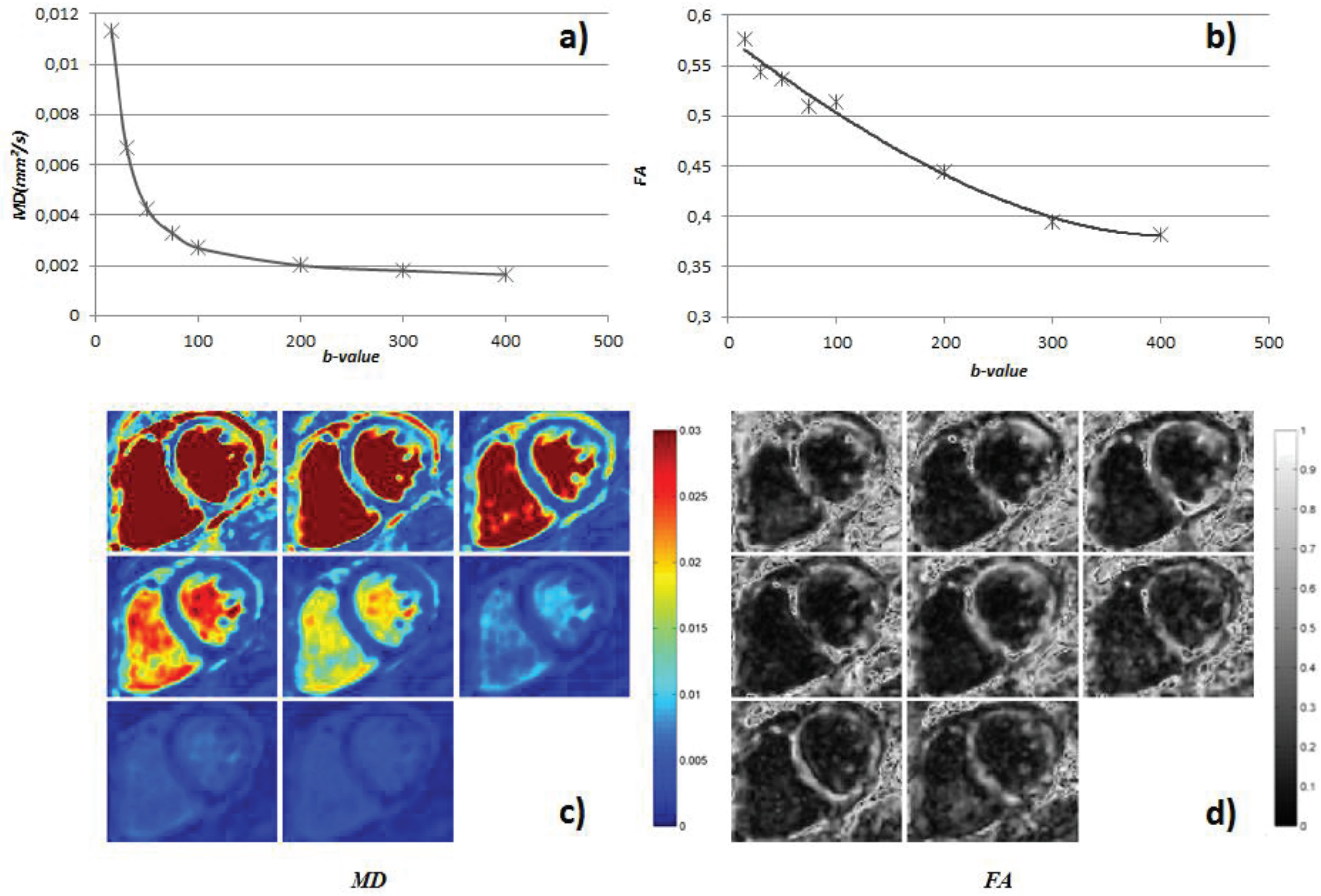

Figure 5.13: Myocardial mean value of MD*(a) and* FA*(b) as a function of the b-value, and* MD *and* FA *parametric maps (c-d) derived from one multi-b multi-dir IVIM dataset, b-values=15, 30, 50, 75, 100, 200, 300, 400 s/mm² from the top left to the bottom right. a)* MD *follows a fast exponential decrease for the low b-value and then shows stabilization after the b-value of 200s/mm². b) FA decreases linearly.*

5.2.3. Discussion

Reproducibility

No statically differences were found between first measurement and second measurement. MD parameter from DTI model and D, f from IVIM were found as highly reproducible while FA shown a lower reproducibility. However for D* parameter a bad reproducibility was found, questioning if the IVIM effect is homogeneously present in our data, assumption on SNR and fitting method are discussed above.

DTI acquisition

For the DTI protocol, the b-value=350 s/mm² was chosen in accordance with the literature to be high enough to not suffer from perfusion effect (Nielles-Vallespin *et al.*, 2013; C. T. Stoeck *et al.*, 2014), the number of direction and TDs was taken from the protocol of our previous study (Wei *et al.*, 2015) for a global acquisition time of 20 min. The diffusion parameter *MD* and *FA* obtained in the LV for all volunteers was (*MD*=$1.72\pm0.09\times10^{-3}$ mm²/s, *FA*=0.36±0.02). Recent studies using a classical STEAM sequence on healthy subjects have revealed equivalent or lower values (C. T. Stoeck *et al.*, 2014)(*MD*=0.9×10^{-3} mm²/s, *FA=0.61*), (Nielles-Vallespin *et al.*, 2013)(*MD*=1.1×10^{-3} mm²/s, *FA*=0.46), (Tunnicliffe *et al.*, 2014)(*MD*=1.2×10^{-3} mm²/s, *FA*=0.54). STEAM sequence was also applied on heart with arterial disease (M. T. Wu *et al.*, 2006) (in the remote zone: *MD*=0.7×10^{-3}mm²/s, *FA*=0.27), on heart with hypertrophic cardiomyopathy (HCM) (McGill *et al.*, 2012) (*MD*=0.8×10^{-3} mm²/s, *FA*=0.61) and on healthy heart but considering the strain effect (Dou *et al.*, 2002) (λi=0.9×10^{-3}mm²/s). The Spin-Echo sequence and SSFP yield higher values (Gamper *et al.*, 2007) (λi=1.8 to 2.3×10^{-3}mm²/s) and (Nguyen *et al.*, 2014) (*ADC*=1.5×10^{-3} mm²/s). FA value are also in accordance with one obtained on the ex-vivo heart with 6 directions and a b-value of 1000 s/mm² using a TRSE sequence (Eggen *et al.*, 2012) (*FA*=0.35) and all diffusion coefficient are also smaller than that of free water molecules at 37°C (*D*=3×10^{-3}mm²/s). Regarding the observations made on the skeletal muscle of the calf (Noehren *et al.*, 2014) where STEAM acquisitions have been shown to have a lower *ADC* and a higher *FA* than a TRSE sequence, our results are in the similar range of values.

Spin echo acquisition with monopolar encoding scheme imposes to acquire images during the most quiescent cardiac phase in diastole, where the motion is minimal. We originally choose this scheme due to it short effective duration in comparison to other ones. Advance encoding scheme like AMC yielding acquisition in systole was not available at the time of this study. Diastolic phase correspond to the moment when the heart is the finest which coupling with a low resolution lead to only 2 or 3 pixels to describe the wall heart. For these reasons advance DTI angular analysis like Helix angle was not conducted. Indeed as shown on

Figure 5.9 epicardium suffers from partial volume and is not present on the totality of the heart. However angulation in the cardiac mid corresponds to the one presented in the literature.

IVIM acquisition

The IVIM parameters obtained with slice following (D=1.41±0.09x10^{-3}mm²/s, D*=43.6±9.25x10^{-3}mm²/s, f=0.122±0.013) provide equivalent result in comparison to the main previous studies using IVIM model on heart. Similar results (D=1.26±0.10x10^{-3}mm²/s, D*=12.87±2.56x10^{-3}mm²/s, f=0.0824±0.0127) obtained by Callot et al. (Callot *et al.*, 2003) were realized on dog heart with a STEAM sequence at end-diastole with a controlled heart rate and respiratory cycle to minimize physiological motion with 14 b-values up to 550s/mm^2. With a STEAM sequence on human heart, Scott et al. (Scott *et al.*, 2014) obtained a lower fraction of perfusion (D=0.86x10^{-3}mm²/s, D*=17x10^{-3}mm²/s, f=0.06, finding $A=1-f=0.94$). Delattre et al. (Delattre *et al.*, 2012) reported slightly higher values (D=2.43±0.98x10^{-3}mm²/s, D*=74.5x10^{-3}mm²/s, f=0.150±0.046) on human heart using a bipolar sequence at end-diastole under breath-hold with 13 b-value and PCAtMIP reconstruction.

As discussed by Callot et al. (Callot *et al.*, 2003) a bias can by introduced in the measurement if the sequence duration is longer than the water exchange. In this condition, water molecules have a high probability to change of compartment massively during the diffusion encoding which break an assumption behind IVIM model. It could explain the differences between Spin Echoes sequence and STEAM sequence with a long mixing time.

Another difference is that previous studies have not proposed pixel-wise maps for the $D*$ parameter, which was calculated from a ROI integrating the mean signal intensity of the whole myocardium, i.e from higher-SNR data. Comparison is therefore not straightforward given the lower robustness of $D*$ estimation especially at lower SNR. Moreover we choose here, to apply a standard least square fitting method without imposing any boundary. Advance fitting method can also improve the results found here and should investigate. Like previous studies to maximize SNR, we had performed IVIM fitting on TRACE images instead of summing individual directional IVIM fit which not ensure that the IVIM model is still applicable. Finally only the work of Delattre et al. (Delattre *et al.*, 2012) has proposed a T1/T2 correction which can explain once again some differences between studies.

Analysis of multi-directional IVIM dataset

The IVIM protocol with 9 b-values, 6 directions, 5 TDs, and 5 slices is a modified version of the IVIM protocol proposed by Delattre et al (Delattre *et al.*, 2012). In this study we proposed to reduce the number of TDs from 10 to 5 and to increase the number of directions acquired from 3 to 6 to ultimately investigate the directionality of f and D^* through IVIM directional maps or DTI tensors. A deep analysis of the directionality of the IVIM parameters and their coupling with the underlying anatomicophysiology and microstructure requires a much more sophisticated model than IVIM and DTI, Karampinos et al have proposed an interesting and improved model for the skeletal muscle, termed intravoxel partially coherent motion (IVPCM) (Karampinos *et al.*, 2010). However, in our study, a simple global analysis conducted on the tensors for all 9 b-values from our IVIM protocol was proposed in a first attempt. A very sharp decrease of *MD* and a clear decrease of *FA*, while the b-value increases, have been observed in all our volunteers. Figure 5.13 shows an example of parametric *FA* and *MD* maps and the evolution of the mean value of these parameters in the myocardium, as a function of the b-values. The variations of the quantitative parameters reveal the influence of the perfusion compartment on the mean calculated diffusivity at low b-value. Complete independence of the diffusion compartment begins to be evident for b-values higher than 300 s/mm² in our data, which is coherent with current knowledge (Yanagisawa *et al.*, 2009). The observed variations of the *FA* parameter are also very likely to be an indication of the sensitivity of the measure to the underlying multi-compartmental micro-structure of the myocardial tissue (Kaneko *et al.*, 2011). Indeed, considering the significance of *FA*, the increase of this parameter at low b-value indicates more directional water diffusivity. *MD* in the DTI model at high b-values relates to the apparent diffusion through elongated myocytes, with a main diffusion coinciding with the main orientation of the myocytes but also to a lower, and non-null, axial diffusion. The measurements of *MD* and *FA* at low b-values are most probably related to the pseudo-diffusion in the capillaries, and would be therefore sensitive to the strong directionality of the micro-capillaries water flux (water exchange through the endothelium cannot affect low b-value diffusion measurements), explaining the increased *FA*.

5.3. Valorization & Deliverables

Pulse-sequence developments exposed in this chapter were realized in C++ on Siemens sequence development framework IDEA version VB17. A customized diffusion single-shot echo planar imaging sequence was implemented for this work including following options from the product sequence:

- Navigators for free breathing acquisition, 2 methods available: cross-pair and 2D pencil beam. Each can play before and/or after the sequence.
- Measure of the reference navigator during the dummy scans.
- Dummy scans handled after navigators for accurate steady state achievement.
- Monopolar preparation mode.
- Specific calculation of TR and ECG management for cardiac triggering.
- Ability to save phase and magnitude image.
- Averaging capacity (concatenation frozen).
- Compatibility with parallel imaging (iPAT, separate ref scans, with slice followed separate scans feature).
- Multi-slices acquisitions.
- TD shifting for PCATMIP method, available for MDDW and Free mode only.
- Gradient reversal for Monopolar and TRSE scheme.
- Inner-volume: modification of the thickness and rotation of the 180RF pulse.
- b-value=0 with short gradient added in one direction for black blood achievement and reduced flow artefacts.

6. Development of Dedicated Post processing and analysis

Slice following approach is an efficient technique to perform free-breathing acquisition while optimizing the acquisition protocol. However as only the head-foot motion is corrected by this technique from a 3D respiratory movement, in-plane motion remains in the images leading to a mis-correspondence between anatomical structures. These displacements can be handled by adapted registration methods.

If the effect of respiratory is well managed, the effect of cardiac motion remains problematic to achieve reproducible diffusion measurements in the heart in vivo. Using spin echo sequence, acquiring images at cardiac phases where the motion is minimal is sometime not enough to prevent all signal loss. Additional strategies for motion correction may become mandatory especially in clinical conditions.

In this chapter, the previous reconstruction steps for correction of cardiac motion based on the PCATMIP method are presented. An improvement of this pipeline is proposed and evaluated for more complex data sets. A novel technique for retrospective motion correction is given and compared to PCATMIP and to standard averaging. Finally an artefact quantification method is described as well as a list of all development realized for this chapter.

6.1.Retrospective correction of residual cardiac motion and problematic

We have already seen that cardiac motion is one of the major sources of motion-induced signal loss in diffusion imaging and affects especially spin echo acquisition. The position of the acquisition in the heart cycle needs to be chosen cautiously and needs to correspond as much as possible to the most quiescent cardiac phases where the motion is minimal. Rappachi et al. have shown the relationship between signal loss and cardiac phase and revealed a short stability in systole and an important one in late diastole (Rapacchi *et al.*, 2011). However for patient with short RR cycle the diastolic period is considerably reduced and the related diastolic stability phase may be short or inexistent. This could lead to important regional signal loss and the muscle signal completely vanishes as show in Figure 6.1.

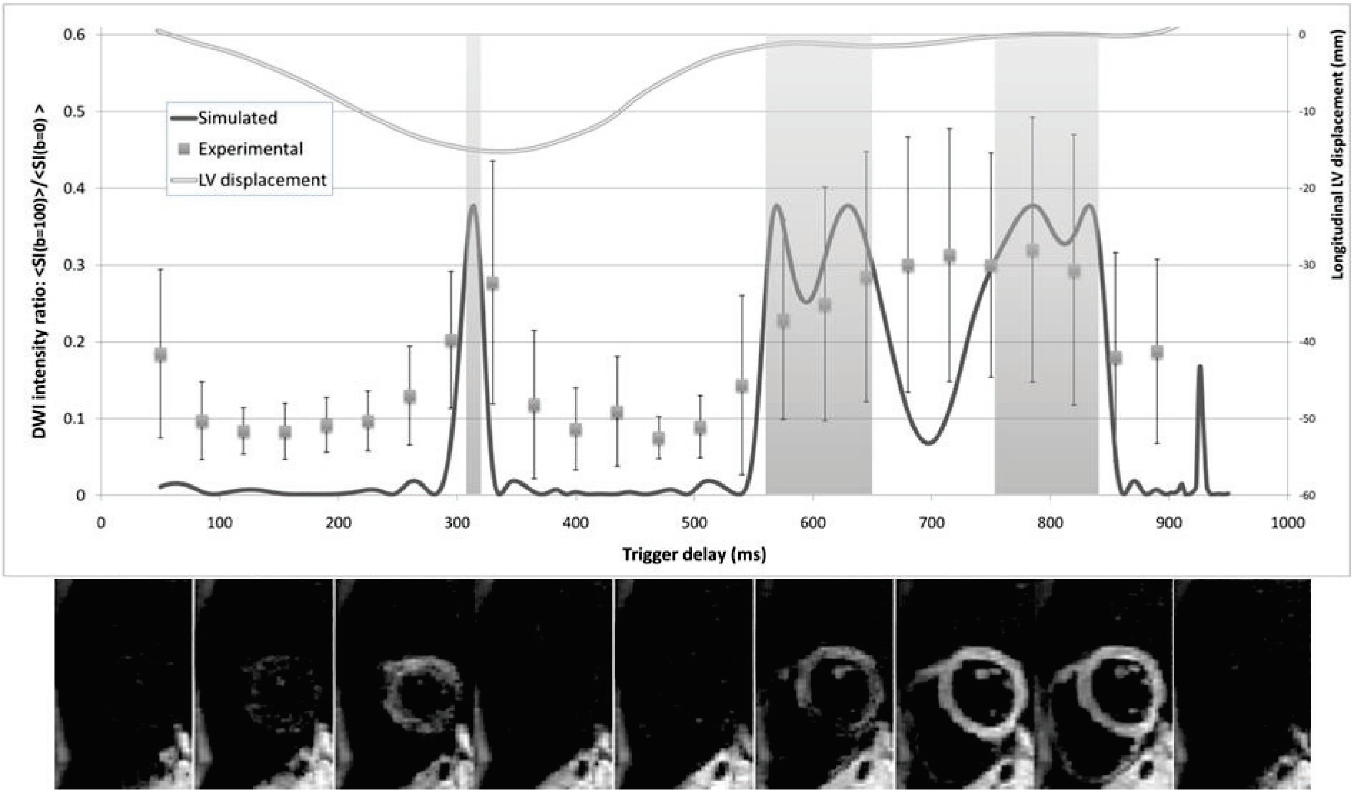

Figure 6.1: Simulation of signal induced by cardiac motion as function of the cardiac position in comparison to real experiment. © (Rapacchi et al., 2011)

Common methods to improve SNR like averaging are not sufficient to restore the signal if the heart totally vanishes due to motion. A technique called PCATMIP was proposed by Pai et al. (Pai *et al.*, 2011) and dedicated to specifically handle this signal drop out condition. The basic assumption behind this method is that motion-induced signal loss is spatially linked with the cardiac phase. Following this idea, playing the sequence at a shifted cardiac phase will create a different motion artefact located at a different position in the heart. If these time-shifted repetitions are close enough in the cardiac cycle, the same information of diffusion is measured and a Temporal Maximum Intensity Projection (TMIP) can be used to recreate a homogenous image of the heart. Indeed as the motion appears as an additional attenuation, the pixel with the highest intensity corresponds to a signal which is the less corrupt by motion.

On a dataset composed of N_{TD} time-shifted repetitions (TDs) and N_B x N_D diffusion weighted images, this algorithm performed a sliding Principal Component Analysis (PCA) filter over the TDs of each DWIs. For each DWI a pixel wise TMIP is played over the repetitions to kept the pixels with the highest intensity.

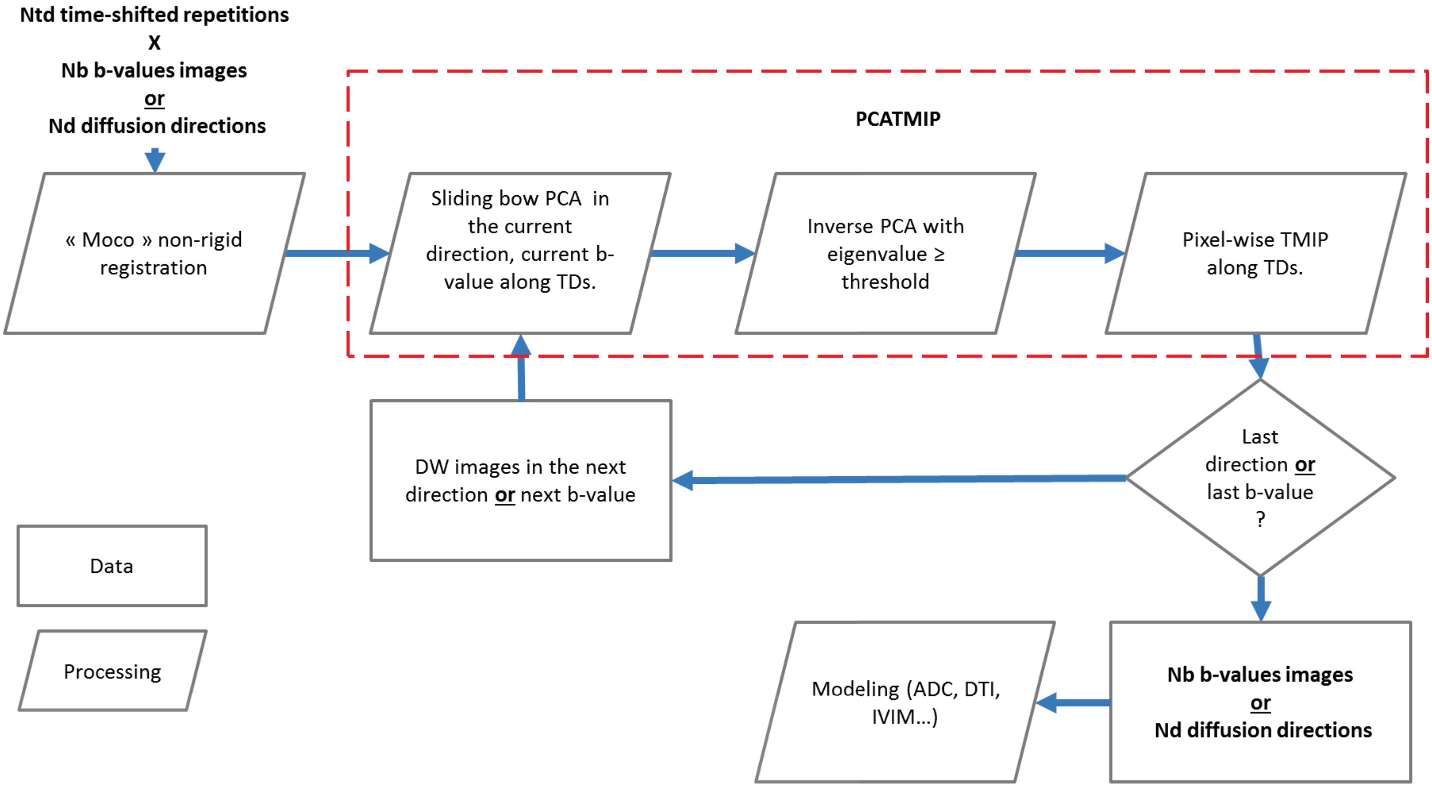

Figure 6.2: Global pipeline of PCATMIP reconstruction

The eventual presence of bulk motion and the difference of heart geometry on a multi-cardiac phase dataset can affect drastically the quality of the reconstruction. In the original work of Rappachi (Rapacchi *et al.*, 2011) and Delattre (Delattre *et al.*, 2012) using the PCATMIP, a non-rigid registration was proposed before any computation (Figure 6.2). A dedicated non-rigid and **non-supervised** algorithm developed by (Chefd'Hotel *et al.*, 2001; Chefd'hotel *et al.*, 2002; Chefd'hotel *et al.*, 2004; Kellman *et al.*, 2008) was used in the previous publications using PCATMIP to register all the DWI and TDs on a common reference. This algorithm called "MOCO" was led by Siemens USA as a compiled code. It works on 2 dimensional stacks of images with 2 registration steps as shown on Figure 6.3. For each b-value **or** each diffusion directions, the first step consists to register the TDs between them. The second step consists to register the b-values or directions between them.

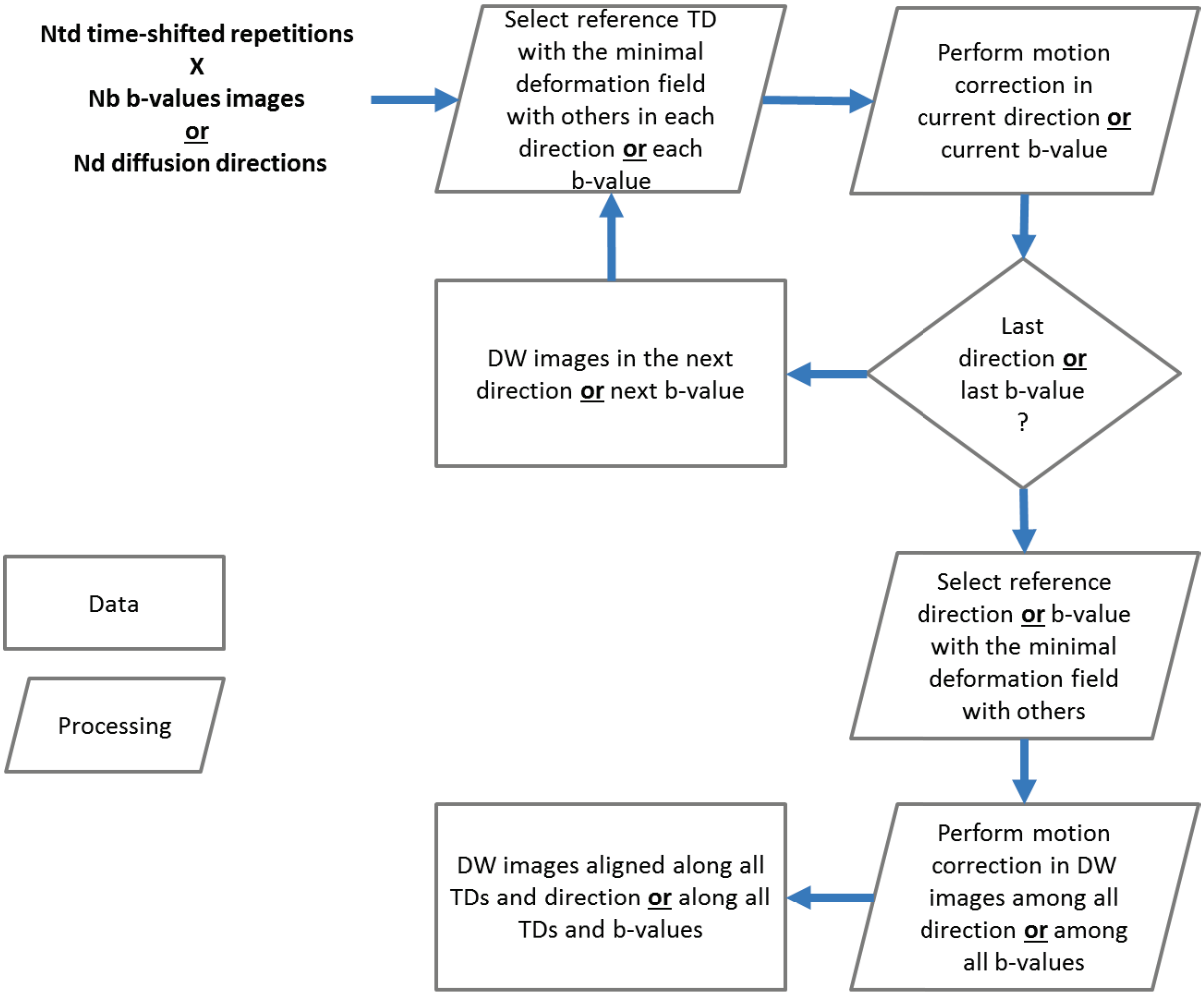

Figure 6.3: Global architecture of MOCO algorithm.

However, since TMIP assigns the pixel values of individual repetitions to the final result, noise spikes outliers can easily be highlighted, leading to overestimation of the true diffusion weighted image intensity by high noise levels. This effect motivates the adjunct of a de-noising filter prior TMIP. Principal Component Analysis denoising filter has been proposed by Pai (Pai *et al.*, 2011) using optimal sliding box that determined optimal by Rappachi (Rapacchi *et al.*, 2011) to be 15x15. This local PCA denoising filter results in an additional blurring in resulting images. This limitation can penalize models where the information can change drastically pixel to pixel like DTI or HARDI models.

Quality of the registration step is of also very important for any pixel by pixel analysis and especially for diffusion acquisition. Therefore registration is a mandatory step in many CDWI publications (Scott *et al.*, 2014; C. T. Stoeck *et al.*, 2014; Wei *et al.*, 2015). As shown in Figure 6.3 the automatic selection of a frame of reference for the MOCO algorithm is linked with the similarity between the data which need to be registered. In the presence of a high number of motion artefacts and/or with acquisitions involving different contrasts, like in the IVIM model, this reference and the deformation field to apply could be hard to determine. Moreover the MOCO algorithm currently associates with PCATMIP works only on 2 dimensions (b-values +TDs or directions + TDs). But in the case of the reproducibility and ultra-trail studies presented in chapter 5, datasets with multiple b-values, multiple directions and multiple TDs were acquired, thus the previously MOCO registration cannot be selected for the post-processing of these acquisitions.

We propose a multi-reference alternative for the registration step prior PCATMIP, enabling registration on a 3 dimension stack of images.

6.2.Improved In plane registrations

6.2.1. Multi reference registration method

Slice following approach is an efficient technique to perform free-breathing acquisition. However as only the head-foot motion is corrected by this method, an in-plane motion remains in the images leading to a mis-correspondence between the structures. In these conditions registration steps are mandatory but need to be adapted to the kind of diffusion acquisitions. We propose here to add a 1D dimensional registration step before any computation to register the time-shift-repetitions among them (Figure 6.4). Indeed complex diffusion protocols may involve 3 dimensions of acquisition (b-values, directions, TDs) but the reconstruction step using methods like PCATMIP or Average, actually works on only 1 dimension (for example, in the case of PCATMIP for a **given** b-value/direction, TDs are fused and only need to be register between them). The idea is then to perform the powerful MOCO algorithm on data with different contrasts only after the images were reconstructed by PCATMIP where images do not suffer from signal loss. Indeed, we believe that applying the multi-contrast algorithm after the reconstruction should improve the quality of registration.

For this first registration step, a fast, non-rigid, contrast-specific diffeomorphic registration algorithm was chosen among methods present in our lab. Reference frame was chosen among TDs being the one with the highest mean intensity i.e. the one with less signal drop out. For the second registration step, MOCO was kept as a powerful multi-contrast algorithm but it is used with multi-directional multi-b-values data only. We propose to quantify the quality of our registration steps on complex IVIM acquisitions using an evaluating method present above.

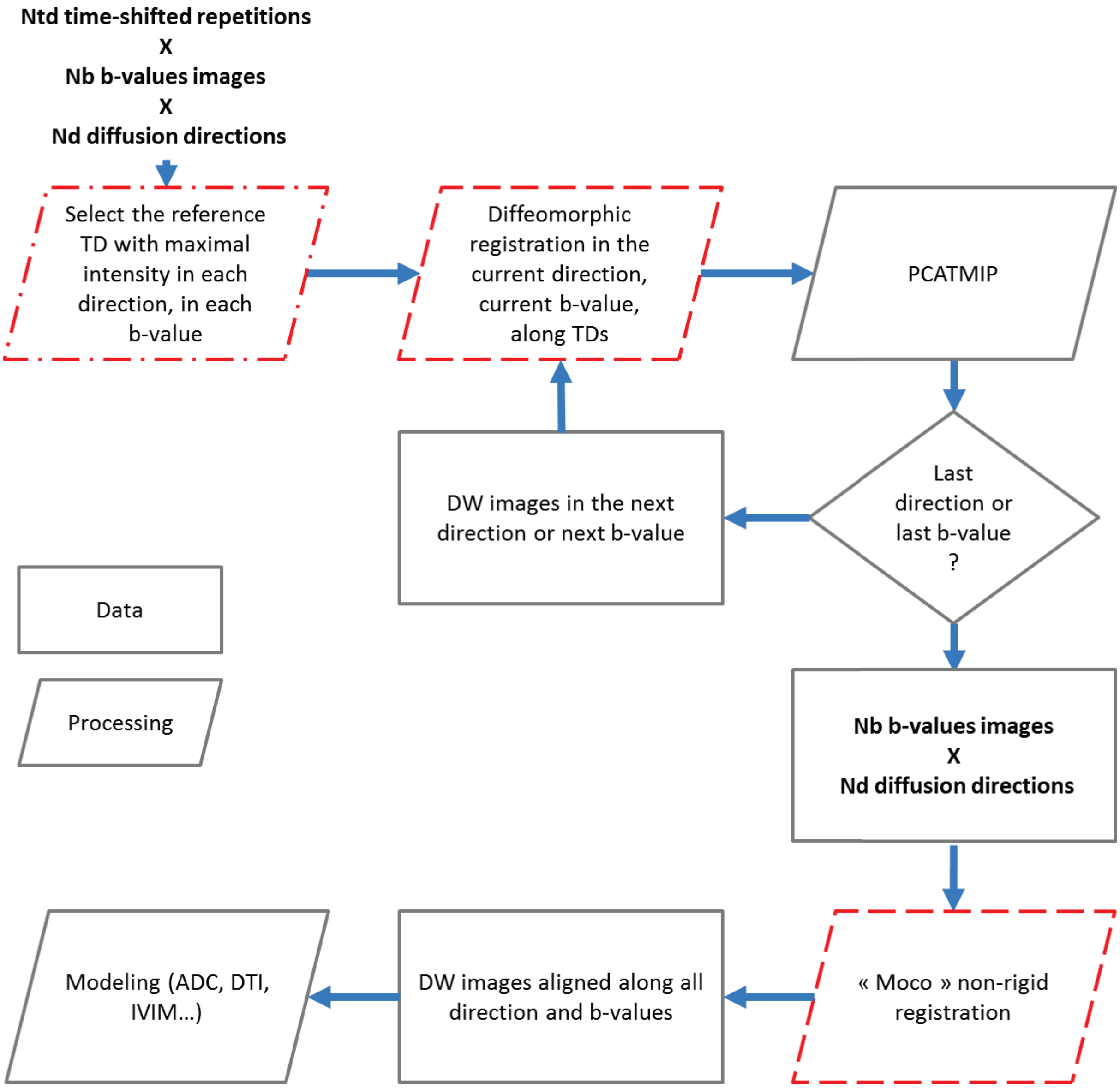

Figure 6.4 : Global pipeline proposed for PCATMIP reconstruction. In dashed red line the two registration steps modified in this chapter.

6.2.2. Validation of the proposed registration

For further in-plane retrospective motion correction evaluation (among inter TDs, inter b-values or inter-directions), the following framework of analysis was proposed. First, a rectangular region of interest (ROI) is selected to restrict the analysis to the left ventricle of the myocardium. Second, a binary mask is obtained for each diffusion weighted image using a defined threshold equal to SI= 80 (see Figure 6.5, step 1). All masks can be summed up, and the image intensity of the resulting calculated image scales with the level of co-registration of all masks, as illustrated in Figure 6.5, step 2. For perfectly co-registered images, the histogram of all pixel intensity is split into two unique bins: 0 and N (Figure 6.5, step 3, right), where N is the dimension of the analyzed diffusion weighted images over TDs, b-values or number of directions, or all. Figure 6.5 summarizes the principle for DW images with 5 TDs, in the case of perfect (binary histogram) and imperfect co-registration. For imperfect co-registration, the histogram widens over all intermediate bins (see step 3, left).

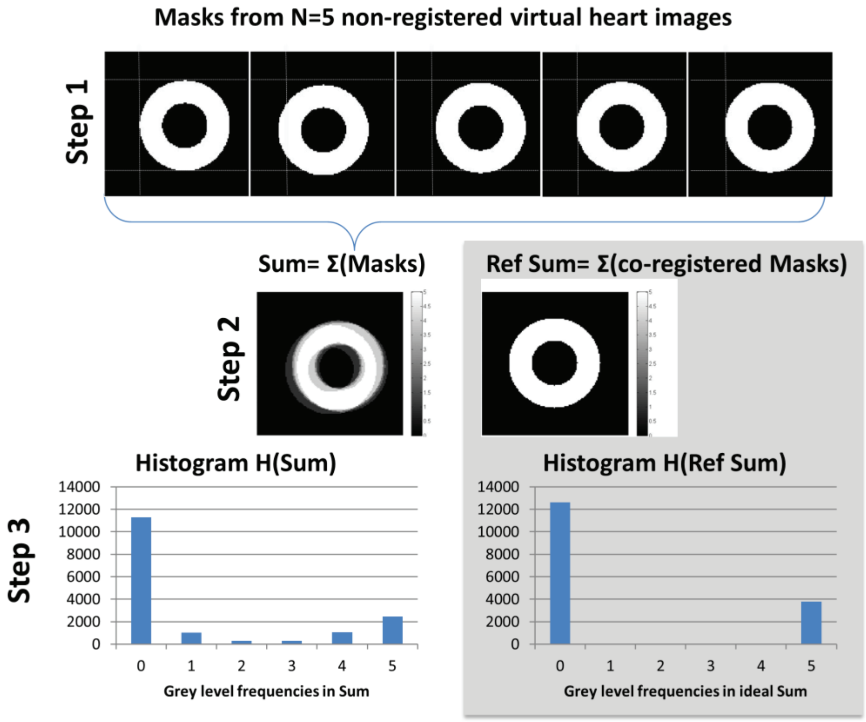

Figure 6.5: Principle of the 3-step co-registration evaluation method. Step 1: masks were generated from DWI images. Step 2: masks were summed. Step 3: For a perfect registered case histogram have only two bin while intermediated bin are present for a no perfect case.

The accuracy of the co-registration directly scales with the number of events per bin over the dimensions of the analyzed series. Using this methodology, we can define an index of co-registration level and evaluate its quality using the following criterion:

$$\text{CorRegIndex} = \frac{hist(0) + hist(N)}{npixel} \qquad 6.1$$

where $npixel$ is the number of pixels in the selected ROI and $hist(i)$ is the number of events of a given bin *i*. The index *CorRegIndex* represents the quality of the registration (units are %) compared with the perfect case where $hist(0) + hist(N) = npixel$. In our case, two registrations are required: one prior to the PCATMIP on all TDs for a given dimension, then a second one to be performed after PCATMIP, along b-values and diffusion directions, for each given slice. Both co-registrations steps were evaluated in the multi-directional IVIM data of the reproducibility study in the whole heart for all the volunteers; all multi-TD images corresponding to the first direction with b-value = 15 s/mm² were analyzed for the first registration, and images corresponding to all directions/b-values were analyzed for the second registration step.

6.2.3. Results

Figure 6.7 shows the generated mask for multi-TD (first row) and multi-b multi-directional (second row) images before and after each registration for one subject. On the IVIM protocol and using the first direction and the first b-value of all volunteers, the index of co-registration over 5 TDs was found to be 76.9±7% before the first registration and 87.3±5% after, resulting in a 10.4% improvement. As shown on the zoomed septum area shown in Figure 6.6, mis-registration artefacts were dramatically improved by the registration algorithm. The same approach was used to quantitatively evaluate the effect of the MOCO registration step between the 48 images resulting of the PCATMIP: the co-registration index improved from 51.6±5% prior to registration to 58.2±6% after registration.

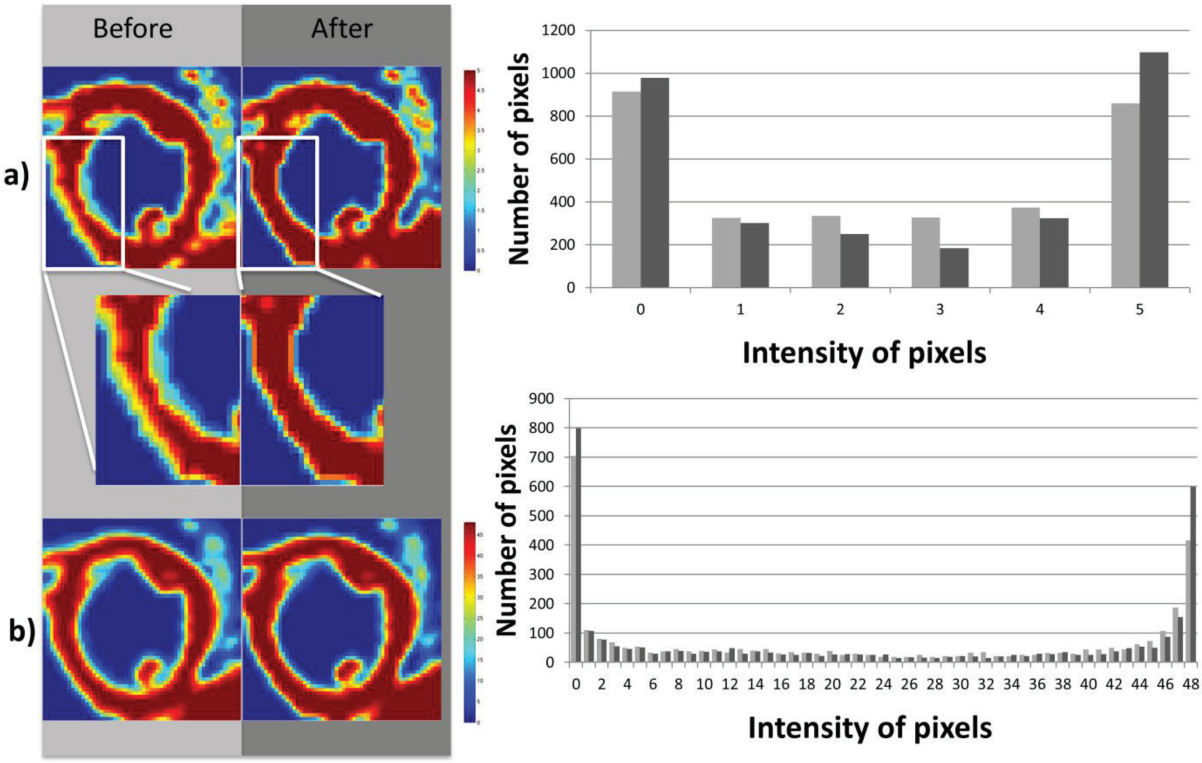

Figure 6.6: Results of the co-registration evaluation of all IVIM data from one volunteer for the two steps: a) illustration prior to PCATMIP on all TDs for b-value=15 s/mm² and for the first direction b) after PCAtMIP on all b-values, all directions.

6.2.4. Discussion

Multi-reference Registration

The registration step was split in two parts where the first step makes a registration on each stack of TD, using for each a separate reference. Consequently, the number of images registered together for this step is equal to the number to TD which is an important difference with the previous pipeline. The algorithm chosen to execute this task is a fast non-rigid contrast specific algorithm but as all non-rigid algorithms may introduce a small amount of data blurring. This specificity raises the same limits as the PCA filtration when it faces high angular data set. In this condition adding an additional registration step is questionable, nevertheless penalty induced by non-aligned data is of greater magnitude than blurring effect related to non-rigid algorithm.

In this method, in a TD stack, the image with the maximum mean signal intensity is chosen as reference. In all type of diffusion acquisition in short axis view, the heart is the main organ impacted by motion. Signal intensity of whole image is thus directly influenced with the presence of the myocardium and its change. However for very low b-value (until 30s/mm²), blood presence in the cavity can altercate this choice of reference.

High intensity blood signal is also very problematic with the multi contrast registration step. For a TE varying around 50ms, blood appears in the cardiac cavity on the images of b-value = 0. MOCO algorithm fails to register these images with the other weighting images where the blood not appears. In order to create a dark blood cavity for the b-value = 0 images, we applied a very small diffusion ponderation (b~= 5s/mm²) in the DTI protocol proposed in chapter 5.2. For IVIM protocol, b-value = 0 was not registered with the other b-values but S_0 signal from model of Lemke (Lemke *et al.*, 2010) was fitted as well as the other parameters. Registration of b-value = 0 reference image remains problematic and should be handle by a specific algorithm taking care of the blood signal.

In conclusion, since the reconstruction pipeline shown in Figure 6.4 is repeated for each slice, it intrinsically means that the individually co-registered slices were thus not aligned. Further work aiming at providing whole heart DTI tractography, will thus need to address this specific issue appropriately in order to ensure the slice-to-slice coherence of the 3D tensor field required by the fiber tracking algorithm.

Validation of the proposed registration

The proposed method to evaluate the registration steps is based on threshold to generate co-registration index maps. Thus presence of motion artifact which makes the heart disappears can negatively affects the result of this method. Indeed the basic assumption behind this index is that the heart is similar on all the images compared. If this condition is strictly respected, another limitation is the choice of the threshold value which can include more or less surrounding artefact like blood remaining signal. However as shown in Figure 6.6 the high contrast between the heart and the cavity helped the threshold to extract the heart and only heart.

To compare the effective scoring of registration and not motion artefact influence, we chose to restrict the evaluation of the first registration step to only the small b-value = 15 s/mm^2. Low b-values are poorly affected by motion and the heart is in the most of the case entire even without PCATMIP reconstruction. For this specific registration step the improvement of the correspondence of structure is important and makes that the following PCATMIP can occur in good conditions.

Second registration was made on the entire IVIM dataset after reconstruction, 48 images with different diffusion ponderations are compared. In this situation threshold value chosen should correspond to both high and low b-value. Presence of motion artefact is also more probable in high ponderation like b-value 400 s/mm^2 even after the PCATMIP reconstruction. These limitations can explain why second co-registration index of the second registration step is lower in comparison of the first one. However, even in these conditions an improvement of the correspondence is noticed.

6.3. Alternative method to minimize residual cardiac motion

PCATMIP is well adapted to manage important signal drop out due to cardiac motion. However this method may fail in the presence of low SNR conditions and could introduce data blurring. Moreover this approach cannot help if the images in the TD dimension do not exhibit any signal loss due to motion, like is the case for low b-values. Alternatively, averaging is efficient to increase the SNR but fails when the heart segments entirely disappear due to local motion.

Here we propose and evaluate a new technique called "Average + cutoff" that takes advantage of both previously mentioned methods (Figure 6.7). The idea is to exclude pixel where the heart entirely disappears by applying a threshold while averaging pixels higher than this threshold. A similar idea was presented in SCMR congress by Aliotta (Aliotta *et al.*, 2015),where the pixels corresponding to a coefficient of diffusion higher than 3mm²/s were exclude.

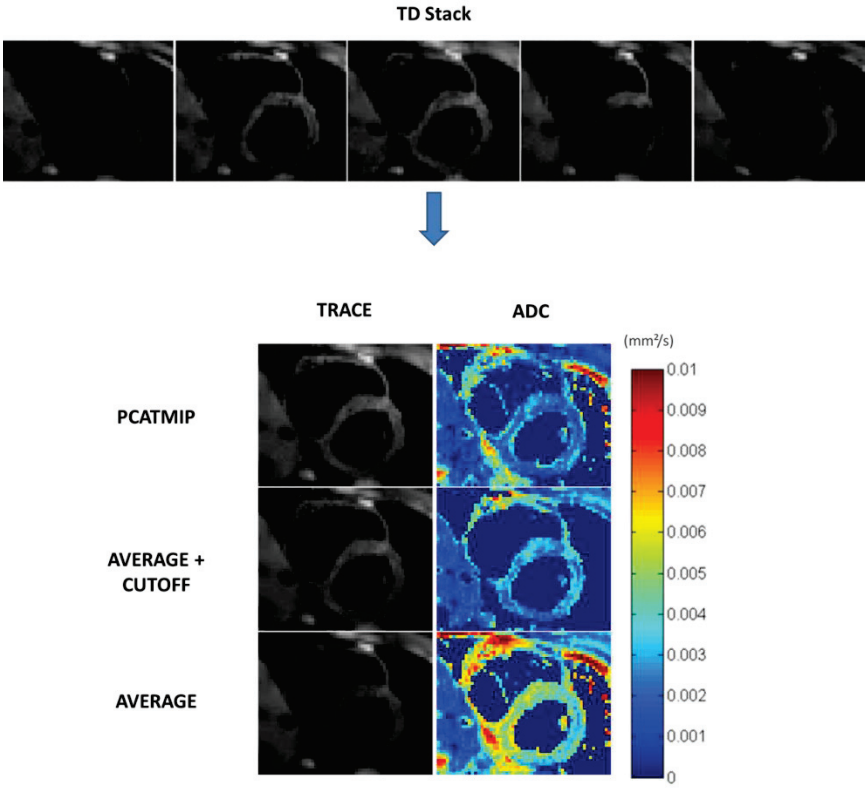

Figure 6.7: Example of a TD stack reconstruct with PCATMIP, Average + cutoff and classical Average.

Results of this method were evaluated using the DTI protocol of the chapter 5.2 on 10 volunteers. The general pipeline presented in Figure 6.4 is kept but the classical Average, Average + Cutoff were used instead of single PCATMIP. Threshold corresponds to the pixels with signal higher than 50, it was chosen to exclude only signal loss leading to the complete vanish of the heart in the image.

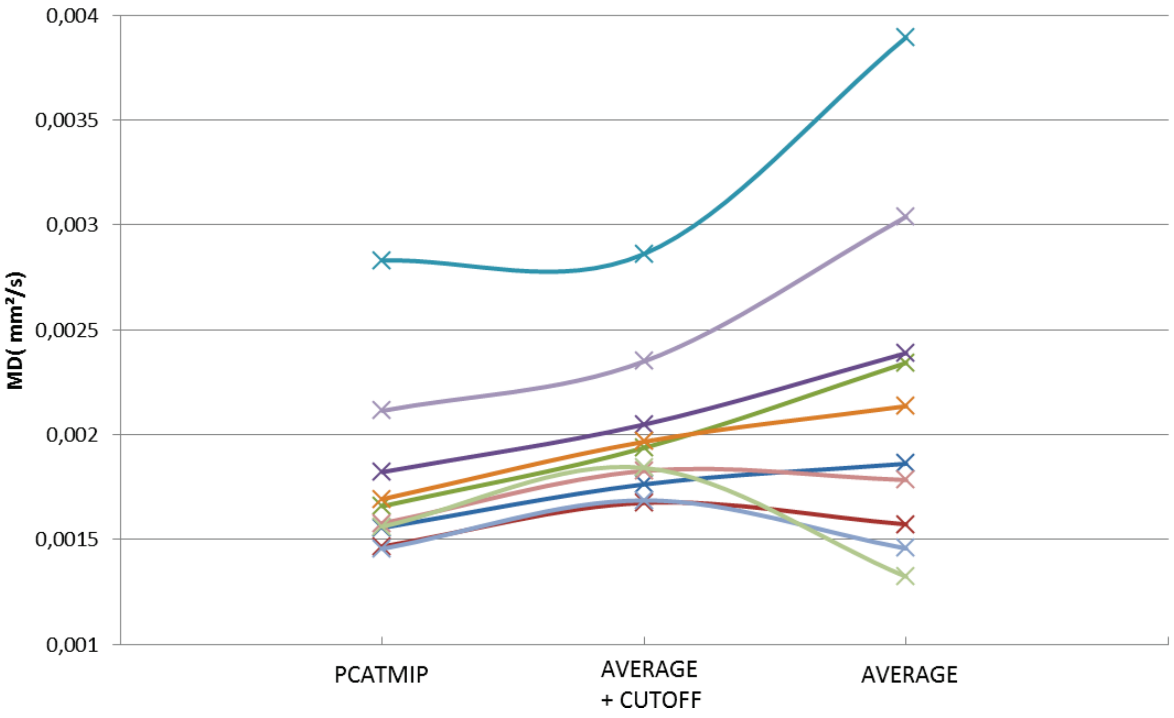

Figure 6.8: MD over the 10 volunteers for the three reconstruction method.

Our results show a global increase of the MD obtained using Average + cutoff in comparison of the PCATMIP measured to 13.73% and to 17.86% for the classical Average. FA variations are about 100% for both reconstruction and increase or decrease indifferently.

Mixing advantages of PCATMIP and Average method into a new reconstruction technique was interesting but enlightens the complexity of the motion corruption in the CDWI data. Indeed differences between MD with PCATMIP and Average + Cutoff processing reveals that the assumption of “all or none” signal loss described by Gamper (Gamper *et al.*, 2007) and Wedeen (Wedeen *et al.*, 1994) has its limitations. In this latest method, we took care to remove pixels with “none” signal by applying a threshold while averaging pixels with “all” signal. But even in these conditions, variation of Average + Cutoff and Average in comparison of PCATMIP are similar which means that increase of MD values in the proposed method are only explained by small signal attenuations keeping the heart present in the image. At a high b-value=350s/mm^2, these small signal losses express very slow movement probably due to remaining cardiac and/or respiratory intra-scan motion. FA is affected randomly in both methods, which only shown the presence of signal loss in a different diffusion encoding direction.

A threshold adapted to each patient can reduce the difference with PCATMIP considerably but exclude automatic reconstruction. This method can also be modified to averaging only the pixel presenting a little percentage of variations in comparison to the max signal but the choice of acceptable variations is the same kind of problem. PCATMIP approach remains robust against all scales of signal loss even ones not leading to total signal drop out.

6.4. Artefact scoring and error quantification

Previous study presented in chapter 6.3 has motived the development of a descriptor allowing quantification of processing errors all along the whole pipeline, and in turn of the quality of diffusion weighted data (and final rate of corruption by motion) that ultimately would enable us to compare objectively acquisition methods. The objective of such metric should be to evaluated improvements in post-processing or acquisition steps, and drive efforts objectively toward a standardization of the estimated of the diffusion parameters. Here we propose a quantification of DWI measurement artefacts based on 3 criterions. On a given set of 2-D raw images $S(x, y, i)$, where $i=0,1 \ldots n-1$ is the screened dimension, $S_0(x,y)$ the reference image, criteria ε_1, ε_2 and ε_3 are defined as:

$$\varepsilon_1(x,y,i) = \frac{S_0(x,y) - S(x,y,i)}{S_0(x,y)} \qquad 6.2$$

$$\varepsilon_2(x,y,i) = \frac{\underset{m=0}{\overset{n-1}{Max}}(S(x,y,m)) - S(x,y,i)}{\underset{m=0}{\overset{n-1}{Max}}(S(x,y,m))} \qquad 6.3$$

$$\varepsilon_3(x,y,i) = \left| \frac{\overline{S(x,y,m)} - S(x,y,i)}{\overline{S(x,y,m)}} \right| \qquad 6.4$$

$$\varepsilon(x,y,i) = \frac{\varepsilon_1(x,y,i) + \varepsilon_2(x,y,i) + \varepsilon_3(x,y,i)}{3} \qquad 6.5$$

Where ε1 represents the normalized signal attenuation due to diffusion, ε_2 the normalized distance from the signal with the highest intensity and ε_3 represents the normalized distance from the mean signal. An example of the individual criterions was given on Figure 6.9 where the dataset is corrupted by a motion artefact.

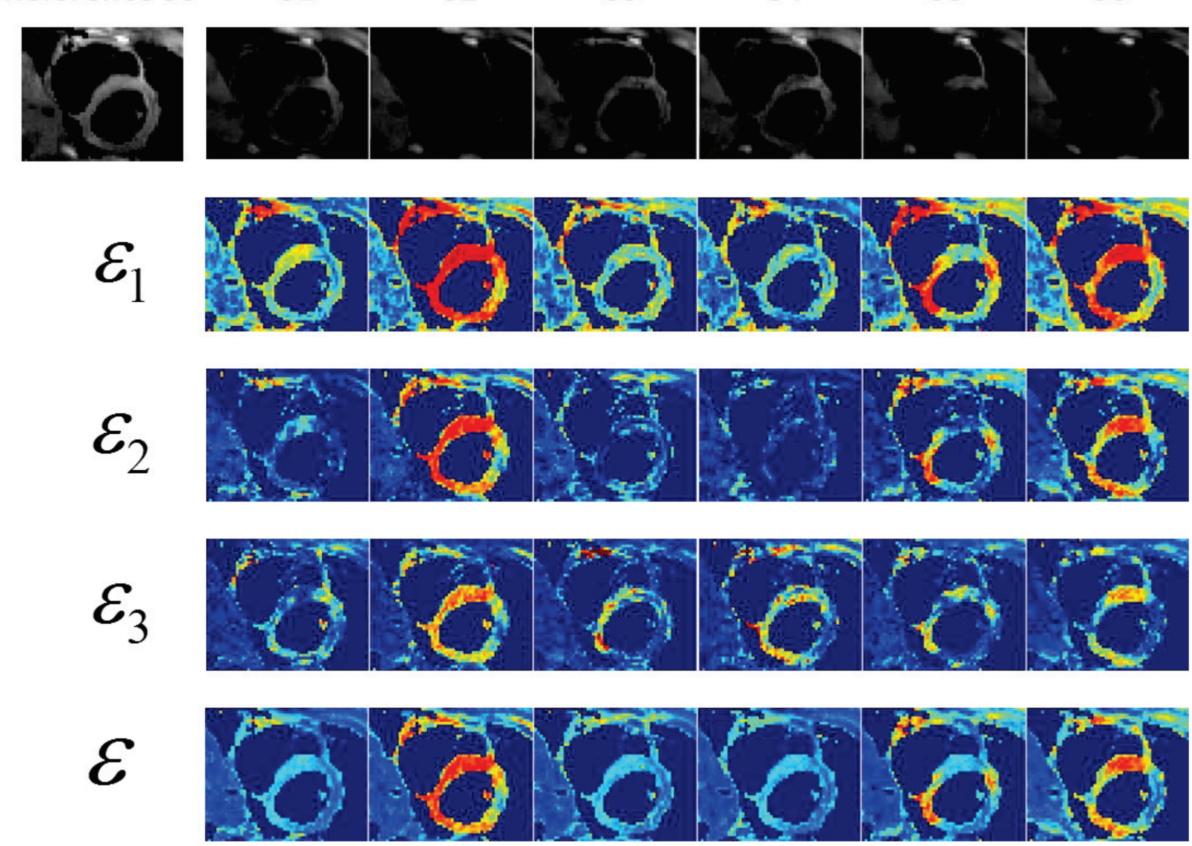

Figure 6.9: Example of a corrupt TD stack analyzed using the three criterions. The resulting error maps highlighted the signal loss.

Three different criteria are proposed to evaluate motion corruption in a stack of measurements. Each of these criteria represents the measured signal interpreted as the distance to different references that are referring to specific limitations. ε_1 represents the normalized attenuation due to diffusion. In previous studies involving healthy myocardium, mean diffusion was reported varying between 0.8 to 1.7 mm^2/s which corresponds respectively, at b-value=200 s/mm^2, a 15% to 30% attenuation. In the occurrence of a complete signal loss (attenuation 100%), differences with normal signal are about 85 to 70% which can reveals by contrast an abnormal zone. Unfortunately this contrast decreased when diffusion and/or b-value increased. In opposite ε_2 and ε_3 represent differences between signals of same nature and thus are independent of coefficient or diffusion or b-value. For a stack of a given screened dimension, ε_2 is the distance from the maximum signal and ε_3 the distance from the mean signal of this stack. Maximum signal can be considered as the less affected by motion which is the general idea behind PCATMIP but suffers from similar limitation regarding the noise. Mean signal is generally used in statistic to sort out outlier in a dataset and has same advantages and drawbacks as averaging.

These criterions can be used to design a systematic evaluation of a stack of diffusion weighted images of similar diffusion weighting (similar b-value), whatever the way they have been obtained and thus evaluated difference in processing pipeline or acquisition strategies. The pixel-by-pixel quantitative score can be summarized into a resulting error maps as given in Figure 6.9 where maps reveal abnormal zones. This score, given between 0 and 1, give a probability of higher corruption by motion, that can then be used to analyze the data and/or the acquisition protocol, or used in a real-time feedback to drive the acquisition.

This score is adequate for the analysis of a stack of images containing the same dimension (for example: a TD stacks of same b-values, same directions) but this technique might be also used to compare a stack of diffusion direction of a same b-value. For example, after PCATMIP correction some diffusion directions can still show important signal loss. This information could be used as an input to identify a corrupted direction and reject it, or to reacquire it, the goal is to not alter the subsequent modelling. However in a stack of same b-value, signals from different diffusion directions of weighted images express the anisotropy of tissue. Using the proposed artefact quantification on such dataset corresponds in scoring the artefacts but also scoring the signal variations due to anisotropy. Impact of anisotropy on artefact scoring using an ex-vivo heart with 192 directions was given in Appendix A.

This methodology was used in chapter 7 to measure artefact scoring for different diffusion preparation schemes. Artefact scores were then compared to physiological motion indicators like cardiac strain, breathing phase in an attempt to quantify the contributions of each native cause of motion artefact.

6.5. Valorization & Deliverables

Developments exposed in this chapter were realized into Matlab. Old and novel reconstruction methods were implemented in an automatic pipeline for this work including:

- Reading and unmosaic of Siemens Diffusion Dicom.
- Selection of reference for registration.
- PCATMIP, Average and Average + Cutoff methods.
- ADC model.
- IVIM model and fitting.
- DTI model with tractography and helix angle maps (both currently not used in this work).
- Calculation of Artefact maps
- Calculation of Co-Registration Index Maps.

The software for fiber visualization used in figure 4.3 was realized using QT and VTK in C++. The development of a plugin for the Osirix software was also started including all steps of the proposed reconstruction pipeline.

7. Evaluation of diffusion encoding scheme in free breathing conditions

As already discussed in chapter 4.6 an approach to handle signal attenuation caused by cardiac motion is to design higher-order motion compensated gradient waveforms for diffusion encoding scheme. These scheme have been proposed as part of spin echo sequence for DWI in human (Nakamura *et al.*, 2014; C. T. Stoeck *et al.*, 2015) and rat (Welsh *et al.*, 2015) in systole and diastole, but also combined with balanced steady-state free precession sequence (Nguyen *et al.*, 2014).

This kind of diffusion preparation have been proposed in late 2014 and early 2015 (in the last years of this thesis) and were not available when the first development of slice following were proposed. The combination of these diffusion preparations and the slice following technique presented in Chapter 4, could be an efficient approach to perform CDWI in patients. However as these schemes impose long duration, the conditions of realization of free-breathing acquisition could not be met and need to be evaluated.

In this chapter we first proposed a description of motion compensated gradient waveforms and specific issues for free breathing applications. Comparisons of all diffusion encoding preparation were realized through simulation, ex-vivo and finally in–vivo measurements. As it was done previously developments and developed method related to this final part of this work will be detailed.

7.1. Second order motion compensation diffusion encoding scheme

Motion compensated gradient waveforms are based on the Gradient Moment Nulling theory (Pipe and Chenevert, 1991) which was originally developed to achieved blood flow motion compensation. The principle is based on the Taylor expansion of the motion occurring during encoding.

Taking back the equation 4.33, describing the phase accumulation imposes by a moving object following a trajectory *x(t)* in the direction of gradient application:

$$\phi(t) = \gamma \int_0^t G(u)x(u)\partial u \qquad 7.1$$

If the movement of *x(t)* is linear it can be decomposed in Taylor series expansion:

$$x(t) = x_0 + v_0 t + \frac{a_0 t^2}{3} + \ldots \qquad 7.2$$

Where x_0 is the position, v_0 the velocity and a_0 the acceleration at the initial time. If we introduce 7.2 into 7.1, the Taylor Expansion of $\phi(t)$ can be rewritten as:

$$\phi(t) = \gamma \int_0^t G(u)(x_0 + v_0 u + \frac{a_0 u^2}{2} + \ldots)\partial u \qquad 7.3$$

This can ultimately be decomposed in the following gradient moment expansion:

$$\phi(t) = \gamma m_0(t)x_0 + \gamma m_1(t)v_0 + \frac{\gamma}{2} m_2(t)a_0 \qquad 7.4$$

Where the nth gradient moment is:

$$m_n(t) = \int_0^t G(u)u^n \partial u \qquad 7.5$$

Imposing a specific moment expansion equal to zero can be used to design motion compensation gradient waveform. By construction, encoding schemes which compensate the moment of order nth also compensate the moments or inferior order like nth-1 nth-2…. Example of 0, 1st and 2nd order in presence of linear motion was given in Figure 7.171.

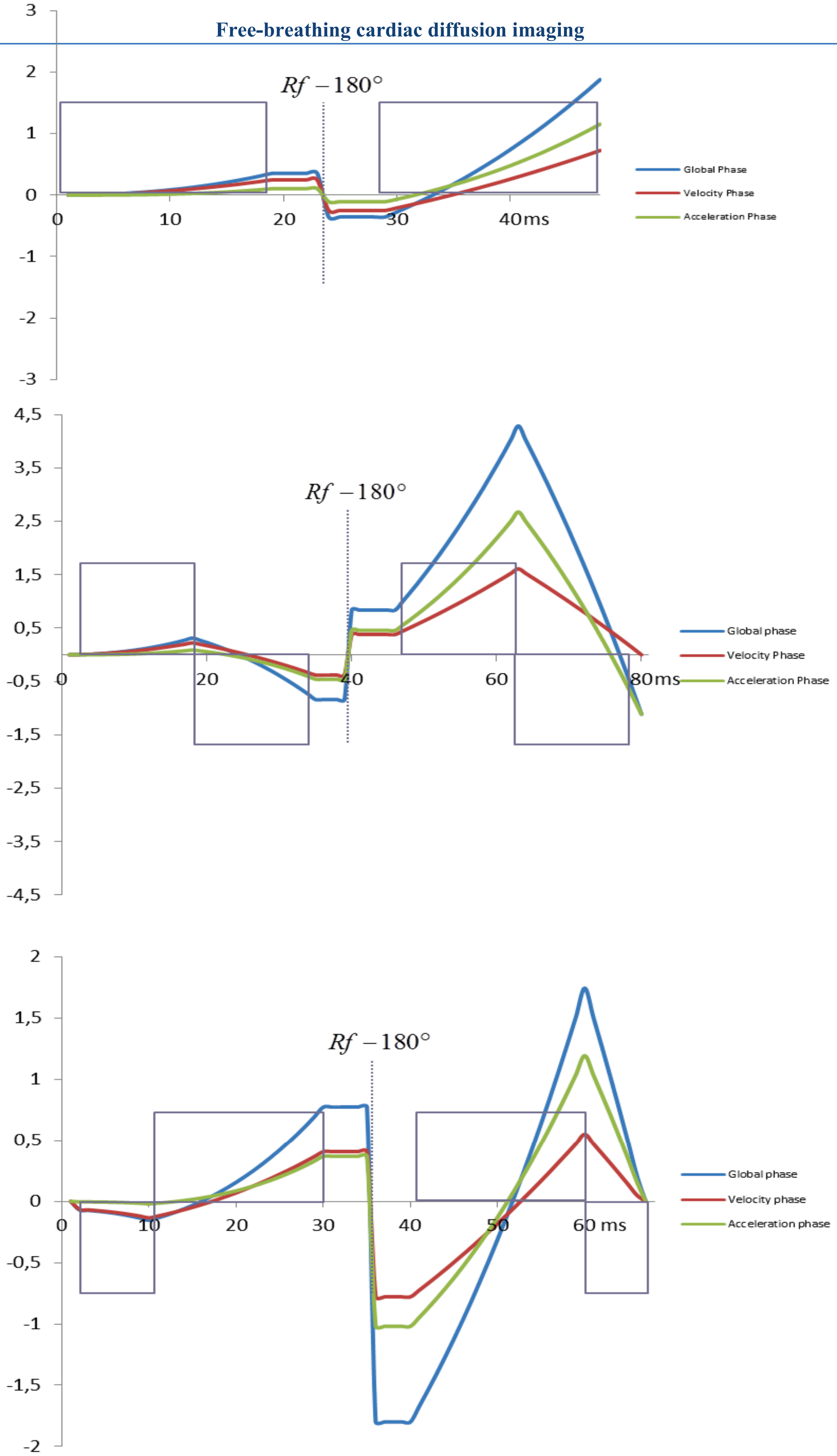

Figure 7.1: Chronogram of diffusion preparation and associate phase diagram simulated for a moving object with uniform acceleration and velocity. From top to bottom: 0, 1st and 2nd motion compensation diffusion encoding scheme;

At a first guess, the applicability of motion compensated encoding scheme to the measure of diffusion can open questions. Indeed as seen in chapter 4, the macroscopic diffusion print in the MR signal is first of all composed by the microscopic motion of particles. Yet the assumption behind the construction of such motion compensated scheme is that the motion is linear during all the application of the gradient, which means that this motion has the same comportment during all the duration of the diffusion encoding scheme. We know that this criterion is not respected by diffusion theory which is the result of Brownian motion. Nevertheless as express in the PDF, it is still possible that few particles have motion behavior close to linear. This effect is of course too minor to be seen or measured by our MR experiment and the motion compensated encoding scheme sensitize the NMR signal to diffusion so far like non motion compensated scheme.

However such limits have a growing importance in the case of measurement of pseudo diffusion like in the IVIM model. A consideration of usage of the IVIM model is that the sequence duration is longer than the ratio between mean capillary segment length l and the speed of blood flow v. If this condition is respected, blood flow has a global none linear motion and thus motion compensated encoding scheme should not play a role. However, differences between non compensated and compensated scheme have been simulated and demonstrated in the work of Wetscherek (Wetscherek *et al.*, 2015) for the diffusion experiment in the liver and pancreas. These results strongly indicate that perfusion effect was handled very differently by motion compensated gradient waveforms.

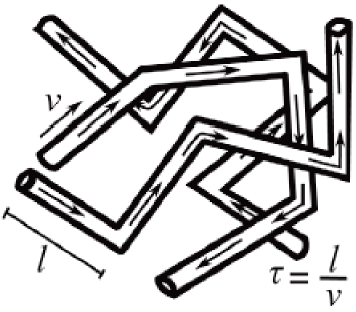

(Lombaert et al., 2012)

In the case of free breathing acquisitions, motion compensated encoding schemes will offer additional advantages. Indeed subsequent phase shifting induced by respiratory intra-scan motion should be compensated in the same time as cardiac motion. However the condition behind the utilization of slice following was that the encoding scheme should be the shortest possible to avoid exposure to slow breathing intra-scan motion, as already exposed in chapter 5.2. Using AMC preparation, for a given b-value the minimum possible TE that can be reached when using these preparations is higher than the minimal TE offered by Monopolar preparation as shown in Figure 7.2.

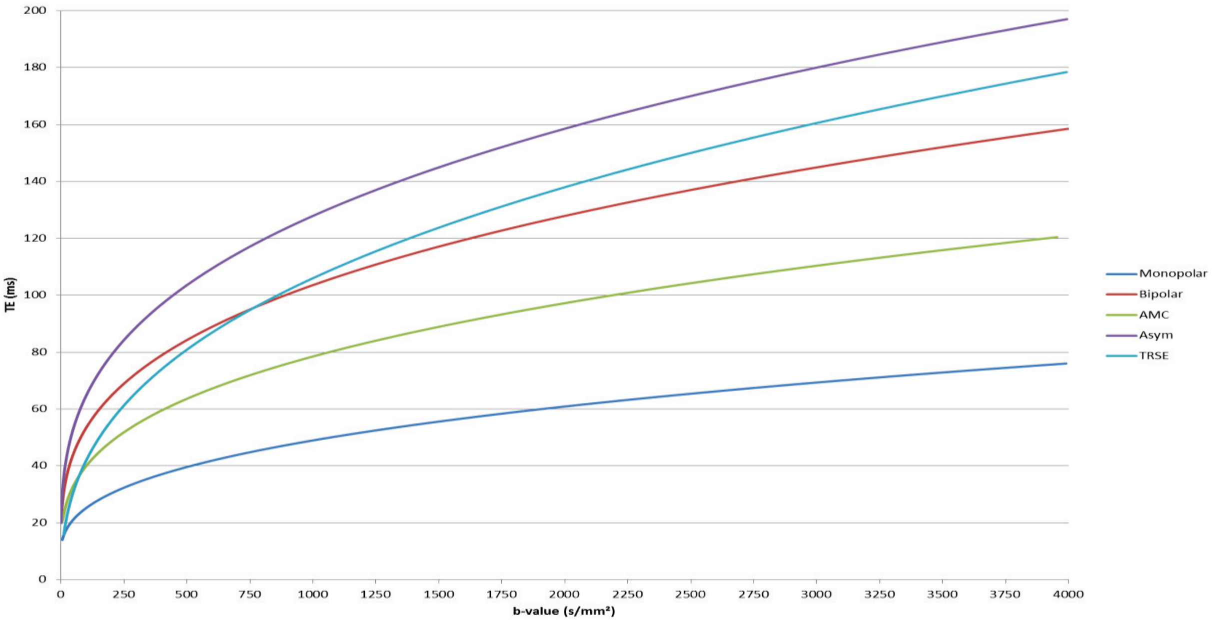

Figure 7.2: TE as a function of b-value for the 5 encoding schemes evaluated in this chapter, G was fixed at 40mT/m and the 180°RF duration at 10ms.

In other words, the AMC scheme could at first sight and without the highlighting from the mathematical approach sounds as a paradoxical approach since it aims to compensate the linear motion by increasing the sequence encoding time i.e. enlarging the exposure window to all kind of motion. Nevertheless the superiority of 2nd Order motion compensated scheme (AMC) against 1rst Order and STEAM sequence has been very recently reported by von Deuster (von Deuster *et al.*, 2015) and co-workers but these works were realized under breath-hold and the AMC preparation was not yet evaluated in the case a free-breathing acquisition. In the following section, we thus propose to evaluate the impact of the cardiac and breathing motion independently of diffusion encoding scheme.

7.2.Simulation of diffusion preparation

As mentioned earlier we engaged a collaboration with the Camille Jourdan Institute of mathematic located in Lyon 1 university, as part of Imène Mekkaoui's thesis. The aim of this study is to propose a numerical simulation to predict the sensitivity of the diffusion signal to cardiac motion under the influence of diffusion gradients. The work realized in the study concern only the physics part (diffusion preparation, physics law,..), all the mathematical developments belong to Imène Mekkaoui's thesis and thus simulation framework and underlying mathematics are only summarized here.

The proposed mathematical model is based on the Bloch-Torrey equation, and takes into account deformations according to the laws of continuum mechanics. The Bloch-Torrey equation is usually used to describe the magnetization in stationary tissues. In moving tissues, the Bloch-Torrey equation is modified in the following way: the diffusion tensor is affected by the deformation, advection term involving the velocity of the displacement is added and the zero order terms are increased by the divergence of the velocity. The phase term of the modified Bloch-Torrey equation is also changed according to the motion:

$$\begin{aligned} &\partial_t M_{xy}(x,t) - div(\mathrm{F}^{-1}(x,t)\mathrm{D}(x)(\mathrm{F}^{-1}(x,t))^t \nabla M_{xy}(x,t)) \\ &+\mathrm{v}(x,t).\nabla M_{xy}(x,t) + (i\gamma\varphi(x,t).G(t) + \frac{1}{T_2} + div(v(v,t)))M_{xy}(x,t) = 0 \text{ in } \Omega \times [0,T] \end{aligned} \qquad 7.6$$

$$M_{xy}(x,t) = 0 \text{ on } \partial\Omega \times [0,T],\ M_{xy}(x,0) = M_{xy}^0 \text{ on } \Omega \times \{0\}. \qquad 7.7$$

The initial condition is M^0_{xy} the thermal equilibrium magnetization, φ is the deformation field which is given, in our case, by an analytical 2D cardiac deformation model [1], $F(x,t)=D\varphi(x,t)$ is the Jacobian matrix of φ and v is the velocity field of the displacement. Dirichlet homogeneous boundary conditions were imposed on the computational domain omega which is represented by a ring mimicking the shape of 2D-short axis of the left ventricle. This mathematical model was solved by coupling a finite element discretization in space with Euler implicit discretization in time. Different diffusion encoding schemes are considered: Monopolar, Bipolar, Asymetric, TRSE, AMC, STEAM and STEAM bipolar.

Magnitude intensity images are simulated for different phases of the cardiac cycle, and ADC error is computed in each case.

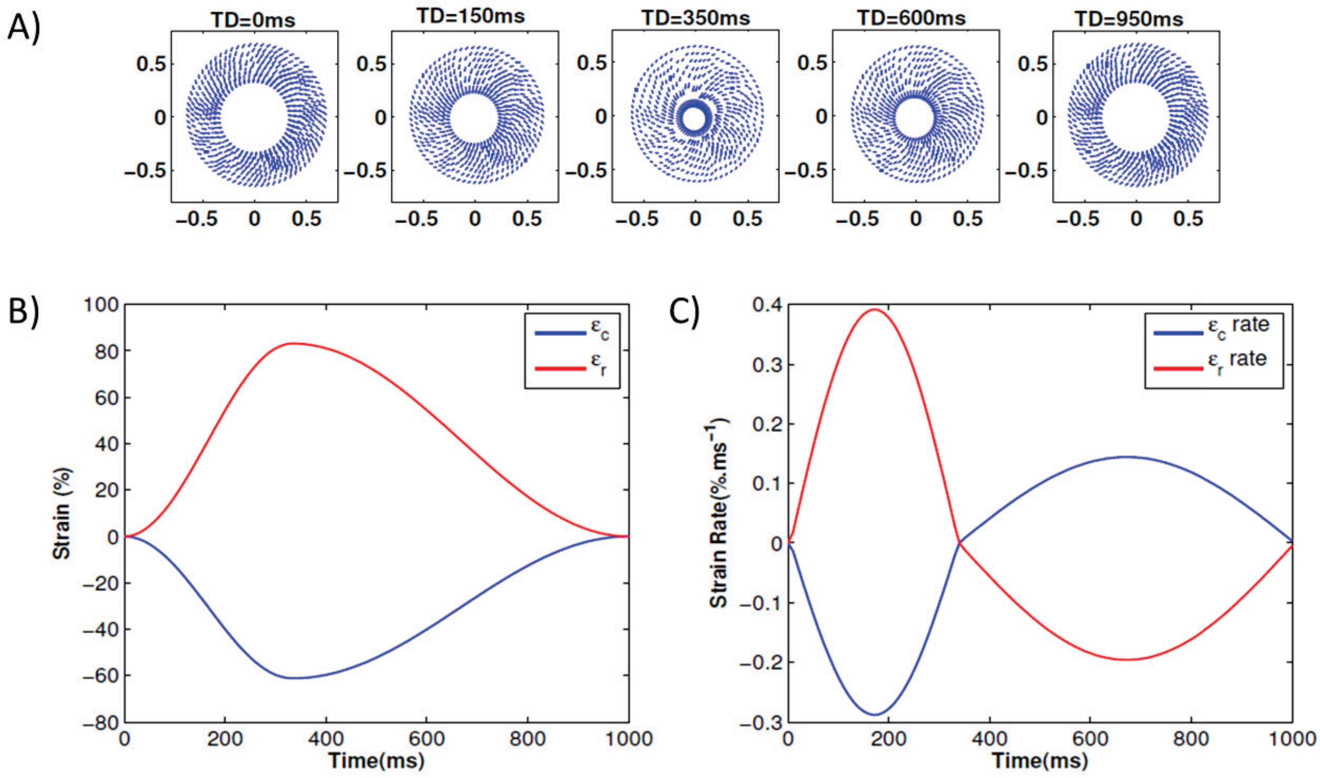

Figure 7.3: A) Displacement field for five different times within the cardiac cycle. Bottom: Simulated global circumferential (blue) and radial (red) strain (B) and strain rate (C) used for simulation. Tsystole= 333ms, Tdiastole=666ms

Simulated strain and strain rate are given in Figure 7.3B and Figure 7.3C. Figure 7.4A showsthe magnitude images along the cardiac cycle for the simulated cardiac deformation given in Figure 7.4B. The resulting global signal intensity and relative error on the ADC estimates are presented in Figure 7.4B and Figure 7.4C, respectively. Our numerical simulations show that motion sensitivity of the diffusion sequence is reduced by using either spin echo AMC diffusion gradients or STEAM. The latter being insensitive to bulk motion, while the first one is unaffected by strain. Our numerical model identifies the “sweet spots” located at end-systole and end-diastole for STEAM sequence, but also the “sweetest cardiac phase” of spin echo sequence located at the time points of null strain-rate, on which the diffusion is unaffected by the strain or cardiac deformation.

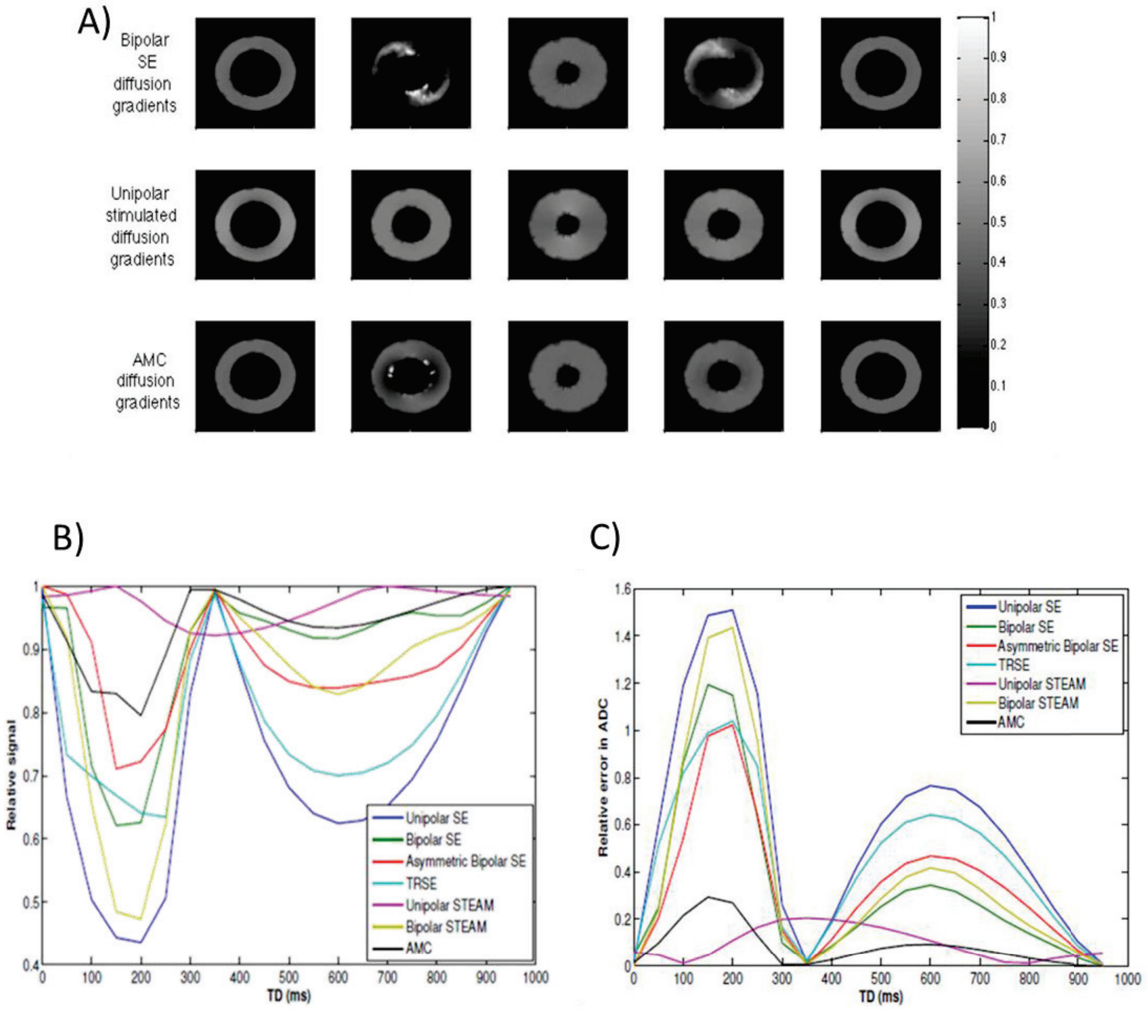

Figure 7.4: A) Magnitude intensity images through the cardiac cycle for three of the seven tested diffusion gradient schemes. B) Global signal intensity over the cardiac cycle and C) corresponding relative ADC error.

7.3. Bench evaluation of all methods with slice-following method on a moving phantom

In order to evaluate the effect of intra-scan motion on the diffusion measurement, we propose measurements on a phantom with different diffusion components in a setup that mimics the breathing motion. Experiments were performed in collaboration with the Centre d'Imagerie BioMedical (CIBM) and Center for cardiovascular Magnetic Resonance Research, University of Lausanne, Switzerland. The goal of this study was to compare the five spin echo diffusion encoding schemes presented in chapter 4 on the same gel phantom with and without pure linear motion.

7.3.1. Method

Two sessions of experiments were conducted. In a first session the phantom was composed of 12 tubes of agarose gel with different sucrose and glucose concentrations.

For the second session, the phantom was reduced to 4 tubes of agarose gel with different sucrose concentration immersed in a box of water gel. Tubes were prepared as follow: De-ionize water was mixed with 2% of agarose at room temperature and warmed in a microwave until the mixture became translucent. The resultant liquid was centrifuged in 4 tubes of 50mL with 4 different sucrose concentrations (0, 5, 10 and 15%). After a resting day, tubes were immersed in a compact gel prepared with a mix of water and ***GelMax***® solution. The whole phantom was placed in a trolley (Figure 7.5) made in Lausanne and ensuring a controlled translation following the Z axis of the scanner using a step by step motor (Huber *et al.*, 2000). The motion results in a sinusoidal periodic translation of 4cm amplitude with a 0.25 Hz frequency.

Images were acquired on site at CIBM using a research MAGNETOM Prisma 3T scanner (Siemens Healthcare, Erlangen, Germany) providing a maximum gradient strength of 80 mT/m, with two 6-channel body matrix coil and 9 channels from the 24-channel spine coil. In this work, SE-EPI sequence with Monopolar (Stejkal Tanner), Asymetric, Bipolar, TRSE and AMC preparation was used. DW images were acquired with a 128 × 80 pixel matrix, rectangular FoV of 350 × 220 mm², and parallel imaging (GRAPPA factor 2, 24 external reference lines). Five interleaved slices of 6 mm thick were obtained with an in-plane resolution of 2.7 × 2.7 mm^2 interpolated in-plane to 1.35 x 1.35 mm^2, with a 2442 Hz/pixel bandwidth. Six diffusion directions with b-values of 0, 25, 50, 75, 100, 150, 200, 300, 400 s/mm^2 were acquired with 3 average. TR was imposed to 5s and TE was equal to 38, 54, 62ms for the Monopolar, TRSE and AMC diffusion encoding scheme, respectively. Slice following method with a tracking factor equal to 1 was used to minimize the in-plane motion as well as the MOCO algorithm.

For the ADC modeling, directions of each b-value were sum in a Trace image and used in the least scare fit for extraction of global coefficient of diffusion D which was compared with and without motion.

For the DTI modeling, MD and FA was given for each b-value and compared with and without motion.

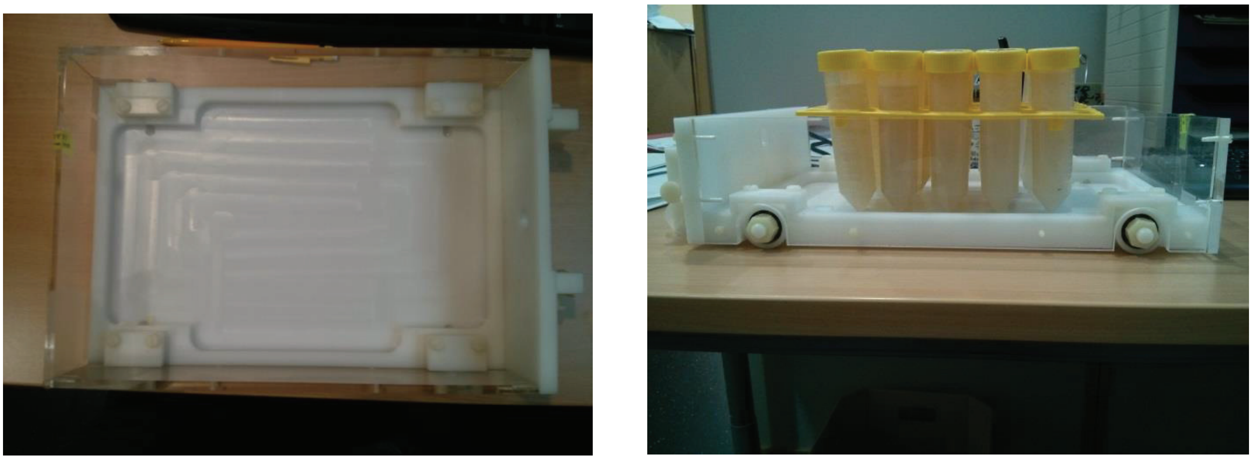

Figure 7.5: Trolley and phantom setup used in this study.

7.3.2. Results

Artefacts

As shown in Figure 7.6, similar artefacts were present in the image of the Asymetric and Bipolar encoding scheme. The number and the strength of oscillation increase with the b-value and in presence of motion. Since all the data corresponding to schemes were corrupted, we excluded them from the study.

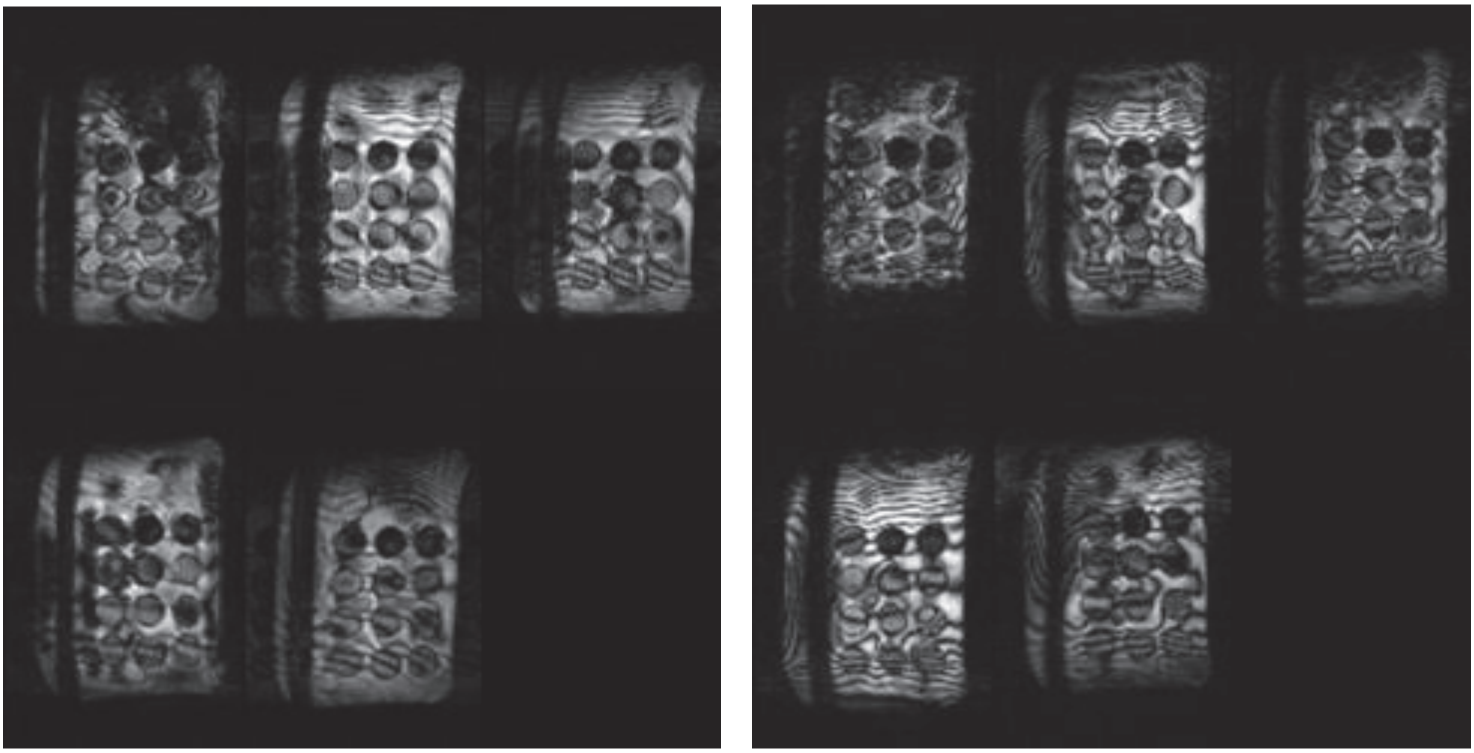

Figure 7.6: Images obtained at b-value = 200 s/mm² for the Asymmetric (left) and Bipolar (right) encoding scheme.

ADC model

For the three diffusion preparations an attenuation of signal is present in the curve with motion in comparison to curve with no motion. A significant decay of the curves with motion is noticed for AMC and TRSE scheme as show on Figure 7.7.

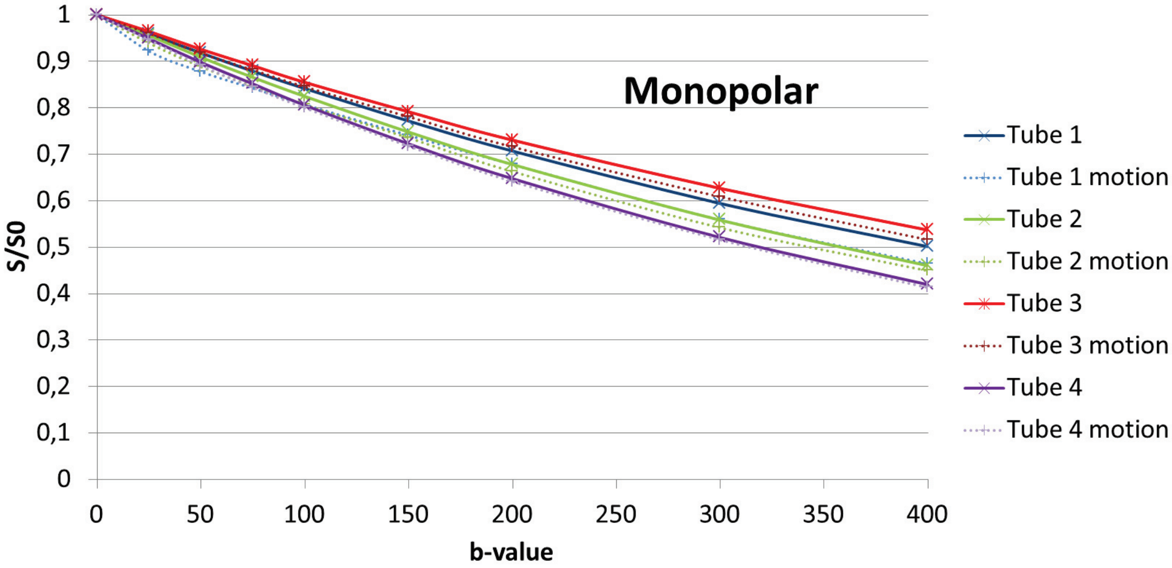

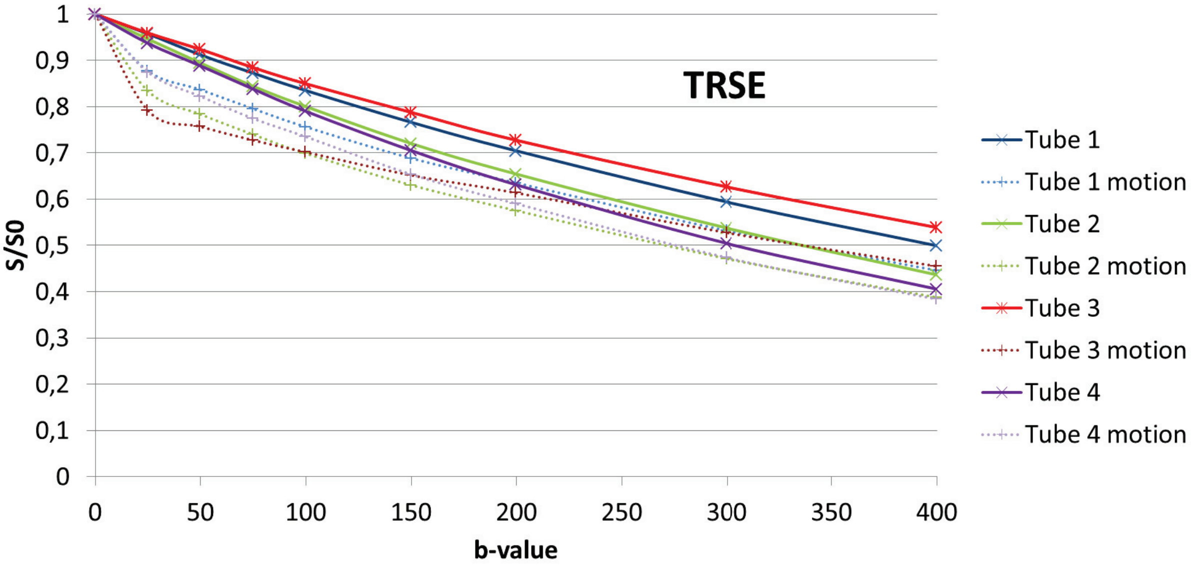

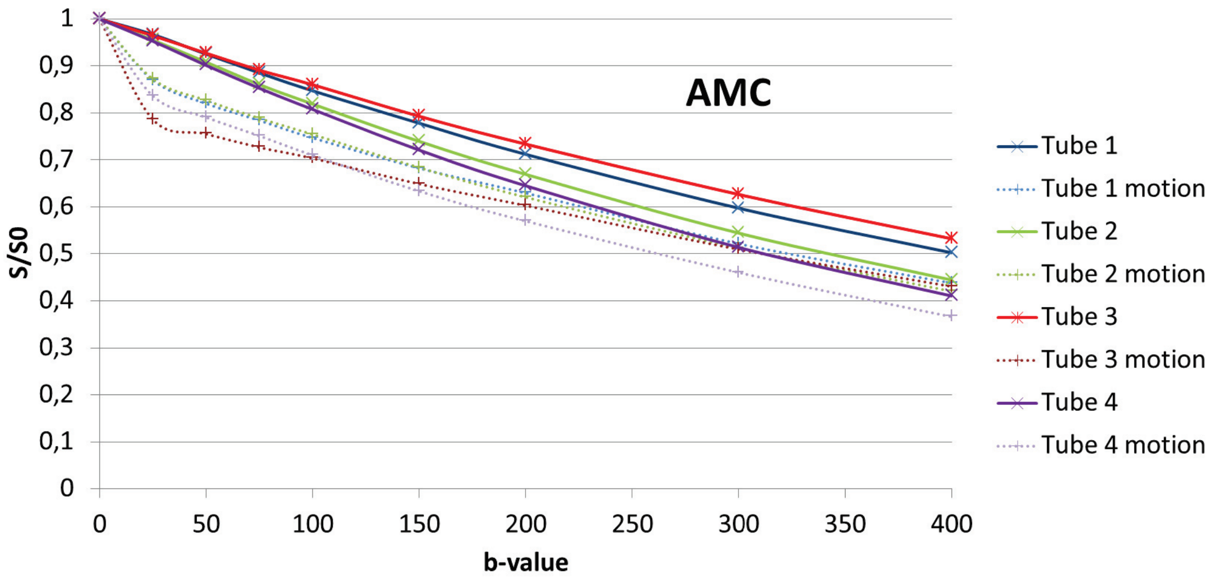

Figure 7.7: Signal curved obtained for each tube, each diffusion preparation for cases with and without motion as a function of b-value.

No difference between preparations was found on ADC value in cases without motion, as show in Table 7-1. The mean errors for all the tubes, calculated using cases without motion as reference, were 2.47, 2.75, 6.66% for the Monopolar, the TRSE and the AMC, respectively.

	ADC(mm²/s)	Monopolar	TRSE	AMC
Tube 1 (10% sucrose)	No motion	0.001762	0.001727	0.001745
	Motion	0.001819	0.001811	0.001821
Tube 2 (5% sucrose)	No motion	0.001958	0.00206	0.00204
	Motion	0.002016	0.002048	0.001934
Tube 3 (15% sucrose)	No Motion	0.01575	0.001545	0.001576
	Motion	0.001674	0.001456	0.001584
Tube 4 (0% sucrose)	No Motion	0.002202	0.00225	0.002243
	Motion	0.002244	0.002208	0.002191

Table 7-1 : ADC Global result for the Monopolar, TRSE and AMC preparation.

DTI model

For the analysis using the DTI model, the diffusion parameter *MD* and *FA* were calculated for each b-value. The FA obtained without motion was considerably higher when the b-value is low even while MD is almost identical (Results for FA and MD for all b-values, all tubes and all preparation are given in Annex B).

The Figure 7.8 and Figure 7.9 show the difference of MD and FA between cases with motion and cases without motion as a function of b-value. For the MD parameter the differences between cases with motion and cases without motion are more important at low b-value but decrease while the b-value increase. The same behavior was notice for all diffusion preparations but differences were less important for the Monopolar scheme at low b-value.

For all schemes the FA difference remained minimal for the b-value 25s/mm^2 and increased until the b-value 75 or 100s/mm^2, and then linearly decreased. Amplitude of these variations was less important for the AMC and TRSE scheme in comparison of the Monopolar.

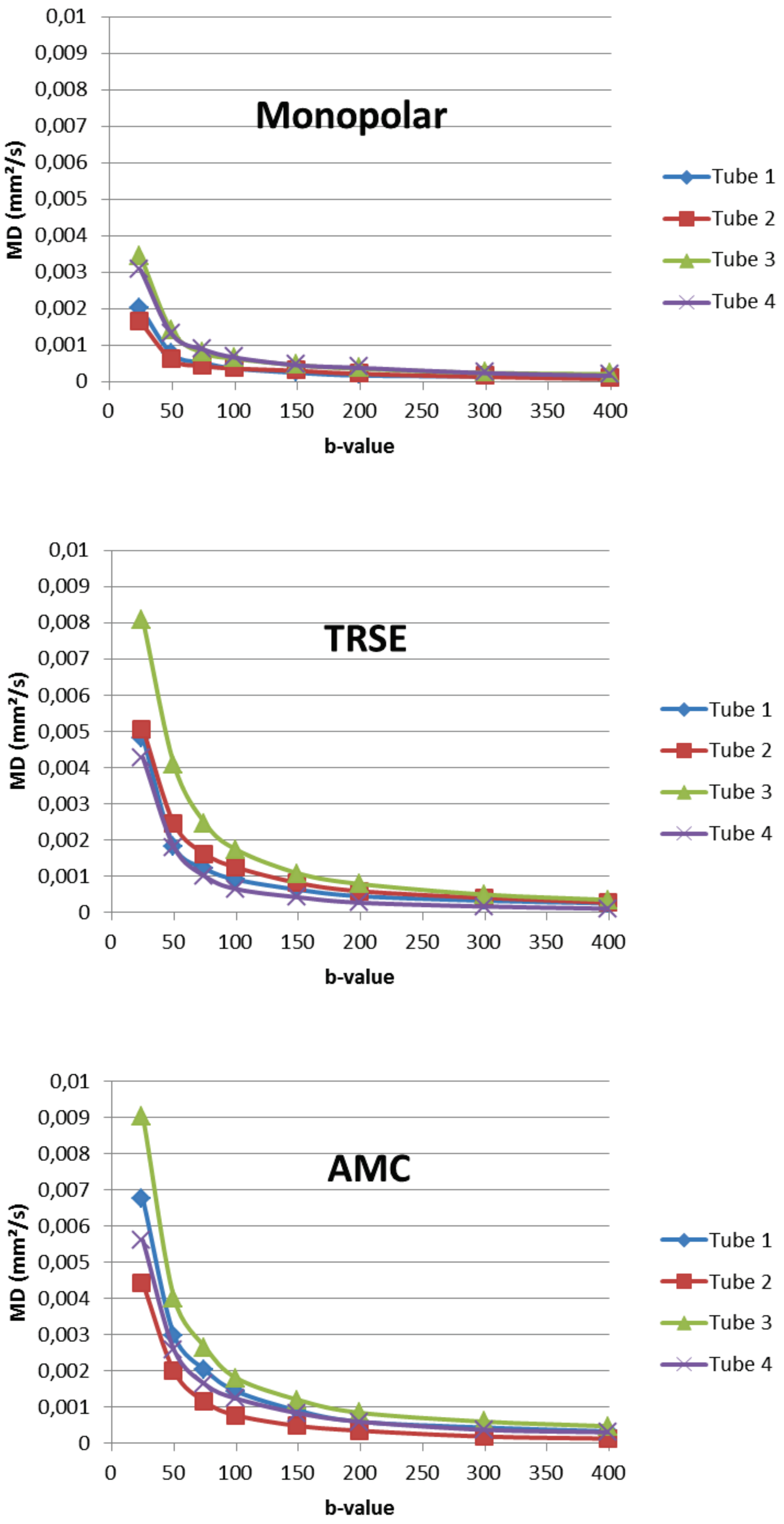

Figure 7.8: Difference of MD between cases with and without motion

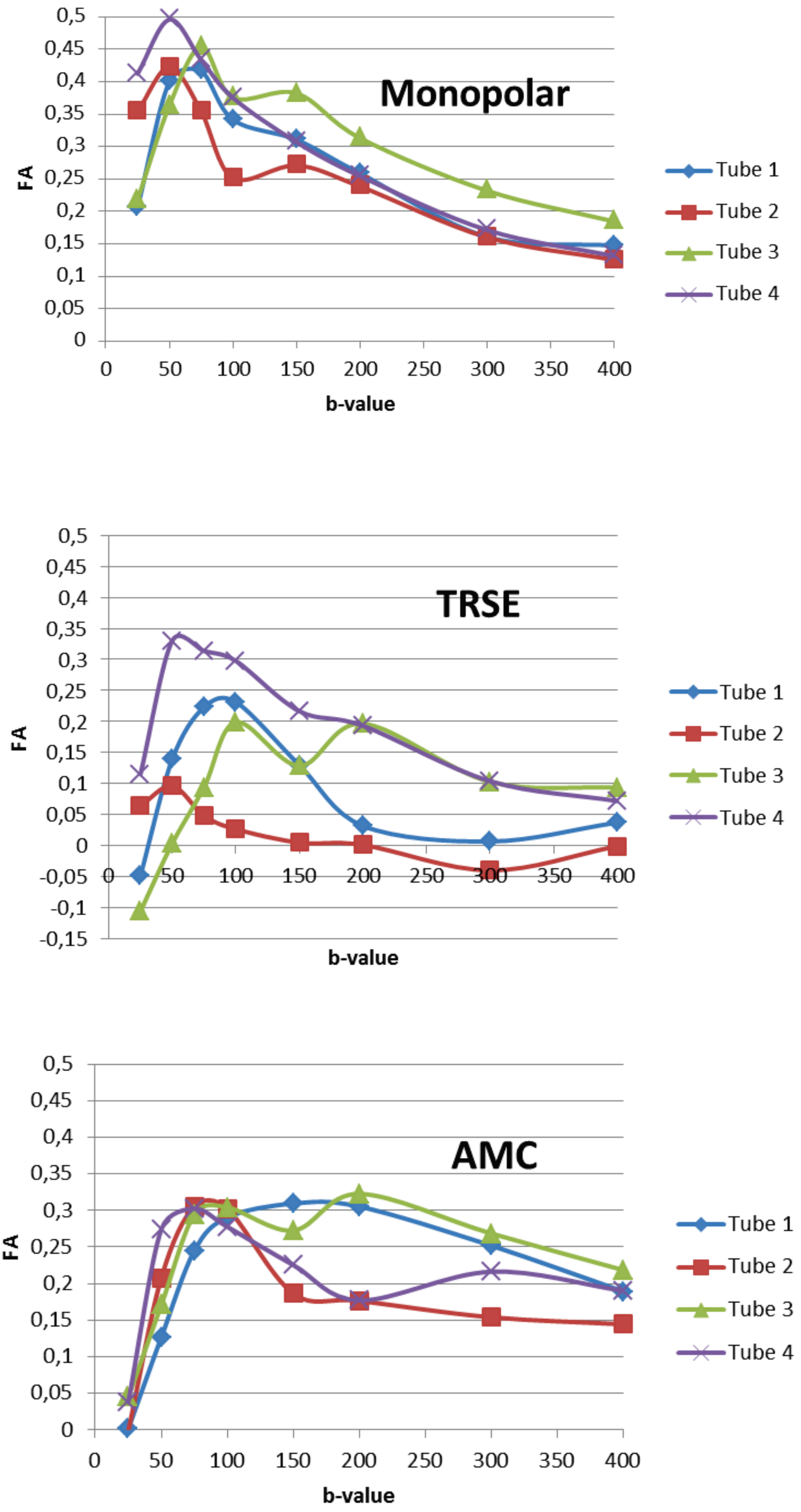

Figure 7.9: Difference of FA between cases with and without motion.

7.3.3. Discussion

In this study we analyzed the impact of a respiratory-like motion (simulated as periodic sinusoidal motion) on diffusion encoding scheme on a phantom composed of 4 tube of agarose with different coefficient of diffusion. The goal was to characterize the potential impact of the respiratory motion independently of cardiac motion which was evaluated on the previous chapter. The chosen periodic movement was slightly higher than a common respiratory motion and represents a sort of worst acquisition scenario. Three diffusion encoding schemes were finally evaluated with and without motion.

In the preliminary session of experiment some tubes were not homogenous due to a bad chemical reaction between agarose gel and glucose, also the high concentration of sucrose (>20%) saturated the mixture. Consequently in the second session only 4 tubes of sucrose were screen. Also in this first session, two diffusion encoding schemes, Asymmetric and Bipolar have given extremely corrupt images by artefacts that could not be used. Cause of these artefacts is not yet determined but our first hypothesis was that the direct alternation of positive and negative gradient of same area specific to these schemes might be the cause. Taking in account the strength of gradient used here, this could also be related to eddy currents or magnetic field inhomogeneity.

For the 3 remaining schemes, the ADC analysis clearly shown that the longer scheme, AMC, give higher errors than the Monopolar and TRSE which have similar error about 2.5%. At first guess, it might be appealing to consider that the balance between scheme duration and motion compensation is in favor of the shorter durations. Moreover TRSE encoding which has no motion compensation has lower result than a 2nd order motion compensated scheme even if the conditions of application of this latest are met (i.e. motion linearity).

Directional analysis through DTI model attested that motion affects particularly specific b-values. Indeed the MD difference between case without motion and case with motion shows that important errors are present at low b-value and that these errors decreased while the b-value increased. For all schemes and all tubes the same comportment was noticed but the amplitude of these errors are less important for the Monopolar scheme at low b-value.

FA measurements present the same kind of behavior but with a higher range of variation. First of all, the FA is considerably over-estimated at low b-value in the case without motion which results in almost null error in comparison on the case with motion. For b-value superior to 75s/mm², the FA difference decrease almost linearly while the b-value increase. However this time, the Monopolar encoding scheme shown higher error. The difference could be explained by the impact of motion on specific directions more pronounced on the case of Monopolar preparation.

Our bench study has demonstrated that the impact of periodic respiratory-like motion on diffusion measurement is b-value dependent with an almost identical behavior for all three diffusion encoding schemes evaluated here.

7.4.Evaluation on in-vivo measurements

In order to evaluate the combined effect of breathing and cardiac motion in real conditions, we then compared the Monopolar, TRSE and AMC diffusion encoding schemes performance on healthy volunteers in diastole. According to the literature AMC has been shown to enable systolic CDWI measurement, therefore our protocol also include an additional measurement of AMC in systole. The idea of this study is to compare the methods for diffusion encoding experimentally and compare it eventually to the results obtained by simulations. We also propose a fairly comparison while rejecting images disrupted by motion artefacts using the criterion defined in chapter 6.4. Within the same protocol, we also performed a strain measurement describing the heart cycle to analyze the link between cardiac motion and the ADC measurement. Finally breathing motion was also retrospectively analyzed by recording two navigators played before and after each images acquisition, the breathing phases stored were compared to errors measurement to extract eventual correlation with artefact presence.

7.4.1. Materials and Methods

Seven healthy volunteers were enrolled in this study, including 6 male and 1 female with a mean age of 30±10 years and a mean heart rate of 61±4 bpm. All subjects gave their written informed consent for this institutional board-approved study protocol.

Images were acquired on a clinical MAGNETOM Aera 1.5T scanner (Siemens Healthcare, Erlangen, Germany) providing a maximum gradient strength 45 mT/m, with a 6-channel body matrix coil and 9 channels from the 24-channel spine coil.

Before the DWI acquisitions, a 30 phases short-axis cine images were obtained in mid position for strain measurement.

In this work, SE-EPI sequence with Monopolar, TRSE and AMC preparation was used. DW images were acquired with a 128 × 80 pixel matrix, rectangular FoV of 350 × 220 mm², and parallel imaging (GRAPPA factor 2, 24 external reference lines). Five Double-oblique short-axis DW images slices of 6 mm thick were obtained with an in-plane resolution of 2.7 × 2.7 mm² interpolated in-plane to 1.35 x 1.35 mm², with a 2442 Hz/pixel bandwidth. Six diffusion directions were acquired with a main b-value of 200s/mm² and a reference b-value of 5s/mm².

TR~=5s (number of slices x RR-interval and for a heart rate equal to 60 bpm), TE was equal to 38, 54, 62ms for the Monopolar, TRSE and AMC diffusion encoding scheme, respectively. No averaging was performed, but 5 TDs shifted every 10ms were acquired for PCATMIP reconstruction. Monopolar, TRSE were acquired in diastole and AMC in diastole and systole, both in the most quiescent cardiac phases where the motion is known to be minimal from the cine images. A cross-pair navigator deriving the top liver position was played before and after the measurement, only the information of the first navigator was used for breathing management by slice following approach; tracking factor was fixed to 0.6. Two complete dummy scans were performed on each slice to reach the magnetization steady state.

Artefact criteria were calculated using the equation 6.8 before PCATMIP reconstruction on the TDs stacks. These error maps were compared to the breathing phases extracted using the navigator information recorded before and after the acquisition measurement window.

For a fair comparison between encoding preparations, second artefact quantification was calculated on the direction stack after reconstruction by PCATMIP. This measure was used to perform a rejection in the ADC measurement. Myocardium wall was divided using AHA segmentation (Cerqueira *et al.*, 2002). For each segment the artefact quantification was compared to a fixed value 0.3, if the segment present an error higher than this value is was excluded from subsequent statistical analysis.

Strain curves were calculated using a feature tracking algorithm (CMR42, Circle) (Figure 7.10) on the cine acquisition and then interpolate linearly to a temporal resolution of 20ms. Strain values were calculated by summing the point of the strain curve corresponding to the acquisition windows including the TD shifting and the sequence duration. For example for the Monopolar preparation, the acquisition window corresponds to the sequence duration 38ms plus 50ms of TD shifting; if the acquisition was launched in diastole at an initial TD of 800ms, the points 750ms (the earliest launch of the sequence) to 838ms (latest time point reach by the sequence) from the strain curve are summed. Each strain measure was associated with a corresponding ADC for a given diffusion encoding scheme.

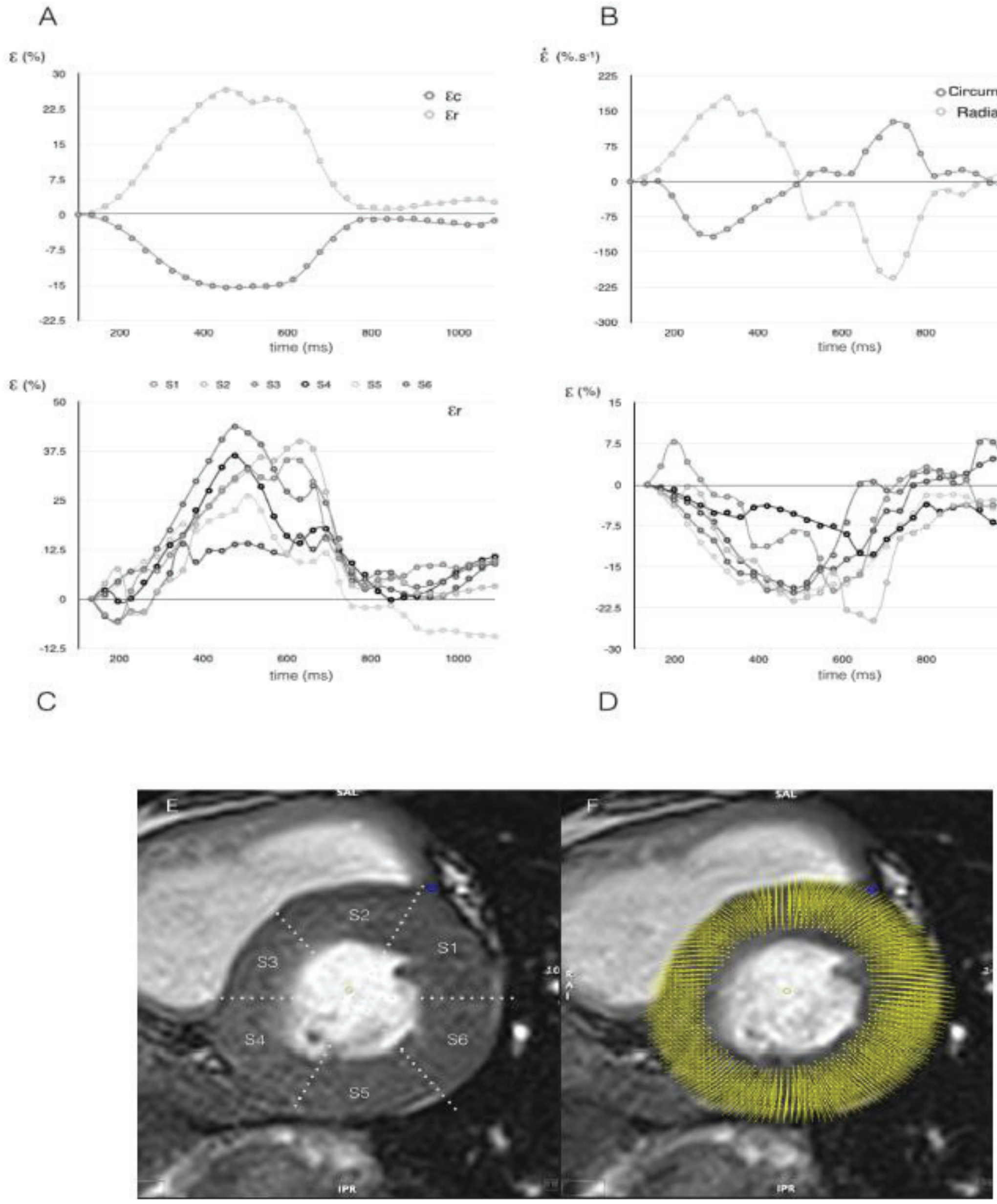

Figure 7.10: (A) Global radial strain (ε_r) and circumferential strain (ε_c) obtained in the myocardium of a normal volunteer using speckle tracking analysis (Circle Cvi42 Tissue Tracking prototype software). (B) Corresponding global radial strain rate ($\dot{\varepsilon}_r$) and circumferential strain rate ($\dot{\varepsilon}_c$). Regional radial strain(C) and circumferential strain (D) in all segments of the mid left ventricular slice shown in the T_2/T_1 (bSSFP) weighted systolic short axis image (E), and showing the important regional variations. (F) displacement map superimposed on the systolic bSSFP image shown in (E).

7.4.2. Results

Without Rejection

Global results for the entire myocardium (all slices, all segments) and for all volunteers are reported in Figure 7.11 for the 4 types of CDWI acquisitions. The mean ADC values ±SD for all volunteers are 2.71±9.3x10^{-3}, 3.13±9.3x10^{-3} mm²/s for Monopolar and TRSE encoding scheme respectively. In AMC case, lower values of ADC were measured, 1.94±1.3.x10^{-3} and 1.44±2.2.x10^{-3} for diastole and systole respectively.

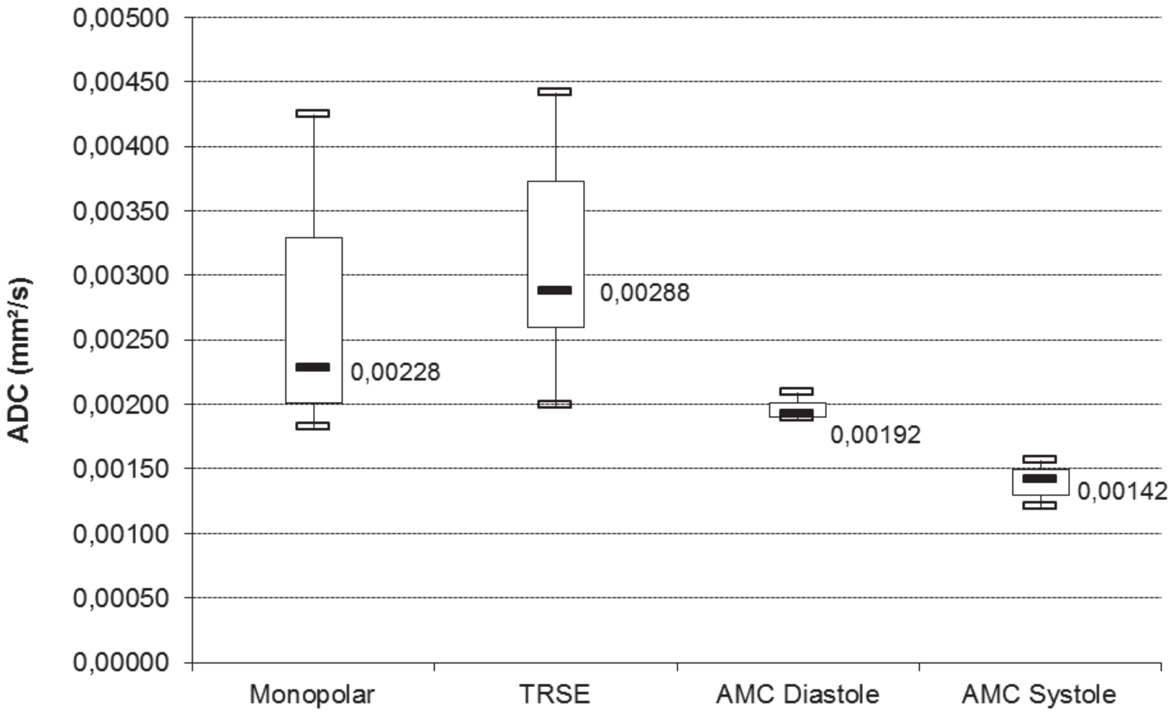

Figure 7.11: Whole heart ADC value obtained on 7 volunteers for the 4 acquisitions.

As shown in Figure 7.12 presenting the result of the artefact quantification, a higher number of artefacts were found in the Monopolar and TRSE dataset while only little for the two AMC cases. The red line displays the threshold value chosen to reject cardiac segment.

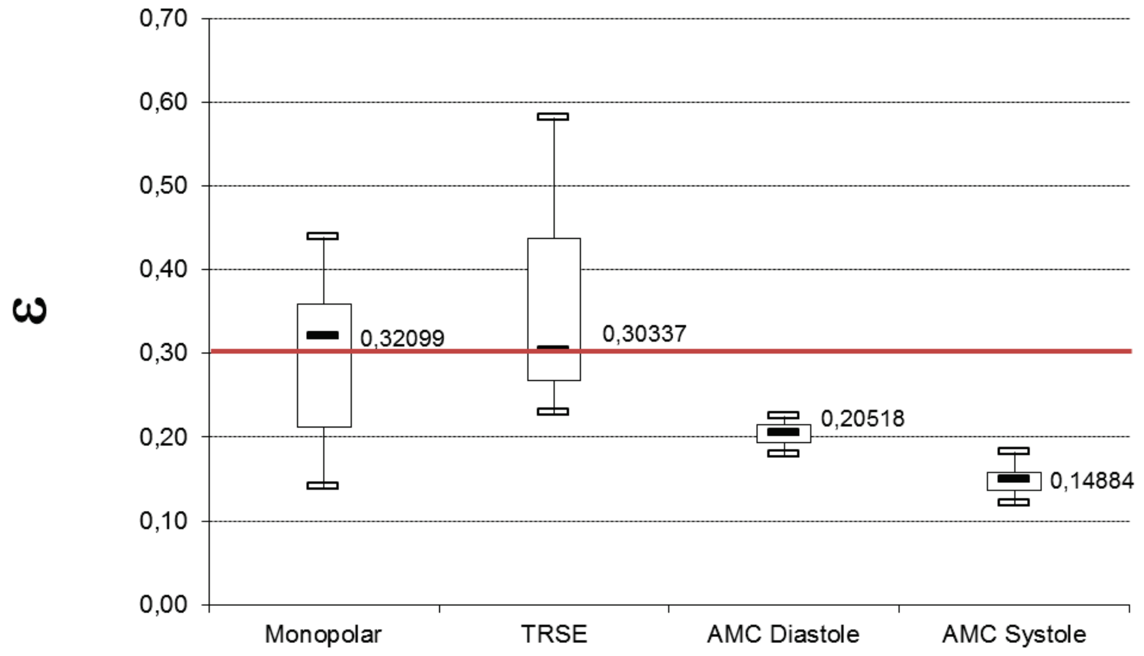

Figure 7.12: Whole heart artefact quantification (ε) obtained on 7 volunteers for the 4 acquisitions.

With Rejection

In a second step, using the artefact quantification presented above a threshold value was chosen to reject cardiac segment, represented by the red line displayed in Figure 7.12. Four acquisitions did not meet the criterion for all segments and all slices, 2 for both Monopolar and TRSE scheme; consequently they were completely removed from the analysis.

Using this criterion of rejection, global ADC measures were considerably reduced for the TRSE and Monopolar encoding scheme as shown in Figure 7.14. Individual ADC changed before and after rejection was displayed for all volunteers in the Figure 7.15.

For diastolic acquisitions, mean ADC values for Monopolar, AMC and TRSE were now similar $1.75 \pm 0.38 \times 10^{-3}$ mm²/s, $1.77 \pm 0.11 \times 10^{-3}$ and $1.83 \pm 0.1 \times 10^{-3}$ mm²/s, respectively. The ADC value obtained in systole remained almost unchanged to $1.41 \pm 0.18 \times 10^{-3}$ mm²/s.

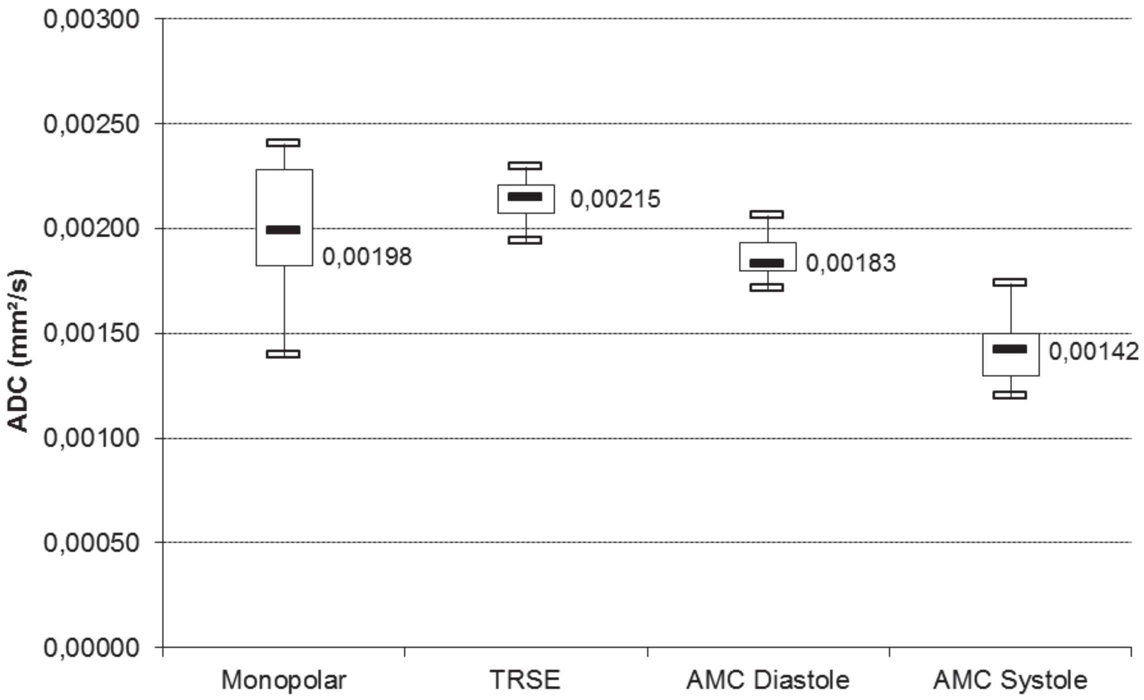

Figure 7.13: Whole heart ADC value obtained on 7 volunteers for the 4 acquisitions after rejection

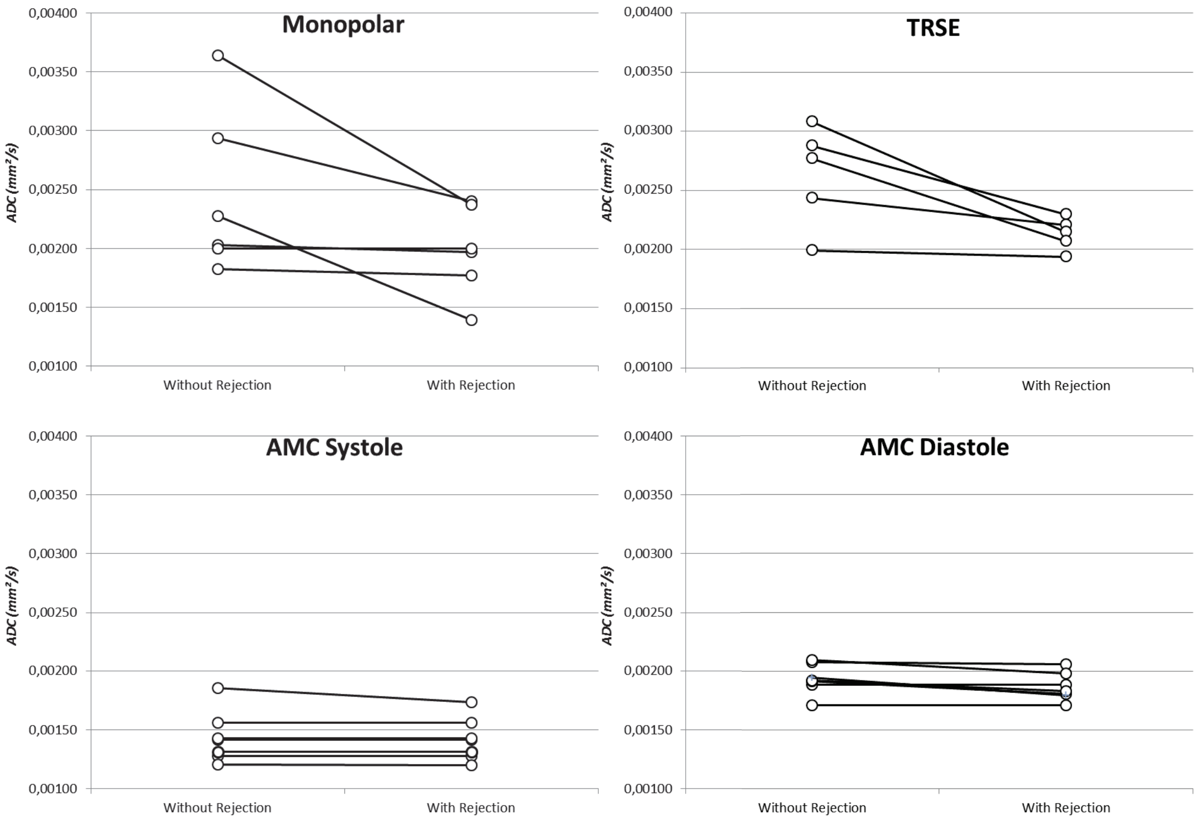

Figure 7.14: Variation of ADC for the 7 volunteers before and after rejection.

Correlation with cardiac phase and breathing phase

On the native measure (without rejection by thresholding), significant correlations were found between the cardiac strain and the artefact quantification for both Monopolar and TRSE diffusion preparation. Coefficient of correlation found were 0.93 and 0.8 for Monopolar and TRSE scheme respectively while low correlation was found for the AMC in systole, 0.66 and no correlation for AMC in diastole, 0.22. Figure 7.16 represent the strain measure as a function of artefact found.

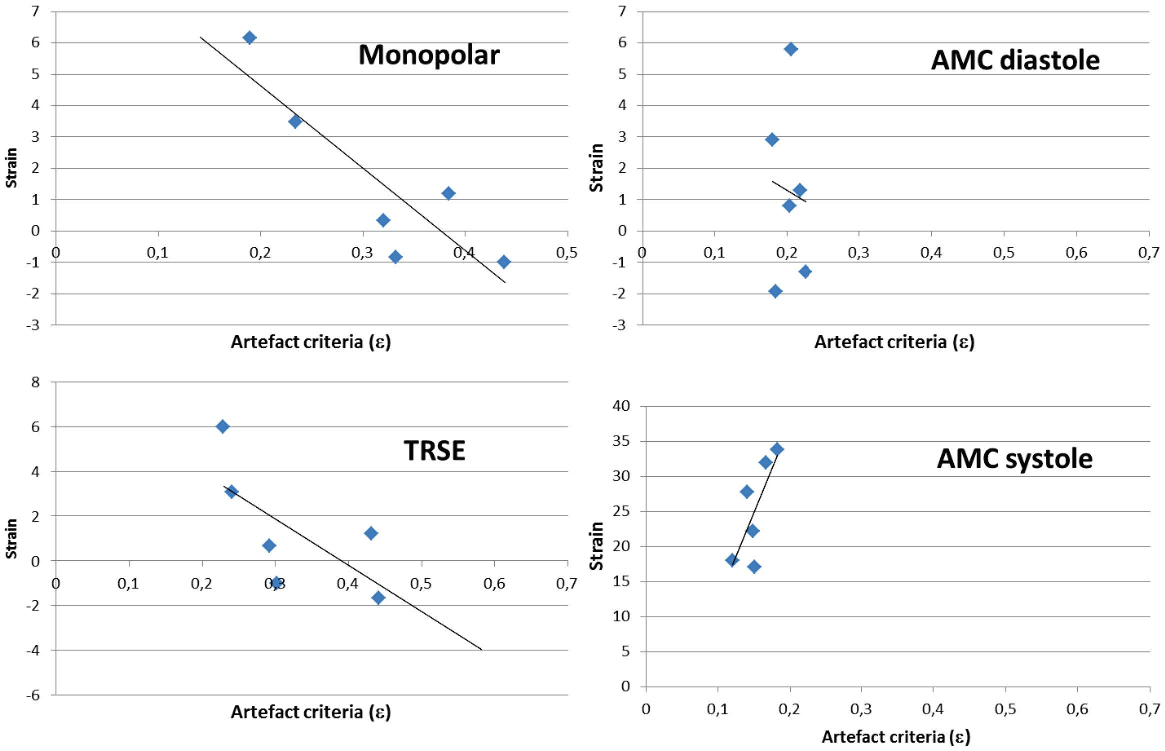

Figure 7.15: Strain measure as a function of artefact criteria.

For each volunteers, error maps were generated on the TDs stack before PCATMIP reconstruction. These maps were compared to their breathing phase measure before and after the sequence acquisition. For all volunteers any correlations were found between breathing phases and motion artefact.

7.4.3. Discussion

In-vivo analysis

Each sequence with different encoding schemes was acquired on 7 healthy volunteers with a protocol that was established to be compliant with clinical constraints. A b-value of 200s/mm² was chosen to provide the best compromise in term of TE and robustness to motion (see ex-vivo and bench study from the previous chapter) but also high enough to not be sensitive to perfusion effect as demonstrated in chapter 5.2.

The mean ADC values reported on all volunteers are higher than in literature for the Monopolar and TRSE encoding scheme. The artefact quantification proposed in chapter 6.4 revealed a high number of artefacts for these two schemes. A low score of artefacts found here for the AMC scheme, demonstrates its robustness against motion. These findings are coherent with the lower correlation found in-vivo between our score of motion corruption per technique and what one can consider as valuable index of deformation but also with previous publication. It is also worth noting, that a higher value was found between the Monopolar acquisition and the previous one of chapter 5.2 which can be explained by the difference between the two protocols. Indeed current protocol is faster than the previous DTI protocol, 2 min against 20min. The number of TDs acquired was reduced to 5 instead of 10 and so on the sliding windows was reduced from 100ms to 50ms. On this short window it is possible that all segments did not have a stable phase.

A fairly comparison measurement was then proposed, rejecting acquisition corrupted by motion. Using this methodology, ADC mean value obtained with the 3 diffusion preparations in diastole were about 1.7×10^{-3} mm²/s and so similar with the one obtained in the study of chapter 5.2. In term of pure diffusion measurement all scheme are equivalent as demonstrated in previous ex-vivo study.

The correlation found between strain measurements and our artefact quantification demonstrates that the increase of ADC value for Monopolar and TRSE encoding is caused by cardiac motion. However no correlation was found on our volunteers between motion artefact and breathing phase before or after the measurement. This means that respiratory intra-scan motion is small enough to not impact significantly the ADC measure which was an assumption behind the slice following method. Having said that, we still cannot exclude a remaining bias of the measure introduce by breathing.

Comparison of in vivo with the simulations and with the study on mobile phantom

The results obtained using simulations clearly show a lower sensibility of AMC sequence to cardiac motion than other preparations which is coherent with in-vivo results. However TRSE and Monopolar diffusion encoding scheme present equivalent result in-vivo where according to simulation, TRSE preparation should be less affected than Monopolar scheme.

As shown on Figure 7.5, the error introduced by cardiac motion using SE sequence follows the cardiac strain rate and is null at two phases in systole and diastole when the strain rate is null. In this study care was taken to place the acquisition in the cardiac cycle at sweetest phase according the cine acquisitions but Monopolar and TRSE scheme were still highly affected by cardiac motion. In comparison to the perfect strain and strain rate curves simulated, the curves obtained by speckle tracking are more contracted at begin of the diastolic phase (see Figure 7.16). And thus during the rest of diastolic phase the strain rate is almost null, and the heart observes a break. The acquisitions realized in diastole are placed here and should correspond to the diastolic quiescent phase.

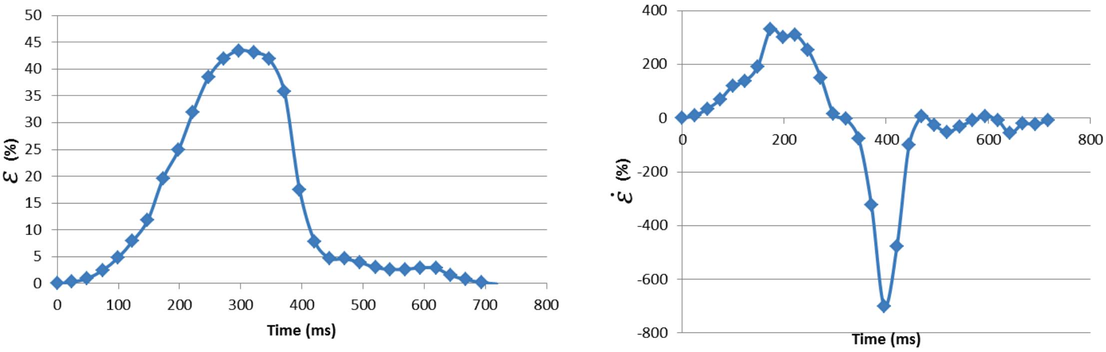

*Figure 7.16: Example of **global** cardiac strain (left) and strain rate curve obtained by speckle tracking on a volunteer.*

The motion impacting Monopolar and TRSE encoding scheme was thus not simulated and could correspond to bulk motion. Also the cardiac contraction is more complex than the global strain and strain rate simulated here. A regional study of the contraction coupled with a more realistic simulation of the cardiac cycle should be investigated, for example in simulating the strain curves obtained by speckle tracking and in comparing directly to the in-vivo result obtained.

7.5. Valorization and deliverables

Developments detailed in this chapter were realized in C++ on Siemens sequence development framework IDEA version VD13A/D. A customized diffusion single-shot echo planar imaging sequence was re-implemented for this work including previous options from the sequence developed in chapter 5 and all diffusion encoding scheme:

- Navigators for free breathing acquisition cross-pair
- Measure of the reference navigator during the dummy scans.
- Dummy scans handled after navigators for accurate steady state achievement.
- Monopolar, Asymetric, Bipolar, AMC, STEAM preparation mode.
- Specific calculation of TR and ECG management for cardiac triggering.
- Ability to save phase and magnitude image.
- Averaging capacity (concatenation frozen).
- Compatibility with parallel imaging (iPAT, separate ref scans, with slice followed separate scans feature).
- Multi-slices acquisitions.
- TD shifting for PCATMIP method, available for MDDW and Free mode only.
- Gradient reversal for Monopolar and TRSE scheme.
- Inner-volume: modification of the thickness and rotation of the 180RF pulse.
- b-value=0 with short gradient added in one direction for black blood achievement and reduced flow artefacts.

PART
III

Applications

8. Clinical application

Time reduction acquisition enabled by the slice following technique has allowed diffusion measurement respecting the clinical constraints. Two pre-clinical studies have been started during this thesis in collaboration with physicians of CHU nord of Saint Etienne.

The first study was realized on sportsman of ultra-endurance race in September 2014 during the “Tor des Géants” in Italy. Images were scan before, just after and 3 days after the race using the primary result of the slice following technique presented in chapter 5. A 6 min ADC diffusion-protocol was acquired on 50 trailers.

At the end of this thesis during the summer 2015, a second pre-clinical diffusion imaging study was realized on 40 patients with various pathologies with an acquisition protocol reduced to 2 min. Slice following and second order motion compensation scheme were used in both systolic and diastolic cardiac phases.

Analysis for both study were conducted by clinicians and are not yet published. In this chapter we propose to present the preliminary results of the ultra-trail study submitted to the SCMR congress 2016. For the clinical cases, 2 acquisitions presenting different clinical scenario were briefly described. It is worth noting that **any** clinical interpretations are given in the present chapter.

8.1. Ultra-Trail study

The developed slice following sequence was deployed in at a longitudinal study on ultra-trailer enrolled for the “Tor des géants” 2014 edition in Italy, the most extreme ultra long mountain marathon (330km length, 24000m climb). Ultra-endurance trail relates to any sporting event involving running longer than the traditional marathon length of 42.195 km (26.2 miles), on a large variety of landscapes (more or less positive elevation) and conditions (snow, or hot temperature), from flat to more hazardous and risky tracks. Ultra-endurance races need generally several days to be completed adding to the physical difficulty induced by the long and intensive exercise, the additional stress of sleeping privation. Ultra-trailers enrolled on extreme mountain-marathon can reach level of inflammation and fatigue that started to raise a very-understandable interest in the scientific community: ultra-marathon represents indeed a unique and outstanding reversible model to study acute consequences of extreme load and stress on human organs. Moreover, each subject being his own control, this model offers in addition a window to screen the inter-individual susceptibility to injuries and limits of the adaptive response. Therefore, added to the fact that the ability to run long distance played a role in the human evolution, the fascination itself suspired by the athletes performance, but also the strenuous demand from friends and colleagues ultra-trailers, were a very strong motivation to explore the underpinning physiology changes induced by ultra-long and extreme race using MRI, and especially at the level of the skeletal and cardiac muscles. Taken together the new capacity of MRI to derive quantitative index using T1, T2 and now diffusion mapping, cardiac MRI could offer a unique capacity to examine soft tissues and show the tissue inflammation. The demonstration that quantitative MRI can follow and characterize changes in the myocardial after exercise, but also during the recovery process would be a reassuring demonstration of the level of maturity of the methods. It is also of interest to see whether it could provide new information comparatively to T1 and T2 mapping.

The motivation is also high to see what additional information can MRI reveal from inflammation, microstructural and functional modifications caused by extreme loading conditions since previous MRI and Ultrasound (US) studies have shown the existence of functional and biochemical alterations in the myocardium after prolonged intense sport exercise, demonstrating transient diastolic dysfunction (Nottin *et al.*, 2009). Increase of blood biomarkers cTnT and NT-proBNP has been reported without focal necrosis identified by delayed enhancement imaging, which lets hypothesize a cytosolic dropping of biomarkers rather than destruction of myocytes (Hansen *et al.*, 2015)

The whole project of carrying an international study on a cohort of ultra-trailers before, immediately and at follow-up 3 days after the race, implies the logistical achievement of installing a 30m long, 45-tonne truck containing a whole-body MRI scanner on the site of the beautiful city of Courmayeur (Aoste Valley, Italie). A country-side biochemistry laboratory for on-site immediate conditioning of all biomedical samples at all time points was also needed. Thanks to the mutual interest of Siemens Headquarters, Swiss local engineers, Medical Team from the Aoste Valley public hospital, it was possible to have a 1.5T cardiac MR system (MAGNETOM Avanto) within an Alliance Medical truck for 3 weeks, in the center of Courmayeur, at less than 100m from the arrival site.

8.1.1. Method

Fifty trailers were then volunteering for a non-invasive and longitudinal quantitative MRI exploration realized prior, during and after the “Tor des géants” ultra-trail. Blood analysis were obtained before, during, just after and 3 days after the race in order to compare quantitative MRI indexes (T1, T2, and ADC) to blood biomarkers.

Images were acquired on a mobile clinical MAGNETOM Avanto 1.5T scanner (Siemens Healthcare, Erlangen, Germany) providing a maximum gradient strength 40 mT/m, with a 6-channel body matrix coil and 9 channels from the 24-channel spine coil. Fifty trailers were enrolled without clinical evidence of personal history of cardiac or pulmonary disease. Subjects were studied before, at arrival, and after recovery (3days). Imaging protocol included comprehensive global and regional LV function analysis and quantitative MRI: T1, T2 and ADC values were obtained using respectively a MOLLI sequence, a radial multi-echo sequence, a Stejskal-Tanner diffusion sequence with slice following. T1, T2 and ADC values at 1.5T were compared with plasma levels of inflammation, myocardial stress and/or damage biomarkers.

The DWI acquisitions parameters were the same as the reproducibility study. Acquisitions were realized using the slice following approach in diastole however the protocol investigated here was a 5 slices coverage ADC protocol with 5 slices, 4 b-values 0, 50, 100, 200 s/mm², 6 directions and 5 TDs. ADC was calculated using a mono-exponential fitting on the 4 b-values. Mean values by slices were then derived using an automatic segmentation technique (CMRsegTool plugin, OsiriX, CREATIS) of the left ventricular cavity.

8.1.2. Preliminary results

Twenty seven finishers (54%) completed the longitudinal study. T2, T1 and ADC values significantly increased immediately after the race. ADC quickly normalized after recovery while T1, T2 markers remained higher than baseline (Figure 8.1). Significant correlations were found between myocardial MR biomarkers and blood (Gal3, ST2, NTproBNP), plasmatic (CRP, CKs, hs-TNT) and cellular (WBC, lymphocytes, neutrophils) ones. Correlations between ADC and blood biomarkers were reported in Table 8-1.

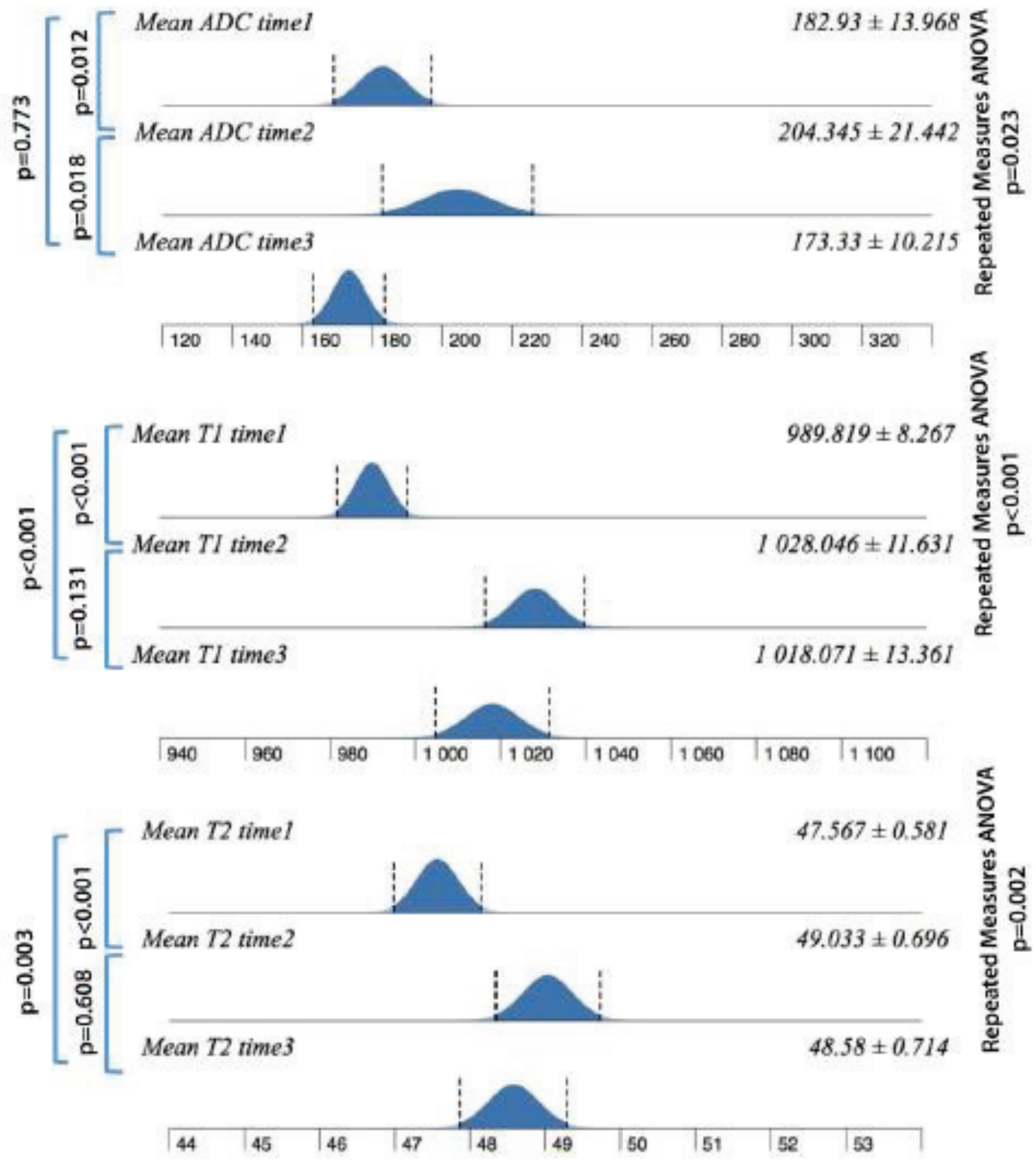

Figure 8.1 : Evolution of ADC, T1 and T2 at the three time point of measure.

Co-variate	Correlation	R-squared	P-value
Age	-0.111	0.012	0.340
FC	0.138	0.019	0.242
Hct	-0.135	0.018	0.249
WBC	0.302	0.091	0.008
Lymphocytes	-0.231	0.053	0.046
Neutrophiles	0.395	0.156	0.000
Hs-TNT	0.323	0.105	0.008
CK	0.276	0.076	0.026
CK-MB	0.263	0.069	0.034
ST2	0.319	0.102	0.009
Gal-3	0.305	0.093	0.013
NT-ProBNP	0.429	0.184	0.000
Myoglobin	0.285	0.081	0.021
HFABP	0.256	0.065	0.039
CRP	0.372	0.139	0.002
Cl	0.288	0.083	0.02
K	-0.136	0.019	0.281
Na	0.299	0.09	0.015
Osmol. Plasm.	0.057	0.003	0.655
Osmol. Urin.	0.294	0.087	0.018

Table 8-1 : Correlation between blood biomarker and ADC. Red value are statically signifiant.

8.1.3. Discussion

To our knowledge this is the first longitudinal study investigating the potential role of quantitative MR diffusion to explore acute stress-related changes in the myocardium. We found that ADC, T1 and T2 mapping are able to identify changes in subjects with varying inflammation levels that may represent additional and unique biomarkers of myocardial inflammation in this new longitudinal model of human's tissue stress. Beyond to a deeper understanding of ultra-endurance's impact that still need to be explored with sports physiologists, this study highlights a potential added value of diffusion measurements to scrutinize acute stress phenomena in the myocardium, that differ from T1 and T2 markers. These results could reveal more about redistribution of water into exercised myocardium and post-extreme exercise recovery, with reversible inflammatory phenomena caused by the ultra-endurance, and a good correlation with blood biomarkers. The study demonstrates the complementary performance of ADC as a newly available imaging indicator, foreseen to be deployed at short-term in the evaluation of innovative strategies for organs protection.

8.2. Clinical study

The combination of the slice following technique and second order motion compensation diffusion encoding scheme was demonstrated in the previous chapter to be a promising solution to reduce the acquisition time and the sensitivity to cardiac motion. Using these techniques, the first clinical applications on patient were realized in systole and diastole using a 2-min ADC similar to the previous one presented in chapter 7. Two different cases representing two different clinical scenarios are briefly described here.

8.2.1. Method

Images were acquired on a clinical MAGNETOM Aera 1.5T scanner (Siemens Healthcare, Erlangen, Germany) providing a maximum gradient strength 40 mT/m, with a 6-channel body matrix coil and 9 channels from the 24-channel spine coil. Forty patients were enrolled on a clinical suspicion of cardiac or pulmonary disease. Subjects were studied during a standard clinical exam and images were acquired before injection of contrast product. Classical clinical protocol includes comprehensive global and regional LV function analysis and quantitative MRI: T2 before injection and T1 before and after injection of contrast product.

The DWI acquisitions parameters were the same as the reproducibility study. Slice following approach and AMC diffusion were used on systolic and diastolic phase. The ADC protocol includes 5 slices, 2 b-values: 0, 200 s/mm², 6 directions and 5 TDs. After PCATMIP post-processing, ADC was extract using the Trace image calculated from the 6 directions images. Mean values by slices were then derived using an automatic segmentation technique (CMRsegTool plugin, OsiriX, CREATIS) of the left ventricular cavity.

8.2.2. Preliminary results

Infarct

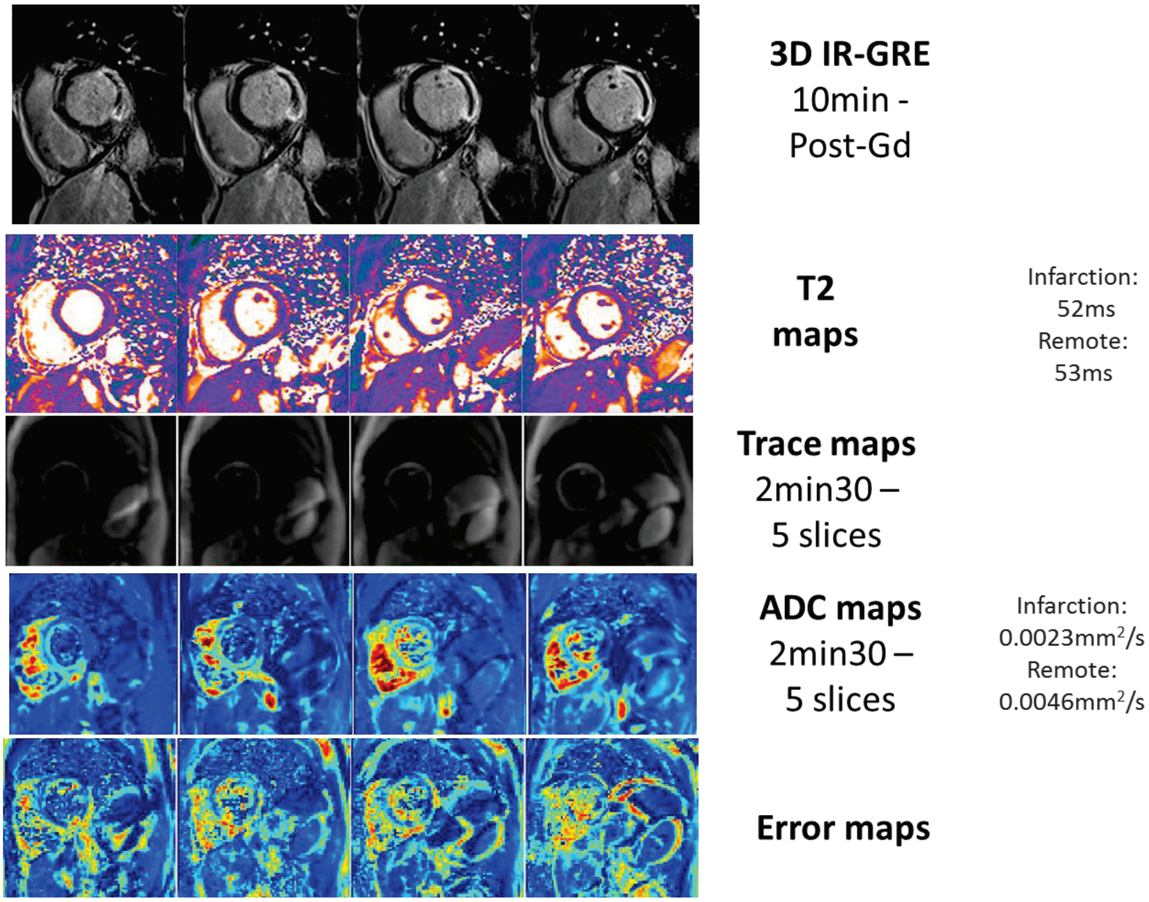

Figure 8.2: Five short axis slices acquired in diastole and systole on HCM patient. Top: Trace. Bottom: ADC maps.

MR images obtained using the delayed enhancement technique presented in Figure 8.3 reveals a lateral myocardial infarction (white area) and an inner no-reflow area (dark areal). The T2 measurements are similar in the remote zone (53ms) and in the infarct (52ms). T2 variations are also not visible on the Trace images generated from directional diffusion acquisitions, while ADC maps are in hypo-signal in all the infarct area. The ADC value measured in the infarct area ($2.3\text{x}10^{-3}$ mm²/s) is slightly higher than in healthy volunteer ($1.7\text{x}10^{-3}$ mm²/s) but the ADC measured in remote area is very high ($4.6\text{x}10^{-3}$ mm²/s). The error maps generated from equation 6.5, attest that this information is relevant and not due to cardiac motion corruption.

HCM

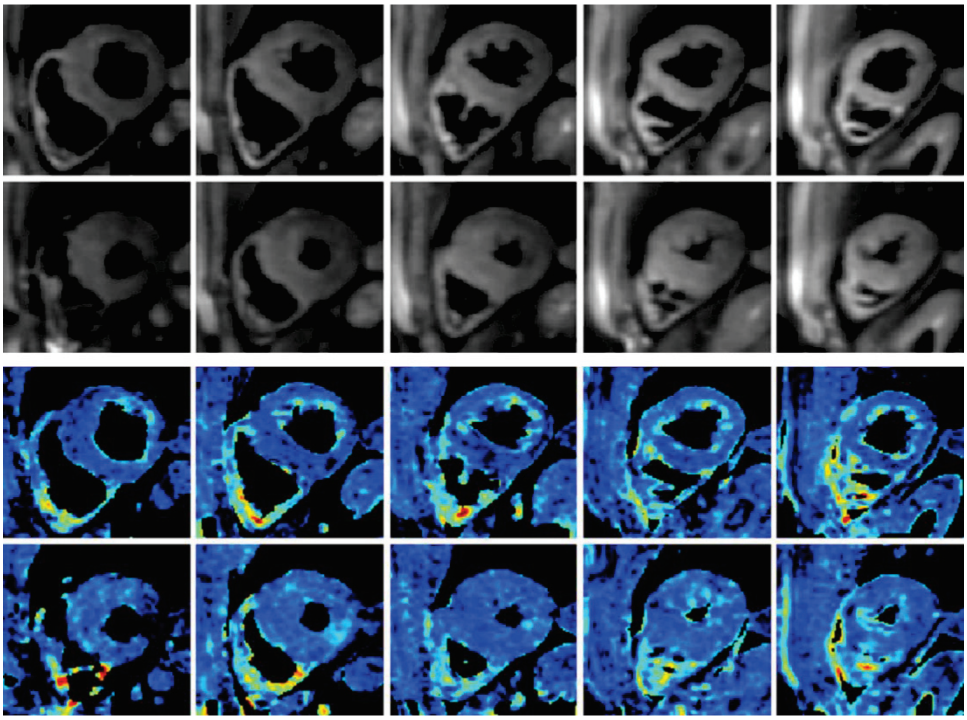

Figure 8.3: Five short axis slices acquired in diastole and systole on HCM patient. Top: Trace. Bottom: ADC maps.

Figure 8.3 represents 5 short axis Trace and ADC images acquired on diastole and systole on a hypertrophic cardiomyopathy patient. Homogenous parametric maps are obtained in both systole and diastole. The ADC value measured in systole ($1.41x10^{-3}$ mm²/s) is slightly lower than the one measured in diastole ($1.7x10^{-3}$ mm²/s). On healthy volunteer the value obtained in chapter 7 in systole ($1.41x10^{-3}$ mm²/s) are lower to one obtained in diastole ($1.75x10^{-3}$ mm²/s). Lower value was obtained using STEAM sequence on healthy volunteer by (C. T. Stoeck *et al.*, 2014) ($1.02x10^{-3}$ mm²/s and $0.88x10^{-3}$ mm²/s) and (Tunnicliffe *et al.*, 2014) ($1.1x10^{-3}$ mm²/s and $1.2x10^{-3}$ mm²/s) in systole and diastole respectively. On HCM patient Md was measure to (McGill *et al.*, 2012) ($0.75x10^{-3}$ mm²/s) in systole using the STEAM sequence.

8.2.3. Discussion

We achieve in this work the proof-of-concept feasibility of in-vivo CDWI in free-breathing conditions using a prospective slice-following correction. The combination of this method and of motion compensated gradient waveforms has allowed the first clinical measurements in diastole and systole. As shown in the Ultra-trail study, ADC is affected by changes variation of tissue inflammation. In the case of the myocardial infarct, ADC increases in the remote region in comparison to healthy volunteer and is equivalent in the infarct zone while T2 is almost similar in the remote and infarct zone. Difference between ADC and T2 shows clearly an impact of infarct tissue in the water diffusion process which could make diffusion an unique biomarker in this pathology. For the HCM case, ADC values find in systole and diastole are lower than in volunteer which is coherent with the previous study on this pathology. These preliminary results are samples of a larger cohort of patient with various pathologies which are currently studied by clinician. This study demonstrates the potential added value of a simple 2 min protocol robust and fully compatible with current clinical constraint.

PART
IV

Conclusion & Perspectives

9. Conclusion & perspectives

In this thesis, MR imaging and reconstruction method have been developed, implemented, optimized and validated in order to provide DWI-related biomarkers applicable to clinical scenarios and time constraints.

The first contribution of this work was the development of a new free-breathing acquisition strategy for cardiac DWI using SE-EPI with the objective to offer a methodology that could be applicable in a clinical scenario. This method compensates the head-foot respiratory induced displacement of the heart by using the information deliver by a navigator through a tracking factor. Slice following strategy provides short scanning time all along the respiratory cycle and thus offers capacity to optimize the protocol durations. Two limitations were discussed in the chapter 5: first, as the heart continues to move during respiratory, sequence duration should be shorten enough to not suffer from intra-scan motion. The second limitation is that the slice following accuracy is directly link to tracking factor between liver and heart positions. A fixed tracking factor of 0.6 was used in this proof-of-concept work, nevertheless advance techniques to estimate a patient specific tracking factor has been proposed and could be investigated in the future. Validation of this method was proposed through a reproducibility study using a DTI and an IVIM protocol and modeling.

Coupling to this technique, our second contribution was to propose an optimal pre and post-processing pipeline based on an improved multi-step registration strategy to handle in-plane displacement remaining in the images. This new reconstruction pipeline was developed to face any kind of diffusion dataset and was implemented in Matlab but also in an Osirix plugin. The registration steps were evaluated and have shown improvement of the correspondence of the structure. Both first and second contributions were published in *Magnetic Resonance in Medicine* named **“In-vivo free-breathing DTI & IVIM of the whole human heart using a real-time slice-followed SE-EPI navigator-based sequence: a reproducibility study in healthy volunteers”**.

The last contribution of this thesis, regarding the implementation and evaluation of second order motion compensation diffusion preparation combined with free-breathing slice following acquisition will constitute the material for a second publication

Our developed tools were used within three experimental studies involving two collaborations: in a first study, experimental work was highlighted by a theoretical work achieved with ***Camille Jourdan mathematical institute***. All published diffusion encoding scheme and cardiac strain motion were simulated using a new mathematical model based on the Bloch-Torrey equation solved using finite element discretization in space. As co-evidenced by our experimental and simulations studies, Monopolar STEAM sequence and AMC sequence were identified as less sensitive to cardiac strain by providing a lower error introduced the diffusion measurement. “Sweet spots” and “sweetest cardiac phase” for STEAM sequence and SE sequence were also clarified by the theoretical simulations in this study. This work was submitted to journal for publication to *Inverse Problems Journal* with the name **“A Mathematical Model and an Efficient Simulation Framework for Diffusion Cardiac Imaging: Application to Quantification of Cardiac Deformation on the Diffusion Signal”**. A second collaboration with the ***Centre d’Imagerie BioMedicale, University of Lausanne*** was dedicated to the evaluation of these diffusion encoding schemes using a mobile phantom mimicking the respiratory motion. Five SE encoding schemes were compared using ADC and a DTI models. Two diffusion encoding schemes were excluded from the study due to important signal artefacts and among the three remaining schemes, AMC revealed a higher sensitivity to intra-scan motion. A volunteer study was realized on volunteers in order to compare diffusion preparations in real conditions using a short 2-minute ADC protocol. Artefact quantification was proposed and used to analyze and reject corrupt data. For each volunteers strain measurement and respiratory phase were also extracted and compared to this artefact scoring. A correlation was found between cardiac strain and artefact presence in the image for two schemes while lower of score of artefact was found for the AMC preparation, promoted if as the method of choice for clinical application. This work will be submitted for publication under the name: **“Quantification of residual motion in diffusion-weighted cardiac MR (DW-CMR): objective quality metrics and validation using 3 diffusion encoding schemes under free breathing conditions”**.

A longitudinal research was conducted and realized on 51 ultra-trailer subjects enrolled from the "Tor des géants" 2014 edition in Italy. Fifty trailers were scan just before the race, 27 finisher just after and 3 days after the race were realized. T1, T2 and diffusion measurement were compared to blood biomarkers to study their performance to screen microstructural inflammation. Results of this study were submitted to ISMRM and accepted for oral and poster presentation at the SCMR congress and the results will hopefully end up being published soon.

Taking into account the methodological achievements of this work (previous chapters have shown that significant and robust results can be obtained within short acquisition time), we consider that the developed technology could be transferred to clinical routine and that a free-breathing sequence using slice-following and compensated gradient waveform preparation could be included into protocols aiming at deeper characterizing the myocardial tissue in various pathological conditions. To date, the 2-min ADC protocol presented in the previous chapter has been completed in diastole and systole in more than 40 patients presenting various pathologies and including, Tako-tsubo (1), myocarditis (10), infarct (12), HCM (4), dilated cardiomyopathy (7) and tumor/abscess (2) and immune diseases (2).

In this thesis, acquisitions were realized at 1.5T with gradient system of 40mT/m and few preliminary test were realized at 3T with gradient strength of 80mT/m. High gradient system could reduce the TE reach by diffusion encoding schemes and/or increase the resolution without any cost in comparison of previous protocol. Nevertheless, our first experiments in-vivo at 3T with gradient of 80mT/m revealed strong distortions and additional development of distortion correction methods will be necessary before application of CDWI SE-EPI sequence in-vivo in such system.

Also we believe that limitations behind slice-following method are not critical in the context of application of CDWI with a low resolution. Respiratory intra-scan motion might be noticeable at higher resolution that will adds to difficulties resulting from longer TE and in turn higher distortion conditions anyway.

Under free-breathing conditions, higher angular resolution or multiple b-values screening result into prolonged acquisition can still be tolerated for investigational research purposes since the subjects is not requested to perform a huge amount of breath-hold. Until now, complex and long protocols like ones involved in neurology were not envisaged in cDWI for patient convenience. For research perspectives, HARDI and high resolution q-space imaging could be interesting to describe precisely the heart architecture in-vivo.

The superiority of 2nd Order motion compensated scheme to handle cardiac motion has been undeniably confirmed in our work and extended to free breathing strategies. In dataset acquired with such scheme, heart is less corrupt by cardiac motion inducing less need for additional pre-processing like PCATMIP. As images suffer from less important signal loss, classical average technique might be an alternative that could in turn increase the SNR and avoid the blurring induced by PCA filtering.

Communications

Glatard T, Marion A, Benoit-Cattin H, Camarasu-Pop S, Clarysse P, Ferreira da Silva R, Forestier G, Gibaud B, Lartizien C, Liebgott H, **Moulin K**, Friboulet D. *Muli-modality image simulation with the virtual imaging platform : Illustration on cardiac MRI and echography*, IEEE International Symposium on Biomedical Imaging (ISBI) 2012, Barcelona, Spain.

Moulin K, Croisille P, Feiweier T, Delattre BM, Wei H, Robert B, Beuf O, Viallon M. *In vivo free-breathing DTI and IVIM of the whole human heart using a real-time slice-followed SE-EPI navigator-based sequence: A reproducibility study in healthy volunteers.* FLY 2014, Lyon, France.

Moulin K, Croisille P, Feiweier T, Delattre BM, Wei H, Robert B, Beuf O, Viallon M. *In vivo free-breathing DTI and IVIM of the whole human heart using a real-time slice-followed SE-EPI navigator-based sequence: A reproducibility study in healthy volunteers.* SCMR 2015, Nice, France.

Moulin K, Croisille P, Feiweier T, Delattre BM, Wei H, Robert B, Beuf O, Viallon M. *In vivo free-breathing DTI and IVIM of the whole human heart using a real-time slice-followed SE-EPI navigator-based sequence: A reproducibility study in healthy volunteers.* ISMRM 2015, Toronto, Canada.

Moulin K, Croisille P, Feiweier T, Delattre BM, Wei H, Robert B, Beuf O, Viallon M. *In vivo free-breathing DTI and IVIM of the whole human heart using a real-time slice-followed SE-EPI navigator-based sequence: A reproducibility study in healthy volunteers.* JFR 2015, Paris, France.

Moulin K, Chazot A, Croisille P, Viallon M. *Comparison of 3 diffusion encoding schemes for cardiac imaging under free breathing conditions.* JFR 2015, Paris, France.

Moulin K, Chazot A, Chaptinel J, Croisille P, Viallon M. *Comparison of 3 diffusion encoding schemes for cardiac imaging under free breathing conditions.* SCMR 2016, San Francisco, USA. **Accepted**

Viallon M, **Moulin K**, Le Goff C, Didier J, Van Heeswijk R, Stuber M, De Bourguignon C, Gergelé L Millet G, Croisille P, Beuf O. *Apparent Diffusion Coefficient (ADC), T1 and T2 quantitative index of the myocardium in athletes before, during and after extreme mountain ultra-long exercise: correlation with myocardial damage and inflammation biomarkers.* SCMR 2016, San Francisco, USA. **Accepted**

Moulin K, Chazot A, Croisille P, Viallon M. . *Quantification of residual motion in diffusion-weighted cardiac MR (DW-CMR): objective quality metrics and validation using 3 diffusion encoding schemes under free breathing conditions.* ISMRM 2016, Singapore. **Submitted**

Publications

Wei H, Viallon M, Delattre BM, **Moulin K**, Yang F, Croisille P, Zhu Y. *Free-breathing diffusion tensor imaging and tractography of the human heart in healthy volunteers using wavelet-based image fusion.* IEEE Trans Med Imaging. 2015 Jan;34(1):306-16. doi: 10.1109/TMI.2014.2356792

Moulin K, Croisille P, Feiweier T, Delattre BM, Wei H, Robert B, Beuf O, Viallon M. *In vivo free-breathing DTI and IVIM of the whole human heart using a real-time slice-followed SE-EPI navigator-based sequence: A reproducibility study in healthy volunteers.* Magn Reson Med. 2015 Aug 24. doi: 10.1002/mrm.25852.

Mekkaoui I, **Moulin K**, Pousin J, Viallon M. *A Mathematical Model and an Efficient Simulation Framework for Diffusion Cardiac Imaging: Application to Quantification of Cardiac Deformation on the Diffusion Signal.* ***Submitted to*** *Inverse Problems.*

Bibliography

1) Lombaert, H., Peyrat, J. M., Croisille, P., Rapacchi, S., Fanton, L., Cheriet, F., Clarysse, P., Magnin, I., Delingette, H. and Ayache, N. (2012) 'Human atlas of the cardiac fiber architecture: study on a healthy population', *IEEE Trans Med Imaging*, 31(7), pp. 1436-47.

2) Mendis, S., Davis, S. and Norrving, B. (2015) 'Organizational update: the world health organization global status report on noncommunicable diseases 2014; one more landmark step in the combat against stroke and vascular disease', *Stroke*, 46(5), pp. e121-2.

3) Messroghli, D. R., Radjenovic, A., Kozerke, S., Higgins, D. M., Sivananthan, M. U. and Ridgway, J. P. (2004) 'Modified Look-Locker inversion recovery (MOLLI) for high-resolution T1 mapping of the heart', *Magn Reson Med*, 52(1), pp. 141-6.

4) Giri, S., Chung, Y. C., Merchant, A., Mihai, G., Rajagopalan, S., Raman, S. V. and Simonetti, O. P. (2009) 'T2 quantification for improved detection of myocardial edema', *J Cardiovasc Magn Reson*, 11, p. 56.

5) Jouk, P. S., Mourad, A., Milisic, V., Michalowicz, G., Raoult, A., Caillerie, D. and Usson, Y. (2007) 'Analysis of the fiber architecture of the heart by quantitative polarized light microscopy. Accuracy, limitations and contribution to the study of the fiber architecture of the ventricles during fetal and neonatal life', *Eur J Cardiothorac Surg*, 31(5), pp. 915-21.

6) Edelman, R. R., Gaa, J., Wedeen, V. J., Loh, E., Hare, J. M., Prasad, P. and Li, W. (1994) 'In vivo measurement of water diffusion in the human heart', *Magn Reson Med*, 32(3), pp. 423-8.

7) Gamper, U., Boesiger, P. and Kozerke, S. (2007) 'Diffusion imaging of the in vivo heart using spin echoes--considerations on bulk motion sensitivity', *Magn Reson Med*, 57(2), pp. 331-7.

8) Pai, V. M., Rapacchi, S., Kellman, P., Croisille, P. and Wen, H. (2011) 'PCATMIP: enhancing signal intensity in diffusion-weighted magnetic resonance imaging', *Magn Reson Med*, 65(6), pp. 1611-9.

9) Rapacchi, S., Wen, H., Viallon, M., Grenier, D., Kellman, P., Croisille, P. and Pai, V. M. (2011) 'Low b-value diffusion-weighted cardiac magnetic resonance imaging: initial results in humans using an optimal time-window imaging approach', *Invest Radiol*, 46(12), pp. 751-8.

10) Delattre, B. M., Viallon, M., Wei, H., Zhu, Y. M., Feiweier, T., Pai, V. M., Wen, H. and Croisille, P. (2012) 'In vivo cardiac diffusion-weighted magnetic resonance imaging: quantification of normal perfusion and diffusion coefficients with intravoxel incoherent motion imaging', *Invest Radiol*, 47(11), pp. 662-70.

11) Nielles-Vallespin, S., Mekkaoui, C., Gatehouse, P., Reese, T. G., Keegan, J., Ferreira, P. F., Collins, S., Speier, P., Feiweier, T., de Silva, R., Jackowski, M. P., Pennell, D. J., Sosnovik, D. E. and Firmin, D. (2013) 'In vivo diffusion tensor MRI of the human heart: reproducibility of breath-hold and navigator-based approaches', *Magn Reson Med*, 70(2), pp. 454-65.

12) Streeter, D. D., Jr., Spotnitz, H. M., Patel, D. P., Ross, J., Jr. and Sonnenblick, E. H. (1969) 'Fiber orientation in the canine left ventricle during diastole and systole', *Circ Res*, 24(3), pp. 339-47.

13) LeGrice, I. J., Smaill, B. H., Chai, L. Z., Edgar, S. G., Gavin, J. B. and Hunter, P. J. (1995) 'Laminar structure of the heart: ventricular myocyte arrangement and connective tissue architecture in the dog', *Am J Physiol*, 269(2 Pt 2), pp. H571-82.

14) Costa, K., Holmes, J. and McCulloch, A. (2001) 'Modelling cardiac mechanical properties in three dimensions', *Philosophical Transactions of the Royal Society of London. Series A: Mathematical,Physical and Engineering Sciences*, 359(1783), pp. pp.1233–1250.

15) Hooks, D. A., Tomlinson, K. A., Marsden, S. G., LeGrice, I. J., Smaill, B. H., Pullan, A. J. and Hunter, P. J. (2002) 'Cardiac microstructure: implications for electrical propagation and defibrillation in the heart', *Circ Res*, 91(4), pp. 331-8.

16) Russel, I. K., Gotte, M. J., Bronzwaer, J. G., Knaapen, P., Paulus, W. J. and van Rossum, A. C. (2009) 'Left ventricular torsion: an expanding role in the analysis of myocardial dysfunction', *JACC Cardiovasc Imaging*, 2(5), pp. 648-55.

17) Hooks, D. A., Trew, M. L., Caldwell, B. J., Sands, G. B., LeGrice, I. J. and Smaill, B. H. (2007) 'Laminar arrangement of ventricular myocytes influences electrical behavior of the heart', *Circ Res*, 101(10), pp. e103-12.

18) Buckberg, G., Hoffman, J. I., Mahajan, A., Saleh, S. and Coghlan, C. (2008) 'Cardiac mechanics revisited: the relationship of cardiac architecture to ventricular function', *Circulation*, 118(24), pp. 2571-87.

19) Mall (1911) 'On the muscular architecture of the ventricles of the human heart', *American Journal of Anatomy*, 11(3), pp. pp.211–266.

20) Rushmer, R. F., Crystal, D. K. and Wagner, C. (1953) 'The functional anatomy of ventricular contraction', *Circ Res*, 1(2), pp. 162-70.

21) Torrent-Guasp, F., Kocica, M. J., Corno, A. F., Komeda, M., Carreras-Costa, F., Flotats, A., Cosin-Aguillar, J. and Wen, H. (2005) 'Towards new understanding of the heart structure and function', *Eur J Cardiothorac Surg*, 27(2), pp. 191-201.

22) Torrent Guasp, F. (1972a) '[Microscopic structure of the left myocardial ventricle. I. Apical half]', *Rev Esp Cardiol*, 25(1), pp. 68-81.

23) Torrent Guasp, F. (1972b) '[Macroscopic structure of the left ventricle. II. The basal half]', *Rev Esp Cardiol*, 25(2), pp. 109-18.

24) Streeter, D. (1979) 'Gross Morphology and Fiber Geometry of the Heart.', *In handbook of physiology: The cardiovascular system.*, pp. pp. 61 – 112.

25) Legrice, I. J., Hunter, P. J. and Smaill, B. H. (1997) 'Laminar structure of the heart: a mathematical model', *Am J Physiol*, 272(5 Pt 2), pp. H2466-76.

26) Stanisz, G. J., Odrobina, E. E., Pun, J., Escaravage, M., Graham, S. J., Bronskill, M. J. and Henkelman, R. M. (2005) 'T1, T2 relaxation and magnetization transfer in tissue at 3T', *Magn Reson Med*, 54(3), pp. 507-12.

27) Firmin, D. and Keegan, J. (2001) 'Navigator echoes in cardiac magnetic resonance', *J Cardiovasc Magn Reson*, 3(3), pp. 183-93.

28) Butts, K., de Crespigny, A., Pauly, J. M. and Moseley, M. (1996) 'Diffusion-weighted interleaved echo-planar imaging with a pair of orthogonal navigator echoes', *Magn Reson Med*, 35(5), pp. 763-70.

29) Atkinson, D., Counsell, S., Hajnal, J. V., Batchelor, P. G., Hill, D. L. and Larkman, D. J. (2006) 'Nonlinear phase correction of navigated multi-coil diffusion images', *Magn Reson Med*, 56(5), pp. 1135-9.

30) Porter, D. A. and Heidemann, R. M. (2009) 'High resolution diffusion-weighted imaging using readout-segmented echo-planar imaging, parallel imaging and a two-dimensional navigator-based reacquisition', *Magn Reson Med*, 62(2), pp. 468-75.

31) Feinberg, D. A., Giese, D., Bongers, D. A., Ramanna, S., Zaitsev, M., Markl, M. and Gunther, M. (2010) 'Hybrid ultrasound MRI for improved cardiac imaging and real-time respiration control', *Magn Reson Med*, 63(2), pp. 290-6.

32) Ooi, M. B., Krueger, S., Thomas, W. J., Swaminathan, S. V. and Brown, T. R. (2009) 'Prospective real-time correction for arbitrary head motion using active markers', *Magn Reson Med*, 62(4), pp. 943-54.

33) van Heeswijk, R. B., Bonanno, G., Coppo, S., Coristine, A., Kober, T. and Stuber, M. (2012) 'Motion compensation strategies in magnetic resonance imaging', *Crit Rev Biomed Eng*, 40(2), pp. 99-119.

34) Le Bihan, D., Breton, E., Lallemand, D., Aubin, M. L., Vignaud, J. and Laval-Jeantet, M. (1988) 'Separation of diffusion and perfusion in intravoxel incoherent motion MR imaging', *Radiology*, 168(2), pp. 497-505.

35) Carr and Purcell (1954) 'Effects of diffusion on free precession in nuclear magnetic resonance experiments', *Physical review*, 94(3).

36) Torrey, H. C. (1956) 'Bloch equations with diffusion terms', *Physical review*, 104, 563.

37) Price, W. (1997) 'Pulsed- field gradient nuclear magnetic resonance as a tool for studying

translational diffusion: Part 1. Basic theory', *Concepts in Magnetic Resonance*, 9(5), pp. pp.299–336.

38) Price, W. (1998) 'Pulsed-field gradient nuclear magnetic resonance as a tool for studying translational diffusion. Part 2. Experimental aspects.', *Concepts in Magnetic Resonance*, 10(4), pp. pp.197–237.

39) Stejskal, E. O. and Tanner, J. E. (1965) 'Spin Diffusion Measurements: Spin Echoes in the Presence of a Time Dependent Field Gradient', *J. Chem. Phys.* , 42, 288.

40) Froeling, M., Strijkers, G. J., Nederveen, A. J., Chamuleau, S. A. and Luijten, P. R. (2014) 'Diffusion Tensor MRI of the Heart – In Vivo Imaging of Myocardial Fiber Architecture', *Current Cardiovascular Imaging Reports*, 7(7).

41) Callaghan, P., Eccles, C. and Xia, Y. (1988) 'NMR microscopy of dynamic displacements: kspace and q-space imaging', *Journal of Physics E: Scientific Instruments*, 21: 820.

42) Wedeen, V. J., Hagmann, P., Tseng, W. Y., Reese, T. G. and Weisskoff, R. M. (2005) 'Mapping complex tissue architecture with diffusion spectrum magnetic resonance imaging', *Magn Reson Med*, 54(6), pp. 1377-86.

43) Cory, D. G. and Garroway, A. N. (1990) 'Measurement of translational displacement probabilities by NMR: an indicator of compartmentation', *Magn Reson Med*, 14(3), pp. 435-44.

44) Callaghan, P. T., Codd, S. L. and Seymour, J. D. (1999) 'Spatial coherence phenomena arising from translational spin motion in gradient spin echo experiments', *Concepts in Magnetic Resonance*, 11:4(181–202).

45) Moseley, M. E., Cohen, Y., Mintorovitch, J., Chileuitt, L., Shimizu, H., Kucharczyk, J., Wendland, M. F. and Weinstein, P. R. (1990) 'Early detection of regional cerebral ischemia in cats: comparison of diffusion- and T2-weighted MRI and spectroscopy', *Magn Reson Med*, 14(2), pp. 330-46.

46) Basser, P. J., Mattiello, J. and LeBihan, D. (1994) 'Estimation of the effective self-diffusion tensor from the NMR spin echo', *J Magn Reson B*, 103(3), pp. 247-54.

47) Kingsley, P. (2006a) 'Introduction to Diffusion Tensor Imaging Mathematics: Part III. Tensor Calculation, Noise, Simulations, and Optimization', *Concepts in Magnetic Resonance*, 28A(2)(155–179).

48) Kingsley, P. (2006b) 'Introduction to Diffusion Tensor Imaging Mathematics: Part II. Anisotropy, Diffusion-Weighting Factors, and Gradient Encoding Schemes', *Concepts in Magnetic Resonance*, 28A(2)(123–154).

49) Kingsley, P. (2006c) 'Introduction to Diffusion Tensor Imaging Mathematics: Part I. Tensors, Rotations, and Eigenvectors', *Concepts in Magnetic Resonance*, 28A(2)(101–122).

50) Le Bihan, D., Breton, E., Lallemand, D., Grenier, P., Cabanis, E. and Laval-Jeantet, M. (1986) 'MR imaging of intravoxel incoherent motions: application to diffusion and perfusion in neurologic disorders', *Radiology*, 161(2), pp. 401-7.

51) Wu, Y. C. and Alexander, A. L. (2007) 'Hybrid diffusion imaging', *Neuroimage*, 36(3), pp. 617-29.

52) Tuch, D. S. (2004) 'Q-ball imaging', *Magn Reson Med*, 52(6), pp. 1358-72.

53) Ozarslan, E., Shepherd, T. M., Vemuri, B. C., Blackband, S. J. and Mareci, T. H. (2006) 'Resolution of complex tissue microarchitecture using the diffusion orientation transform (DOT)', *Neuroimage*, 31(3), pp. 1086-103.

54) Descoteaux, M., Deriche, R., Le Bihan, D., Mangin, J. F. and Poupon, C. (2009) 'Diffusion propagator imaging: using Laplace's equation and multiple shell acquisitions to reconstruct the diffusion propagator', *Inf Process Med Imaging*, 21, pp. 1-13.

55) Lemke, A., Laun, F. B., Simon, D., Stieltjes, B. and Schad, L. R. (2010) 'An in vivo verification of the intravoxel incoherent motion effect in diffusion-weighted imaging of the abdomen', *Magn Reson Med*, 64(6), pp. 1580-5.

56) Mathieu, O., Cruz-Orive, L. M., Hoppeler, H. and Weibel, E. R. (1983) 'Estimating length density and quantifying anisotropy in skeletal muscle capillaries', *J Microsc*, 131(Pt 2), pp. 131-46.

57) Poole, D. C. and Mathieu-Costello, O. (1990) 'Analysis of capillary geometry in rat subepicardium and subendocardium', *Am J Physiol*, 259(1 Pt 2), pp. H204-10.

58) Karampinos, D. C., King, K. F., Sutton, B. P. and Georgiadis, J. G. (2010) 'Intravoxel partially coherent motion technique: characterization of the anisotropy of skeletal muscle microvasculature', *J Magn Reson Imaging*, 31(4), pp. 942-53.

59) Reese, T. G., Heid, O., Weisskoff, R. M. and Wedeen, V. J. (2003) 'Reduction of eddy-current-induced distortion in diffusion MRI using a twice-refocused spin echo', *Magn Reson Med*, 49(1), pp. 177-82.

60) Stoeck, C., Deuster, C. v., Toussaint, N. and Kozerke, S. (2013) 'High-resolution single-shot DTI of the in-vivo human heart using asymmetric diffusion encoding', *21st Annual Meeting of ISMRM, Salt Lake City, Utah, USA*, p. pp. 0480.

61) Nakamura, T., Shibukawa, S., Muro, I., Kajihara, N. and Nishio, H. (2014) 'Improvement of visualization of cardiac wall in diffusion-weighted imaging using cardiac triggering and acceleration motion correction', *22nd Annual Meeting of ISMRM, Milan, Italy*, p. pp. 2417.

62) Nguyen, C., Fan, Z., Sharif, B., He, Y., Dharmakumar, R., Berman, D. S. and Li, D. (2014) 'In vivo three-dimensional high resolution cardiac diffusion-weighted MRI: a motion compensated diffusion-prepared balanced steady-state free precession approach', *Magn Reson Med*, 72(5), pp. 1257-67.

63) Stoeck, C. T., von Deuster, C., Genet, M., Atkinson, D. and Kozerke, S. (2015) 'Second-order motion-compensated spin echo diffusion tensor imaging of the human heart', *Magn Reson Med*.

64) Welsh, C., Di Bella, E. and Hsu, E. (2015) 'Higher-Order Motion-Compensation for In Vivo Cardiac Diffusion Tensor Imaging in Rats', *IEEE Trans Med Imaging*.

65) Dou, J., Tseng, W. Y., Reese, T. G. and Wedeen, V. J. (2003) 'Combined diffusion and strain MRI reveals structure and function of human myocardial laminar sheets in vivo', *Magn Reson Med*, 50(1), pp. 107-13.

66) Reese, T. G., Weisskoff, R. M., Smith, R. N., Rosen, B. R., Dinsmore, R. E. and Wedeen, V. J. (1995) 'Imaging myocardial fiber architecture in vivo with magnetic resonance', *Magn Reson Med*, 34(6), pp. 786-91.

67) Tseng, W. Y., Reese, T. G., Weisskoff, R. M., Brady, T. J. and Wedeen, V. J. (2000) 'Myocardial fiber shortening in humans: initial results of MR imaging', *Radiology*, 216(1), pp. 128-39.

68) Tseng, W. Y., Dou, J., Reese, T. G. and Wedeen, V. J. (2006) 'Imaging myocardial fiber disarray and intramural strain hypokinesis in hypertrophic cardiomyopathy with MRI', *J Magn Reson Imaging*, 23(1), pp. 1-8.

69) Wu, M. T., Tseng, W. Y., Su, M. Y., Liu, C. P., Chiou, K. R., Wedeen, V. J., Reese, T. G. and Yang, C. F. (2006) 'Diffusion tensor magnetic resonance imaging mapping the fiber architecture remodeling in human myocardium after infarction: correlation with viability and wall motion', *Circulation*, 114(10), pp. 1036-45.

70) Wu, M. T., Su, M. Y., Huang, Y. L., Chiou, K. R., Yang, P., Pan, H. B., Reese, T. G., Wedeen, V. J. and Tseng, W. Y. (2009) 'Sequential changes of myocardial microstructure in patients postmyocardial infarction by diffusion-tensor cardiac MR: correlation with left ventricular structure and function', *Circ Cardiovasc Imaging*, 2(1), pp. 32-40, 6 p following 40.

71) McGill, L. A., Ismail, T. F., Nielles-Vallespin, S., Ferreira, P., Scott, A. D., Roughton, M., Kilner, P. J., Ho, S. Y., McCarthy, K. P., Gatehouse, P. D., de Silva, R., Speier, P., Feiweier, T., Mekkaoui, C., Sosnovik, D. E., Prasad, S. K., Firmin, D. N. and Pennell, D. J. (2012) 'Reproducibility of in-vivo diffusion tensor cardiovascular magnetic resonance in hypertrophic cardiomyopathy', *J Cardiovasc Magn Reson*, 14, p. 86.

72) Ferreira, P. F., Kilner, P. J., McGill, L. A., Nielles-Vallespin, S., Scott, A. D., Ho, S. Y., McCarthy, K. P., Haba, M. M., Ismail, T. F., Gatehouse, P. D., de Silva, R., Lyon, A. R., Prasad, S. K., Firmin, D. N. and Pennell, D. J. (2014) 'In vivo cardiovascular magnetic resonance diffusion tensor imaging shows evidence of abnormal myocardial laminar orientations and mobility in hypertrophic cardiomyopathy', *J Cardiovasc Magn Reson*, 16, p. 87.

73) Scott, A. D., Ferreira, P. F., Nielles-Vallespin, S., Gatehouse, P., McGill, L. A., Kilner, P., Pennell, D. J. and Firmin, D. N. (2014) 'Optimal diffusion weighting for in vivo cardiac diffusion tensor imaging', *Magn Reson Med*.

74) Tunnicliffe, E. M., Scott, A. D., Ferreira, P., Ariga, R., McGill, L. A., Nielles-Vallespin, S., Neubauer, S., Pennell, D. J., Robson, M. D. and Firmin, D. N. (2014) 'Intercentre reproducibility of cardiac apparent diffusion coefficient and fractional anisotropy in healthy volunteers', *J Cardiovasc Magn Reson*, 16(1), p. 31.

75) McGill, L. A., Scott, A. D., Ferreira, P. F., Nielles-Vallespin, S., Ismail, T., Kilner, P. J., Gatehouse, P. D., de Silva, R., Prasad, S. K., Giannakidis, A., Firmin, D. N. and Pennell, D. J. (2015) 'Heterogeneity of Fractional Anisotropy and Mean Diffusivity Measurements by In Vivo Diffusion Tensor Imaging in Normal Human Hearts', *PLoS One*, 10(7), p. e0132360.

76) Dou, J., Reese, T. G., Tseng, W. Y. and Wedeen, V. J. (2002) 'Cardiac diffusion MRI without motion effects', *Magn Reson Med*, 48(1), pp. 105-14.

77) Stoeck, C. T., Kalinowska, A., von Deuster, C., Harmer, J., Chan, R. W., Niemann, M., Manka, R., Atkinson, D., Sosnovik, D. E., Mekkaoui, C. and Kozerke, S. (2014) 'Dual-phase cardiac diffusion tensor imaging with strain correction', *PLoS One*, 9(9), p. e107159.

78) Deux, J. F., Maatouk, M., Vignaud, A., Luciani, A., Lenczner, G., Mayer, J., Lim, P., Dubois-Rande, J. L., Kobeiter, H. and Rahmouni, A. (2011) 'Diffusion-weighted echo planar imaging in patients with recent myocardial infarction', *Eur Radiol*, 21(1), pp. 46-53.

79) Wei, H., Viallon, M., Delattre, B. M., Moulin, K., Yang, F., Croisille, P. and Zhu, Y. (2015) 'Free-breathing diffusion tensor imaging and tractography of the human heart in healthy volunteers using wavelet-based image fusion', *IEEE Trans Med Imaging*, 34(1), pp. 306-16.

80) Wedeen, V. J., Weisskoff, R. M. and Poncelet, B. P. (1994) 'MRI signal void due to in-plane motion is all-or-none', *Magn Reson Med*, 32(1), pp. 116-20.

81) Lau, A. Z., Tunnicliffe, E. M., Frost, R., Koopmans, P. J., Tyler, D. J. and Robson, M. D. (2014) 'Accelerated human cardiac diffusion tensor imaging using simultaneous multislice imaging', *Magn Reson Med*.

82) von Deuster, C., Stoeck, C. T., Genet, M., Atkinson, D. and Kozerke, S. (2015) 'Spin echo versus stimulated echo diffusion tensor imaging of the in vivo human heart', *Magn Reson Med*.

83) Viallon, M., Mewton, N., Thuny, F., Guehring, J., O'Donnell, T., Stemmer, A., Bi, X., Rapacchi, S., Zuehlsdorff, S., Revel, D. and Croisille, P. (2012) 'T2-weighted cardiac MR assessment of the myocardial area-at-risk and salvage area in acute reperfused myocardial infarction: comparison of state-of-the-art dark blood and bright blood T2-weighted sequences', *J Magn Reson Imaging*, 35(2), pp. 328-39.

84) Tseng, W. Y., Reese, T. G., Weisskoff, R. M. and Wedeen, V. J. (1999) 'Cardiac diffusion tensor MRI in vivo without strain correction', *Magn Reson Med*, 42(2), pp. 393-403.

85) Wang, Y., Riederer, S. J. and Ehman, R. L. (1995) 'Respiratory motion of the heart: kinematics and the implications for the spatial resolution in coronary imaging', *Magn Reson Med*, 33(5), pp. 713-9.

86) Taylor, A., Jhooti, P., Keegan, J., Firmin, D. and Pennel, D. (1998) 'Improved MR coronary angiography using real-time navigator echoes and a subject specific calculated adaptive motion correction factor', *Proceedings of the Sixth Meeting of the International Society for Magnetic Resonance in Medicine. Berkeley, Calif: International Society for Magnetic Resonance in Medicine*, p. 322.

87) Nehrke, K., Bornert, P., Manke, D. and Bock, J. C. (2001) 'Free-breathing cardiac MR imaging: study of implications of respiratory motion--initial results', *Radiology*, 220(3), pp. 810-5.

88) Ries, M., de Senneville, B. D., Roujol, S., Berber, Y., Quesson, B. and Moonen, C. (2010) 'Real-time 3D target tracking in MRI guided focused ultrasound ablations in moving tissues', *Magn Reson Med*, 64(6), pp. 1704-12.

89) Ivancevic, M. K., Kwee, T. C., Takahara, T., Ogino, T., Hussain, H. K., Liu, P. S. and Chenevert, T. L. (2009) 'Diffusion-weighted MR imaging of the liver at 3.0 Tesla using TRacking Only Navigator echo (TRON): a feasibility study', *J Magn Reson Imaging*, 30(5), pp. 1027-33.

90) Takahara, T., Kwee, T. C., Van Leeuwen, M. S., Ogino, T., Horie, T., Van Cauteren, M., Herigault, G., Imai, Y., Mali, W. P. and Luijten, P. R. (2010) 'Diffusion-weighted magnetic resonance imaging of the liver using tracking only navigator echo: feasibility study', *Invest Radiol*, 45(2), pp. 57-63.

91) Piccini, D., Littmann, A., Nielles-Vallespin, S. and Zenge, M. O. (2012) 'Respiratory self-navigation for whole-heart bright-blood coronary MRI: methods for robust isolation and automatic segmentation of the blood pool', *Magn Reson Med*, 68(2), pp. 571-9.

92) Moghari, M. H., Hu, P., Kissinger, K. V., Goddu, B., Goepfert, L., Ngo, L., Manning, W. J. and Nezafat, R. (2012) 'Subject-specific estimation of respiratory navigator tracking factor for free-breathing cardiovascular MR', *Magn Reson Med*, 67(6), pp. 1665-72.

93) Kellman, P. and Hansen, M. S. (2014) 'T1-mapping in the heart: accuracy and precision', *J Cardiovasc Magn Reson*, 16, p. 2.

94) Winkler, M. L., Ortendahl, D. A., Mills, T. C., Crooks, L. E., Sheldon, P. E., Kaufman, L. and Kramer, D. M. (1988) 'Characteristics of partial flip angle and gradient reversal MR imaging', *Radiology*, 166(1 Pt 1), pp. 17-26.

95) Mukherjee, P., Chung, S. W., Berman, J. I., Hess, C. P. and Henry, R. G. (2008) 'Diffusion tensor MR imaging and fiber tractography: technical considerations', *AJNR Am J Neuroradiol*, 29(5), pp. 843-52.

96) Lin, L. I. (2000) 'Total deviation index for measuring individual agreement with applications in laboratory performance and bioequivalence', *Stat Med*, 19(2), pp. 255-70.

97) Bland, J. M. and Altman, D. G. (1999) 'Measuring agreement in method comparison studies', *Stat Methods Med Res*, 8(2), pp. 135-60.

98) Eggen, M. D., Swingen, C. M. and Iaizzo, P. A. (2012) 'Ex vivo diffusion tensor MRI of human hearts: relative effects of specimen decomposition', *Magn Reson Med*, 67(6), pp. 1703-9.

99) Noehren, B., Andersen, A., Feiweier, T., Damon, B. and Hardy, P. (2014) 'Comparison of twice refocused spin echo versus stimulated echo diffusion tensor imaging for tracking muscle fibers', *J Magn Reson Imaging*.

100) Callot, V., Bennett, E., Decking, U. K., Balaban, R. S. and Wen, H. (2003) 'In vivo study of microcirculation in canine myocardium using the IVIM method', *Magn Reson Med*, 50(3), pp. 531-40.

101) Yanagisawa, O., Shimao, D., Maruyama, K. and Nielsen, M. (2009) 'Evaluation of exercised or cooled skeletal muscle on the basis of diffusion-weighted magnetic resonance imaging', *Eur J Appl Physiol*, 105(5), pp. 723-9.

102) Kaneko, N., Matsuda, R., Toda, M. and Shimamoto, K. (2011) 'Three-dimensional reconstruction of the human capillary network and the intramyocardial micronecrosis', *Am J Physiol Heart Circ Physiol*, 300(3), pp. H754-61.

103) Chefd'Hotel, C., Hermosillo, G. and Faugeras, O. (2001) 'A variational approach to multi-modal image matching.', *Variational and Level Set Methods in Computer Vision, 2001. Proceedings. IEEE Workshop on*, pp. 21-28.

104) Chefd'hotel, C., Tschumperlé, D., Deriche, R. and Faugeras, O. (2002) 'Constrained Flows of Matrix-Valued Functions: Application to Diffusion Tensor Regularization', *Computer Vision - ECCV 2002,* , pp. 251-265.

105) Chefd'hotel, C., Tschumperlé, D., Deriche, R. and Faugeras, O. (2004) 'Regularizing Flows for Constrained Matrix-Valued Images.', *Journal of Mathematical Imaging and Vision 20*, 1 (1).

106) Kellman, P., Chefd'hotel, C., Lorenz, C. H., Mancini, C., Arai, A. E. and McVeigh, E. R. (2008) 'Fully automatic, retrospective enhancement of real-time acquired cardiac cine MR images using image-based navigators and respiratory motion-corrected averaging', *Magn Reson Med*, 59(4), pp. 771-8.

107) Aliotta, E., Rapacchi, S., Hu, P. and Ennis, D. B. (2015) 'Increased maximum gradient amplitude improves robustness of spin-echo cardiac diffusion-weighted MRI', *Journal of Cardiovascular Magnetic Resonance 2015*, 17(Suppl 1), p. P388.

108) Pipe, J. G. and Chenevert, T. L. (1991) 'A progressive gradient moment nulling design technique', *Magn Reson Med*, 19(1), pp. 175-9.

109) Wetscherek, A., Stieltjes, B. and Laun, F. B. (2015) 'Flow-compensated intravoxel incoherent motion diffusion imaging', *Magn Reson Med*, 74(2), pp. 410-9.

110) Huber, M. E., Stuber, M., Botnar, R. M., Boesiger, P. and Manning, W. J. (2000) 'Low-cost MR-compatible moving heart phantom', *J Cardiovasc Magn Reson*, 2(3), pp. 181-7.

111) Cerqueira, M. D., Weissman, N. J., Dilsizian, V., Jacobs, A. K., Kaul, S., Laskey, W. K., Pennell, D. J., Rumberger, J. A., Ryan, T., Verani, M. S., American Heart Association Writing Group on Myocardial, S. and Registration for Cardiac, I. (2002) 'Standardized myocardial segmentation and nomenclature for tomographic imaging of the heart. A statement for healthcare professionals from the Cardiac Imaging Committee of the Council on Clinical Cardiology of the American Heart Association', *Int J Cardiovasc Imaging*, 18(1), pp. 539-42.

112) Nottin, S., Doucende, G., Schuster, I., Tanguy, S., Dauzat, M. and Obert, P. (2009) 'Alteration in left ventricular strains and torsional mechanics after ultralong duration exercise in athletes', *Circ Cardiovasc Imaging*, 2(4), pp. 323-30.
113) Hansen, C. H., Ritschel, V., Halvorsen, S., Andersen, G. O., Bjornerheim, R., Eritsland, J., Arnesen, H. and Seljeflot, I. (2015) 'Markers of thrombin generation are associated with myocardial necrosis and left ventricular impairment in patients with ST-elevation myocardial infarction', *Thromb J*, 13, p. 31.

Annex A

Impact of anisotropy on artefact quantification was evaluated using an ex-vivo heart acquired with 192 directions at b-value 700s/mm². FA (0.3898) and MD (0.7815 x 10^{-3} mm²/s) are in higher range than in-vivo acquisition which represent of worst acquisition scenario. Mid short axis slice was divided in segment as shown in Figure 0.1. Variations of signal attenuation (S/S0) on left ventricle due to anisotropy represent at maximum 20% of difference (see Figure 0.2). The corresponding artefact quantification obtained on the 192 direction stack has a maximum variation due to anisotropy to 14%. A Mean artefact criteria over all segment was found to 0.246 while the maximum value was found to 0.375.

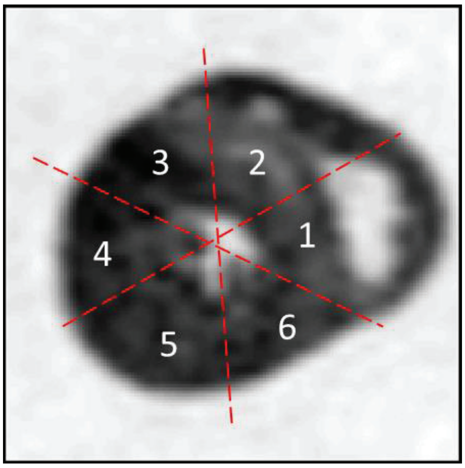

Figure 0.1:Ex-vivo short axis slice divided into 6 segments.

Figure 0.2: Top: variation of attenuation (S/S0) between the 192 directions for the 6 segments. Bottom: corresponding variation of artefact quantification between the 192 directions for the 6 segments.

Annex B

Ex vivo phantom global result for MD (mm²/s)

Monopolar no motion					Monopolar motion			
Tube 1	Tube 2	Tube 3	Tube 4	b-value	Tube 1	Tube 2	Tube 3	Tube 4
0,001811	0,002024	0,001611	0,002225	25	0,003825	0,003654	0,00503	0,005286
0,001771	0,00196	0,001537	0,002197	50	0,002539	0,002567	0,00292	0,003499
0,001758	0,001968	0,001551	0,002201	75	0,002285	0,002407	0,002347	0,003093
0,00175	0,001964	0,001541	0,0022	100	0,00212	0,002334	0,002181	0,002872
0,001763	0,001962	0,001557	0,002201	150	0,002017	0,00227	0,002018	0,002663
0,001772	0,001966	0,00156	0,002199	200	0,001954	0,002191	0,001926	0,002585
0,001764	0,001961	0,001567	0,002201	300	0,001918	0,002101	0,001815	0,002446
0,00176	0,001958	0,001563	0,002206	400	0,00191	0,002041	0,00178	0,002377

TRSE no motion					TRSE motion			
Tube 1	Tube 2	Tube 3	Tube 4	b-value	Tube 1	Tube 2	Tube 3	Tube 4
0,001786	0,002214	0,001802	0,002611	25	0,006613	0,007285	0,009876	0,006884
0,001846	0,002234	0,001586	0,002375	50	0,003672	0,004684	0,005668	0,004175
0,00182	0,002262	0,001629	0,002357	75	0,003028	0,003877	0,004088	0,003354
0,001806	0,002231	0,001622	0,002359	100	0,002713	0,003475	0,003357	0,003004
0,001778	0,002192	0,001584	0,002329	150	0,002404	0,003004	0,002662	0,002745
0,001755	0,002125	0,001588	0,002303	200	0,002203	0,002711	0,002372	0,002572
0,001738	0,002072	0,001555	0,002282	300	0,002061	0,002473	0,002048	0,002445
0,001737	0,002075	0,001544	0,002257	400	0,00199	0,002347	0,001889	0,002361

AMC no motion					AMC motion			
Tube 1	Tube 2	Tube 3	Tube 4	b-value	Tube 1	Tube 2	Tube 3	Tube 4
0,001613	0,001889	0,002092	0,002025	25	0,008354	0,006299	0,01112	0,007621
0,001573	0,001922	0,001593	0,002087	50	0,004556	0,003911	0,005603	0,004666
0,001628	0,001999	0,001544	0,00213	75	0,003649	0,003145	0,004192	0,003756
0,001656	0,001994	0,001499	0,00214	100	0,00309	0,002763	0,003299	0,003374
0,001671	0,002009	0,001539	0,002182	150	0,002568	0,002488	0,002733	0,003011
0,001698	0,002005	0,001541	0,002193	200	0,002291	0,002352	0,002381	0,002786
0,001717	0,002026	0,001553	0,00222	300	0,002147	0,00221	0,002149	0,002589
0,00172	0,002026	0,001572	0,002226	400	0,002048	0,002154	0,00204	0,002528

Table 0-1 : MD Global result for the three diffusion preparation, all tubes, all b-values

Ex vivo phantom global result for FA

Monopolar no motion					Monopolar motion			
Tube 1	Tube 2	Tube 3	Tube 4	b-value	Tube 1	Tube 2	Tube 3	Tube 4
0,428341	0,351836	0,450031	0,303529	25	0,634152	0,706219	0,667942	0,715623
0,204128	0,159853	0,260573	0,122286	50	0,603897	0,582204	0,623544	0,61787
0,121842	0,095413	0,155279	0,086427	75	0,537893	0,44986	0,608468	0,520091
0,130871	0,105507	0,172497	0,086315	100	0,472179	0,357093	0,547874	0,46144
0,081394	0,065946	0,094979	0,051327	150	0,391905	0,3368	0,477009	0,358284
0,066655	0,050554	0,073942	0,041495	200	0,325369	0,289191	0,387038	0,296035
0,051144	0,044376	0,063813	0,038407	300	0,212037	0,204543	0,295717	0,20974
0,047976	0,040362	0,051383	0,029825	400	0,195424	0,165774	0,235993	0,161148

TRSE no motion					TRSE motion			
Tube 1	Tube 2	Tube 3	Tube 4	b-value	Tube 1	Tube 2	Tube 3	Tube 4
0,551164	0,428638	0,576053	0,377265	25	0,502855	0,493096	0,470476	0,492687
0,410798	0,288628	0,419245	0,18968	50	0,550063	0,384831	0,422932	0,519808
0,310052	0,260534	0,287309	0,15443	75	0,533156	0,308886	0,381425	0,468153
0,247982	0,253234	0,207431	0,11841	100	0,479524	0,280128	0,406434	0,416166
0,219473	0,210706	0,199918	0,096015	150	0,349185	0,215687	0,328771	0,312618
0,195152	0,161386	0,133724	0,075964	200	0,227115	0,162721	0,33048	0,269166
0,162534	0,169705	0,107681	0,057482	300	0,169443	0,130047	0,210564	0,161492
0,147402	0,144032	0,088339	0,065653	400	0,184977	0,143507	0,181953	0,137712

AMC no motion					AMC motion			
Tube 1	Tube 2	Tube 3	Tube 4	b-value	Tube 1	Tube 2	Tube 3	Tube 4
0,566962	0,502586	0,520296	0,468219	25	0,56843	0,500918	0,565151	0,506361
0,404318	0,26506	0,415378	0,217242	50	0,531018	0,47291	0,586258	0,491615
0,237083	0,162353	0,267444	0,129087	75	0,481822	0,467883	0,561563	0,431684
0,194773	0,123044	0,248472	0,117908	100	0,485299	0,425459	0,552744	0,395673
0,162321	0,104453	0,216598	0,09794	150	0,471901	0,290972	0,489268	0,323317
0,109514	0,077862	0,1329	0,061486	200	0,414879	0,254246	0,455683	0,238621
0,085942	0,052846	0,090864	0,043477	300	0,337874	0,206899	0,359422	0,259838
0,076571	0,054568	0,090502	0,047429	400	0,265894	0,198993	0,309057	0,2378

Table 0-2 : FA Global result for the three diffusion preparation, all tubes, all b-values